HEAT TRANSFER NEAR THE TRANSITION TO TURBULENT FLUIDIZATION

by

Ana Stefanova

B.A.Sc. University "Saints Cyril and Methodius", 1995
M.A. Sc. University "Saints Cyril and Methodius", 2000

A THESIS SUBMITTED IN PARTIAL FULFILLMENT OF THE
REQUIREMENTS FOR THE DEGREE OF

DOCTOR OF PHILOSOPHY

in

THE FACULTY OF GRADUATE STUDIES

(Chemical and Biological Engineering)

THE UNIVERSITY OF BRITISH COLUMBIA

(Vancouver)

March, 2009

ABSTRACT

The turbulent fluidization flow regime, a transitional flow regime situated between bubbling and fast fluidization, has received relatively little attention in the heat transfer literature, despite its advantages for operating commercial gas-solid fluidized bed reactors. This work investigates simultaneously bed–to–surface heat transfer coefficients and changes in the local hydrodynamics near the transition from bubbling to turbulent fluidization flow regimes.

Experiments were conducted with fluid cracking catalyst (FCC) and alumina particles in columns of different diameters, a 0.29 m ID column at UBC in Vancouver, Canada, and a 1.56 m ID column at CSIRO Minerals in Clayton, Australia. Radial and axial locations of the heat transfer surface, static bed height and superficial gas velocity were varied. Two distributor configurations were examined in the smaller column: perforated plate and bubble cap. The transition to turbulent fluidization was determined based on changes in trends and features of pressure and optical probes signals.

To measure the bed-to-immersed surface heat transfer coefficients, a modular electrically heated vertical tube was designed. The results showed maximum heat transfer coefficients near the onset of turbulent fluidization and increased uniformity of the radial and axial distributions of heat transfer coefficients when the turbulent fluidization regime became dominant. It was discovered that the transition to turbulent fluidization was more complex and occurred gradually across the bed in the larger column. However, the maximum heat transfer coefficient was not affected by the column size. The Froude number, based on the column diameter, provided a good scaling parameter in regions of similar flow structure.

A novel transparent heat transfer probe was designed for transient local heat transfer measurement at the column wall and simultaneous evaluation of the hydrodynamics at the heat transfer surface. This study provided insight into the changing dominant mechanism of heat transfer at the onset of turbulent fluidization.

A probabilistic heat transfer model was developed, based on the packet renewal theory and the probability of having particle packets corresponding to each hydrodynamic regime at the heat transfer surface. The novelty of the model is the contribution of packets of intermediate voidage, typical for turbulent fluidized beds, to the total heat transfer coefficient.

TABLE OF CONTENTS

LIST OF TABLES

LIST OF FIGURES

NOMENCLATURE

A_{eff} Effective heat transfer surface area of the transparent wall probe, m^2

Ar Archimedes number, $Ar = g\, d_p^{\,3} \rho_g\, (\rho_p - \rho_g)/\mu_g^{\,2}$

A_s Heat transfer surface area, m^2

A_t Column cross-sectional surface area, m^2

A_{xy} Surface area in estimating heat losses from transparent wall probe, m^2

Bi Biot number, $Bi = h\Delta x/k$

C_r Correlation coefficient employed by Wender and Cooper (1958), -

c_{pp} Particle heat capacity, J/kgK

c_{pg} Gas heat capacity, J/kgK

D_b Mean bubble diameter, m

D_t Column diameter, m

d_p Mean particle diameter, m

d_{pi} Sieve diameter of particles , m

d_t Diameter of the tube, m

E Covariance function

$F(f)$ Fourier transform

Fr Froude number, $Fr = U/(gD_t)^{0.5}$

f Frequency, Hz

f_A Fractional surface coverage, -

f_b Frequency of bubbles, Hz

f_d Frequency of dense phase packets, Hz

f_n Natural frequency, Hz

G Greyscale value (0 is black and 255 is white), -

G_s Solids fluxs, kg/m^2s

g Gravitational acceleration, m/s^2

h	Heat transfer coefficient, W/m^{2}K
H	Expanded bed height, m
H_0	Static bed height, m
H'	Dense bed height corresponding to minimum fluidization voidage, m
h_{cond}	heat transfer coefficient due to conduction, W/m^{2}K
h_{conv}	Heat transfer coefficient due to convection, W/m^{2}K
h_g	Heat transfer coefficient due to gas convection, W/m^{2}K
h_{max}	Maximum heat transfer coefficient, W/m^{2}K
h_{pa}	Time-average particle packet heat transfer coefficient, W/m^{2}K
h_{pai}	Instantaneous particle packet heat transfer coefficient, W/m^{2}K
h_{rad}	Heat transfer coefficient due to radiation, W/m^{2}K
I	Electrical current, A
k_{eff}	Effective thermal conductivity of particle packet , W/mK
k_g	Gas thermal conductivity, W/mK
k_{wall}	Effective thermal conductivity near the wall, W/mK
L	Bed dimension (D_t or H), m (in Glicksman, 2003)
l_t	Length of heat transfer surface, m
Nu	Nusselt number, $Nu = h\, d_p / k_g$
P	Power, W
Pr	Prandtl Number, $Pr = c_{pg}\, \mu_g / k_g$
p	Pressure, Pa
Δp_{bed}	Pressure drop across the dense bed, Pa
Δp	Differential pressure, kPa
Q_g	Generated heat, W
Q_l	Heat losses, W
R	Reduced column radius ($R = R_t - r_t$), m
R_{air}	Thermal resistance through insulating gas layer of the wall probe, K/W

Ra_L	Rayleigh number, $Ra_L = Gr_L\ Pr = g\ \rho\ \alpha\ \Delta T\ d^3\ /\mu\ k_g$
R_e	Electrical resistance, ohm
Re_D	Tube Reynolds number, $Re_D = U\ D_t\ \rho_g\ /\ \mu_g$
Re_p	Particle Reynolds number, $Re_p = U\ d_p\ \rho_g\ /\ \mu_g$
R_f	Thermal resistance through polyester film of transparent wall probe, K/W
R_{plex}	Thermal resistance through outside plexiglass plate, K/W
R_s	Thermal resistance through inner plexiglass plate, K/W
R_t	Column radius, m
R_w	Thermal resistance in packet renewal model, K/W
r	Distance from column axis to heater axis, m
r_t	Radius of heater tube, m
T	Temperature, ^{0}C
T_b	Bed temperature, ^{0}C
T_s	Surface temperature, ^{0}C
t	Time, s
t_{cb}	Contact time of particle associated with bubbles, s
t_{ce}	Contact time of clusters in dense phase, s
t_{di}	Time when dense phase is present at probe, s
t_{pc}	Average particle contact time, s
t_{tot}	Total sampling time, s
U	Superficial gas velocity, m/s
U_c	U at onset of turbulent regime, m/s
U_k	U at onset of turbulent regime defined from leveling off the standard deviation of pressure fluctuations, m/s
U_{mb}	U at onset of bubbling, m/s
U_{mf}	Minimum fluidization velocity, m/s
U_{ms}	Minimum slugging velocity, m/s

U_{opt}	U corresponding to maximum heat transfer coefficient, m/s
U_{tr}	Transport velocity, m/s
V	Voltage, V
V_b	Bubble velocity, m/s
x_i	Fraction of particles having diameter $< d_{pi}$
z	Distance above distributor, m
Δz	Vertical interval, m

Greek symbols

δ_d	Fraction of time during which probe is in contact with dense phase (dense phase fraction), -
δ_f	Gas layer thickness, m
δ_{int}	Fraction of time during which probe is in contact with intermediate phase (immediate phase fraction), -
δ_v	Fraction of time during which probe is in contact with voids (void phase fraction), -
$\bar{\varepsilon}$	Overall mean bed voidage, -
ε	Voidage, -
ε_0	Loose packed bed voidage, -
ε_{cs}	Time-mean cross-sectional voidage, -
ε_{int}	Voidage of intermediate phase, -
ε_{mf}	Voidage at minimum fluidization, -
ε_N	Normalized local voidage, -
ε_{pa}	Particle packet voidage, -
φ	Particle shape factor, -
κ	Dimensionless constant introduced by Martin (1980), $\kappa = 2$ to 4
μ_g	Gas viscosity , Pa s^{-1}
ρ_p	Particle density, kg/m^3

ρ_g	Gas density, kg/m^3
σ_{AP}	Standard deviation of absolute pressure fluctuations, kPa
σ_{DP}	Standard deviation of differential pressure fluctuations, kPa
τ	Contact time at the wall of individual packet, s

Subscripts

(1), (2), (3)	Methods (1), (2) and (3)
d	dense
g	gas
h	heater
int	intermediate
max	maximum
mf	minimum fluidization
min	minimum
ms	minimum slugging
N	normalized
OP	optical probe
opt	optimum
p	particle
sl	slugging
v	void

Abbreviations

AP	Absolute pressure
DP	Differential pressure
CFB	Circulating fluidized bed
SE	Standard error
SD	Standard deviation

ACKNOWLEDGEMENTS

C h a p t e r   1

1. INTRODUCTION

1.1. History and applications of fluidized beds

Due to their excellent solid-fluid contacting, fluidized beds, in which small solid particles are suspended and kept in motion by fluid flow, are applied in variety of chemical and physical processes. The first industrial fluidized-bed application began in the 1920's with coal gasification, but really took off with the needs of the petroleum industry, with the development of the fluidized bed catalytic cracking process in the 1940's. Today, fluidized bed application extends to many industries besides petrochemical and coal, such as polymer production, power production, metallurgy, nano-particles, electrochemistry, food processing, pharmaceuticals, water and waste treatment and many others.

One major application of gas-solid fluidized beds is chemical reactors (Grace et al., 2005). Many of the fluidized bed reactors for catalytic reactions operate with small (catalyst) particles at relatively high superficial gas velocities, 0.5-1.5 m/s, and require controlled isothermal operation. Experience in operating these units has shown that increased gas velocities lead to a more homogeneous flow structure, improved mixing and high heat transfer rates. These are features of the turbulent fluidization flow regime, a transitional fluidization regime situated between bubbling and fast fluidization. Major applications of turbulent fluidization include acrylonitrile production, oxychlorination, Fisher-Tropsch synthesis, fluid catalytic cracking (FCC) catalyst regeneration, ore roasting and fluid bed driers.

To allow for isothermal operation, heat can be removed or added by heat transfer surfaces located upstream or downstream from the fluidized bed, immersed vertical or horizontal tubes in the bed, or heat transfer surfaces at the walls of the column. A typical configuration of a fluidized bed reactor with immersed tubes is shown in Figure 1.1. The major components are the reactor vessel (column) (1), distributor plate (2), solids return system (3) and heating or cooling equipment (4).

Despite the advantages of fluidized bed reactors (e.g., ability to operate in a continuous state, uniform particle mixing and uniform temperatures), there are some disadvantages, a major one being a lack of understanding. Much of the information required to design and operate fluidized bed reactors is empirical, based on experience with existing units.
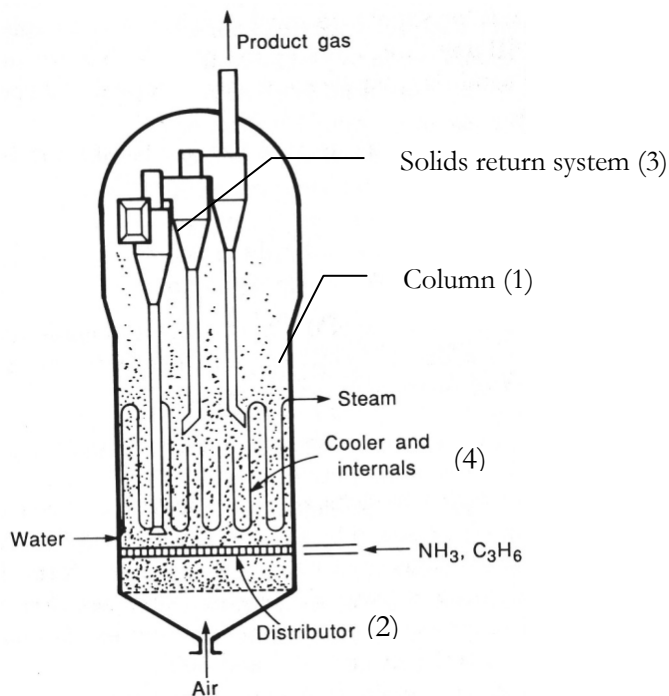
Figure 1.1. Fluidized bed reactor for acrylonitrile production (Kunii and Levenspiel, 1991).

1.2. Fluidization flow regimes and transitions

To characterize the fluidization properties of solid particles, Geldart in (1973) divided them into four groups: C-cohesive ($d_p < 30$ μm), which fluidize poorly due to inter-particle forces; A-aeratable ($d_p \approx 30$–100 μm) characterized by excellent fluidization properties and small bubbles; B- bubble readily ($d_p \approx 100$-800 μm), and D - dominantly inertial ($d_p > 800$ μm) (Grace et al., 2006).

Gas-solid fluidized beds can be operated in different fluidization flow regimes as the superficial gas velocity, U, increases. When U reaches the minimum fluidization velocity, U_{mf}, the drag force overcomes the weight of the particles and they becomes fluidized. For group B particles, U_{mf} usually coincides with the minimum bubbling velocity, U_{mb}, whereas for group A particles,

bubbling is delayed until a slightly higher U is reached. With the onset of bubbling fluidization, the motion of particles is enhanced. The vertical movement of particles in the bed is closely associated with the rising bubbles through the mixture of solids and interstitial gas (dense phase), as they lift particles in their wakes and create drift. Particles in the bed are also displaced horizontally due to bubbles coalescing, splitting and erupting on the bed surface.

| Bubbling | Slugging | Turbulent | Fast – upper zone |
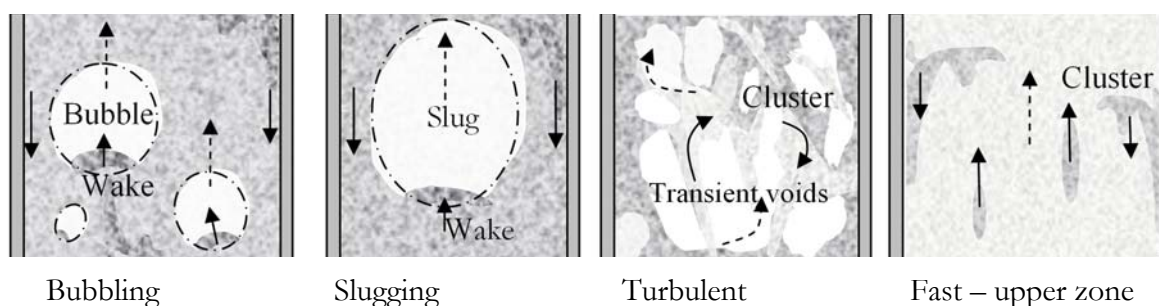
Figure 1.2. Typical flow structure in specific fluidization regimes. Dashed arrows represent gas flow; solid arrows represent solids flow.

When the superficial gas velocity is increased further, the bed might undergo a transition to slugging or turbulent fluidization depending on the ratio H/D_t and the stability of the bubbles. Slugging fluidization will most likely occur in laboratory-scale units of group B and D particles rather than in large industrial units. In slugging beds, the bubbles coalesce into single voids (slugs), causing periodic fluctuation of the bed level as they rise and burst at the surface. Gas and solids mixing rates are lower compared to bubbling beds. When bubbles (or slugs) can grow until they become unstable and break up, the bed undergoes a transition to turbulent fluidization, the onset of which is denoted by the superficial gas velocity, U_c. The definition of and methods to determine U_c vary (Bi et al., 2000). U_c has been found to depend on: measurement method, particle size distribution, solids circulation rate, static bed height, column diameter, particle properties, pressure, temperature and presence and type of internals. Turbulent fluidized beds are characterized by increased homogeneity, rapid mixing and favourable heat transfer, high entrainment and a diffuse bed surface. The local flow structure appears to be transitional between bubbling and fast fluidization and contains features of both. With a further increase of superficial gas velocity, the transport velocity, U_{tr}, is reached and significant particle entrainment occurs, reducing the bed to a region near the distributor. The entrained particles are captured and re-circulated to the bed in a unit configuration known as a circulating fluidized bed (CFB). The flow structure in the bottom region is similar to the turbulent bed, while the upper

region consists of a dilute suspension in which particle clusters or streams are suspended. Typical flow structures in different fluidization regimes are illustrated in Figure 1.2.

The transition from one regime to another is gradual, and often the boundaries between regimes are ambiguous. In addition, the dominant flow structure in different regions might belong to different fluidization regimes (for example, bubbling in the lower region of the bed and slugging or turbulent in the upper region). To allow for the gradual transition and overlap between fluidization flow regimes, a probabilistic model based on the probability of the bed exhibiting behaviour typical of a certain fluidization regime was applied by Abba (2003) and Constantineau (2006).

1.3. Bed-to surface heat transfer in fluidized beds

Heat is transferred between a surface and fluidized bed in three ways: conduction from particles, convection by gas, and radiation, i.e., the overall heat transfer coefficient is given by:

$$h = h_{cond} + h_{conv} + h_{rad} \tag{1.1}$$

Which of these modes of heat transfer and in what proportion relative to the total heat transfer depend on particle and gas properties and operating conditions. For fluidized bed reactors with small catalyst particles and $T < 600\ ^{0}C$, h_{cond} is dominant (see Botterill, 1986).

The bed-to surface heat transfer is affected by many parameters:

- Particle properties (mean diameter, d_p , density, ρ_p, heat capacity, c_{pp}, thermal conductivity, k_p , shape, coatings, size distribution)

- Gas properties (density, ρ_g, thermal conductivity, k_g, heat capacity, c_{pg}, viscosity, μ_g)

- Superficial gas velocity (U)

- Pressure (*p)*

- Temperature (*T)*

- Static bed height (H_0)

- Unit size and configuration (distributor, column diameter, D_t, bed height, H)

- Heat transfer surface geometry and configuration: size (surface length, l_t, tube diameter, d_t), location (relative radial position, r/R, relative axial position, z/H) and orientation.

Many of these parameters have been studied (see reviews of Gelperin and Einstein, 1971; Saxena, 1989; Botterill, 1986) and their effects have been well established, especially in bubbling beds of group B particles and laboratory columns. For small particle systems, where h_{cond} is dominant, heat transfer is controlled by the volumetric heat capacity of particles, ρ_p, c_{pp}, and gas thermal conductivity, k_g (Saxena, 1989).

The effect of hydrodynamic regime transition has rarely been considered in the literature. Starting from the minimum fluidization velocity, the heat transfer coefficient increases and reaches a maximum. Some researchers suggest that the maximum, which occurs because decreasing particle concentration ultimately nullifies the increasing frequency of particle exchange, corresponds to the onset of turbulent fluidization (Sun and Chen, 1989; Basu et al., 1986; Staub, 1979). From the reviewed data (Table B.2 in Appendix B), increasing U beyond the value corresponding to the maximum heat transfer coefficient, results in two different trends: (1) the heat transfer coefficient reaches an asymptotic maximum and does not change much with further increase in velocity; and (2) the heat transfer coefficient decreases with increasing superficial gas velocity. The first trend was usually reported for smaller and lighter group A particles in larger columns, while the second was found for group B particles and small, laboratory-scale columns. There is lack of data in the literature on heat transfer for group A particles extending to higher superficial gas velocities typical of the turbulent fluidization regime.

The effects of bed dimensions (H_0, D_t) on heat transfer coefficients have been reported differently in the literature (Gelperin and Einstein, 1971). Since the effect of scale is very important, more research is needed.

1.3.1. Previous work on heat transfer in turbulent fluidization regime

Although interest in the transition to and the hydrodynamics of the turbulent fluidization regime has been high in the past two decades, little work has been reported on heat transfer in this regime. Only Staub (1979, 1982), Ku et al. (1981), Basu et al. (1986), Sun and Chen (1989), Hashimoto et al. (1990) and Leu et al. (1997) reported on turbulent fluidization heat transfer. In

reviews of fluid bed heat transfer, only Botterill (1986) and Kunii and Levenspiel (1991) mention the existence of the turbulent fluidized bed.

Experimental studies of turbulent fluidized beds, have confirmed that the heat transfer coefficient is higher for smaller particles. Leu at al. (1997) investigated group A and B particles using their measurements as well as literature data. Sun and Chen (1989) utilized two sizes of group A particles, whereas Basu et al. (1986) used two sizes of group B particles. In the study of Staub (1979), the particles were large, close to the B-D boundary.

Staub (1979), Basu et al. (1986) and Sun and Chen (1989) reported maximum heat transfer coefficients near the onset of turbulent fluidization. The maximum was said to occur because the particle renewal on the tube surface becomes overbalanced by the increasing coverage by voids.

Data preceding the onset of turbulent fluidization were not shown by Leu et al. (1997), so it was impossible to distinguish the maximum heat transfer coefficient. However, they noticed that in the turbulent regime for group A particles, the local bed-to-wall heat transfer coefficient increased with increasing bed voidage, whereas for group B particles the opposite was found.

Most measurements were performed with small probes, except for Staub (1979) who had a horizontal tube bank immersed in the bed. The column diameter varied from 0.1 m in Basu et al. (1986) to 0.8 m in Sun and Chen (1989), but no general conclusion could be deduced on its effect.

Hashimoto et al. (1990) measured the heat transfer coefficient in the freeboard region of a turbulent fluidized bed in two different units, varying the pressure and temperature. For the same gas velocity, the particle convective heat transfer coefficient varied greatly with the type of gas, temperature, pressure and the geometry of the apparatus. The concentration of particles in the freeboard and the amount of particles recycled were considered the most important factors governing the heat transfer.

Modeling of heat transfer in the turbulent fluidization flow regime was only attempted by Hashimoto et al. (1990), for the freeboard of a turbulent bed, and Staub (1979), for immersed tube banks. Staub (1979) suggested that in the turbulent fluidized bed regime, solids flow and heat transfer correlations based on bubbling bed flow will not predict performance. They

proposed a turbulent fluidized bed solids flow model and a heat transfer model (see Appendix A) that showed satisfactory agreement with their immersed tube bank heat transfer data.

Although very few experimental studies on heat transfer report explicitly on beds operated in the turbulent fluidization regime, there are undoubtedly studies in the literature where the hydrodynamic regime was not determined, but where the turbulent flow regime was present.

1.3.2. Models and correlations

Overall, the heat transfer coefficient can be written as

$$h = \delta_d\, h_{\mathrm{pa}} + (1 - \delta_d)h_{\mathrm{g}} + h_{rad} \tag{1.2}$$

where, δ_d is the fraction of time during which the surface is exposed to particles, h_{pa} is the time-mean heat transfer coefficient of the particle packet during its residence at the surface, h_g is the gas convection heat transfer coefficient and h_{rad} is heat transfer by radiation. For particles smaller than 1mm in diameter and temperatures $<600^0$C the gas convection and radiation component can be neglected. The time-mean heat transfer coefficient is then:

$$h = h_{\mathrm{cond}} = \delta_d\, h_{\mathrm{pa}} \tag{1.3}$$

For small particles, heat is able to penetrate multiple layers of particles in the packet and transient conduction through a semi-infinite packet can be considered. The most popular mechanistic heat transfer model is the packet renewal model first proposed by Mickley and Fairbanks (1955). This model assumes that particle packets arrive at the surface where they transfer heat by conduction in a transient manner before being replaced by other packets or clusters. They proposed the following relationship for the instantaneous heat transfer coefficient:

$$h_{pai} = \sqrt{\frac{k_{eff}\, \rho_p c_{pp}\left(1 - \varepsilon_{pa}\right)}{\pi\tau}} \tag{1.4}$$

The heat transfer is then dependent on the thermal conductivity of the packet (k_{eff}), its volumetric heat capacity ($c_{pp}\,\rho_p(1-\varepsilon_{pa})$), and the time ($\tau$) spent at the surface before being replaced. For a bubbling bed, the packet is usually assumed to be at minimum fluidization conditions, i.e. $\varepsilon_{pa} = \varepsilon_{mf}$.

The time-average heat transfer coefficient of the packet can then be obtained by integration of equation (1.4), leading to:

$$h_{pa} = \frac{1}{t} \int_0^t \sqrt{\frac{k_{eff} \rho_p c_{pp}\left(1 - \varepsilon_{pa}\right)}{\pi \tau}} d\tau = \sqrt{\frac{2k_{eff} \rho_p c_{pp}(1 - \varepsilon_{pa})}{\pi t_{pc}}} \qquad (1.5)$$

In bubbling beds, the contact time of packets is assumed to be directly related to the bubble frequency, and the average particle contact time, t_{pc} can then be written as:

$$t_{pc} = \frac{\delta_d}{f_d} \approx \frac{1 - \delta_b}{f_b} \qquad (1.6)$$

where, $\delta_d = 1 - \delta_b$ is the fraction of time that the surface is occupied by the dense phase, and f_d and f_b are the frequencies of the arrival of dense phase packets and bubbles, respectively.

In bubbling beds with random renewal by bubbles, the time-averaged h for small particles at low temperatures, and utilizing equation (1.6), is given by (Kunii and Levenspiel, 1991a):

$$h = h_{cond} = 1.13\sqrt{(1 - \delta_b)k_{eff}\rho_p(1 - \varepsilon_{mf})c_{pp}f_b} \qquad (1.7)$$

The effective thermal conductivity of the particle packet, k_{eff}, can be estimated from the gas and particle thermal conductivities. There are several correlations in the literature for estimating k_{eff}, some of which appear in Appendix A.

An additional thermal resistance is often introduced (e.g. Baskakov, 1964). Without this, the packet renewal model tends to over-predict the heat transfer. Many researchers therefore include a heat conduction resistance through a gas layer of thickness, δ_f, i.e.,

$$R_w = \delta_f / k_{wall} \qquad (1.8)$$

Then, from equation (1.3), the heat transfer coefficient becomes:

$$h = \frac{\delta_d}{\frac{1}{h_{pa}} + R_w} \qquad (1.9)$$

Some relationships to estimate the gas film resistance are presented in Table A.2 of Appendix A. The effective thermal conductivity near the wall, k_{wall}, is often assumed equal to the gas conductivity, k_g. The existence of the gas film has been explained in terms of non-continuum effects near the point of contact between the surface and the particle. On the other hand, analysis by Molerus et al. (1995) provides arguments for the thin gas layer for small particles explained by a lateral force on rigid spherical particles under laminar shear flow conditions.

The packet renewal model has been extended to fast fluidized beds (e.g. Lints and Glicksman, 1993), and modified to accommodate typical hydrodynamics. In that case, the particle packets were clusters or streamers with lower density than the dense packets found in bubbling beds. In a similar manner, it might be possible to extend the applicability of the packet renewal model into the range of superficial gas velocities corresponding to the turbulent bed by examining the local hydrodynamics. The packet renewal model has been found to work well in bubbling fluidization and in the upper zone of fast fluidized beds if the proper hydrodynamics are included (Kunii and Levenspiel, 1991; Chen et al., 2005).

Another approach to modeling bed-to-surface heat transfer is to use "particle models", where the heat transfer is considered to be from single particles, particle strings or particle layers. One such model is that of Martin (1980) based on an analogy between particle motion in fluidized beds and random kinetic motion of gaseous molecules. Although it is unlikely that the same phenomena that govern the motion of gas molecules are responsible for particle motion in a fluidized bed, the model has been reported to give good predictions (Martin, 1984). Details of this model are given in Appendix A.3.

The number of empirical and semi-empirical correlations available in the literature is vast. Many reviews have been provided evaluating correlations for determination of bed-to-surface heat transfer coefficients in gas-solid fluidized beds (e.g. Botterill, 1986; Saxena 1989; Kunii and Levespiel, 1991; Oka and Anthony, 2003). Considering that heat transfer in fluidized beds is affected by many factors, the applicability of the correlations is usually limited to a narrow range of conditions. Comparison of different heat transfer correlations in the literature and experimental data for bubbling beds showed deviations of the order of 100% (Chen et al., 2003).

Molerus and Wirth, 1997 developed the following semi-empirical correlation applicable to a wide range of operating conditions by combining dimensionless groups and empirical correlations:

$$h = \frac{k_g}{l_l}\left[\frac{0.125(1-\varepsilon_{mf})\left[1+33.3\left\{\sqrt[3]{\left[(U-U_{mf})/U_{mf}\times(\rho_p c_{pp}/k_g g)\right]}(U-U_{mf})\right\}^{-1}\right]^{-1}}{1+(k_g/2c_{pp}\mu)\left\{1+0.28(1-\varepsilon_{mf})^2\left[\rho_g/\rho(\rho_p-\rho_g)\right]^{0.5}\left[\sqrt[3]{\left[\rho_p c_{pp}/k_g g\right]}(U-U_{mf})\right]^2 U_{mf}/(U-U_{mf})\right\}} + 0.165\mathrm{Pr}^{1/3}\left(\frac{\rho_g}{\rho_p-\rho_g}\right)^{1/3}\left[1+0.05\left(\frac{U-U_{mf}}{U_{mf}}\right)^{-1}\right]^{-1}\right] \quad (1.10)$$

where $l_l = \left[\dfrac{\mu}{\sqrt{g}(\rho_p-\rho_g)}\right]^{2/3}$ is a characteristic length.

The particle diameter and bed voidage are not explicitly included, but their effect is incorporated through U, U_{mf} and ε_{mf}. Comparison of this correlation with experimental data for different particle and gas properties and operating conditions showed a close match (Molerus and Wirth, 1997), even at higher gas velocities where turbulent fluidization might have occurred.

Other correlations that might be applicable to the turbulent fluidization regime are also listed in Appendix A.3. More data are needed to evaluate the applicability of these correlations to turbulent beds.

1.4. Outstanding issues

- Maximum heat transfer coefficients have been reported to correspond closely to the onset of the turbulent flow regime. Given the advantage of operating at or near the maximum heat transfer coefficient when heat transfer is important, it is of value to investigate, understand and model heat transfer in this flow regime. Research is needed to clarify why a maximum heat transfer coefficient is reached with increasing U.

- Although many commercial reactors operate in the turbulent fluidization flow regime, there is a lack of correlations that acknowledge the transition to turbulent fluidization. The lack of experimental data explicitly reported to be in the turbulent fluidization regime makes it difficult to establish the applicability of heat transfer models and correlations to turbulent beds.

- Knowledge of the effect of scale–up on bed hydrodynamics and heat transfer is required. Larger units have been reported to give higher mixing rates and to exhibit different flow structures than scaled-down counterparts (Matsen, 1996). This could be due to different flow

regimes in columns of different size. Increased diameter and lower H/D_t have been found to decrease the transition velocity U_c (Sun and Chen, 1989, Ellis et al., 2004). How column size affects heat transfer needs to be determined.

- In order to design and position heat transfer surfaces for optimal operation it is necessary to know the radial and axial distribution of the bed-to-surface heat transfer coefficient. This issue has not been addressed in the turbulent fluidization regime.

- Although the basic mechanisms for heat transfer in fluidized beds are established, models that give reliable predictions for a wide range of operating conditions and that follow the transition from one flow regime to another are not available.

1.5. Objectives

To address some of the issues identified above the following objectives were set for this work:

- Conduct simultaneous measurements of hydrodynamics and heat transfer from an immersed vertical tube in a bed of group A particles, while varying the superficial gas velocity, radial position, tube length, bed height and gas distributor.

- Test different methods for determining the onset of the transition to turbulent fluidization to reduce the uncertainty related to U_c.

- Examine the effect of the transition to turbulent fluidization on the bed-to-surface heat transfer in columns of different diameter.

- Develop a novel, transparent heat transfer probe to provide visual accessibility of the heat transfer surface while the transient instantaneous heat transfer coefficient is measured to provide valuable information on the dominant heat transfer mechanism.

- Test the existing bed-to-surface heat transfer models and empirical correlations in the turbulent fluidization flow regime.

- Extend the applicability of the packet renewal model to superficial gas velocities belonging to turbulent regime, both for an immersed tube and the wall.

1.6. Thesis outline

The thesis is in seven chapters. Chapter 2 describes the experimental apparatus, instrumentation and data analysis methods used to meet some of the objectives. Chapter 3 presents the results and discussion on the overall and local bed hydrodynamics and the transition to turbulent fluidization. Several methods to obtain the transition velocity are examined and compared. The hydrodynamics results of this chapter set the stage for the immersed tube heat transfer study presented in Chapter 4, where the effects of superficial gas velocity, static bed height, radial and axial location, particle properties, distributor, and column diameter are presented and discussed.

In Chapter 5, the focus shifts to transient heat transfer at the wall, describing the design of the transparent probe, data analysis methods and the results of simultaneous measurements of the transient heat transfer and local hydrodynamics. This gives insight into the change in dominant heat transfer mechanism. Heat transfer data from Chapters 4 and 5 are compared to existing heat transfer models and correlations in Chapter 6. Furthermore, the observations of the hydrodynamics and heat transfer from the previous chapters are utilized to develop a probabilistic approach to heat transfer modeling based on the packet renewal theory. Chapter 7 summarizes the conclusions from this work and suggests topics of interest for future research. Additional information is given in the appendices.

2. EXPERIMENTAL METHODS

2.1. Experimental plan

To meet the objectives stated in the previous chapter, an experimental investigation was planned and conducted. The experiments were performed in two columns, one of 0.29 m diameter at the University of British Columbia, and the other of 1.56 m diameter at CSIRO Minerals, Clayton Australia. The operating conditions and variables changed during the experimental runs are summarized in Table 2.1. Two particle types were used, one was fluid catalytic cracking catalyst (FCC) and the other refractory grade alumina. The effect of two distributor configurations, two vertical tube lengths, three static bed heights, various radial positions of the heater (from $r/R = 1$, touching the inside of the column wall, to $r/R = -1$, touching the inside of the column wall on the opposite side) and various superficial gas velocities.

Table 2.1. Experimental plan –operating conditions

D_t, m	Bed material	Distributor plate	Total length of heating surface, m	Static bed height, m	Radial position of the heater	Superficial gas velocity, m/s
0.29	FCC	Perforated	0.101	0.80	-1 to 1	0 to 1
0.29	FCC	Perforated	0.101	1	0	0 to 1
0.29	FCC	Perforated	0.101	1.2	0 to 1	0 to 1
0.29	FCC	Perforated	0.505	0.8	0	0 to 1
0.29	FCC	Perforated	0.505	1.2	0	0 to 1
0.29	FCC	Bubble cap	0.101	0.8	0	0 to 1
0.29	Alumina	Perforated	0.505	0.8	0	0.1 to 1.2
0.29	Alumina	Bubble cap	0.101	0.8	0 to 1	0 to 1.2
1.56	Alumina	Bubble cap	0.101	0.8	0 to 0.8	0.1 to 1.2
0.29	Alumina	Bubble cap	0.056	0.8	wall	0.03 to 1.2

2.2. Fluidization column - 0.29 m ID

Most heat transfer experiments were performed in the 0.29 m ID, 4.5 m high Plexiglas fluidization column shown in Figure 2.1 and described previously by Ellis (2003). Air is supplied by a positive displacement type Roots URAI blower (1) with a maximum flow rate of 425 Nm^3/h at 69 kPa. The air flow to the column is controlled by a ball valve (2) in the bypass line and measured by an orifice plate (3).

The column (6) has 59 ports distributed vertically along the wall on opposite sides. The top of the column is expanded to facilitate the return of particles to the upper surface of bed when they are ejected into the freeboard. Solids entrained through the abrupt exit are collected by two cyclones. The primary cyclone (9a) discharges solids into a primary return leg (10a). The gas and fine particles leaving the top of the primary cyclone enter a secondary cyclone (9b) where more solids are collected and returned to the bed via a secondary return leg (10b). Each return leg is equipped with a butterfly valve (11a, 11b). The two return legs merge before connecting to a section equipped with a flapper valve (12), controlling the particle flow to the bed by pressure balance. The exit from the secondary cyclone is connected through a bag house filter (13) to the ventilation system.

2.2.1. Distributor plate

Two distributor plates were used in the 0.29 m ID column, perforated and bubble cap distributors. The perforated plate distributor (5) consists of two aluminum perforated plates, each having 98 holes in an equilateral triangular pattern with centres 32 mm apart. The diameter of the holes on the upper plate is 5.6 mm, whereas it was 6.4 mm on the lower one, giving an open area ratio of 3.8%. To prevent the particles from falling through the holes, a 38 μm (400-mesh) stainless steel screen was sandwiched between the two plates.

The other distributor was a bubble cap distributor shown on Figure 2.2. Eighteen bubble caps are distributed in an equilateral triangular pattern, with 62 mm between centres. Three spacers were inserted between the cap and the plate for each nozzle to ensure that the cap was parallel to the plate with a uniform 4.5 mm gap. The open area ratio is 1%.
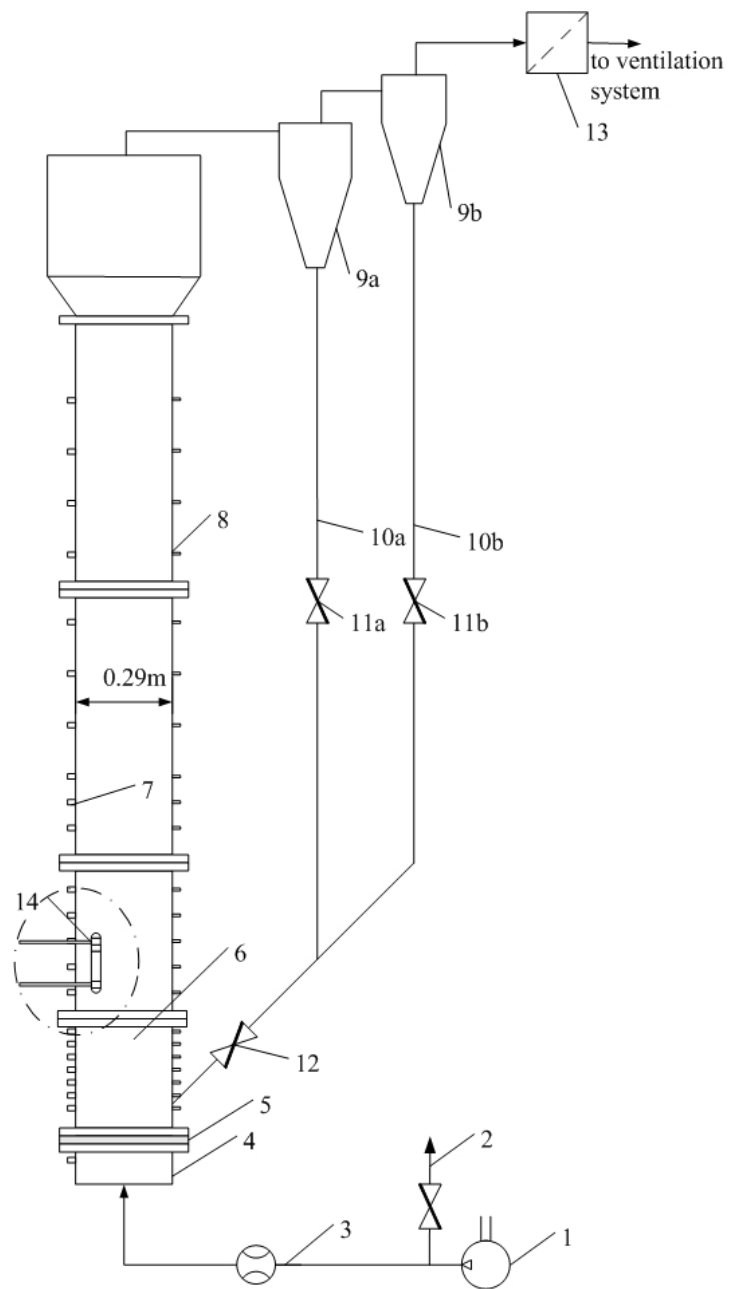
Figure 2.1. Experimental unit at UBC, 0.29 m ID

1-blower, 2-bypass line, 3-orifice plate, 4-windbox, 5-distributor, 6-column, 7- ½" NPT ports, 8- ¼" NPT ports, 9 a & b – cyclones, 10- return legs, 11-ball valves, 12- flapper valve, 13- bag house filter, 14- heater
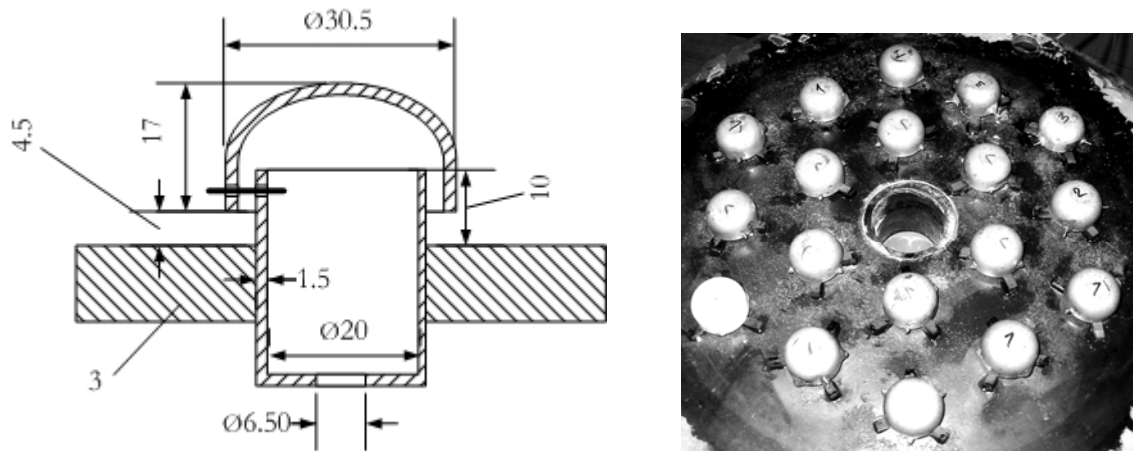
Figure 2.2. Bubble cap distributor for 0.29 m column (All dimensions in mm).

2.2.2. Immersed heat transfer tube

To measure the heat transfer coefficients from an immersed object to the bed and ensure flexibility in investigating the effect of different parameters, a tube assembled from a number of heating (1) and insulating (2) sections (modules), shown in Figure 2.3, was designed and manufactured. The modular design of the heater tube allows the tube length to be varied, by adding and removing heating sections (heaters). In order to determine the local heat transfer coefficient along the tube, each heating section was individually heated, with a Teflon insulating section between neighbouring sections to minimize axial conduction. All sections of the tube were hollow to allow the electrical and thermocouple wires (3) to pass through the core of the tube and then out of the column. When all the heating and insulating sections are arranged, a 3 mm stainless steel rod (4), threaded at its ends, passes through and fastens at the ends with two nuts (5). This holds the heater tube parts tightly together and ensures strength. The end nuts are embedded in semi-spherical Teflon caps (6) to reduce the disturbance of the flow (Di Natale et al., 2007). Horizontal tubes (7) are connected to the insulation sections at the end (8) to support the tube and to allow positioning at different radial positions inside the column. The heater tube is shown mounted in the column in Figure 2.4. Four 3/4" (19 mm) NPT ports, located at a 70^0 angle from the 1/2" (12.7 mm) NPT ports used (see Figure 2.7) for pressure measurement, were used to support and position the heater tube.

1. Heater
2. Insulating section
3. Electrical and thermocouple wires
4. Rod
5. Nuts
6. Teflon caps
7. Support tubes
8. End insulating sections
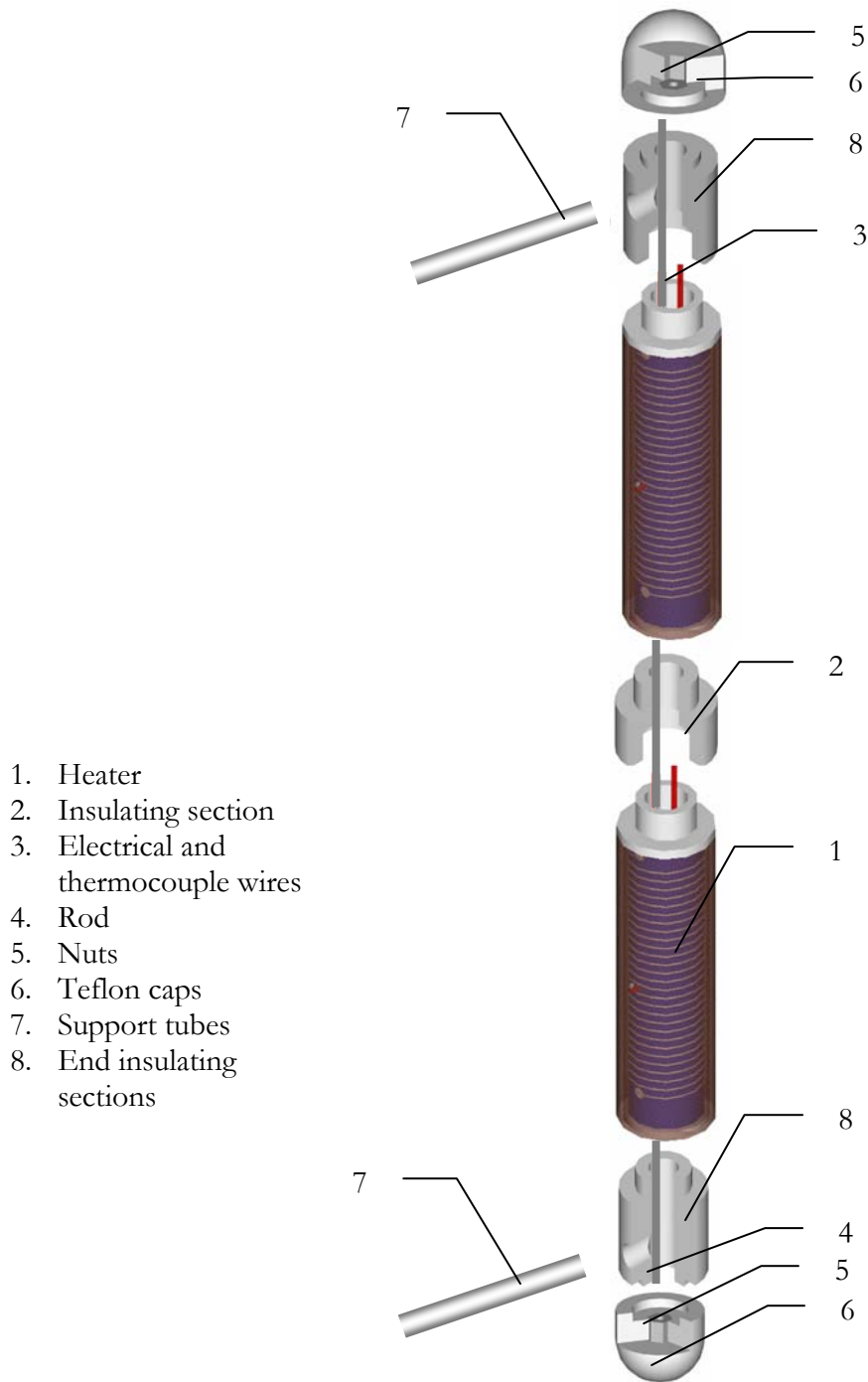
Figure 2.3. Heater tube parts and assembly for a multiple heating section arrangement.

T_{tt}
T_{s1}
T_{s2}
T_{s3}
T_{s4}
T_{s5}
T_{tb}
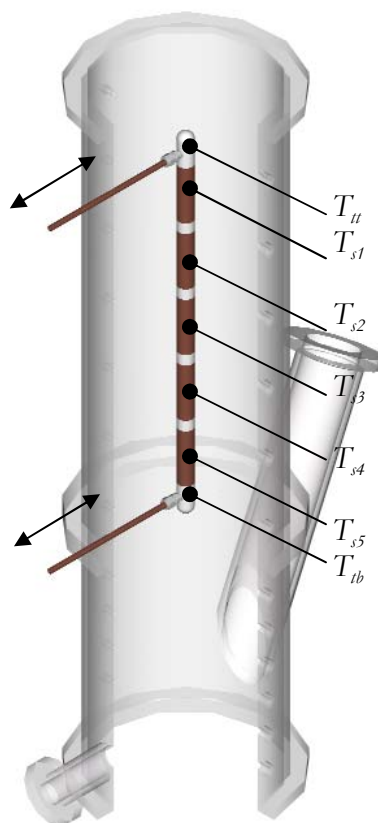
Figure 2.4. Heater tube mounted in 0.29 m ID column with five heating sections.

The design of one heating section is illustrated on Figure 2.5. The heater core (1) is a hollow Teflon cylinder wrapped with Garlock[1] to protect it from accidental high temperatures. 22 AWG (Ø0.64 mm) Ni-Cr heating wire (2) was wound around the core. The wire ends were led back inside the hollow heater core and then through the subsequent section. The core-wire arrangement is inserted in a 28.6 mm OD, 0.101 m long (0.6 mm wall thickness) copper shell (3) for a smooth surface and an even temperature distribution (Figure 2.5). Electrically insulating and thermally conductive cement (Omega OB 600) was injected to fill the space between the heating wire and the copper shell. Care was taken to prevent air from being trapped in this space. Two 22 AWG (Ø0.64 mm) T-type thermocouples (4) were cemented in the middle of the heater surface on opposite sides of the heater to measure the surface temperature. Tenma 72-7295 power supplies with adjustable voltage (0-40 V) provided DC power to the heated sections.
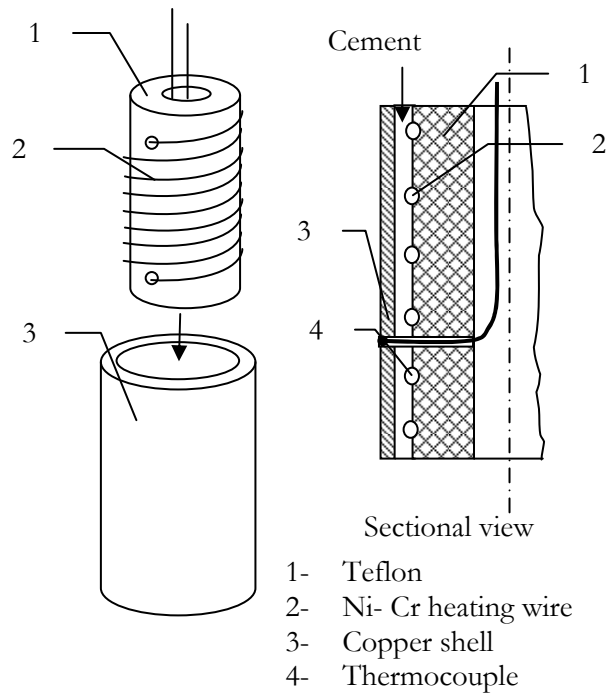
Figure 2.5. Heating section assembly and sectional view (not to scale and simplified)

2.2.3. Instrumentation and data acquisition

Pressure

The pressure distribution along the column was measured by 11 differential and 7 gage pressure transducers (Omega 142 PC series) connected to the ¼" (6.3 mm) ports along the column. These ports are covered with 38 μm mesh to prevent particles from entering the sampling line. For different static bed heights, the locations of the pressure transducers were changed to capture the bed expansion. The locations of the transducers for $H_0 = 1.2$ m appear on Figure 2.6. All pressure transducers were calibrated and the calibrations were entered into the data logging software. The expanded bed height, mean bed voidage and mean cross-sectional voidage are all estimated from pressure measurements (see section 2.5.2).

---

[1] Gasket material withstanding high temperatures
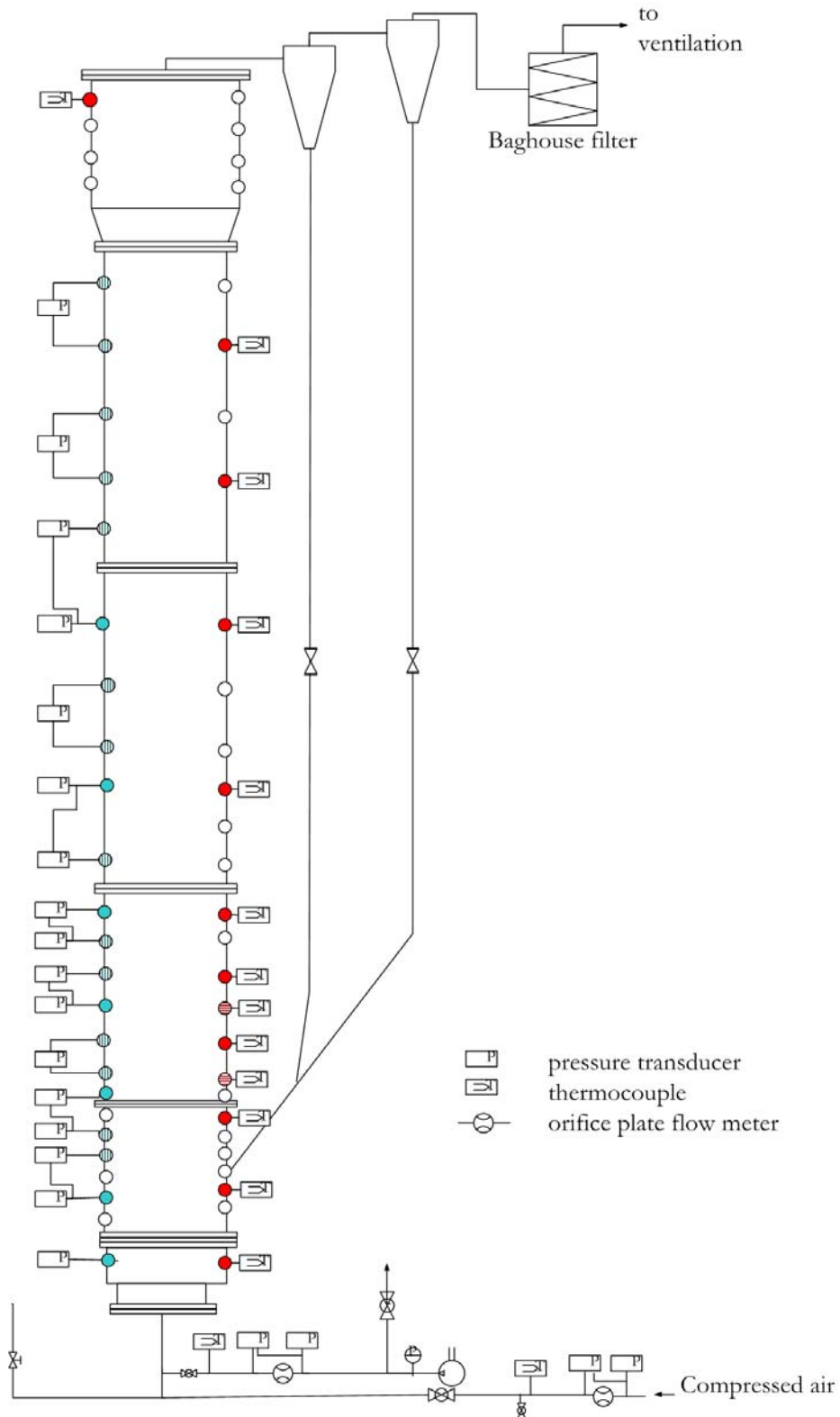
Figure 2.6. Axial location of pressure sensors and thermocouples for H_0 = 1.2 m on 0.29 m ID column.

Temperature

Bed temperature, T_b was measured by sheathed T-type thermocouples (3 mm sheath diameter, 304 mm long) located along the column on the side opposite the pressure ports, as shown in Figure 2.6. The calibration of each thermocouple was checked for two points (0 ^{0}C and 100 ^{0}C) before it was installed. The radial position of all thermocouples was maintained at 0.08 m from the column wall (see Figure 2.7).

The heater surface temperature, T_S, was measured by two T-type 0.381 mm thermocouples embedded in the surface of each heating section. These thermocouples were also calibrated using two point (0° and 100°C) calibration.

To assist in estimating the heat losses, the temperature inside the heater tube was measured by three axially distributed T-type (0.381 mm) thermocouples (T_{tt} - top, T_{tm} – middle (located inside the heater), and T_{tb} - bottom) (Figure 2.7).

Local voidage

Optical fibre probes with a bundle diameter of 4 mm and a minimum straight section length of 500 mm were used to measure the local voidage. A 1.5 mm thick epoxy window was glued on the tip as suggested by Liu et al. (2001), Ellis (2003) and Cui et al. (2000) to improve the linearity of the response. The probes contain arrays of randomly arranged emitting and receiving optical fibres each having a diameter of 15 μm. Light emitted from the emitting fibres of the probes is reflected from the particles and then received by the receiving fibres. The signal is then processed by an optical signal analyzer, Voidmeter P-4, and converted to voltage. The intensity of the reflected light gives information on particle concentration. The probes were calibrated for FCC particles by a calibration column which showed a linear trend. The calibration procedure and the operation of the optical probes were described in detail by Ellis (2003), Liu et al. (2001) and Issangya (1998). Before and after each run, the calibration was checked using two points: packed bed $\varepsilon = \varepsilon_0$ (maximum voltage), and empty column $\varepsilon = 1$ (0 Voltage). Tests were also preformed to check the measuring volume of the probes. The measuring volume of the probe in air with no obstacles in front of the probe is a cone, 20 mm high and 15 mm in basal diameter.

During the heat transfer experiments with the immersed vertical tube, the voidage probes were located below and above the heater (0.47 m and 0.75 m above the distributor plate respectively). At each radial position investigated, the optical probes were moved with the heater, the vertical axis of the heater aligned with the tip of the probes. Several tests were performed where the radial voidage profile was measured for different radial positions of the heater to see the effect of the presence of the heater on the flow pattern in the bed. The test showed no significant effect of the location of the heater on the radial distribution of local voidage.
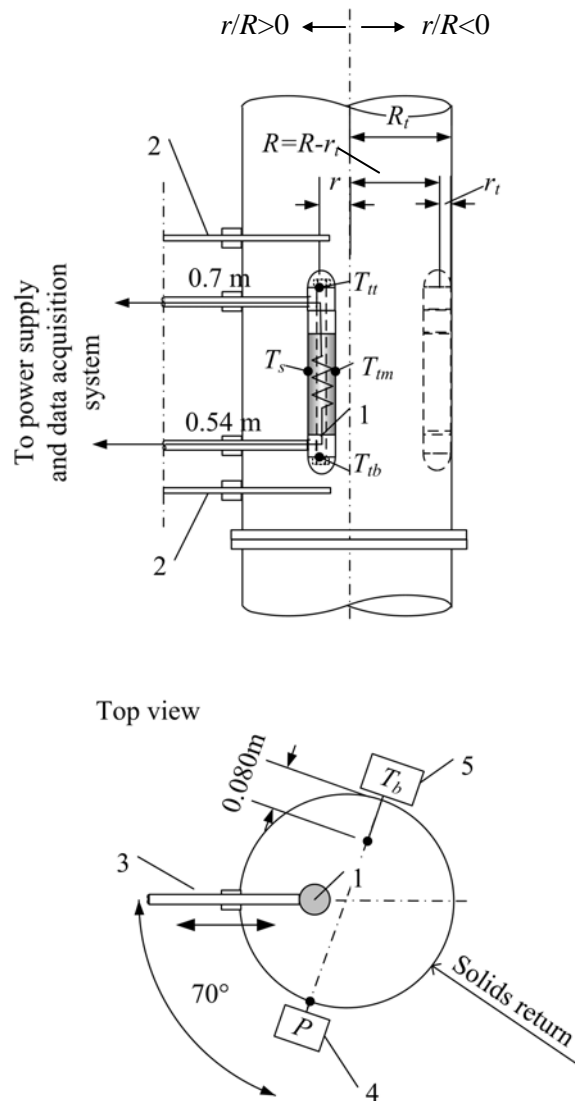
Figure 2.7. Test section of 0.29 m ID column showing heater and optical probe locations.

1 - heater, 2 - optical probes, 3 - support arms, 4 - pressure sensors, 5 - thermocouples

Heat transfer coefficient

The heat transfer coefficient was calculated from an energy balance and its definition:

$$h = \frac{VI - Q_l}{A_s (T_s - T_b)}$$

(2.1)

The current, *I*, and voltage output, *V*, from the power supply were logged to a PC after passing through a circuit equipped with a current sensor and a voltage divider. The estimation of heat loss, Q_l, is described in section 2.6.1 and Appendix C. The heating surface area is $A_s = \pi\, l_t\, d_t$ where the length of the heating section is l_t = 0.101m and the diameter of the tube is d_t = 0.028 m.

Data logging

The data logging system consisted of two 32 channel multiplexers (Computer Boards, Inc., CIO-EXP32), one to connect the pressure transducers as well as the current and voltage sensors and the other for recording temperatures. The multiplexers were connected to an analog/digital converter card (Computer Boards, Inc., CIO-DAS08) installed in a PC (Pentium II, 266 MHz). The voltage signal from the optical probe was connected directly to the analog/digital converter. After steady state was reached, the data were logged for 5-10 min. at 5 s intervals using a custom-made Visual Basic program (TFBHT9.exe). For fast sampling, Labtech Notebook software was used and pressure and local voidage fluctuations were recorded for 100 s at 50 Hz (Pressfast6.ltc).

2.3. Fluidization column – 1.56 m ID

Larger-scale experiments were conducted in a 1.56 m ID, 15 m tall, stainless steel fluidization column at CSIRO Minerals in Clayton, Australia. Photographs of the column appear in Figure 2.8. Air was supplied by two positive displacement Roots blowers achieving a maximum pressure of 60 kPa. Check valves are installed at each blower outlet line to prevent backflow. The flow rate to the column was adjusted by regulating the output pressure from the blower. Fine adjustment of the flow rate was accomplished by a manual valve in the pipe leading to the plenum chamber. A flowchart of the set-up is given in Figure 2.9. The air flow rate was measured by an orifice plate (with a 0.152 m opening). Two Sensym LX18 series pressure

transducers, one measuring the pressure drop across the orifice and the other the absolute pressure in the upstream line, were used to calculate the flow. The temperature was measured upstream by a K-type thermocouple.

The top of the column is equipped with two cyclones placed symmetrically. Particles captured by the cyclones are returned to the bed through an aerated loop seal. For the current experiments, only one side of the symmetrical solids return system was used with the entrance to the other half of the solids return system blocked at the cyclone entrance. Solids not captured by the cyclone were collected in a bag filter. To control the solids return, air was supplied to the loop seal from a third blower (BL-3 on Figure 2.9).

Figure 2.8. Photos of 1.56 m ID column at CSIRO Minerals

To eliminate any difference in particle properties, the alumina particles used in the experiments in the large column were shipped from the same Australian supplier to our laboratory at UBC for smaller-scale experimentation. Likewise, the instrumentation: heater probe, optical probe, pressure transducer and data acquisition system were shipped from UBC to CSIRO Minerals in Australia.
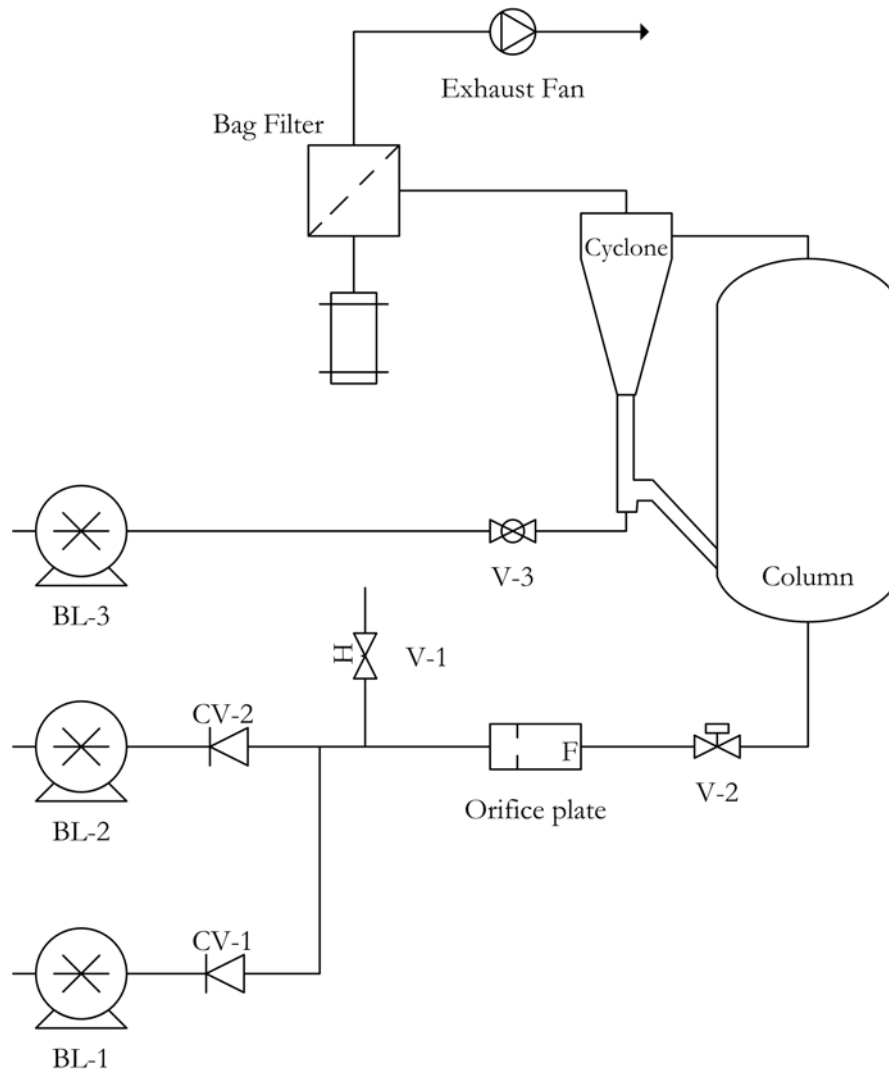
Figure 2.9. Flowchart of experimental set-up for D_t = 1.56 m column

2.3.1.   Distributor plate

Air was introduced into the column by a scaled-up counterpart of the distributor plate described in section 2.2.1 above. This plate had 18 nozzles (33 mm diameter opening), positioned 150 mm from each other and covered by bubble caps (Figure 2.10). The open area ratio is 0.8%. The spacing between the bubble cap and the plate is 4.5 mm, ensured by three spacers between the plate and the bubble cap (Figure 2.12). There was no bubble cap at r=0. Instead, the opening in

the centre of the column was used to drain particles from the column. More details of the distributor are given by Sanderson and Rhodes (2003) and Ellis (2003).
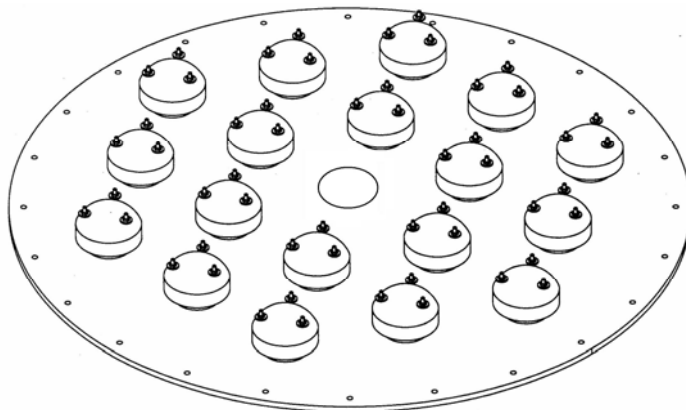
Figure 2.10. Bubble cap distributor in 1.56 m column.

2.3.2. Traversing arm

The same heater as described in section 2.2.2 was used in the experiments in the large column. The heater assembled from one heating section was attached to a traversing arm as shown in Figure 2.11. Power to the heater was supplied by the same DC-regulated power supply (Tenma 72-7295) as in the 0.29 m column.

The traversing arm (38 mm diameter stainless steel tube) had two pressure taps welded to it on opposite sides as shown in Figure 2.11. To prevent particles from entering the pressure taps, stainless steel (size 15) filters were installed. This arrangement of the pressure taps was chosen to allow for the use of the same taps to measure the pressure drop across the heater when it was oriented vertically and horizontally. The distance between the pressure taps for both probe orientations is shown on Figure 2.11.

The same optical voidage probe as in the 0.29 m column was led through the traversing arm, coming out near the middle of the heater and bent slightly, so that its tip was ~10 mm from the heater surface. Detailed drawings of the support arm and assembly are provided in Appendix B. The same principles and procedures apply to the optical probe as were described in section 2.2.3.
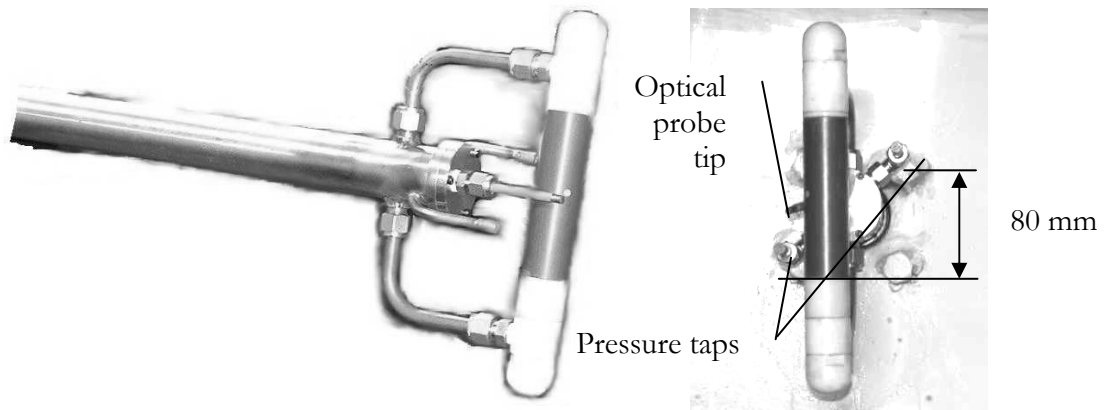
Figure 2.11. Immersed heat transfer probe mounted on traversing arm containing pressure taps and optical voidage probe viewed from different angles

The traversing arm was moved in a radial direction to obtain measurements at different radial positions. The radial positions at which measurements were taken and the location of distributor bubble caps are given in Figure 2.12. The traversing arm was 0.6 m above the distributor plate.
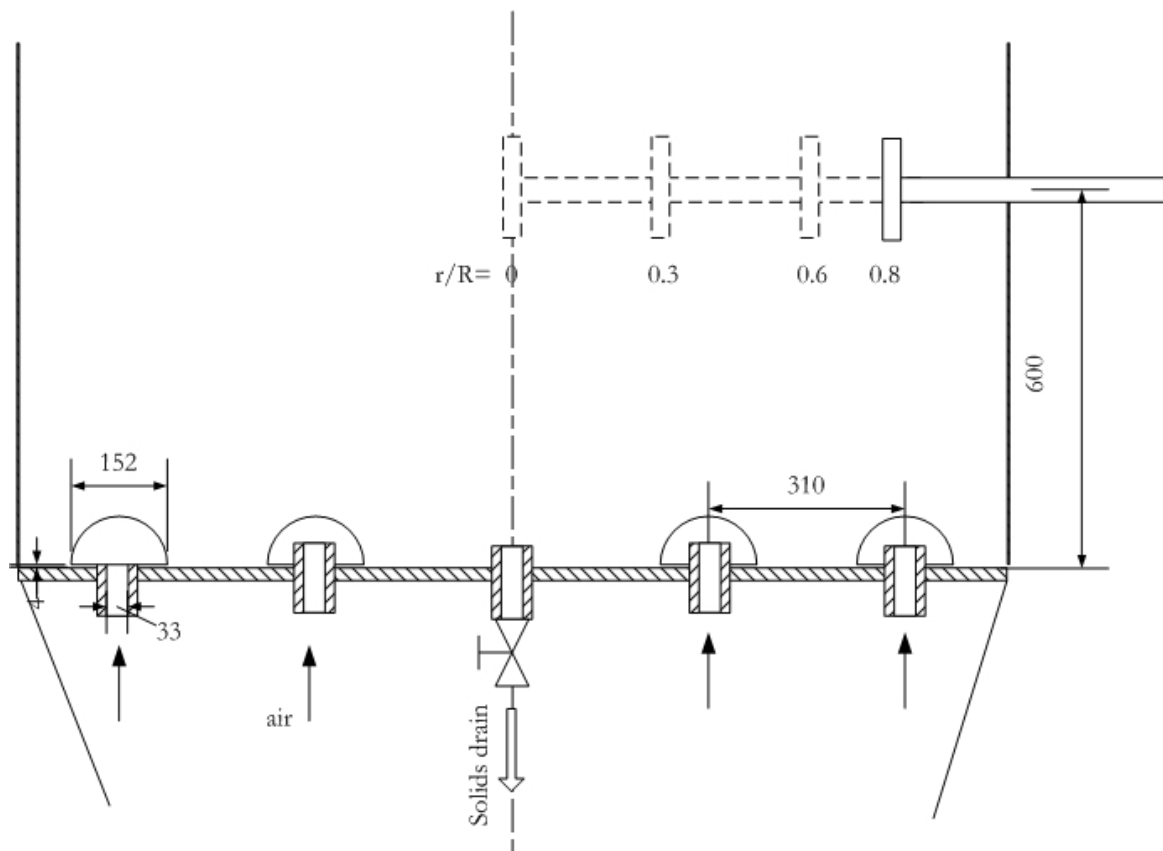
Figure 2.12. Radial positions of the immersed heat transfer probe relative to distributor plate and bubble caps. Distances are in mm.

Figure 2.13a shows the instrumented traversing arm installed in the column closest to the wall (*r/R* = 0.84), viewed from inside the column. The support arm was fixed to the column by a Swagelok fitting, and purged by air to prevent particles from blocking it. Figure 2.13b shows the mounting of the support arm on the column wall.
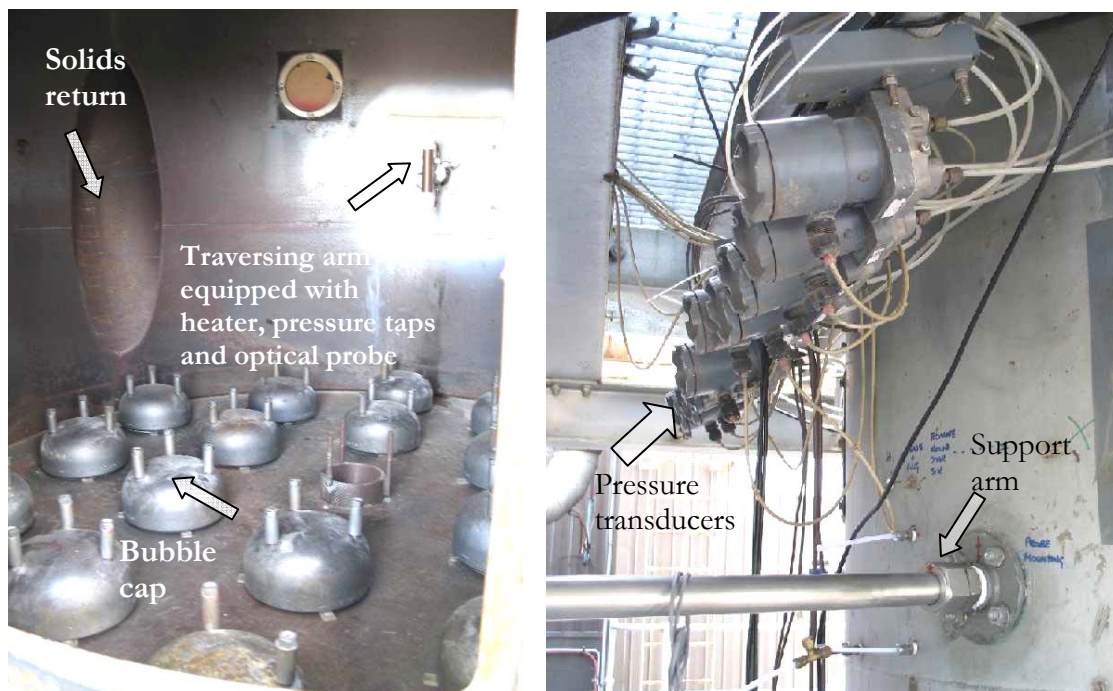
Figure 2.13. Support arm mounted on column wall: a) photo from inside column, b) photo from outside.

2.3.3. Other instrumentation and data acquisition

Pressure sensors

Moore XTC Model 341 series pressure transducers (P1 to P7 on Figure 2.14) measured the pressure distribution along the column. Filters were installed to prevent particles from entering the signal lines.

Omega PC 142 series pressure transducers provided information on the hydrodynamics in the vicinity of the heater probe. One differential and one absolute pressure sensors were located at the column wall, (PD2 and PG7 on Figure 2.14). The pressure taps attached to the traversing arm shown in Figure 2.11 were connected to the other pair of pressure transducers.
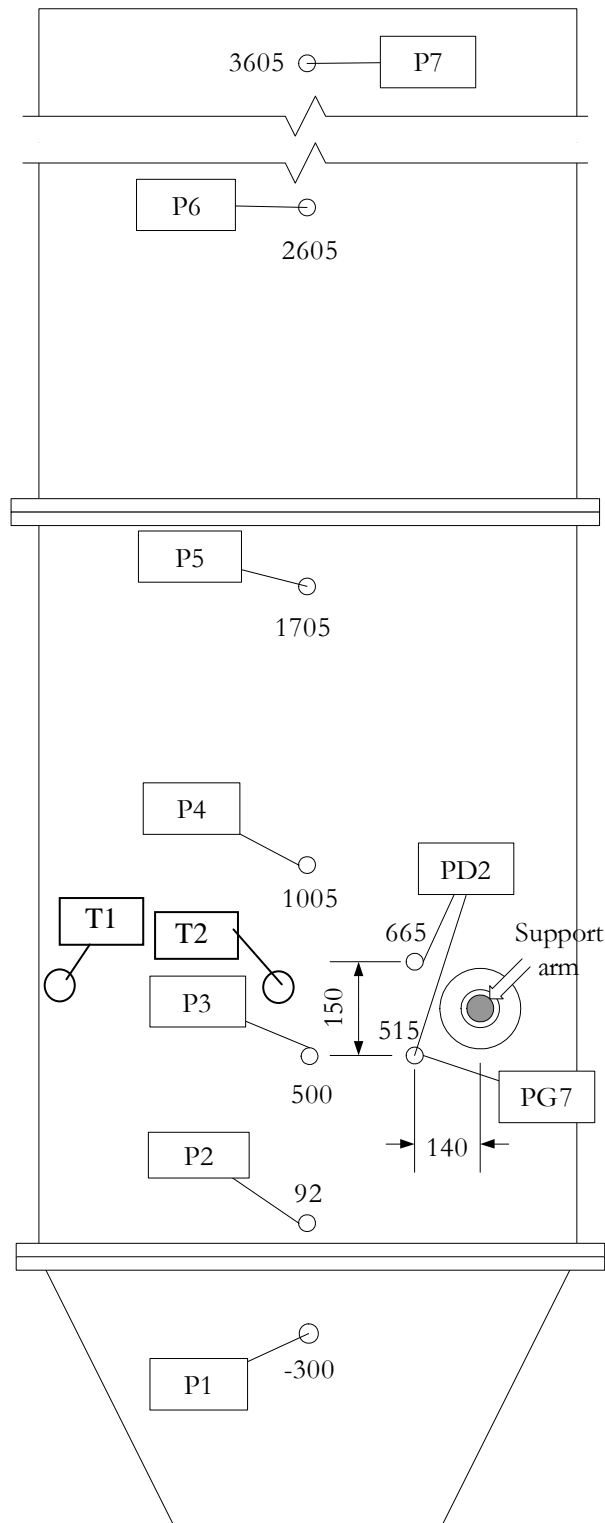
Figure 2.14. Pressure transducers locations on wall of 1.56 m ID column. Numbers represent distance above distributor in mm.

Temperature

Bed temperatures were measured by T-type thermocouples. Two thermocouples (3 mm sheath diameter, 304 mm long) were installed in the bed. One (T1 in Figure 2.14) was about 5 mm from the wall (see Figure 2.14). The other (T2 in Figure 2.14) was immersed in the bed, with its tip ~250 mm from the column wall, supported by a 25 mm OD tube to prevent it from bending due to the forces acting on the tube when the bed was fluidized. The tip of the thermocouple protruded about 5 mm beyond the end of the 25 mm OD tube. Both thermocouples showed similar temperatures, confirming temperature uniformity in the bed.

Data logging

Two separate systems were used for data logging. The first was based on the same Computer Board DA system as in the 0.29 m column at UBC, consisting of an analog input card CIO-DAS08 and two multiplexers CIO-EXP16 and CIO-EXP32. This system recorded both heat transfer and local hydrodynamics data. The other system was a DAQbook 2000A with input card IOTech DBK 80, belonging to CSIRO Minerals. This system was used to obtain axial pressure profiles. The Computer Board system was connected to a HP Vectra VE (P3, 500 MHz) desktop computer whereas the IOTech system was connected to an IBM ThinkPad T23 (P3, 1133 MHz) laptop computer belonging to CSIRO Minerals.

The software used with the Computer board system was written in Visual Basic (recording data every 5 s for 5-10 minutes) and Labtech Notebook Pro, recording pressure and voidage fluctuations at 50 Hz for 100 s. The axial pressure profile was recorded with DAQView on the IOtech system at 50 Hz for 5 min.

2.4. Bed material

Two types of particles were used in the experiments: fluid cracking catalyst (FCC) and refractory grade alumina. These particles were chosen as representatives of group A and group AB, which are commonly utilized in industrial units operated in the turbulent fluidization regime. The FCC particles were only employed in the 0.29 m column, whereas the alumina particles were tested in both columns. Their properties are listed in Table 2.2.

Table 2.2. Properties of particulate materials

Material & column size	d_p,* μm	ρ_p, kg/m³	c_{pp}, J/kgK	ε_0,	U_{mf}, m/s	$U_{c, m/s}$		
						(2.3)	(2.4)	(2.5)
FCC D_t = 0.29 m	70±5	1600	1060	0.45	0.0025			
H_0 = 0.8 m						0.48-0.51	0.70-0.80	0.60-0.64
H_0 = 1.2 m						0.48-0.51	0.75-0.87	0.71-0.77
Alumina H_0 = 0.8 m	82±7	2700	766	0.6	0.007			
D_t = 0.29m						0.63-0.71	1.00-1.43	0.83-1.03
D_t = 1.56m						0.63-0.71	0.62-0.83	0.34-0.37

* Scatter from sampling on different days

Samples of the bed material taken before and after running for some time were analyzed for particle size distribution. The particle size distribution was determined by sieve analysis, with the mean particle diameter calculated as:

$$d_p = \frac{1}{\sum \dfrac{x_i}{d_{pi}}}$$

(2.2)

where x_i is the mass fraction of particles of diameter d_{pi}. The particles size distributions and mean particle diameter are provided in Figures 2.15 and 2.16.

The packed bed voidage, ε_0, particles density, ρ_p, and minimum fluidization velocity, U_{mf}, were measured. For ρ_p, the volume displacement method was used, whereas U_{mf} was obtained from a plot of bed pressure drop as a function of superficial gas velocity in a 0.1 m ID column.

The velocity of the onset of turbulent fluidization, U_c, was estimated from:

$$\mathrm{Re}_c = 1.243 Ar^{0.447} \quad \text{(Bi and Grace, 1995)}$$

(2.3)

$$\mathrm{Re}_c = \frac{\left(\dfrac{H_0}{D_t}\right)^{0.43} Ar^{0.74}}{\sqrt{4.2\left(\dfrac{H_0}{D_t}\right) + 3.1 Ar^{0.33}}} \quad \text{(Ellis et al., 2004)}$$

(2.4)

and

$$\mathrm{Re}_c = 0.459 Ar^{0.454} \left(\frac{H_0}{D_t} \right)^{0.183 \ln(d_p \rho_p) + 0.83} \qquad \text{(Dunham et al., 1993)} \qquad (2.5)$$

where Re_c is based on the mean particle diameter.

Equation (2.4) was derived only for group A particles, whereas equation (2.3) included group B particles, but did not consider the effect of bed dimensions. Equations (2.4) and (2.5) were obtained from measurements of absolute pressure fluctuations and include the column diameter and static bed height. As shown in Table 2.2, the variation in the calculated U_c can be more then 100%. Therefore, careful analysis is needed to determine the transition to the turbulent fluidization flow regime.

The particles (FCC or alumina) were added to the 0.29 m ID column from the top, either by pneumatic conveying using a vacuum system or manually. To reduce electrostatic charges, an antistatic powder (Larostat 519, ~1% by mass) was mixed with the FCC particles and the column was electrically grounded. When Larostat was not used, the instrumentation was affected by the generation of electrostatic charges, as reflected by frequent outliers found in the thermocouple signal, which could probably be due to dissipation of the electric charges at the metal parts of the sensor.

For the experiments in the 1.56 m column, about 1800 kg of alumina particles were added to the column. The particles were conveyed from 500 kg bags in which they were supplied, to a barrel on the second floor of the column using a vacuum pump. Once the barrel was full, the particles were emptied into the column and the process was repeated until a static bed height of 0.8 m was achieved.
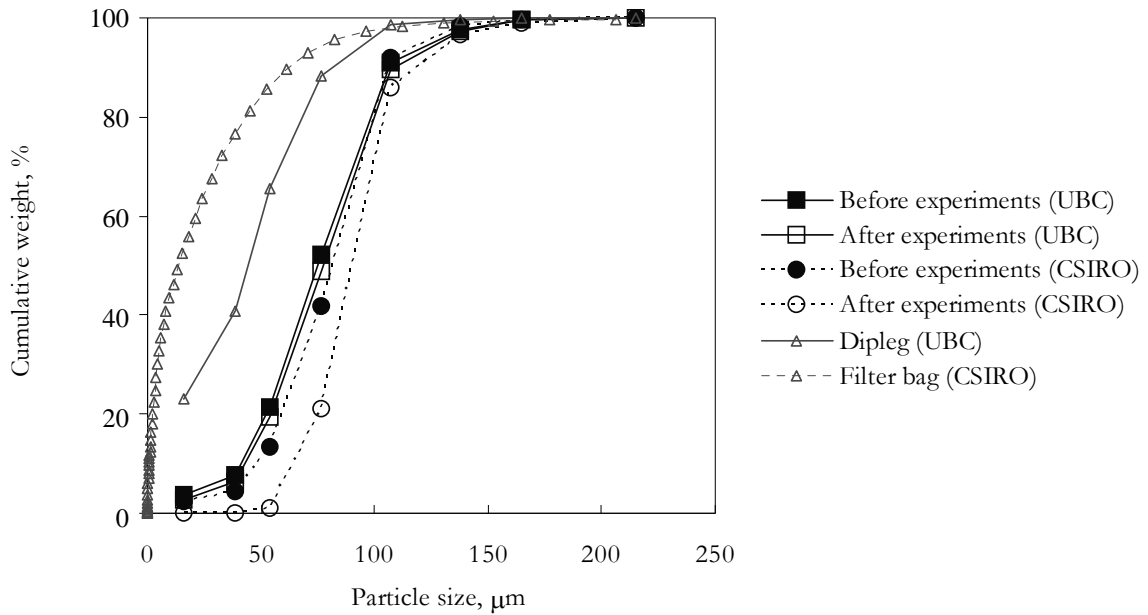
Figure 2.15. Particle size distribution of alumina particles at start and end of experiments in 0.29 m ID (UBC) and 1.56 ID (CSIRO) columns.
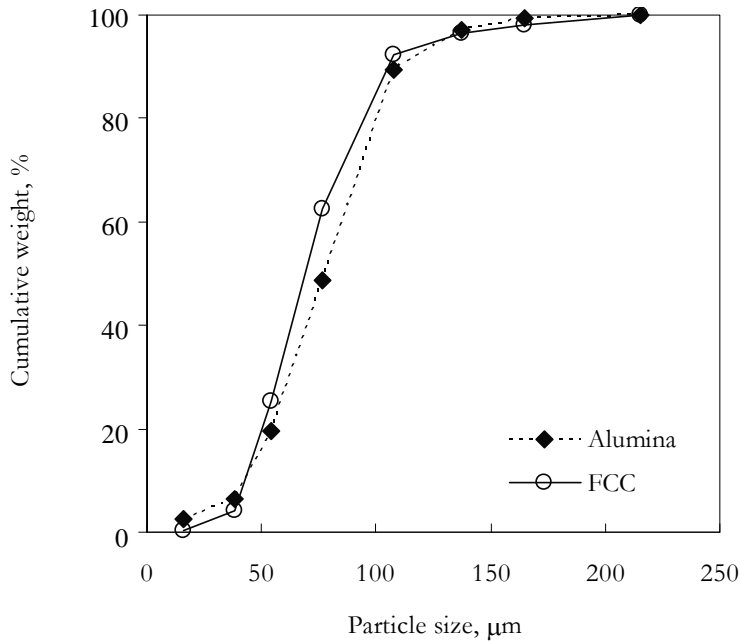
Figure 2.16. Particle size distribution of FCC and alumina particles at start of experiments in 0.29 m ID column.

2.5. Pressure and local voidage data analysis

2.5.1. Time series

Before the data were analyzed, the signal was checked for outliers. For the optical probe, voltages exceeding the value corresponding to a dense packed bed were replaced with the dense packed bed value. On average only 0.05 % of data points were replaced in this manner. Typical signals from the optical probe are shown in Figure 2.17. The arithmetic mean and mode are also plotted.

To analyze and extract information from the pressure signal, it is necessary to understand the underlying physical phenomena. Analysis of pressure fluctuations (van der Schaaf et al., 2002) assumes that there are two components, one originating from bubble coalescence, gas flow fluctuations, bubble eruption and bed mass oscillations causing pressure waves that propagate upwards and downwards from the point of origin, and the other caused by voids passing the probe and gas turbulence which generate only local fluctuations which do not propagate as pressure waves. Because of the complexity of the pressure signal, the maximum standard deviation of the measured pressure signal may not reflect changes in flow structures related to turbulent fluidization. Pressure probes are generally unable to provide unambiguous information on the local hydrodynamics unless differential pressure is measured across a small interval or the signal is treated to distinguish between pressure wave and local fluctuations (e.g coherent and incoherent components of the pressure signal considered by van der Schaaf et al. (2002)).

To characterize the magnitude of the fluctuations of the signal around its mean, the standard deviation was calculated for both pressure (absolute and differential) and optical signals:

$$\sigma = \sqrt{\frac{n\sum x_i{}^2 - \left(\sum x_i\right)^2}{n(n-1)}} \tag{2.6}$$
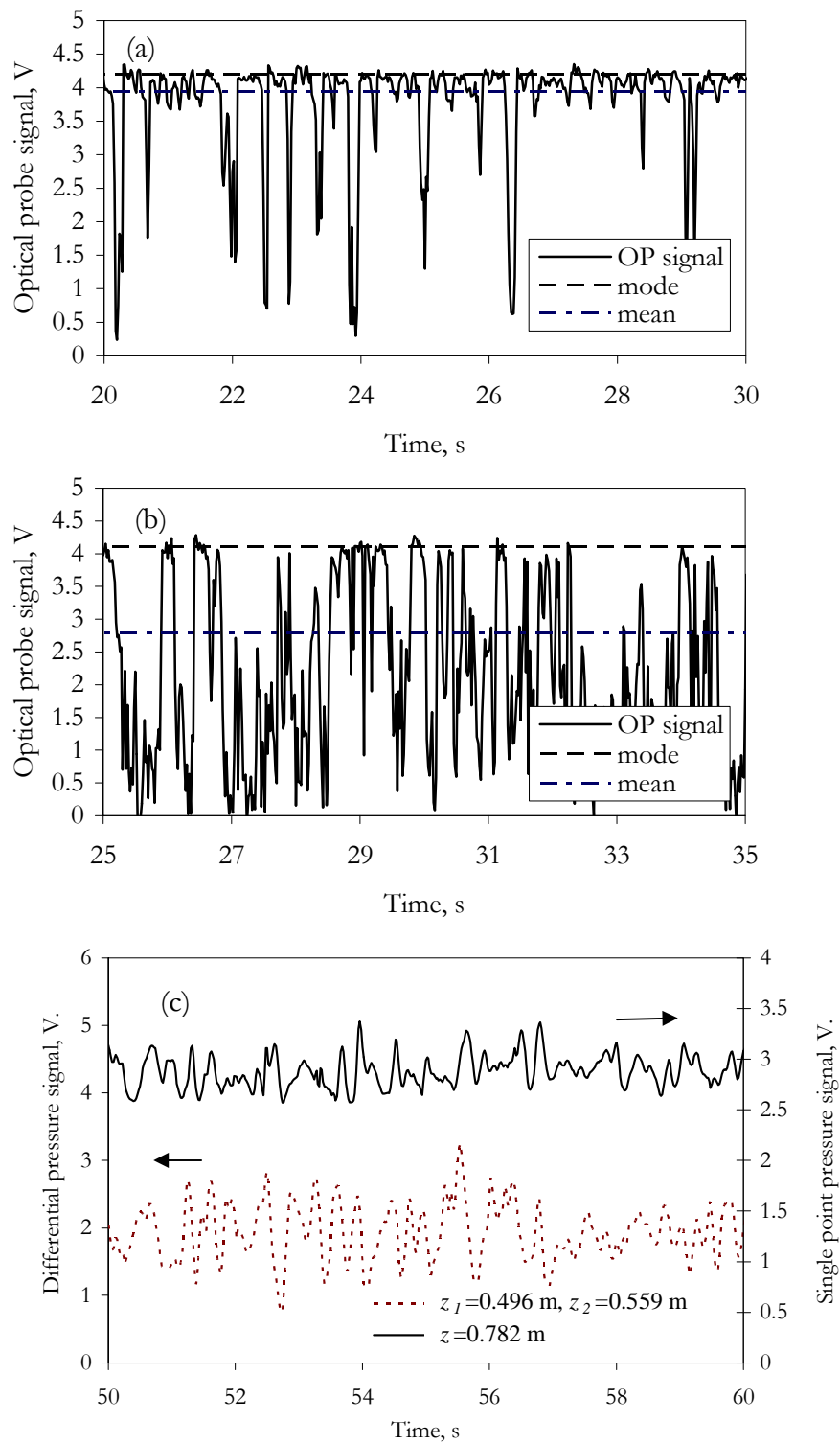
Figure 2.17. Time series of experimental signals from local probes: a) optical probe, $U = 0.1$ m/s, $z = 0.47$ m, b) optical probe, $U = 0.7$ m/s, $z = 0.47$ m, c) absolute and differential pressure, $U = 0.9$ m/s (FCC, perforated plate, $H_0 = 1.2$ m, $r/R = 0$)

Because of the specific nature of the optical probe signal, third and fourth statistical moments skewness and kurtosis were calculated:

$$Kurtosis = \left\{ \frac{n(n+1)}{(n-1)(n-2)(n-3)} \Sigma \left(\frac{x_i - \overline{x}}{\sigma} \right)^4 \right\} - \frac{3(n-1)^2}{(n-2)(n-3)} \qquad (2.7)$$

$$Skewness = \frac{n}{(n-1)(n-2)} \Sigma \left(\frac{x_i - \overline{x}}{\sigma} \right)^3 \qquad (2.8)$$

showing the "peakedness" and degree of asymmetry, respectively.

Non-statistical methods have also been used to analyze the time series such as power spectrum and autocorrelation functions. The power spectrum gives information on how energy is distributed among the different frequencies as an aid to understanding the flow structure:

$$P(f) = |F(f)|^2 = \left| \frac{1}{2\pi} \int x(t) \exp(-ift) dt \right|^2 \qquad (2.9)$$

where: $x(t)$ = time series, t = time, $F(f)$ = Fourier transform, f = frequency and $P(f)$ = power. In this study, time series were converted to the frequency domain using a modified Matlab algorithm (scaling parameter was included in the fft.m algorithm) for fast Fourier transformation.

The autocorrelation function gives information on the periodicity/predictability of the signal, and it can be used to establish characteristic frequencies. This frequency can be calculated from the time lag of the first peak in the autocorrelation function after 0 lag. By definition the autocorrelations at 0 lag must equal 1. The autocorrelation function (Chatfield, 2001) is:

$$c_{xx}(\tau) = \frac{1}{\sigma_x^2} E\big[\big(x(t) - \overline{x}\big)\big(x(t+\tau) - \overline{x}\big)\big] \qquad (2.10)$$

where $x(t)$ = time series, $\overline{x}$ = mean, τ = time lag, t = time, σ_x = standard deviation and E = covariance function. Here the autocorrelation was calculated using Matlab's Garch toolbox for time series analysis (autocorr.m).

The cross-correlation function (Chatfield, 2001):

$$c_{xy}(\tau) = \frac{1}{\sigma_x \sigma_y} E\left[\left(x(t) - \overline{x}\right)\left(y(t+\tau) - \overline{y}\right)\right] \tag{2.11}$$

is another form of the correlation function where, instead of correlating the same signal with different offsets, the correlation is established between two different points. Here: σ_x, σ_y are the standard deviations of the two individual time series, E is the cross-covariance function of the $x(t)$, $y(t)$ time series, τ is time lag and $\overline{x}$ and $\overline{y}$ are means. From the cross-correlation of the signals from the two optical probes separated by a vertical distance of 0.28 m, information on the scale of eddies or other entities relative to the separation distance can be deduced.

The power spectrum and the correlation functions were calculated for normalized absolute and differential pressure and voidage signals. The pressure signal was normalized by its time-mean value, whereas the optical probe signal was normalized in the form: $V_{opN} = (V-V_{max})/(V_{min}-V_{max})$ or in terms of local voidage: $\varepsilon_N = (\varepsilon-\varepsilon_{mf})/(1-\varepsilon_{mf})$.

As we investigate the onset of turbulent fluidization and the change in the dominant mechanism of heat transfer in an attempt to understand the relationship between these two phenomena, the data analysis approach in this work is exploratory, with graphical interpretation of trace plots, scatterplots, histograms, etc. (Tunkey, 1977), rather than classical statistical analysis.

2.5.2. Macroscopic hydrodynamics

Expanded bed height, mean bed voidage and cross-sectional mean voidage were calculated based on time-mean pressure measurements. The expanded bed height H was determined from the axial pressure profiles at the intersection of two straight lines: a least-square-fit through the points in the dense bed region and a horizontal line in the freeboard as illustrated in Figure 2.18. The overall mean bed voidage was calculated from the momentum balance (Gidaspow, 1994) based on the common assumption that the pressure drop across the bed corresponds to the weight of particles per unit area, so that

$$\overline{\varepsilon} = 1 - \frac{\Delta p_{bed}}{g\rho_p H} \qquad (2.12)$$

where, Δp_{bed} is the pressure drop across the dense bed, H is the expanded bed height and g is the acceleration of gravity. Figure 2.18 illustrates how Δp_{bed} and H were determined for $U = 0.8$ m/s.
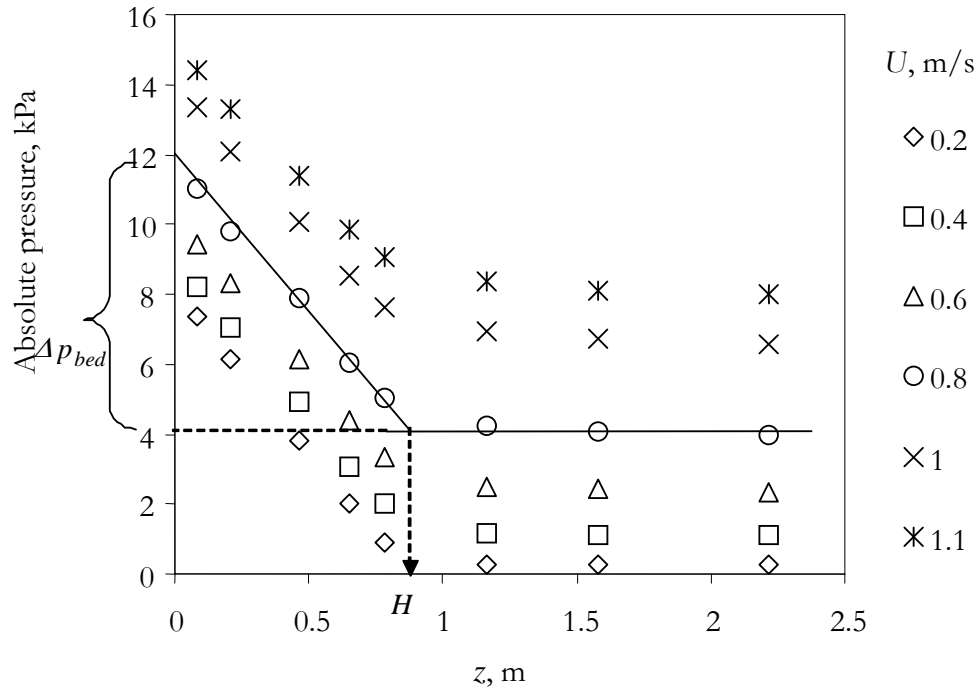
Figure 2.18. Axial pressure profile (Alumina, $D_t = 0.29$ m, $H_0 = 0.8$ m)

In a similar manner, the cross-sectional mean voidage was estimated from the differential pressure, Δp, across a given vertical section, Δz:

$$\varepsilon_{CS} = 1 - \frac{\Delta p}{\Delta z \rho_p g} \qquad (2.13)$$

The onset of turbulent fluidization is characterized by increased entrainment from the bed, which can be determined from a change in the slope of the corresponding dense bed height at minimum fluidization (Rhodes, 1996; Ellis, 2003) estimated as:

$$H' = H \frac{(1 - \bar{\varepsilon})}{(1 - \varepsilon_{mf})} \qquad (2.14)$$

where, ε_{mf} is the voidage at minimum fluidization.

2.6. Uncertainty analysis

Measured variables are subject to random and systematic errors originating from the instrument, calibration, installation, data acquisition, concept applied, method of installation of instruments, etc. In order to obtain the overall uncertainty of the experimental results, we need to combine the uncertainties of the measured variables. The general uncertainty in determining heat transfer coefficients can be estimated (Coleman and Steele, 1998) by:

$$\left(\frac{Y_h}{h}\right)^2 = \left(\frac{V}{h}\frac{\partial h}{\partial V}\right)^2 \left(\frac{Y_V}{V}\right)^2 + \left(\frac{I}{h}\frac{\partial h}{\partial I}\right)^2 \left(\frac{Y_I}{I}\right)^2 + \left(\frac{T_s}{h}\frac{\partial h}{\partial T_s}\right)^2 \left(\frac{Y_{T_s}}{T_s}\right)^2 + \left(\frac{T_b}{h}\frac{\partial h}{\partial T_b}\right)^2 \left(\frac{Y_{T_b}}{T_s}\right)^2 + \left(\frac{A_s}{h}\frac{\partial h}{\partial A_s}\right)^2 \left(\frac{Y_{A_s}}{A_s}\right)^2$$

The uncertainty of the heat transfer coefficient within a 95% confidence level, assuming no heat losses, is estimated to be ±5%, where the uncertainties of the measured variables are based on the accuracy of the instruments.

2.6.1. Estimation of heat losses

A more detailed uncertainty analysis includes errors introduced by heat losses from the ends of the immersed heater tube and its support. To estimate theses heat losses, a two-dimensional model using FEHT software was set-up (Incropera and DeWitt, 2001). The model assumes convective heat transfer from the tube surface, heat generation from the heating element and two-dimensional conduction through the Teflon support. A simplified schematic is shown in Figure 2.19. Temperature distribution and heat flux can be obtained from the model. The ratio of the heat lost to the heat supplied to the heater calculated from the model was correlated to the heat transfer coefficient for the given conditions (Figure 2.20). For heat transfer coefficients in the range 100 - 400 W/m^2K, Q_l/Q was found to be in the range of 2-5%. More details are provided in the Appendix C.

If we consider an uncertainty of 20% in estimating the heat losses (originating from the assumptions and correlations used) in the error analysis, the overall uncertainty of the measured heat transfer coefficients (Y_h/h) increases to $\pm 9\%$.
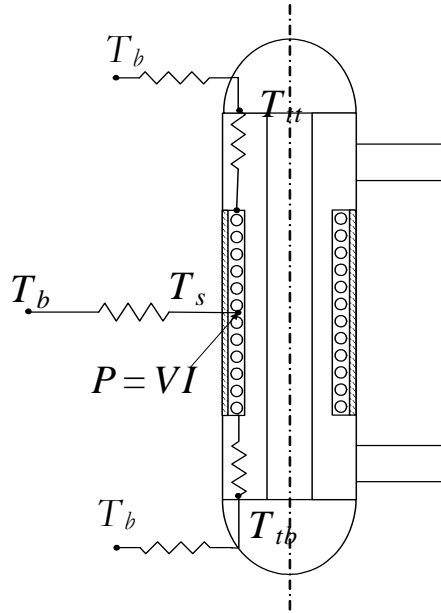
Figure 2.19. Schematic showing heat losses. Drawing not to scale.
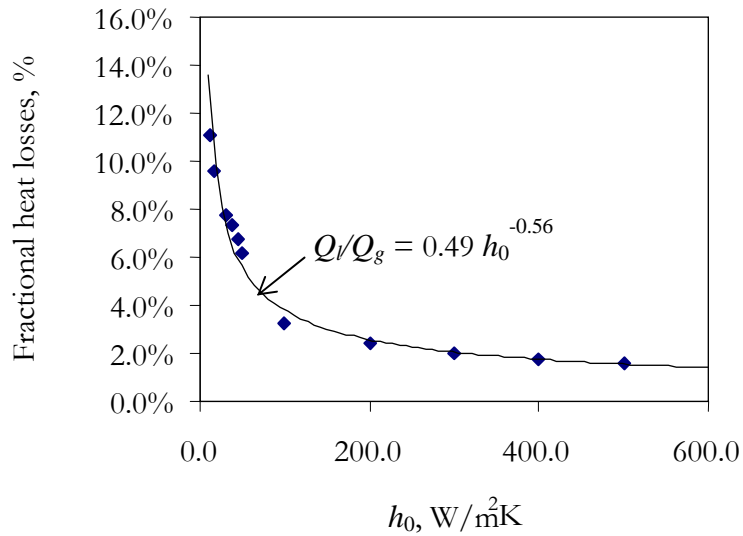
Figure 2.20. Correlation for estimation of heat losses. (h_0 is heat transfer coefficient estimated neglecting heat losses).

Chapter 3

3. HYDRODYNAMICS AND TRANSITION TO TURBULENT FLUIDIZATION

3.1. Introduction

Several studies performed in turbulent fluidized beds (reviewed in Chapter 1) indicate that the heat transfer coefficients change as the local flow structure evolves from bubbling to turbulent fluidization. The onset of the transition in these studies was determined using different methods. Sun and Chen (1989) fluidized catalyst particles belonging to group A in a relatively large 0.8 m ID column and defined the onset of turbulent fluidization as the condition corresponding to the maximum of the normalized peak-to-peak standard deviation of pressure fluctuations. In the work of Basu et al. (1986), which involved sand particles belonging to group B, the onset of turbulent fluidization was defined as the velocity at which entrainment of particles from the bed increased sharply corresponding to a sudden increase in bed voidage. Staub (1979) investigated large particles and detected turbulent fluidization from the maximum standard deviation of pressure fluctuations. He also reported that immersed tube banks shifted the transition to the turbulent fluidization flow regime to lower superficial gas velocities.

There is an ongoing debate in the fluidization research community about whether turbulent fluidization should be considered as a separate hydrodynamic regime and about the criteria used to determine the onset of the turbulent fluidization flow regime (Rhodes, 1996; Bi et al., 2000; Grace, 2000). The uncertainty related to determining U_c, arising from different experimental methods and transition criteria (Brereton and Grace, 1992; Bi and Grace, 1995; Rhodes, 1996) make the analysis of the effect of onset of turbulent fluidization on heat transfer challenging. Another issue is that measures like the maximum standard deviation of differential pressure fluctuations or voidage fluctuations may occur locally rather than being global. Thus, different regions of the bed may be simultaneously subject to different flow regimes. For example, Staub (1979) reported a turbulent region near the immersed tube bank, while other regions in the bed were subjected to bubbling.

Grace (2000) suggested that there are three types of transitions from the bubbling to the turbulent fluidization flow regime, which may account for the inconsistency in the reported studies. In Type I, typical for smaller group A particles, the flow undergoes a sudden change; large voids break-up into smaller, erratic and irregularly shaped voids of brief lifespan. Type II, observed with larger particles (group B), usually occurs when slug flow precedes the transition. The transition is then more gradual, with intermittency between slugging and turbulent flow. The type III transition is found for shallower beds (H/D_t < 2) of larger particles that do not reach maximum bubble size. Due to the limited bed height, slug flow is never achieved and the transition is influenced by the distributor. In the present study, some parameters that affect the onset of turbulent fluidization were varied (particle properties, H_0, D_t, gas distributor) in order to determine the effect of the changing flow structure near the onset of turbulent fluidization on heat transfer. All three types of transition were observed in this work, type I for a fluidized bed of FCC particles in a column of 0.29 m ID; type II for alumina particles in the same 0.29 ID m column; and type III for alumina particles in a shallow bed of large diameter (1.56 ID m column).

In the absence of a standard methodology for determining the onset of turbulent fluidization covering the three transition types, it was necessary to establish criteria which capture the change in hydrodynamic features and trends associated with turbulent fluidization before considering a heat transfer analysis. An experimental study of local and overall hydrodynamics was performed simultaneously with the heat transfer measurements. Using the experimental results for overall and local hydrodynamics, different methods for establishing the transition velocity, U_c, were examined. The term turbulent fluidization used in this work designates bed hydrodynamics characterized by break-down of the two-phase flow structure associated with increased entrainment of particles from the bed and vigorous gas-solid contacting.

3.2. Determining the onset of turbulent fluidization

One of the most challenging tasks in this study was to determine the onset of turbulent fluidization. A gradual transition with increasing gas velocity occurred, starting from the top of the bed, where break-up of large bubbles occurs, accompanied by increased entrainment of particles, and progressing downwards (Ellis, 2003) until fully turbulent fluidization of the bed is complete.

The most widely accepted method for determining the onset of the transition is from a plot of the standard deviation of absolute or differential pressure fluctuations vs. superficial gas velocity. The velocity at which the standard deviation of the pressure fluctuations reaches a maximum is designated as U_c. However, there is debate in the fluidization research community whether U_c based on pressure fluctuations can be the sole criterion for the onset of this transitional state (e.g. Brereton and Grace, 1992; Bi, 1999; Rhodes, 1996; Andreux et al., 2005). This method usually works well for fine particles belonging to group A (type I turbulent fluidization). However, for the other two types of transition, observed with larger particles, when the bed undergoes slugging or is relatively shallow and the transition is affected by the distributor, the transition criteria are not well established.

Some researchers (see Bi et al., 2000) have used the criterion of increased entrainment of particles from the bed to determine the onset of turbulent fluidization. The transition is then linked to a sudden change in a plot of bed density, voidage or dense bed height corresponding to the minimum fluidization conditions, H' (see equation (2.14)), vs. superficial gas velocity.

Other criteria in the literature focus on changes of local flow structure identified by optical or capacitance probes (Lancia et al., 1988; Nakajima et al., 1990). By plotting the time-mean local voidage vs. superficial gas velocity, the onset of turbulent fluidization is said to occur when there is a change in trend, explained by a change in local flow structure, such as break-up of large voids. Other methods include maximum of standard deviation of local voidage and zero skewness of the local voidage distribution (Bi and Grace, 1995).

Table 3.1 summarizes studies with group B or A-B particles and the different methods used. The results appear to be affected by the analysis method, and some studies indicate that the maximum standard deviation of pressure fluctuations does not correspond to the onset of turbulent fluidization (Brereton and Grace, 1992; Bi, 1999). Some studies (Lancia et al., 1988; Makkawi and Wright, 2002) report two characteristic velocities, U_c, and U_k, that reflect changes in flow features. Andreux et al. (2005) identified a transition velocity lower then U_c at which a change occurred in the slope of a plot of time-average voidage vs. superficial gas velocity and when the dominant frequency of local voidage fluctuations, measured by an optical probe, reached a maximum. This velocity, U_c', did not mark a sudden change in the global bed structure. The authors attributed the

Table 3.1. Summary of studies on type II or III transition to turbulent fluidization

Conditions	U_c , U_k, U_c' m/s	Criterion	Reference
D_t=0.2 m H_0/D_t =4.25 z=0.1 and 0.7 m Sand, d_p =87 μm ρ_p=2500 kg/m³	U_c=0.8	U_c – Change in slope of fraction of time optical probe is inside voids vs. U.	Nakajima et al. (1990)
D_t=0.152 m H_0/D_t = 6.6 z=0.23-0.69 m Sand, d_p =148 μm ρ_p=2650 kg/m³	U_c=0.5	U_c – Maximum standard deviation of pressure fluctuations. However, visual observation and instantaneous pressure signal features indicate that this does not correspond to onset of turbulent fluidization.	Brereton and Grace (1992).
D_t=0.102 m H_0/D_t= 9.8 z=0.28 m Sand, d_p =215 μm ρ_p=2640 kg/m³	$U_{c\,OP}$=0.17 $U_{c\,DP}$=0.27	$U_{c\,OP}$–Maximum standard deviation of local voidage (corresponded to onset of slugging rather then turbulent fluidization). $U_{c\,DP}$-Standard deviation of pressure fluctuations, but this did not mark onset of turbulent fluidization.	Bi (1999)
D_t=0.152 m H_0/D_t= 2 z=0.25-0.30 m Sand, d_p =250 μm ρ_p=2585 kg/m³	U_c'=0.45 U_c= 0.85	U_c' - Maximum dominant frequency of local voidage (OP) and break point in time-mean voidage profile. U_c – maximum standard deviation of pressure fluctuations.	Andreux et al. (2005)
D_t=0.1 m H_0/D_t=5 z=0.3-0.4 m Glass, d_p =257 μm ρ_p=2500 kg/m³	U_c=0.27 U_k =0.71	U_c – maximum in probability distribution function (PDF) of fraction of time capacitance probe is inside voids. U_k – minimum in PDF of fraction of time capacitance probe is inside voids. Break point in local average voidage, at U_c and U_k.	Lancia et al. (1988)
D_t=0.1 m H_0/D_t =10 z=m Glass, d_p =362 μm ρ_p=2500 kg/m³	U_c=0.85	U_c – change in slope of rise velocity of voids vs. U (rise velocity of voids was determined from cross-correlation of pressure signals).	Lee and Kim (1989)
D_t=0.132m H_0/D_t= 1 z=0-0.138 m Glass, d_p =530 μm ρ_p=2640 kg/m³	U_c=0.87 U_k =1.4	U_c – Maximum standard deviation of average solid fraction, maximum standard deviation of local voidage, maximum normalized amplitude of pressure fluctuations. Change in slope for average solids fraction vs. U at U_c and U_k.	Makkawi and Wright (2002)

gradual transition to a change in the local flow structure caused by increased gas flow through the dense phase as large voids start to break-up. An increase in gas flow through the dense phase (dense phase expansion) was measured by Cui et al. (2000) in the turbulent fluidization regime. Andreux et al. (2005) found that U_c', defined as the velocity at which a maximum fraction of gas flow through the bubbles (75-80%) is observed, is more representative of the transition to turbulent fluidization. They suggested the model of Davidson and Harrison (1963) be used to determine the fraction of gas flowing through the bubbles for group B particles.

Given the uncertainty related to the pressure fluctuation method, local and overall hydrodynamics, as well as visual observations, were used in this work to determine the velocity (or range of velocities) marking the onset of the transition to turbulent fluidization.

3.2.1. Macroscopic hydrodynamics

Expanded bed height, *H*, dense bed height, *H'* corresponding to the minimum fluidization voidage, average overall bed voidage, $\bar{\varepsilon}$, cross-sectional mean voidage, ε_{cs} (see equations (2.12)-(2.14)) are presented in this section to determine any changes in trends with increasing *U*.

3.2.1.1. FCC particles in 0.29 m column

The expanded bed height, together with the bed height corresponding to the minimum fluidization voidage, from several runs repeated on different days are shown in Figure 3.1. The results show that the bed expanded approximately 20% from that at minimum fluidization conditions at its maximum. The limited bed expansion is assumed to be due to the changing local flow structure and increased entrainment of particles. Beyond the maximum, large scatter was noticeable at high *U*, which suggests that the bed expansion was affected by the solids return system. The relative humidity of the air on different days might have affected the flowability of the solids (with particles sticking to the walls due to electrostatic charges for dry conditions) in the return system, controlled by the pressure balance across the flapper valve.

Rhodes and Geldart (1986) used the mass of solids contained in the dense bed:

$$M_{bed} = \frac{\Delta p_{bed} A_t}{g} = HA_t(1-\bar{\varepsilon})\rho_p = H'A_t(1-\varepsilon_{mf})\rho_p \tag{3.1}$$

to correct for the mass of solids in the freeboard and the return loop. From (3.1) the dense bed height corresponding to the voidage at minimum fluidization is: $H'=H(1-\bar{\varepsilon})/(1-\varepsilon_{mf})$. Its decline indicates a decreased amount of particles in the dense bed due to entrainment. For the bed height corresponding to minimum fluidization shown in Figure 3.1, there is a change in slope at $U \approx 0.45$ m/s suggesting an increased entrainment of particles.
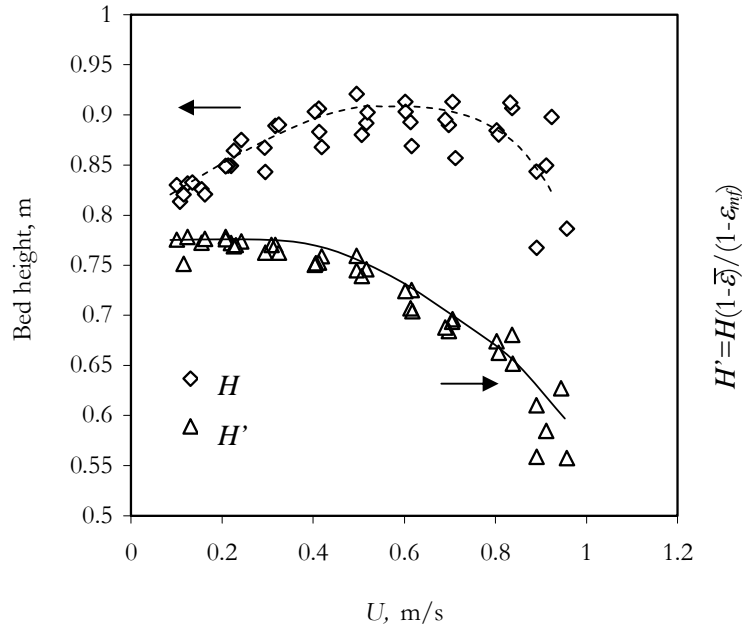
Figure 3.1. Expanded bed height, H, and dense bed height corresponding to minimum fluidization voidage, $H'=H(1-\bar{\varepsilon})/(1-\varepsilon_{mf})$, vs. superficial gas velocity. Data from repeated runs included. (FCC, D_t=0.29 m, perforated plate distributor, H_0=0.8 m)

The bed expansion is also observed from the cross-sectional mean voidage calculated from the differential pressure measured near the bed surface over a 0.127 m vertical distance (z_1=0.782 m and z_2=0.909 m), shown in Figure 3.2. This differential pressure sensor captured the change in two mechanisms: (1) bed expansion (due to the growth of voids with increasing superficial gas velocity) and (2) increased entrainment of particles from the bed. The cross-sectional mean voidage decreased as the bed expanded and more particles were present in the measuring volume until a minimum was reached at $U \approx 0.45$ m/s. Increasing the superficial gas velocity further did not contribute to additional bed expansion. Once the entrainment from the bed became significant (at $U \approx 0.65$ m/s), the voidage in the measuring section started to increase. No sudden change in average overall bed voidage (diamonds on Figure 3.2) was observed with increasing U, as long as

the pressure sensors used in the calculation were always covered by a dense bed. A sudden increase in average overall bed voidage was only observed if a sensor above the dense bed surface was included in the calculations.
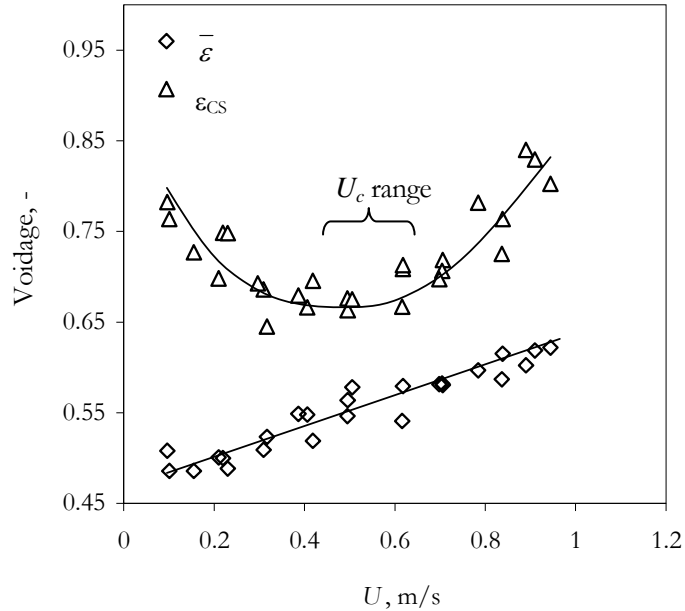
Figure 3.2. Average overall bed voidage, $\overline{\varepsilon}$, and cross-sectional mean voidage, ε_{cs}, at z = 0.78-0.9 m, vs. superficial gas velocity. Data from repeated runs included. (FCC, D_t=0.29 m, perforated plate distributor, H_0=0.8 m)

From the analysis of the macroscopic hydrodynamics of the bed as a function of the superficial gas velocity, changes in trends started at $U \approx 0.45$ m/s when the expanded bed height reached a maximum and the dense bed height corresponding to the minimum fluidization voidage, $H'=H(1-\overline{\varepsilon})/(1-\varepsilon_{mf})$ began to decrease. Another change in trend was observed at $U \approx 0.65$ m/s where a sudden increase in cross-sectional average voidage at the top of the bed was observed and the expanded bed height started to decrease.

3.2.1.2. Alumina in 0.29 m column

It was expected that, with the alumina particles in the 0.29 m column, slugging might be encountered. The calculated velocity for the onset of slugging is 0.12 m/s (Hovmand & Davidson, 1971), and the bed is sufficiently deep, $H > z_{sl}$=0.48 m (Baeyens & Geldart, 1974). The bubble diameter calculated by the correlation of Darton et al. (1977) reaches half the column diameter at

0.19 m/s when bubble size, velocity and frequency are significantly influenced by the column wall (Hovmand & Davidson, 1971). Although the criteria for onset of slugging were satisfied, typical slugging with strong periodic fluctuations was never observed. Periodic fluctuations associated with slugging were observed intermittently in the instantaneous local voidage (see Figure 3.21), interspersed with periods of more random fluctuations. The fraction of time that the random fluctuations were observed increased gradually as the superficial gas velocity increased.
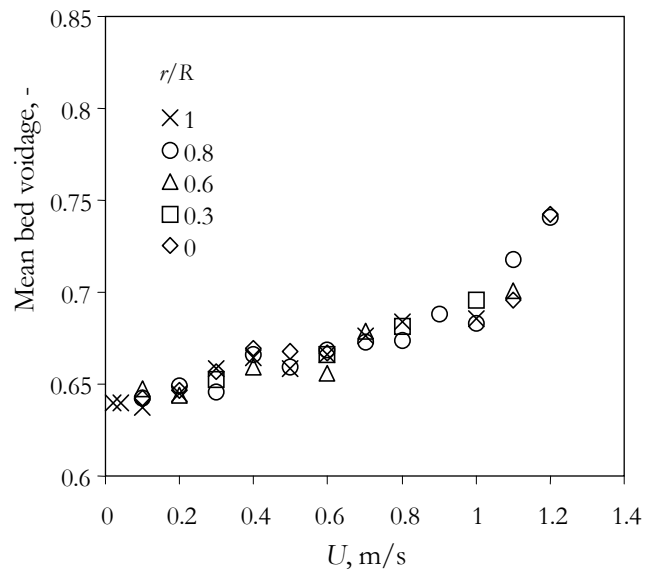
Figure 3.3. Mean bed voidage vs. *U*. *r/R* is the dimensionless radial heater position. (Alumina, D_t=0.29 m, bubble cap distributor, H_0=0.80 m)

The macroscopic hydrodynamics of the bed exhibit similar trends as for the FCC particles but with the critical superficial gas velocity shifted to a higher value. A maximum bed expansion of 16% was observed between 0.6 and 0.8 m/s (data not shown). The experimental results for the average overall bed voidage and dense bed height corresponding to the minimum fluidization voidage are given in Figures 3.3 and 3.4, respectively. The average overall bed voidage increased continuously up to ~1 m/s where a sharp increase occurred. The dense bed height corresponding to the minimum fluidization voidage (*H'*) (Figure 3.4) and the cross-sectional mean voidage near the bed surface (not shown) exhibited changes near 0.6 m/s, indicating increased entrainment.
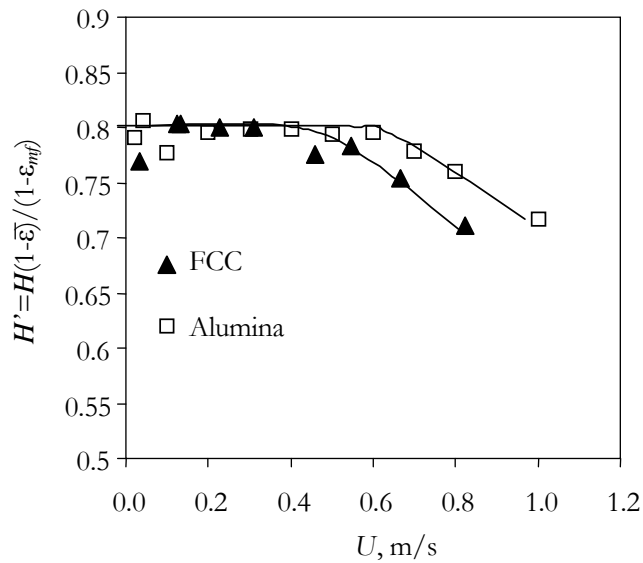
Figure 3.4. Dense bed height corresponding to minimum fluidization voidage (D_t = 0.29 m, bubble cap distributor, H_0 = 0.80 m)

3.2.1.3. Alumina in 1.56 m column

The effect of the increased column diameter was investigated with $H_0 \approx 0.8$ m. The actual static bed height was in the range 0.7 - 0.9 m due to particle entrainment over the course of the experiments. A sudden decrease in *H'* was observed at ~1 m/s only on certain days, although *H'* decreased slightly for $U > 0.4$ m/s (Figure 3.5).
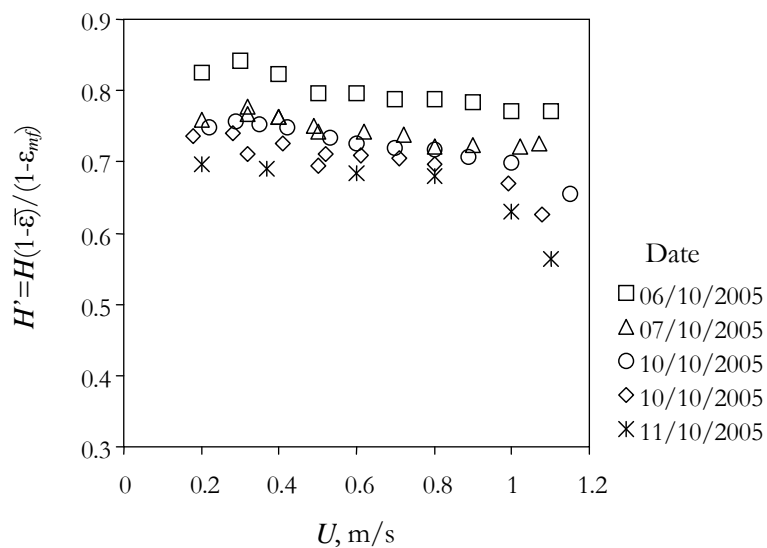
Figure 3.5. Height of dense bed corresponding to minimum fluidization voidage, *H'* vs. *U* (Alumina, D_t=1.56 m, $H_0 \approx 0.8$ m)

49

Cross-sectional mean voidages from differential pressure measured at the wall, with taps at 0.515 m and 0.665 m above the distributor plate, are shown in Figure 3.6. No sudden change in trend was observed here as the sensors were always immersed in the dense bed.
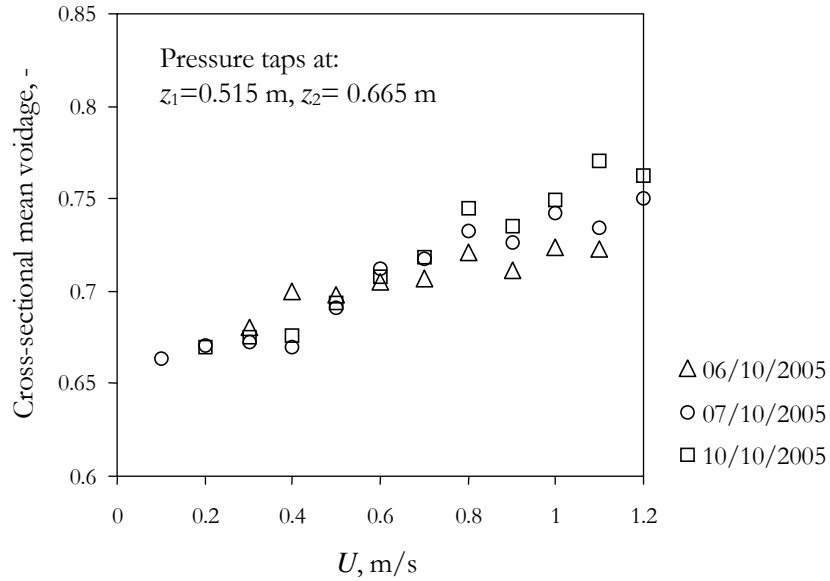
Figure 3.6. Time- mean cross-sectional voidage from differential pressure measurement at the wall vs. U (Alumina, $D_t = 1.56$ m, $H_0 \approx 0.8$ m)

3.2.2. Pressure fluctuations

The most common method of determining U_c is at the maximum of the dimensional standard deviation of absolute (single-point) pressure fluctuations. Assuming that at lower gas velocities, the dominant cause of pressure fluctuations is the coalescence and eruption of voids rising in the bed, the maximum standard deviation of pressure fluctuations may indicate that voids have reached a maximum size, becoming unstable. Other methods based on pressure fluctuations include determining the maximum dimensionless (normalized by the time mean pressure) standard deviation of pressure fluctuations. Bi and Grace (1995) reviewed these methods and showed that they produce different results. Their study compared dimensional and dimensionless standard deviations of pressure fluctuations, as well as changes in trends or features of the profiles of the power spectrum function and autocorrelation function applied to the pressure time series. These methods were applied to absolute (single-point) and differential pressures (two-point) in this study.
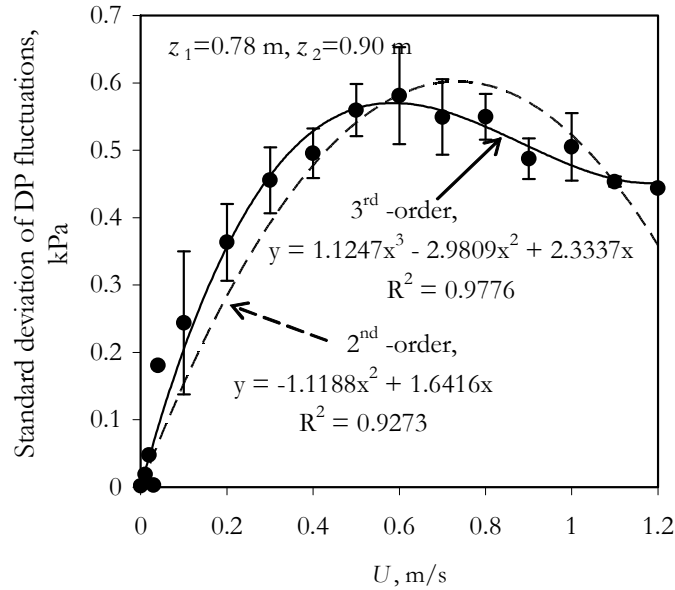
Figure 3.7. Standard deviation of differential pressure (DP) fluctuations vs. superficial gas velocity fitted with 2nd and 3rd order polynomials. Error bars show the variation from repeated measurements (Alumina, D_t=0.29 m, bubble cap distributor, H_0=0.8 m).

To find the maximum standard deviation of pressure fluctuations, a polynomial curve was fitted through the data points because of the scatter of the data. It was found that a 2nd-order polynomial did not fit the profiles well when the standard deviation of pressure fluctuations levelled off (most common with differential pressure), giving consistently higher values for U_c compared with a 3rd-order polynomial (e.g. see Figure 3.7). Fitting a polynomial through the data enables us to pinpoint a single velocity, but with a large error if the maximum is broad. The confidence level associated with fitting a polynomial curve to determine U_c at its maximum was analyzed by Ellis (2003) from a purely statistical point of view. In some cases, the analysis showed errors >10% of the determined U_c, suggesting curves being too broad. Because of the large errors associated with the maximum pressure fluctuation method, the confidence interval should always be reported. For the purpose of the heat transfer study, a range of velocities where transition to turbulent fluidization occurred was determined here rather than a single U_c value. The range of U_c was determined from different methods, and for different axial positions of the pressure sensors, which varied from 0.46 m to 0.78 m.

3.2.2.1. Standard deviation of pressure fluctuations

The standard deviation of absolute pressure fluctuations for FCC particles and H_0=0.8 m, plotted against *U,* is shown in Figure 3.8. The maximum was found to be in the range of velocities where the minimum cross-sectional voidage near the bed surface was observed (Figure 3.2). Data from runs performed on different days with the heater at different axial and radial positions and with different distributors are included in Figure 3.8. It appears that the radial position of the heater does not significantly affect the occurrence of a maximum standard deviation of pressure fluctuations at the wall (Figure 3.8a).

The maximum standard deviation of pressure fluctuations for different axial location of the sensor, 0.46 m < *z* ≤ 0.78 m, occurred at higher velocities (0.6 ~ 0.7 m/s) for the bubble cap distributor than for the perforated plate (Figure 3.8.b). At lower gas velocities, the standard deviation of pressure fluctuations for the bubble cap distributor overlapped with the one measured with the perforated plate distributor. Beyond 0.4 m/s the standard deviation of pressure fluctuations for the bubble cap distributor continued to rise, whereas for the perforated plate distributor it reached a maximum and began to decrease. However, from the results on macroscopic hydrodynamics, the bubble cap distributor showed no effect on the transition velocity and changes in trend of *H'* vs. *U* (Figures 3.1 and 3.4.) occurred at similar superficial gas velocities for both distributors.
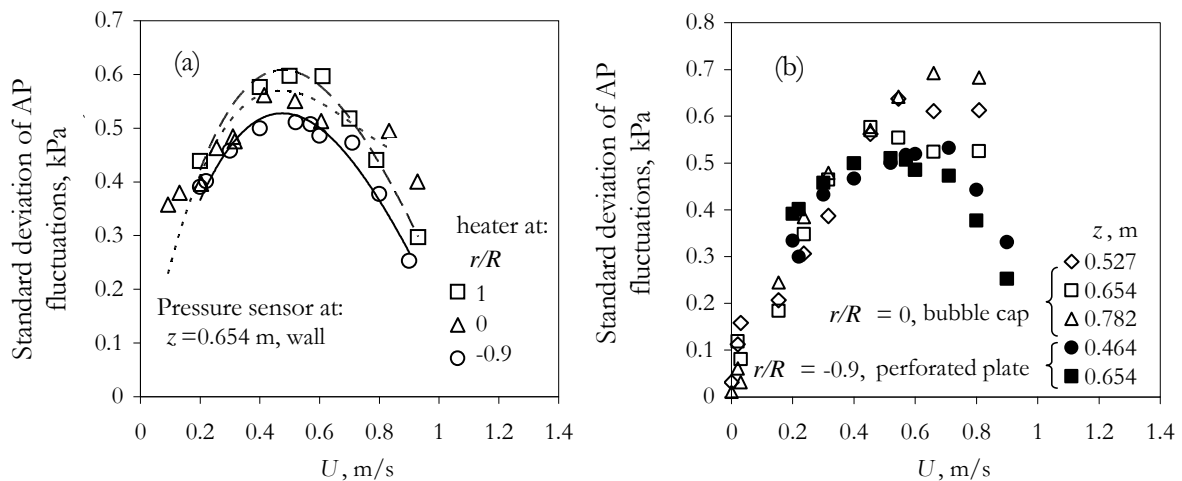
Figure 3.8. Standard deviation of absolute (AP) pressure fluctuations vs. superficial gas velocity: a) Effect of radial location of the immersed heater tube *r/R* (perforated plate); b) Effect of distributor and distance of pressure sensor above distributor plate. (FCC, D_t=0.29 m, H_0=0.8 m).

Standard deviations of absolute pressure fluctuations, σ_{AP}, for alumina particles at the wall of the 0.29 m column at the level of the heater (z_{AP}=0.5 m) with U are presented in Figure 3.9a. No significant effect of the radial location of the immersed heater tube is observed. A change in trend occurred at ~0.6 m/s where the standard deviation of pressure fluctuations levelled off. It remained unchanged over a range of velocities (0.6 ≤ U ≤ 1 m/s), and then slightly decreased (U>1 m/s) corresponding to the increase in the average bed voidage, illustrated on Figure 3.3. Compared with FCC particles (see Figure 3.8a), the plot of the standard deviation of absolute pressure fluctuations as a function of superficial gas velocity is flatter and U_c is higher.
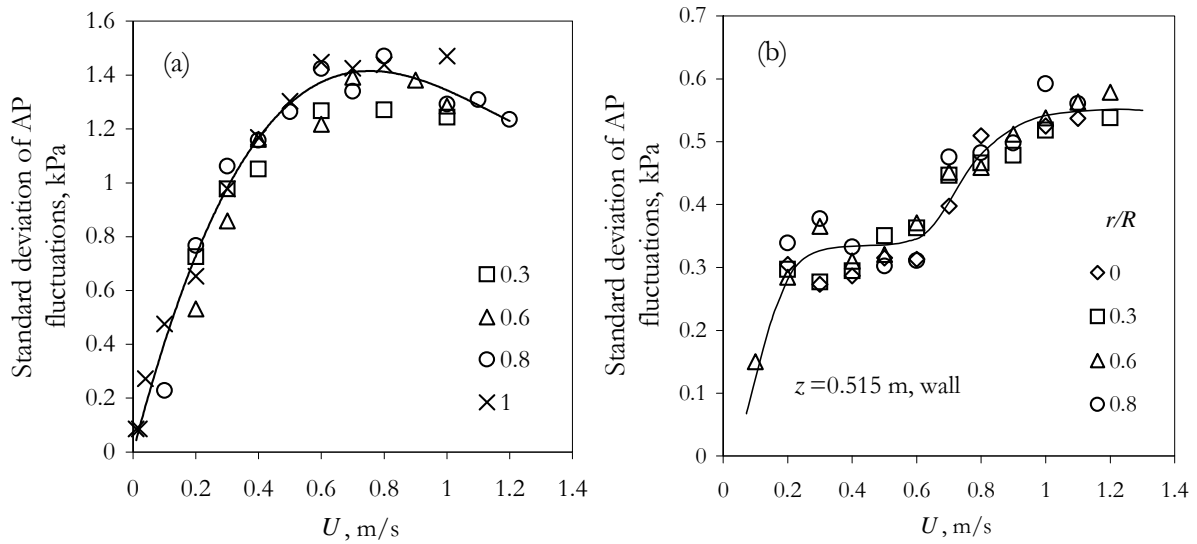
Figure 3.9. Standard deviation of absolute pressure fluctuations at the wall vs. superficial gas velocity a) D_t=0.29 m, b) D_t=1.56 m. r/R denotes penetration of the heater in the bed. (Alumina, bubble cap distributor, H_0=0.8 m)

The standard deviation of absolute pressure fluctuations at the wall of the 1.56 m column, 0.515 m above the distributor, is presented in Figure 3.9b based on data taken on different days at various radial positions. The data appear to be reproducible and not affected by the penetration of the traversing arm in the bed. The intensity of the fluctuations does not change significantly between 0.2 and 0.6 m/s. For U > 0.6 m/s, it starts to increase more rapidly up to ~1 m/s where it levels off. Similar profiles (not shown on figure) were observed for the standard deviation of differential pressure fluctuations at the wall, covering a 0.150 m vertical distance, from 0.515 to 0.665 above the distributor. These profiles differ from that observed in the smaller column, where the standard deviation of pressure fluctuations increased, levelled off and then decreased. Hence, U_c cannot be

detected from the dimensional standard deviation of pressure fluctuations vs. superficial gas velocity plot in the range of superficial gas velocities investigated for the larger column.
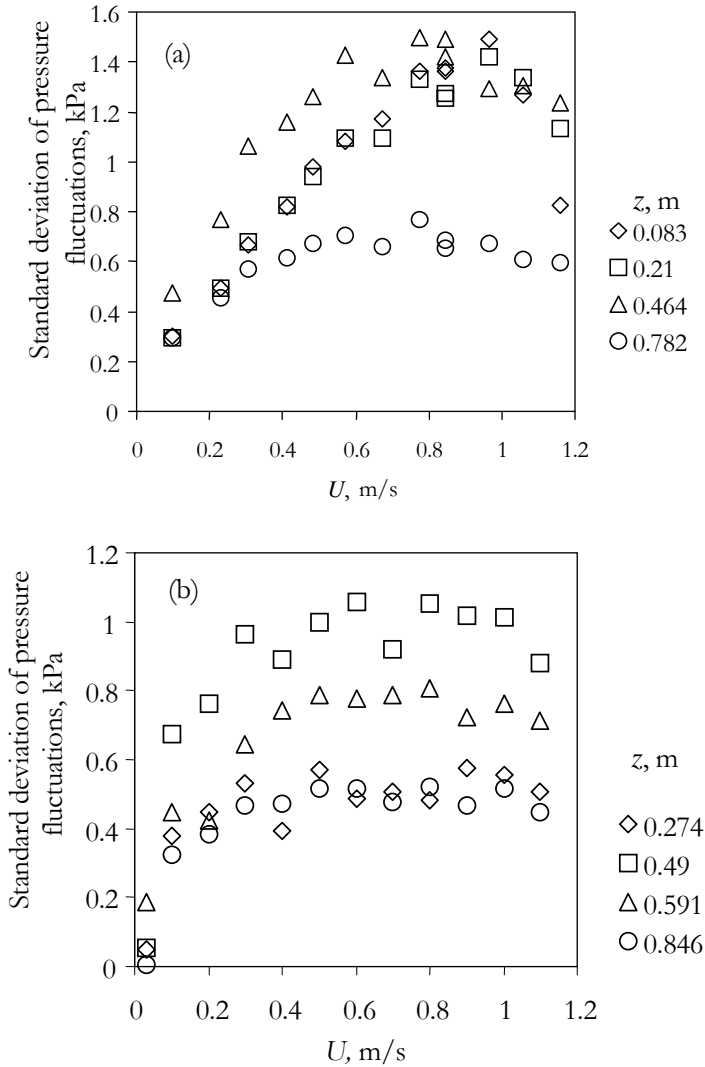
Figure 3.10. Standard deviation of pressure fluctuations vs. superficial gas velocity a) absolute pressure, b) differential pressure (Alumina, D_t =0.29 m, bubble cap, H_0=0.8 m)

The occurrence of a maximum absolute pressure standard deviation was affected by the height of the pressure sensor (Figure 3.10a). For a sensor in the region affected by the heater ($z > 0.464$ m), the increase in standard deviation with superficial gas velocity levelled off near 0.6 m/s, whereas for $z \leq 0.464$ m, the standard deviation exhibited more pronounced maxima at higher gas velocities, ~0.8 m/s (Figure 3.10a). The standard deviation of differential pressure fluctuations,

σ_{DP}, measured at the column wall at different heights is plotted in Figure 3.10b. An increase in standard deviation is observed at low gas velocities, whereas for a wide range of velocities $U = 0.5$-1 m/s the standard deviation of differential pressure fluctuations did not change significantly.

Figure 3.11 illustrates the trend of the standard deviation of differential pressure fluctuations vs. U for FCC particles between $z_1=0.782$ m and $z_2=0.909$ m. In most cases the profile become relatively flat for $U > 0.4$ m/s. The standard deviation of differential pressure fluctuations declined after reaching a flat maximum only for a sensor near the bed surface (Figure 3.11, $H_0=0.8$ m). This might be due to the increased voidage in the test section.

Normalizing the standard deviation by dividing by the time-mean differential pressure should take into account the effect of increased voidage. The normalized standard deviation of the differential pressure fluctuations, plotted in Figure 3.11 (solid triangles), continuously increased, without exhibiting a maximum.
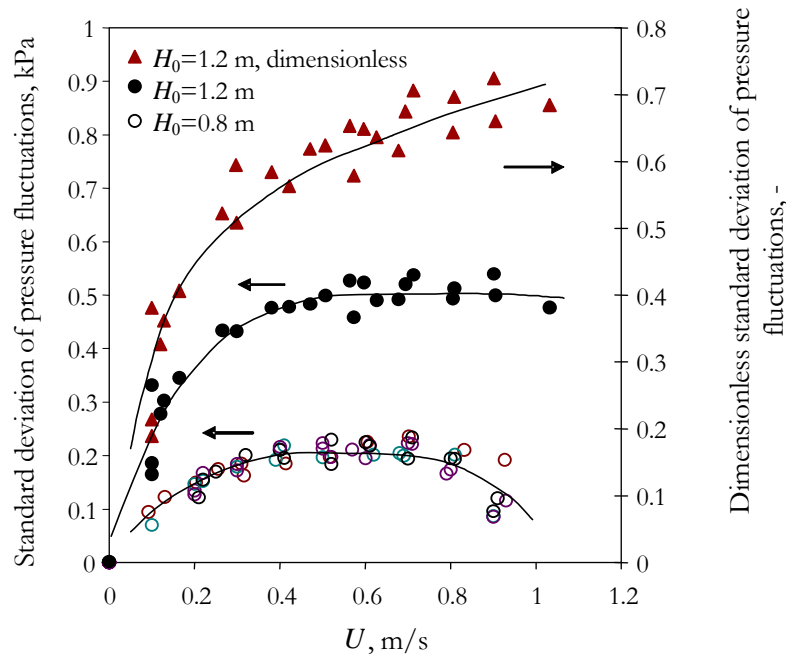
Figure 3.11. Standard deviation of differential (DP) pressure fluctuations vs. superficial gas velocity. Effect of H_0 and normalization. (FCC, $D_t=0.29$ m, perforated plate distributor, $z_1=0.782$ m, $z_2=0.909$ m)

3.2.2.2. Frequency domain analysis

0.29 m column

Converting the pressure signal to the frequency domain gives additional information on the local flow structure. To be able to analyze and extract information from the pressure fluctuations, it is necessary to understand the underlying physical phenomena. The dominant frequency in the power spectrum may shift from one source of pressure fluctuations to another (depending on source intensity) making the attribution of the dominant frequency challenging.
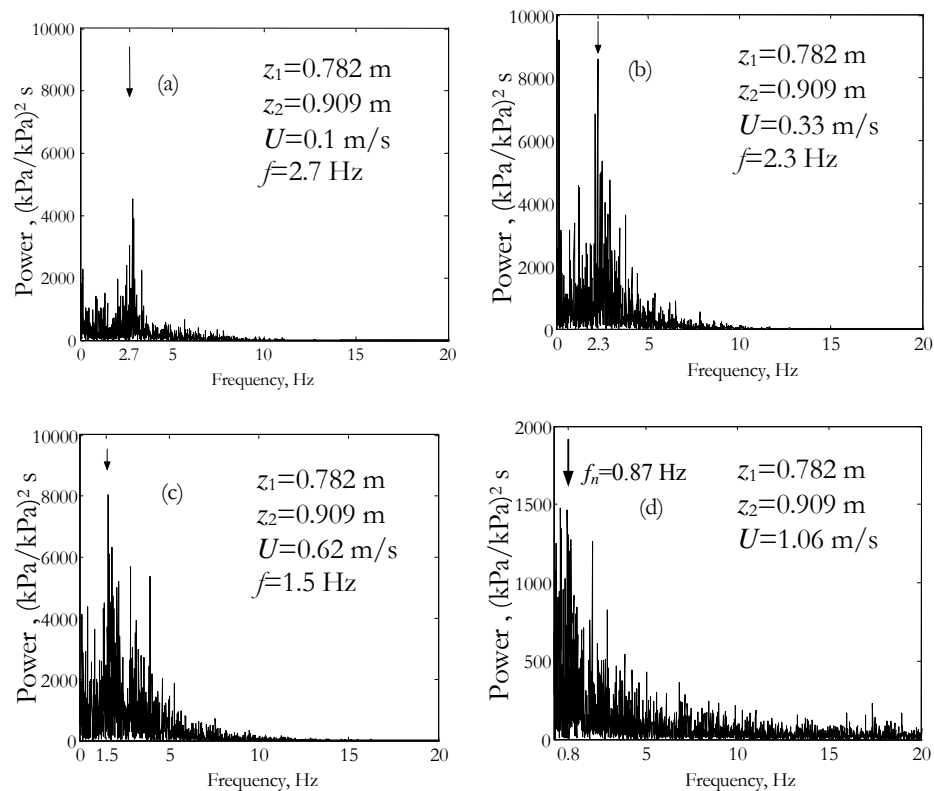
Figure 3.12. Power spectrum of differential pressure signals (FCC, D_t=0.29 m, perforated plate distributor, H_0=0.8 m).

The power spectra of the differential pressure signals at different U are shown in Figure 3.12. At 0.1 m/s, the peak in the power spectrum distribution was near 2.7 Hz which can be attributed to passing voids. For low superficial gas velocities, the peak was pronounced and symmetrical. With increasing U, multiple peaks appear in Figure 3.12c and the dominant frequency is difficult to identify. At 1.06 m/s, the power intensity decreased and high frequency ($f > 5$ Hz) content becomes present in the signal (Figure 3.12d). It appears that one of the peaks coincides with the

"natural" frequency for homogenous fluidization calculated by Verloop and Heertjes (1974), f_n=0.87 Hz, marked in Figure 3.12d. Similar trends and features of the power spectra were detected for alumina particles in the 0.29 m column, with the dominant frequency in the range 2.3 -3.1 Hz for $0.1 \leq U < 0.6$ m/s and an identifiable peak for high U. The evolution of the power spectrum of the normalized absolute and differential pressure signal with U for alumina particles is shown in Figure 3.13.
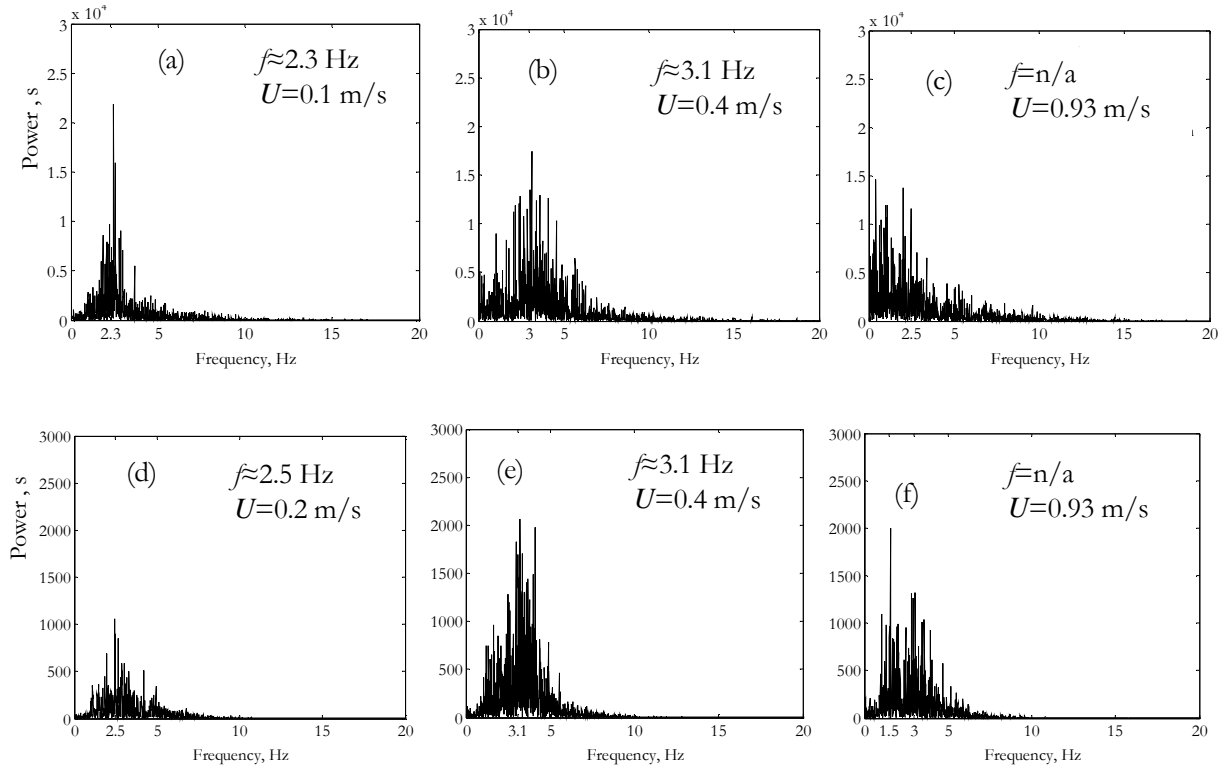
Figure 3.13. Power spectra of normalized differential (a-c) and absolute (d-f) pressure fluctuations: a) U=0.1 m/s; b) and e) U=0.4 m/s, c) and f) U=0.93 m/s, d) U=0.2 m/s (Alumina, D_t=0.29 m, H_0=0.8 m, z_{AP}=0.46 m, z_{DP1}=0.46 m, z_{DP2}=0.52 m)

1.56 m column

The power spectra of the normalized pressure signal shown in the second column of Figure 3.14 and Figure 3.15 reveal changed flow structures beyond 0.6 m/s. For, U=0.2 m/s, there is a relatively broad peak near 1.8 Hz for both absolute and differential pressures. As U is increased, a second peak emerges at ~3.6 Hz, gradually reaching the same intensity as the peak at lower frequencies (at U=0.5 m/s, Figure 3.14). Svensson et al. (1996a, 1996b), who investigated large
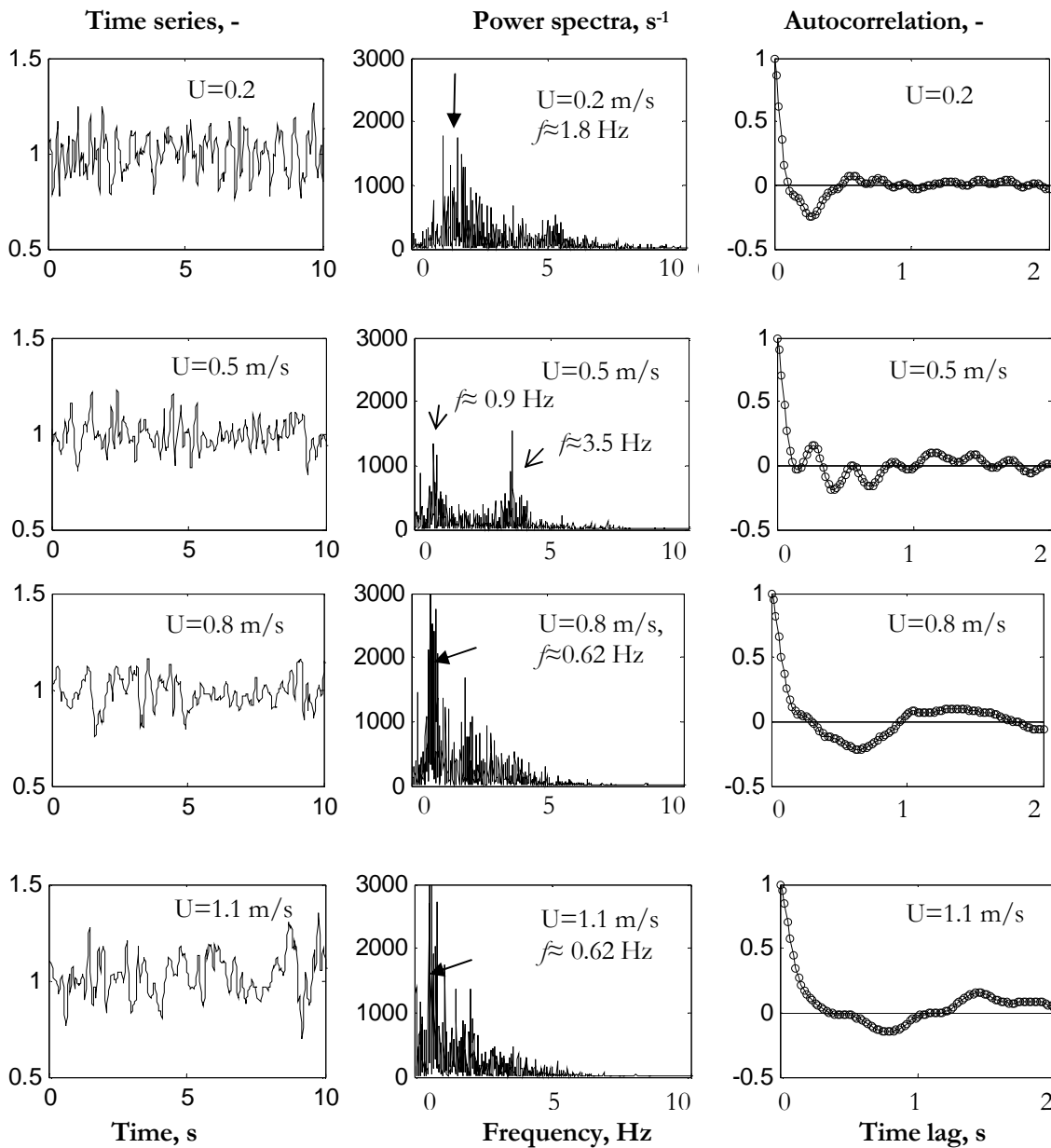
Figure 3.14. Normalized absolute pressure time series, power spectrum and autocorrelation (Alumina, D_t=1.56 m, H_0=1.56 m)

columns, reported double peaks in the power spectra. They attributed the peak at the higher frequency to multiple bubbling and that at lower frequency to formation of a single large void, distorted and containing particles, occupying most of the bed, its formation probably related to the large volume of the air supply system and low pressure drop across the distributor. For $U > 0.6$ m/s, the dominant peak in the power spectrum shifts to lower frequencies, ~0.62 Hz. Similar results were reported by Svensson et al. (1996a, 1996b) at higher gas velocities. They called this the

"exploding bubble" flow regime, where the void formed at the distributor was geometrically unsustainable for the dense bed height and erupted at the surface as it was created. They were unable to determine the onset of turbulent fluidization based on the standard deviation of normalized differential pressure fluctuations, as no maximum in the plot against U was observed.
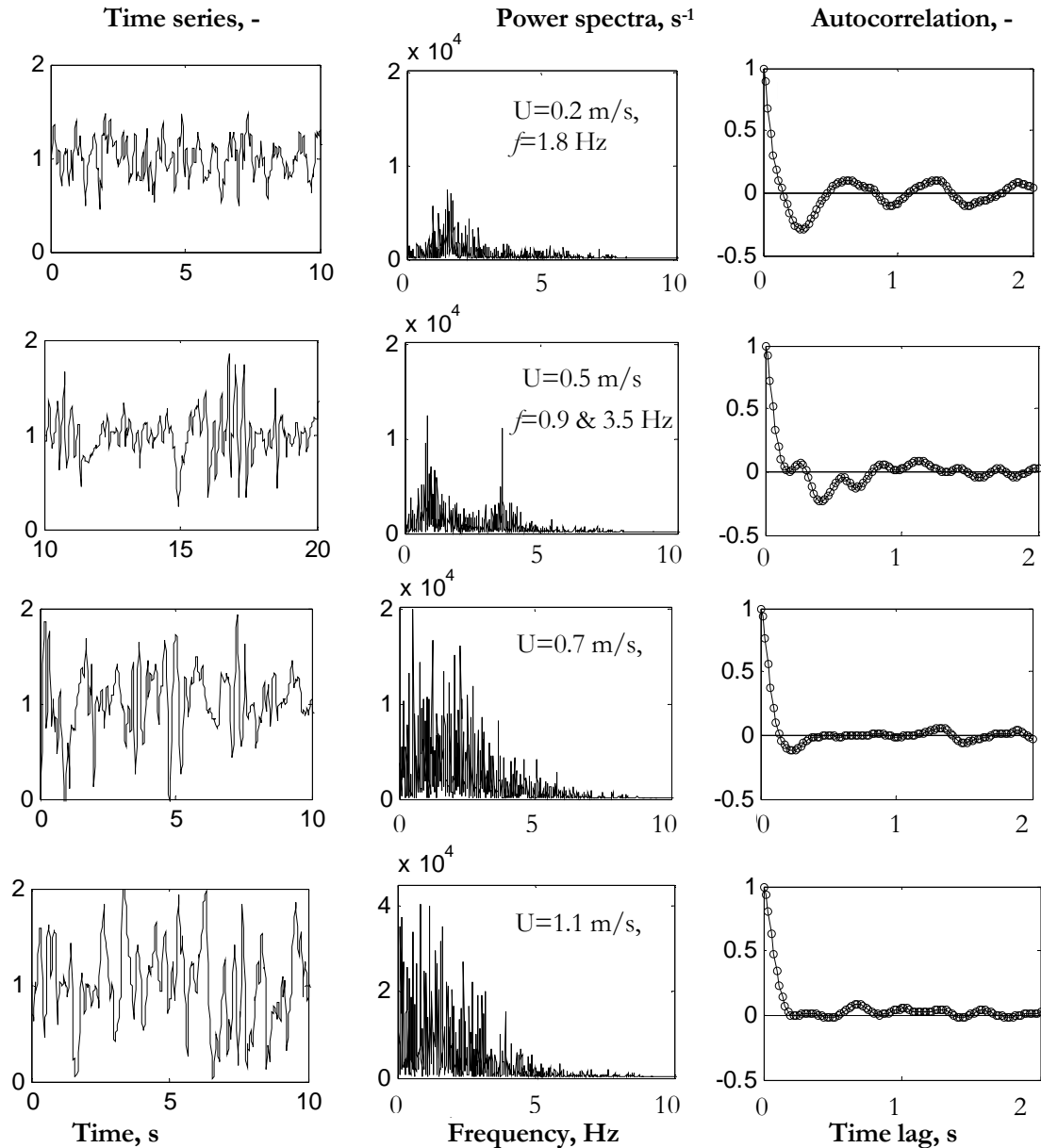
Figure 3.15. Normalized differential pressure time series, power spectrum and autocorrelation (Alumina, D_t=1.56 m, H_0=1.56 m)

The power spectrum of the normalized differential pressure signal (Figure 3.15) is similar to the power spectrum of the normalized absolute pressure at lower gas velocities. At higher gas

velocities, a peak in the power spectrum could not be detected and the intensity of the power of the fluctuations significantly increased (note higher y-axis scale for power spectrum at U=1.1 m/s on Figure 3.15). Similar characteristic frequencies were found from the autocorrelation function of the pressure signal presented in the third column of Figures 3.14 and 3.15.

3.2.3. Local voidage

3.2.3.1. 0.29 m column

Figure 3.16a presents typical local time-mean voidage data from the centre of the column plotted against superficial gas velocity. Slightly higher local voidages were measured for $H_0 = 0.8$ m, attributed to the closeness of the bed surface. At low velocities, the time-mean local voidage increased steeply with increasing U. For $U \approx U_c$, the voidage trend changed. Similar changes near the onset of turbulent fluidization were reported by Nakajima et al. (1990), Andreux et al. (2005) and Lancia et al. (1988), who attributed the change to the breakdown of large voids and increased interstitial air flow. The breakdown of bubble/dense phase flow was noted in the optical probe signal for $U = 0.72$ m/s (in the turbulent fluidization regime), shown in Figure 3.1b. The signal is more scattered around the mean and individual voids cannot be identified. The standard deviation of the local voidage reached a maximum (see Figure 3.16b) in the range of velocities where U_c is
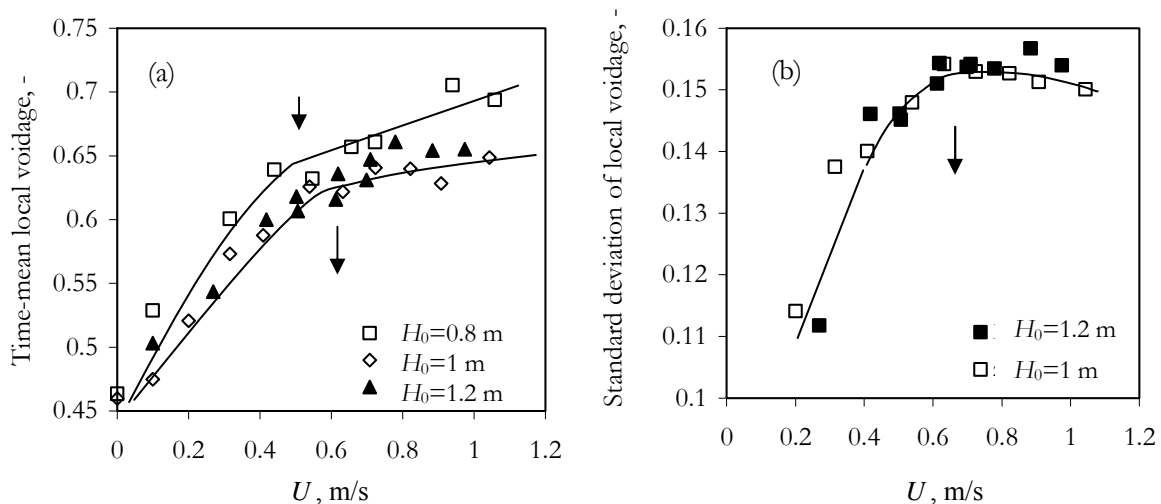
Figure 3.16. Local voidage as function of superficial gas velocity a) time-mean, b) standard deviation (FCC, D_t=0.29, perforated plate distributor, r/R=0, z_{OP}=0.47 m)

expected (Bi et al., 2000). The static bed height only had effect for $H_0/D_t < 3$ ($H_0 = 0.8$ m), where changes in local flow structure appeared at lower U. The superficial gas velocities corresponding to change in local voidage corresponds to the range where U_c was defined from the pressure fluctuations.

The probability density of voidage in Figure 3.17 confirms that bed homogeneity increases with increasing U. The peak at $\varepsilon \approx 0.48$ (attributed to the dense phase) became less pronounced with increasing gas velocity, suggesting that the dense phase presence in the signal decreased. A plot of kurtosis of local voidage against superficial gas velocity appears in Figure 3.18. With increasing superficial gas velocity, the "peakedness" of the distribution decreased. Beyond 0.4 m/s the kurtosis is negative and independent of increasing gas velocity, indicating a relatively flat distribution. The static bed height, H_0 only had an effect for $U<U_c$. The skewness, shown on Figure 3.19, is negative. Beyond $U \approx 0.9$ m/s the skewness is close to zero indicating a symmetrical distribution due to increased homogeneity of the flow structure and "disappearance" of a continuous dense phase in the central region of the bed.
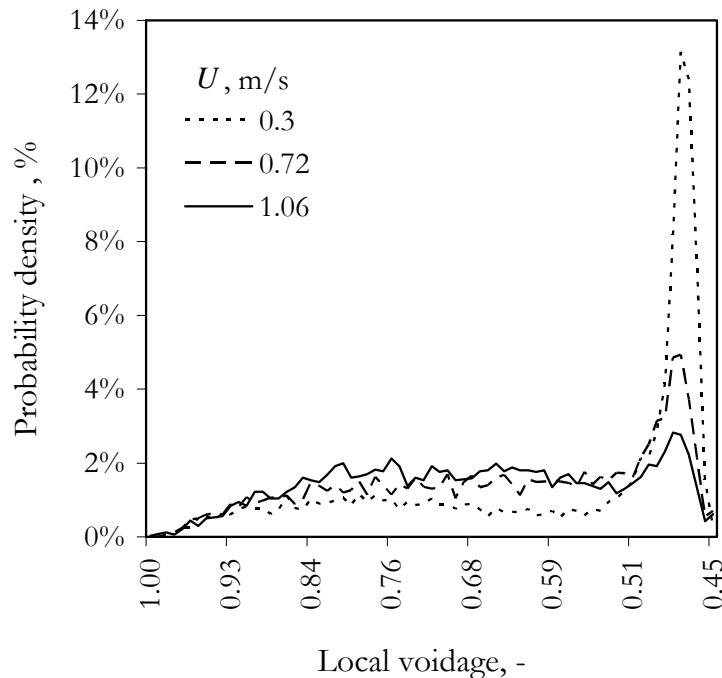
Figure 3.17. Probability distribution of local voidage (FCC, D_t=0.29, perforated plate distributor, H_0=0.8 m, r/R=0, z=0.75 m)
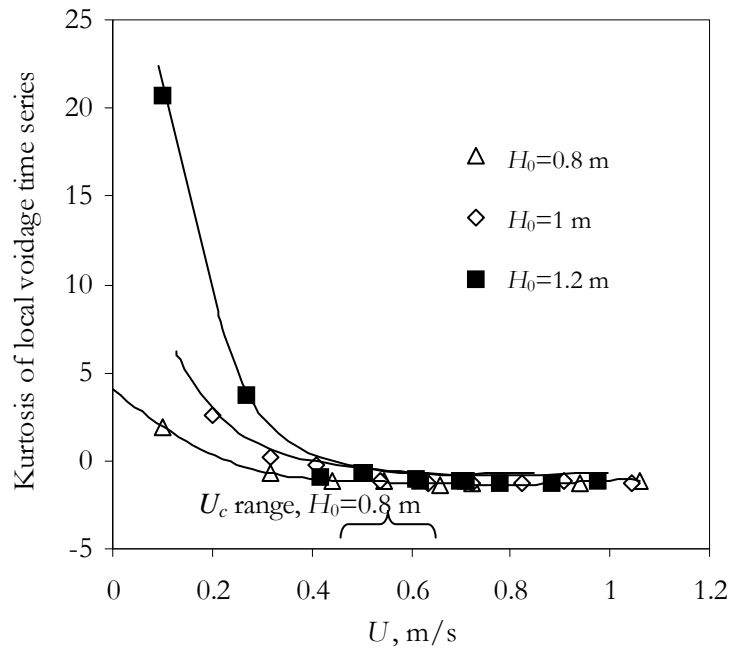
Figure 3.18. Kurtosis of local voidage distribution (FCC, D_t=0.29, perforated plate distributor, r/R=0, z=0.47 m)
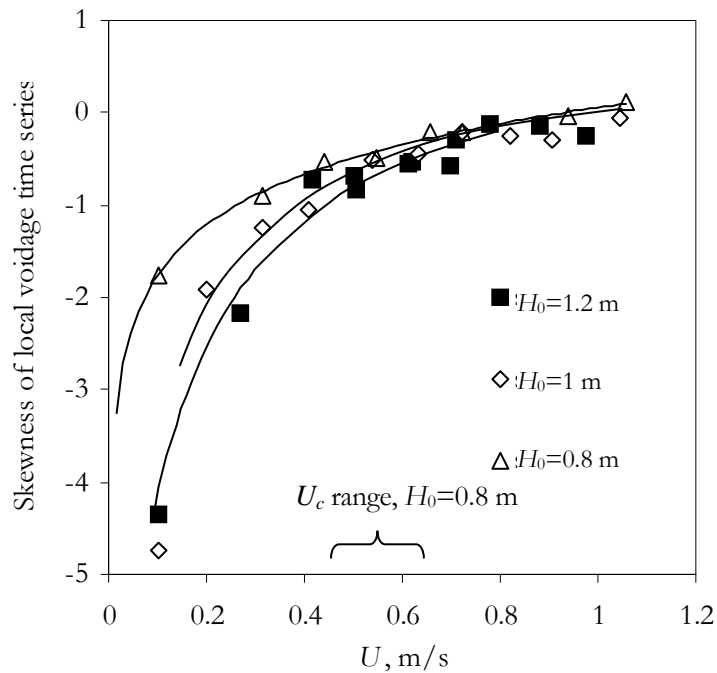
Figure 3.19. Skewness of of local voidage distribution vs. U and effect of H_0. (FCC, D_t=0.29 m, perforated plate distributor, r/R=0, z=0.47 m)

The local time-mean voidage for alumina particles at different radial positions, 0.47 m above the distributor, is plotted against the superficial gas velocity in Figure 3.20. A steep increase in time-

mean voidage vs. superficial gas velocity bed was observed in the centre up to 0.12 m/s, where slugging was predicted. With a further increase in gas velocity the voidage in the core of the column did not change significantly, whereas in the wall region it continued to increase. The local voidage across the bed become uniform for $U{\approx}0.4$-0.6 m/s. With further increase in U, the trend changed, with voidage increasing more steeply in the centre than near the walls. This is typical for turbulent fluidization (Nakajima et al., 1990; Ellis, 2003).
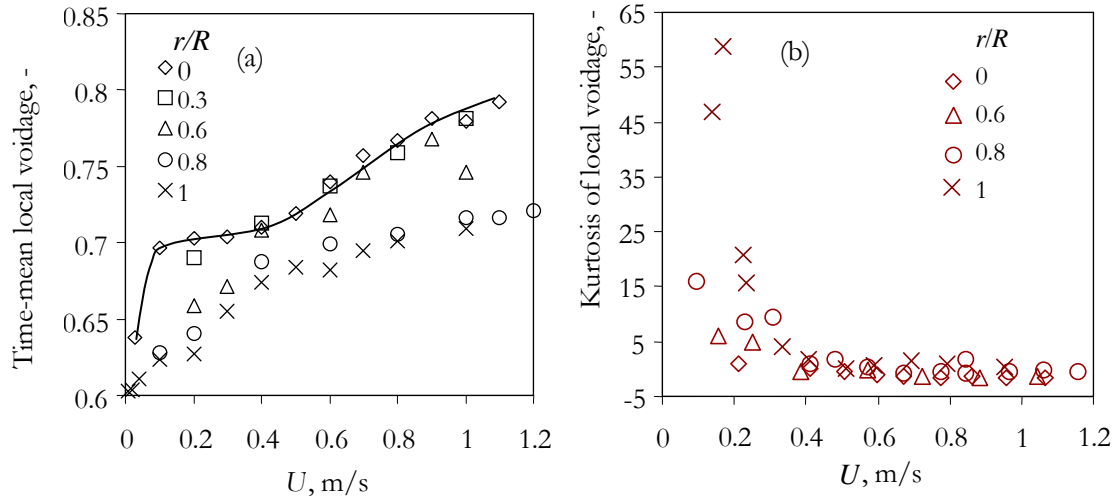
Figure 3.20. Local voidage a) time-mean and b) kurtosis vs. *U* and effect of radial position of probe, *r/R*. (Alumina, bubble cap distributor, *D$_t$*=0.29 m, *H$_0$*=0.80 m, *z*=0.47 m)

The standard deviation, kurtosis (Figure 3.20b) and skewness of the local voidage signal, all exhibited changes in trend near 0.4-0.6 m/s for *r/R*>0.3, indicating more randomly distributed signals and increased homogeneity across the bed at higher gas velocities, typical for turbulent fluidization. The kurtosis plot on Figure 3.20b indicates that the local flow structure transformation progresses from the core towards the wall with increasing *U*. The change in the local flow structure identified from the optical probe occurred at a lower value of *U* than the maximum standard deviation of pressure fluctuations obtained by curve fitting.

Typical time series and power spectra of normalized optical probe signal are shown in Figure 3.21. For *U*=0.2 m/s and *r/R*=0, the peak frequency occurred at ~2.5 Hz, corresponding to the peak in the pressure power spectrum. The instantaneous optical probe signal at *U*=0.6 m/s reveals intermittent flow, alternating between bubbling/slugging and turbulent-like. In the turbulent

fluidization regime, $U>0.6$ m/s, the power is distributed among low frequencies and no peak frequency can be established.
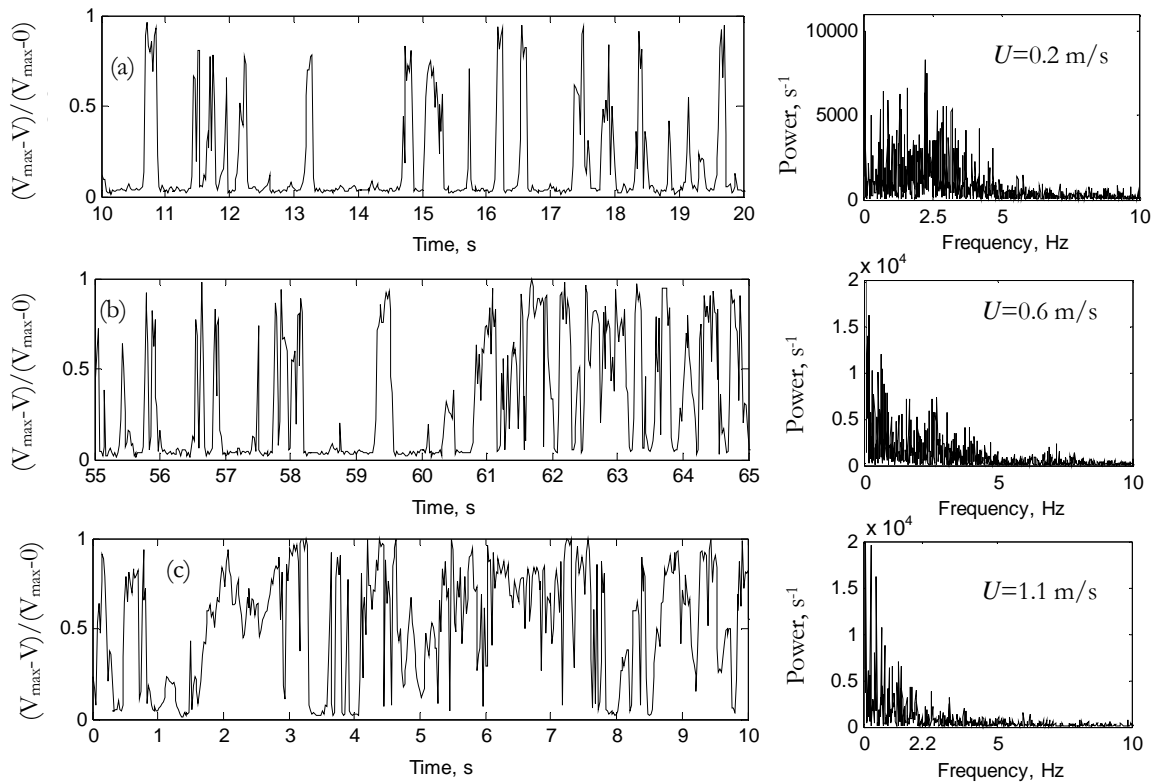
Figure 3.21. Instantaneous normalized local voidage and corresponding power spectra (Alumina, D_t=0.29 m, bubble cap distributor r/R =0, U=0.2, 0.6 and 1.1 m/s, z=0.47 m)

The cross-correlation function (Figure 3.22) of the optical probe signal above and below the heater shows a strong positive peak at a time lag of ~0.2 s at U=0.2 m/s and r/R=0. As the gas velocity increased, the peak became less pronounced, and beyond 0.6 m/s the estimated cross-correlation coefficients were widely distributed among time lags. The strong cross-correlation coefficients indicate that the flow entity observed at the lower optical probe is also detected by the upper optical probe. The lack of correlation between the optical probe signals at high superficial gas velocities (U = 1 m/s) may be due to flow entities or turbulent eddies of smaller scale (smaller than the distance between the two optical probes), typical of turbulent fluidization.
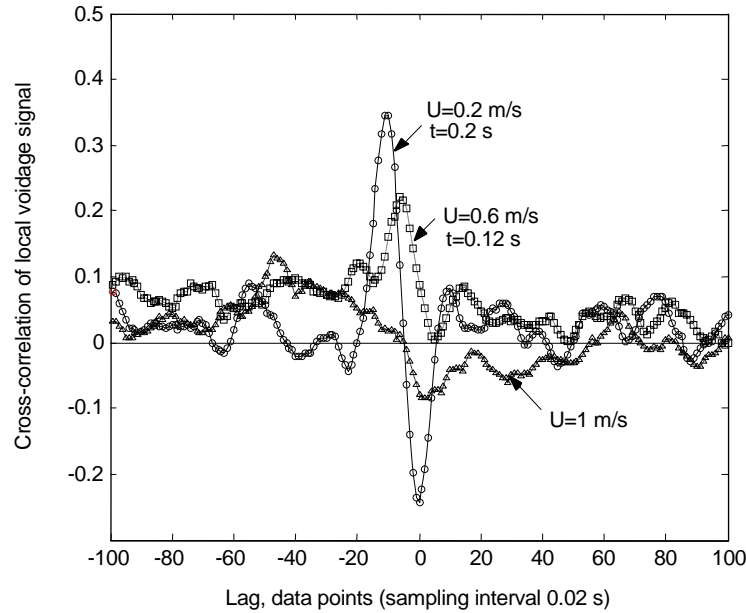
Figure 3.22. Cross-correlation functions of the optical probe signals at *z*=0.47 m and *z*=0.75 m at *U*=0.2, 0.6 and 1 m/s (Alumina, D_t=0.29 m, bubble cap distributor, H_0=0.8 m, *r/R*=0)

3.2.3.2. 1.56 m column

The time-mean local voidages from the optical probe at different radial positions is shown in Figure 3.23 as a function of superficial gas velocity. It is apparent that at low velocities the flow is not uniform, with voids rising mainly near *r/R*=0.6 while the rest of the bed remains relatively dense. The radial uniformity improved when *U* exceeded 0.6 m/s where local voidages measured at different radial locations merged. The local flow underwent a significant change with increasing *U*, as explained below.

Superficial gas velocity range: 0.2 ≤ U ≤ 0.6 m/s

A typical signal from the optical probe and the corresponding power spectrum function in the bed regions of high voidage appear on Figure 3.24. At *U*=0.2 m/s and *r/R*=0.8, the signal was typical for bubbles passing the probe, and the power spectrum function has a peak at ~1.8 Hz, in agreement with the peak found in the pressure signal for the same conditions. With a further increase of the gas velocity, the void trajectory shifted to *r/R*=0.6, causing the local voidage near *r/R*=0.8 to decrease. The signal from the optical probe at *U*=0.4 m/s and *r/R*=0.6 (Figure 3.24 b) revealed a different flow structure than that at *r/R*=0.8 and *U*=0.2 m/s. The signal suggests

unstable voids as the velocity increased beyond 0.2 m/s. The power was more evenly distributed across the frequencies except for a peak near 0.6 Hz.
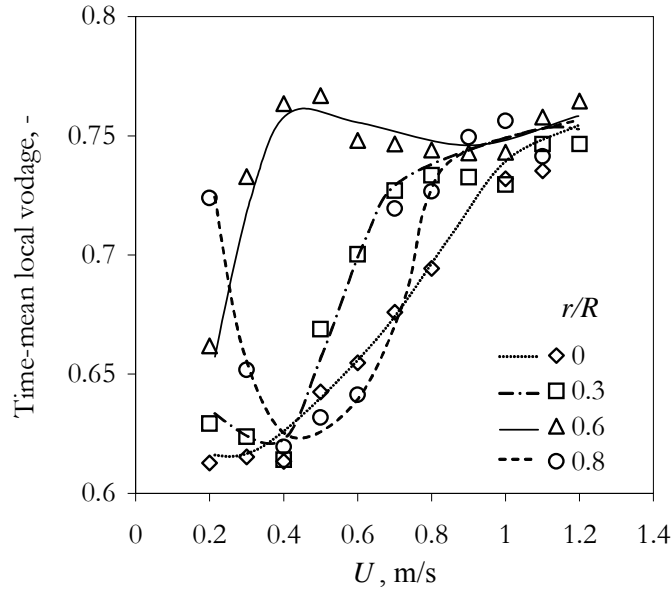
Figure 3.23. Time-mean local voidage vs. *U* for different radial positions of the traversing arm. (Alumina, *D_t*=1.56 m, *H_0*=0.8 m, *z*=0.6 m)

In the central region (*r/R*=0 and 0.3), above the region where there was no active bubble cap, the time-mean local voidage was low, close to that at minimum fluidization and did not change significantly with increasing gas velocity up to 0.4 m/s. Beyond 0.4 m/s, as the flow in the region of highest local voidage (*r/R*=0.6) began to resemble that of turbulent fluidization, more gas entered the relatively dense region in the centre of the bed and near the walls. The optical probe signals at *r/R* = 0 and 0.4 ≤ *U* ≤ 1.1 m/s, presented in Figure 3.25a-d, illustrate this change. The trend of increasing local voidage near the wall and in the centre continued until the time-mean local voidage reached ~0.75 for all radial locations. According to Andreux et al. (2005), the maximum fraction of gas that can pass through the bubble (void) phase is 75-80%, beyond which the bubble flow becomes unsustainable and transition to turbulent flow occurs.
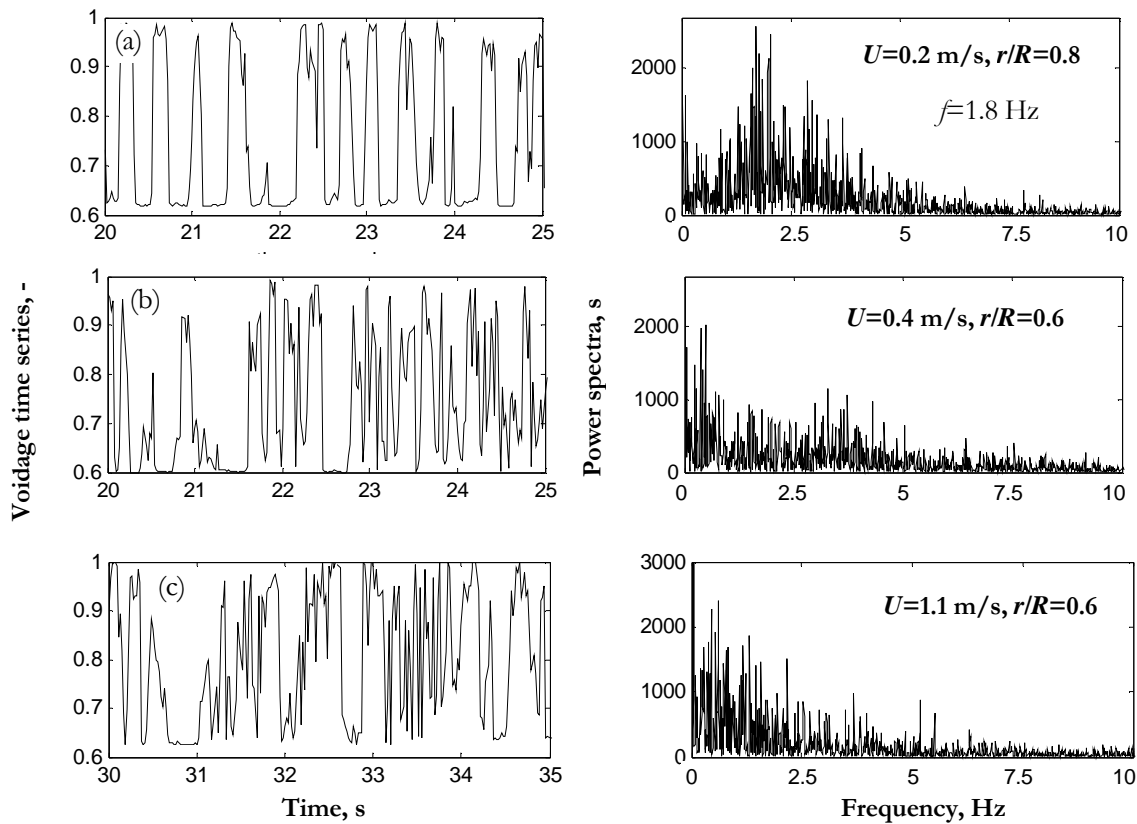
Figure 3.24. Local voidage time series and power spectra in regions of high void activity (Alumina, D_t=1.56 m, H_0=0.8 m)

The local change in flow structure could not be detected by the standard deviation of pressure fluctuations at the wall of the column as σ_{AP} and σ_{DP} remained relatively unchanged over the range $0.2 < U \leq 0.6$ m/s (Figure 3.9). In this range of velocities the power spectra of the pressure signals, both absolute and differential, did not change significantly, except that the higher frequency peak appeared (Figure 3.14).

Voidage time series, -   **Power spectra, s^{-1}**
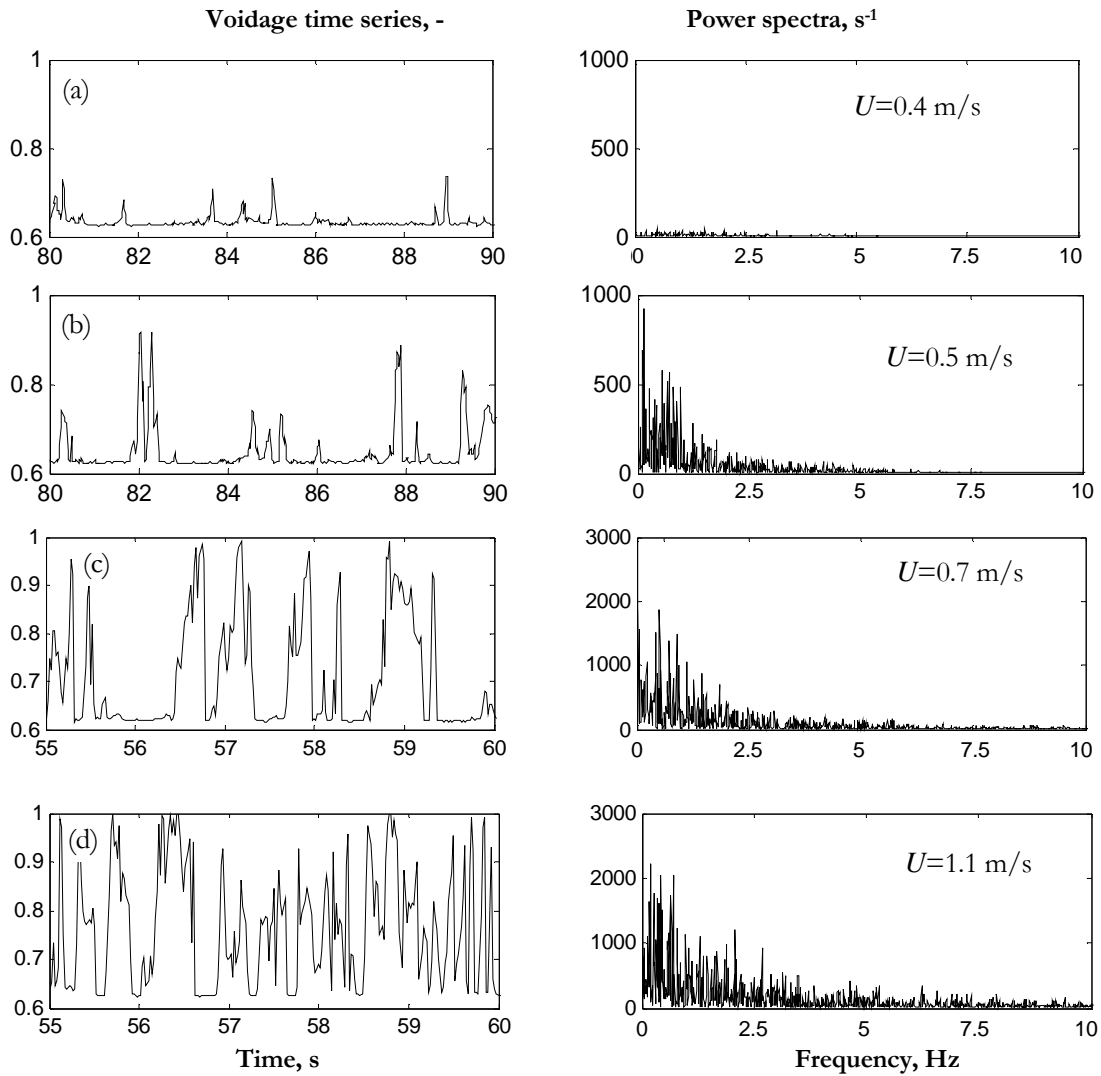
Figure 3.25. Optical probe signal at *r/R*=0 and a) *U*=0.4 m/s, b) *U*=0.5 m/s, c) *U*=0.7 m/s, d) *U*=1.1 m/s (Alumina, *D$_t$*=1.56 m, *H$_0$* ≈ 0.8 m).

Superficial gas velocity range: 0.7 ≤ U ≤ 1.2 m/s

For *U* > 0.6 m/s the local voidage became more uniformly distributed across the bed and did not change significantly with increasing gas velocity. The signal from the optical probe has the same appearance and a similar power spectrum distribution at most radial positions (Figure 3.24c and d) except at *r/R*=0. For *r/R*=0, this occurs for *U* ≥ 1 m/s (Figure 3.25d).

The standard deviation of absolute pressure fluctuations began to increase beyond *U*=0.6 m/s and reached a maximum near 1 m/s (Figure 3.9). For velocities 0.7 ≤ *U* ≤ 1.2 m/s, the power spectrum of the normalized absolute pressure reveals a strong peak at low frequencies, ~0.62 Hz,

skewed to the right. However, the power spectrum of the normalized differential pressure signal (Figure 3.15) exhibited higher intensity fluctuations at low frequencies, with no clearly identifiable peak. This is probably due to disintegration of large voids.

To summarize, from pressure and voidage data, the transition to turbulent fluidization is more gradual for the larger column than the smaller one. It starts with instability of the large voids, caused either by bubbles that are too large to be sustained in the dense bed or decreased distance between bubbles This marks the onset of the transition towards the turbulent fluidization flow regime. As a consequence, the dense phase gradually broke down and the bed became more uniform in the radial direction. The transition was completed at 1 m/s, with the centre of the bed exhibiting a similar turbulent-like flow structure as the rest of the bed.

3.2.4. Visual observations

The 0.29 m transparent column was observed for increased entrainment in the freeboard, appearance of distorted unstable voids at the wall, increased horizontal movement of particles, and general turbulent appearance. Figure 3.26 shows a photograph at the transparent column wall for the turbulent fluidization flow regime. Voids are marked by white arrows, while the direction of fast particles is denoted by black arrows. The dashed oval marks a region of slowly moving particles.
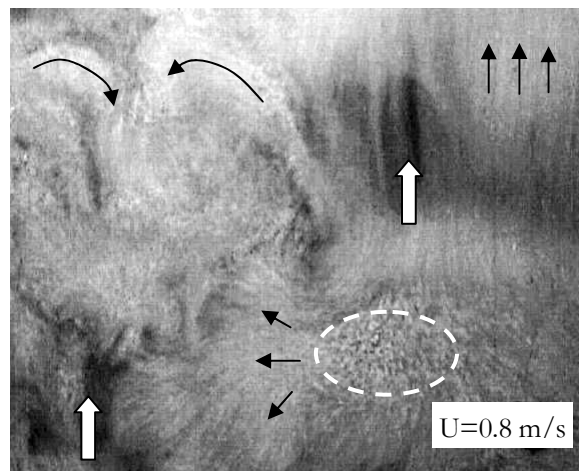
Figure 3.26. Photographic image at wall of 0.29 m column (FCC, D_t=0.29 m, H_0=0.8 m, z=0.6 m, U=0.8 m/s, exposure 1/60 s)

3.3. Discussion

The experimental results confirm what was noted in Bi et al. (2000) and Grace (2000) regarding three types of transition; a relatively abrupt transition characterized by maximum standard deviation of absolute pressure fluctuation for group A particles, more gradual transition for group B particles in deep beds, and a transition, still gradual, but affected by the distributor (controlling the circulation patterns) for shallow beds.

For FCC particles, the compared methods, maximum standard deviation of pressure fluctuations, bed expansion and changes in local voidage, produced value of U_c in a relatively narrow range, ~0.45 m/s for H_0=0.8 m and ~0.6 m/s for H_0=1.2 m.

Alumina particles used in the experiments are near the border between the A and B groups of Geldart's classification. For this kind of particle, the transition to turbulent fluidization appears to extend over a wider range of velocities than for FCC (group A) near the heater. If the transition velocity for the onset of turbulent fluidization, U_c, is defined as the velocity where the two-phase (bubble/dense phase) flow structure starts to break down, the critical velocity for the alumina particles in the 0.29 m column based on the local voidage analysis and bed expansion was observed near 0.6 m/s. Based on the same definition, U_c in the large column started in the region of high voidage near 0.4 m/s, and then progressed radially towards the dense regions near the walls and in the centre. The transition was completed at ~1 m/s when the two-phase flow structure almost completely disappeared throughout the entire bed. The break-up of the two-phase flow structure extended over a range of velocities, depending on radial location, in the large column.

The common method of defining U_c at the maximum of the standard deviation of pressure fluctuations was found not to be reliable for the alumina particles. The first issue arose because the maximum was flat (extending over a range of velocities). If a regression line is fitted through the standard deviation data plotted against superficial gas velocity, the estimated maximum is sensitive to the choice of the regression curve. The local voidage data for the smaller column showed that the change in flow structure at $U \approx$ 0.4-0.6 m/s, corresponded to where the standard deviation of pressure fluctuations levels off, rather than where a maximum occurred. This leads to a second issue with this method: in some cases, the standard deviation of pressure fluctuations increases monotonically with superficial gas velocity, so that a maximum cannot be determined, although the

local voidage measurements show changes in local flow structure. For example, in the 1.56 m column, although the local voidage signal at $r/R=0.6$ shows turbulent-like flow structure at U as low as 0.4 m/s, the highest standard deviation of pressure fluctuations was near 1 m/s when a typical flow structure for turbulent fluidization was achieved across the bed.

Because of the complexity of the pressure signal, the maximum standard deviation of pressure fluctuations may not reflect changes in local flow structures related to turbulent fluidization and should be used in combination with other methods.

3.4. Summary

- With the onset of turbulent fluidization, increased entrainment of particles is observed from the bed height corresponding to the minimum fluidization voidage and the cross-sectional voidage measured near the bed surface. The axial profiles of cross-sectional voidage indicated a more diffuse bed surface. Vigorous mixing with eddying particle clusters (streams) and distorted, unstable voids interspersed with short periods of downwards bulk motion of solids were observed visually at the column wall. The two-phase flow structure gradually disappears, indicated by the probability density plots of local voidage, and the bed becomes more homogenous. The local voidage measured by an optical probe does not increase as steeply in the turbulent bed as in a bubbling bed due to the different flow structure. Radial profiles of local voidage were more symmetrical in the turbulent fluidization region.

- It was shown that different criteria produce different results for the onset of turbulent fluidization. For FCC particles and a perforated plate distributor, U_c from the maximum pressure fluctuations coincided with that indicated from the local voidage and bed expansion. For alumina particles, the bed expansion and local voidage methods usually indicate a lower transition velocity than that obtained from the maximum standard deviation of pressure fluctuations. This was also true for the bubble cap distributor and FCC particles. However, the velocity at which the standard deviation of pressure fluctuations leveled off corresponded to U_c determined from local voidage methods.

- For the FCC particles, the onset of turbulent fluidization for $H_0 = 0.8$ m occurs in the range of velocities $U_c = 0.45$ - 0.65 m/s for $0.46 < z < 0.78$ m. With increasing bed height,

H_0 = 1 and 1.2 m, the transition shifted to higher velocities (U_c = 0.6 - 0.8 m/s), in good agreement with published correlations (Table 2.2).

- A maximum standard deviation of absolute pressure fluctuations for $z \geq 0.46$ m for alumina particles in the smaller column occurred over a range of velocities $0.6 \leq U < 0.8$ m/s. Compared to published correlations based on absolute pressure fluctuations including the ratio H/D_t (Table 2.2), the predicted transitional velocity is generally higher ($0.83 \leq U_c \leq 1.43$ m/s) than in the vicinity of the heater. Below the heater, for $z < 0.46$ m, the maximum was more pronounced and shifted to higher U (0.8-1 m/s) which corresponds to the range of predicted U_c. This may indicate that the presence of the tube shifted U_c to lower values. The optical probe results suggest turbulent fluidization flow structures for $U > 0.6$ m/s at $z = 0.47$ m for all radial positions.

- Different circulation patterns were found in the 0.29 m and 1.56 m columns at lower gas velocities. The flow in the larger, relatively shallow bed was greatly influenced by the distributor configuration, which also influenced the nature of the transition to turbulent fluidization. At higher gas velocities, with the onset of turbulent fluidization, the local flow structure became similar in the two columns.

- The onset of transition to turbulent fluidization cannot be established from the standard deviation of pressure fluctuations in the large column. The transition is gradual, progressing radially from regions of higher voidage to regions of low voidage. This transition is influenced by the circulation patterns in the bed, affected by the distributor configuration. More accurate results on the transition from two-phase to turbulent fluidization were obtained from the optical probe. It appears that the transition first started at $r/R = 0.6$ at $U \approx 0.4$ m/s and progressed radially until $U \approx 1$ m/s.

- Since the onset of turbulent fluidization can occur locally and is affected by many parameters such as distance from the distributor, immersed objects and radial location, correlations should be viewed with caution. The most reliable way to measure the changes in local flow structure leading to turbulent fluidization was to use and optical probe.

Chapter 4

4. HEAT TRANSFER FROM AN IMMERSED VERTICAL TUBE

4.1. Introduction

Heat is often removed or added by heat transfer surfaces immersed in the bed in industrial fluidized beds. Although heat transfer to immersed tubes has been studied extensively, the transition to turbulent fluidization has rarely been acknowledged in heat transfer studies (see Chapter 1). This regime of operation is typical and beneficial for many chemical reactors. There is lack of data in the literature for small, group A particles, that extend to higher superficial gas velocities, where turbulent fluidization conditions are likely to be present.

Experimental results on heat transfer from an immersed vertical tube in a fluidized bed of FCC particles (typical for group A) showing the effects of superficial gas velocity, U, static bed height, H_0, distance above the distributor, z, radial location, r/R, and distributor design as the bed underwent transition to turbulent fluidization are presented in the first half of this chapter. The heat transfer experiments were performed in the 0.29 m ID, 4.5 m high Plexiglas fluidization column described in Chapter 2.

Another outstanding issue is the effect of column diameter on the heat transfer coefficients. Ellis et al. (2004) and Chapter 3 indicated that transition to turbulent fluidization is affected by the column diameter. How heat transfer is affected by the shifted transition velocities in columns of different size needs to be examined.

The second half of this chapter presents experimental results on the effect of column diameter on the heat transfer coefficient for different superficial gas velocities and radial locations. This information is valuable for scale-up; applying laboratory-scale data to large commercial units.

4.2. Experimental results for FCC particles in 0.29 m column

4.2.1. Effect of superficial gas velocity and static bed height

The dependence of heat transfer coefficients on superficial gas velocity for H_0=0.8 m is plotted in Figure 4.1 for a vertical tube on the axis of the bed. The range of velocities corresponding to the transition to the turbulent fluidization regime is indicated on the figure. The error bars represent ±2 standard deviations of the signal from the mean. Below U_c, i.e. in the bubbling flow regime, the heat transfer coefficient increased with increasing gas velocity. In the range of velocities where the onset of turbulent fluidization was observed, the heat transfer coefficient reached a shallow maximum, after which it slightly decreased, probably due to increased voidage at high superficial gas velocities.
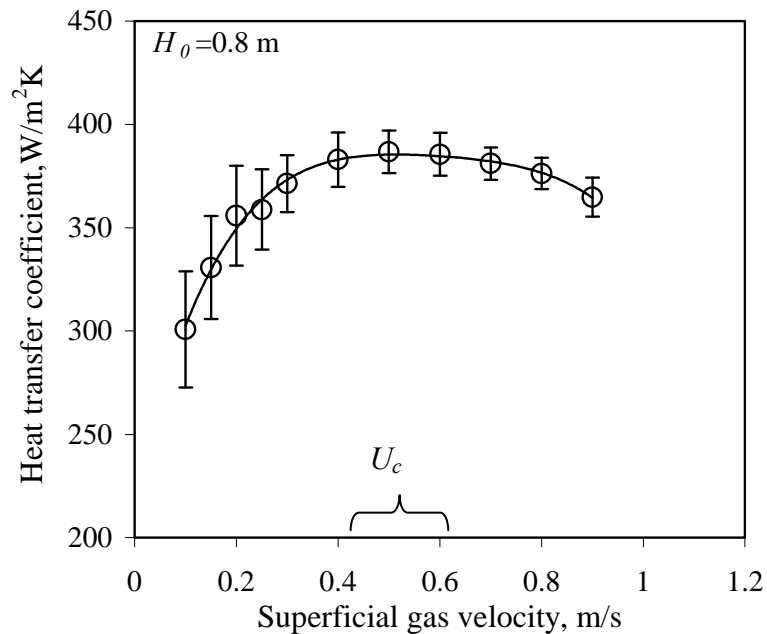
Figure 4.1. Tube-to-bed heat transfer coefficient vs. superficial gas velocity. Error bars correspond to ±2 standard deviations. (FCC, D_t=0.29 m, perforated plate distributor, H_0=0.8 m, r/R=0, z=0.6 m)

The results of experiments with the heater suspended at the same height above the distributor plate ($z = 0.6$ m) and the same radial location ($r/R = 0$) while the static bed height was varied are plotted in Figure 4.2. A change in trend in the heat transfer coefficient vs. superficial gas velocity plot is observed near the onset to turbulent fluidization for all static bed heights investigated. For

$H_0 = 1.0$ and 1.2 m where $H_0/D_t > 3$ and $z/H_0 \leq 0.6$, the increasing bed depth did not significantly affect the heat transfer coefficient, nor the onset of turbulent fluidization (Chapter 3). There was about a 25% difference between the heat transfer coefficients in the 0.8 m and 1.2 m deep beds at low gas velocities, this difference diminishing as U increased beyond 0.6 m/s where there was a high probability that the bed was in the turbulent regime. Different circulation patterns (Mathur et al., 1986) and the proximity of the splash zone for $H_0 = 0.8$ m may explain the higher heat transfer coefficients. For $H_0 = 0.8$ m, the heater was in the upper region of the bed ($z/H_0=0.75$), while for $H_0 = 1.2$ m, the heater was in the middle of the bed ($z/H_0=0.5$). Stein et al. (2000) reported increased particle velocities close to the free surface. This may have contributed to higher heat transfer rates for $H_0 = 0.8$ m and $U < U_c$. The effect of increased static bed height on heat transfer undoubtedly depends on the void circulation patterns in the bed. Beyond the onset of the turbulent flow regime, the effect of bed depth became negligible.
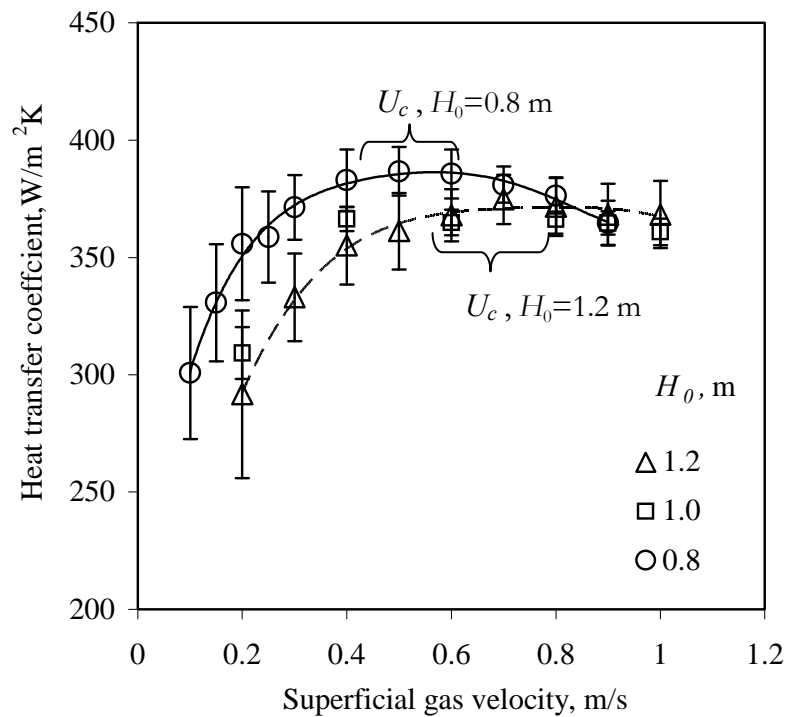
Figure 4.2. Effect of static bed height on *h* vs. *U* with the tube at a fixed distance from the distributor, *z*=0.6 m. Error bars ±2 standard deviations. (FCC, *D_t*=0.29 m, perforated plate distributor, *r/R*=0)

Our experimental hydrodynamic study with FCC particles shows that the maximum standard deviation of pressure fluctuations corresponded to the onset of turbulent fluidization (Chapter 3). The trends of the heat transfer coefficient and standard deviation of pressure fluctuations with increasing gas velocity is compared in Figure 4.3a and b. Both the time-mean heat transfer coefficient and the standard deviation of pressure fluctuations were normalized in the following form: $(x-x_{max})/(x_{max}-x_{min})$, where x is the time-mean value at a given superficial gas velocity, and x_{max} and x_{min} are the maximum and minimum value over the range of U investigated. Normalized values of both absolute and differential pressure fluctuations are plotted in Figure 4.3. The comparison shows that the increase of the heat transfer coefficient follows a very similar trend as the increase in standard deviation of pressure fluctuations. Moreover, the maximum heat transfer coefficient occurs at the same superficial gas velocity as the maximum of the standard deviation of pressure fluctuations. However, beyond U_c the heat transfer coefficient does not necessarily follow the trend of the pressure fluctuations (Figure 4.3b).

For small particles at low temperatures, like the FCC in our room temperature experiments, particle convection is the dominant heat transfer mechanism. The frequency of exchange of particles at the surface and the particle concentration near the surface therefore play dominant roles. In bubbling beds, bubble behaviour determines the circulation patterns of the particles, the frequency of exchange, and the time spent by particles at the surface. The particles travel mostly in the vertical direction, carried upward in bubble wakes, with their velocities depending on the velocity of the rising bubbles. Coalescence and splitting cause some lateral movement of the particles. Particles close to the bed surface are accelerated by erupting bubbles, and then fall back onto the bed surface where they join the slowly downwards-flowing dense phase near the walls and/or between bubbles. From a heat transfer point of view, larger, faster bubbles near the heating surface contribute to higher heat transfer coefficients because they transport fast, "fresh" particles in their wakes. As U increases, the particle contact time decreases (Hamidipour et al., 2005a). However, the bubbles also expose the surface to more gas which carries and exchanges much less heat than the particles. The heat transfer coefficient is decreased while the surface is exposed to gas. However, because larger bubbles also travel faster, they do not spend much time at the heater surface and the effect of increased voidage is overcome by the effect of increased particle exchange. Due to this mechanism, the heat transfer coefficient continues to increase, in

spite of the continuing increase in voidage with increasing gas velocity. When U approaches the transition region, the increase of the heat transfer coefficient slows down, corresponding to the gradual evolution towards the turbulent bed flow structure.
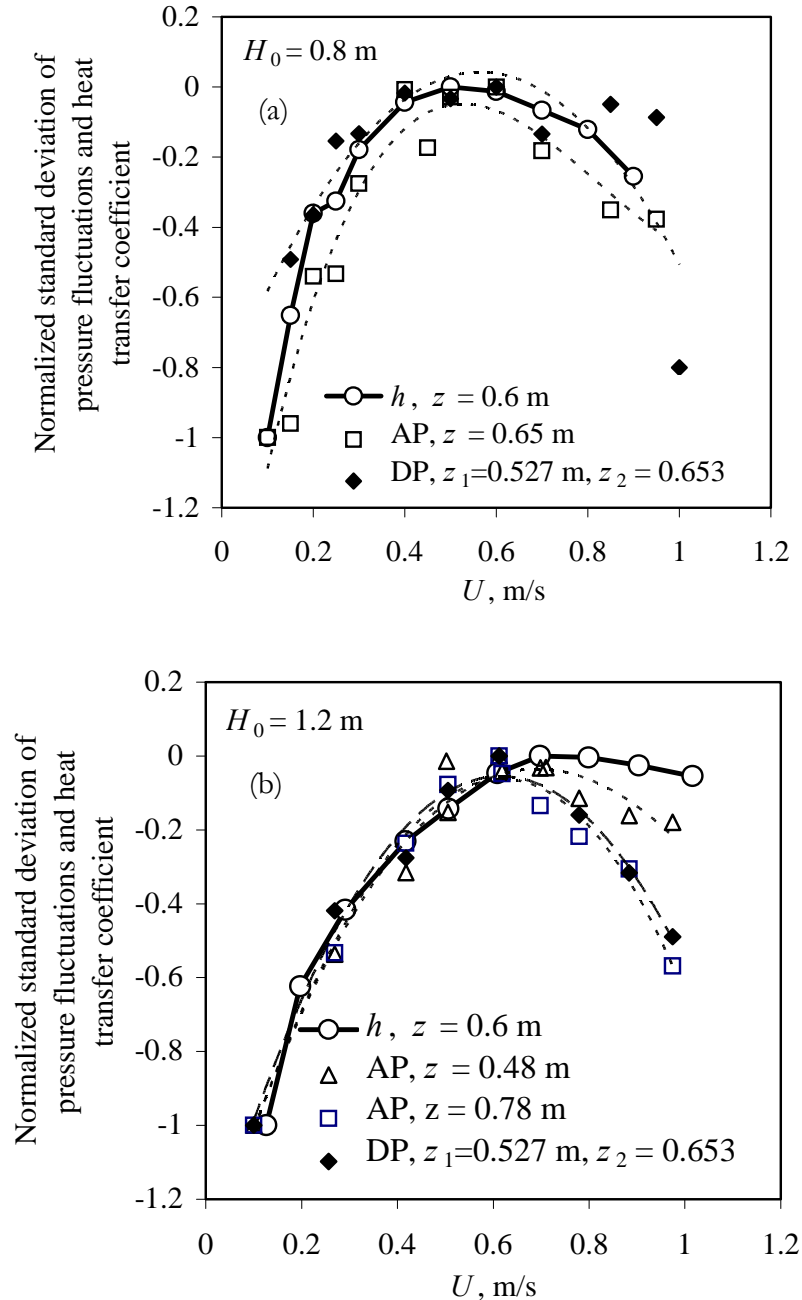
Figure 4.3. Comparison of normalized heat transfer coefficient and normalized standard deviation of pressure fluctuations (absolute and differential) as functions of superficial gas velocity for: a) H_0=0.8 m, b) H_0=1.2 m (FCC, perforated plate distributor, r/R=0)

In the range of velocities corresponding to the onset of turbulent fluidization, the mechanism by which particles are exchanged at the heater surface begins to change as large bubbles become unstable and break up. Void size becomes constant or even decreases (Mostoufi and Chaouki, 2004). Chapter 3 shows that the flow structure became more homogenous, and it is difficult to distinguish between the void and the dense phase in the turbulent fluidization flow regime. The time-mean local voidage increases less rapidly beyond U_c, and its standard deviation reaches a maximum. The particle movement in the radial direction increases, possibly related to the erratic movement of voids and their frequent coalescence and splitting. Ellis (2003) reported that, as the bed enters the turbulent flow regime, the distribution of the measured local voidage broadened, as did the radial distribution of particle velocities. The magnitude of the particle velocity did not undergo a marked transition to the turbulent regime. Note that in her study, measurements were only taken in the vertical direction, while visual observation suggests that there is increased lateral movement of particles in the turbulent flow regime.

Hamidipour et al. (2005a, 2005b) measured contact frequency, contact time and contact length at the wall by radioactive particle tracking. The tracer particles used in their study were rather large (d_{tracer}=420 and 500 μm) compared to the FCC particles (70 μm) so the results should be treated with caution. They found that the distributions of contact frequency, contact time and distance were wide in the turbulent flow regime. For FCC particles, mean contact time, distance and frequency did not change with increasing U. For their sand particles (d_p=385 μm), the contact frequency and contact time decreased with increasing U, reaching a minimum at U_c and then increasing. The vertical contact distance continuously increased with increasing U. Heat transfer models (Martin, 1984) usually consider the particle contact time to decrease with increasing U. The mechanism of heat transfer in the turbulent fluidization regime and the applicable published models are discussed in Chapter 6.

4.2.2. Radial profiles

Radial profiles of the measured time-mean heat transfer coefficients are shown in Figure 4.4 for H_0 = 0.8 m. The profiles become flatter with increasing superficial gas velocity. When the heater touched the column wall (i.e. $r/R = \pm 1$), channelling and gas bypassing were induced between the

heater and the column wall, resulting in lower heat transfer coefficients. For U beyond U_c, fluidization improved in wall region.

For $U < U_c$, the heat transfer coefficient always decreased towards the wall. The asymmetry of the profile at U=0.1 m/s is probably due to uneven fluidization, confirmed by the measurement of the radial voidage profiles discussed below.
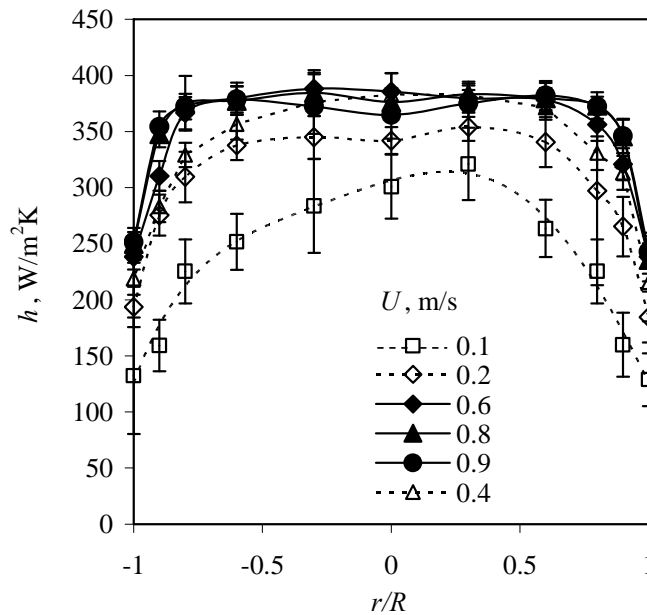
Figure 4.4. Effect of superficial gas velocity on radial profiles of h. Error bars indicate ±2 standard deviations. (FCC, perforated plate distributor, H_0=0.8 m) (open symbols: bubbling regime; filled symbols: turbulent regime)

To establish the effect of the radial location of the heater on the flow, radial profiles of local voidage were determined with the heater fixed at one radial position. These showed that the heater location did not significantly affect the shape of the profile. An asymmetric radial distribution of local voidage, with a maximum at r/R≈0.5 (Figure 4.5), was found at low gas velocities for the radial positions of the heater investigated. The shape of the profile is probably due to a preferential path of the rising voids, on one side of the column. Visual observation confirmed that more voids rose on one side of the column. An asymmetry of the radial voidage profiles was also reported by Ellis (2003) in the same 0.29 m column using FCC particles without any immersed object. Uneven fluidization is likely promoted by low pressure drop across the distributor at low U, as the air supply system was designed for high gas velocities. As the velocity is increased, the radial voidage

profiles became symmetric (see Figure 4.5). The radial profiles of the standard deviation, kurtosis, and skewness of the local voidage showed asymmetry in the same region ($r/R \approx 0.5$) at low gas velocities. At higher U, the distribution of local voidage near the walls still has a strong peak at low voidage, while the peak is less pronounced and the distribution more symmetrical in the central region of the column. This corresponds to flow patterns in the bed, with more gas rising in the central region and streams of particles descending near the walls.
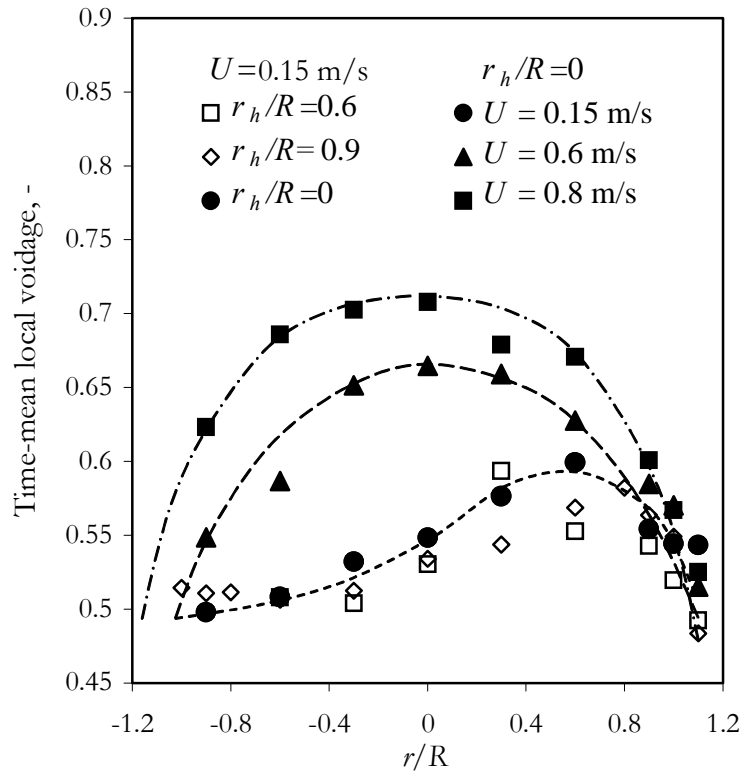
Figure 4.5. Radial profiles of local voidage and effect of radial location of heater, r_h/R, and superficial gas velocity, U. (FCC, perforated plate, D_t=0.29 m, H_0=0.8 m, U_c=0.45~0.65 m/s, z=0.47 m)

For $U > U_c$, the radial profiles of the heat transfer coefficient became flat and almost independent of gas velocity. In the bubbling flow regime, high heat transfer coefficients at a given radial position can be attributed to increased bubble activity, bringing fresh particles to the surface, counterbalanced by increasing surface coverage by gas. Although higher voidage has been found in the centre of the bed in the turbulent regime, and it increased with increasing gas velocity (Figure 4.5), the heat transfer coefficient changed little with increasing U due to the

counterbalancing effects of increased frequency of particle contact at the heater surface and increased voidage.

4.2.3. Axial profiles and effect of particle properties

The distribution of the heat transfer coefficient in the axial direction is also important. Some applications have heat exchange surfaces located near the bed surface to control heat transfer (Kunii and Levenspiel, 1991b), with the control over h achieved by varying the bed height. Lower bed levels expose the heat exchange surface to the freeboard where the particle concentration is lower, thus reducing h.

The axial distribution of the heat transfer coefficient was measured using an electrically heated tube of outer diameter 28.6 mm consisting of 5 identical heaters aligned end-to-end (Figures 2.3 and 2.4), insulated and individually heated (Chapter 2). The overall tube length was 730 mm, whereas the heating length of each heater was 101 mm. The results for the tube along the bed axis, appear in Figure 4.6a and b for static bed heights of 0.8 and 1.2 m, respectively, with the tube fixed with its bottom 0.51 m above the distributor plate in both cases.

For H_0=0.8 m, a large portion of the heater tube was above the static bed height. At low gas velocities there was a sharp decrease of h beyond the expanded bed height due to the exposure of the heater tube to the freeboard where the particle concentration was low. With increasing superficial gas velocity the axial heat transfer profiles flattened, as the bed expanded and more fine particles were carried over into the freeboard. With the onset of turbulent fluidization, the axial profiles of h became almost uniform (bold symbols in Figure 4.6a), and did not change significantly with superficial gas velocity in the range investigated.

For H_0=1.2 m, the heater tube was completely immersed in the upper half of the dense bed. The heat transfer coefficient then increased with increasing distance from the distributor, reaching the highest values near the top of the bed (Figure 4.6b). With increasing U the measured h became less affected by height.
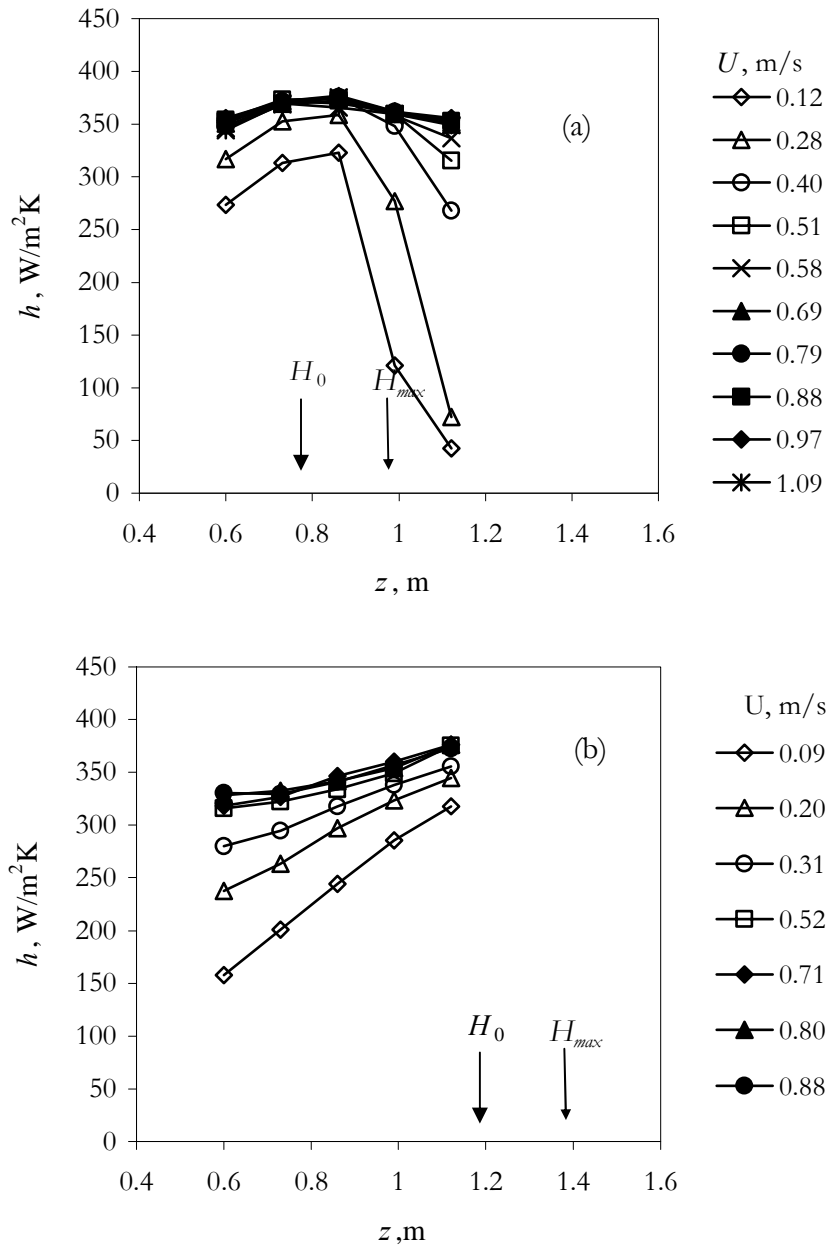
Figure 4.6. Effect of superficial gas velocity on axial profiles of bed-to-tube time-average heat transfer coefficient. a) H_0=0.8 m b) H_0=1.2 m) (open symbols: bubbling regime; filled symbols: turbulent regime) (FCC, D_t=0.29 m, perforated plate distributor, r/R=0)

Axial heat transfer profiles for alumina particles are shown in Figure 4.7. At low gas velocities the trends are similar to those for the FCC particles, i.e. high h near the bed surface, decreasing in the freeboard due to decreasing particle concentration. With increasing U, the heat transfer coefficient

in the freeboard increased, but not as much as for the FCC particles. However, U was only investigated up to 0.74 m/s, which might still be in the transition region, without reaching fully turbulent conditions.
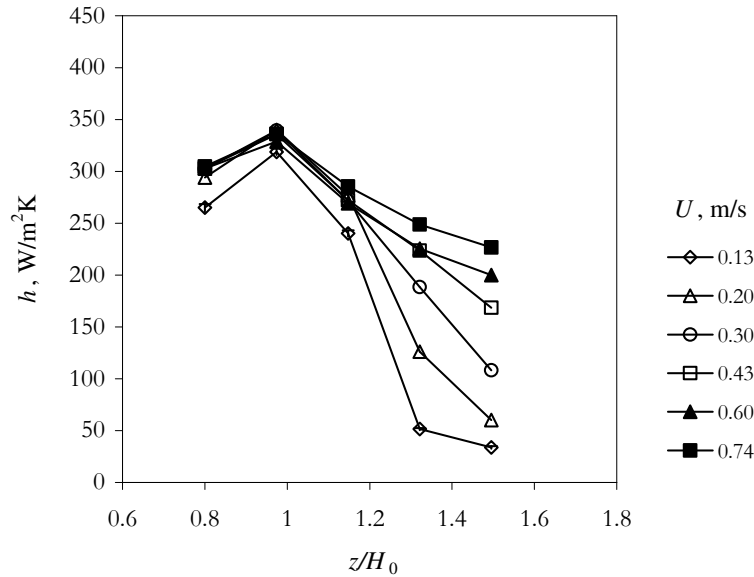
Figure 4.7. Effect of superficial gas velocity on axial profiles of h (Alumina, D_t=0.29 m, bubble cap distributor, H_0=0.8 m) (open symbols: bubbling regime; filled symbols: turbulent regime)

The effects of static bed height and axial position were reviewed by Gelperin and Einstein (1971). Lack of agreement in the literature on of the effects of z and H_0 may be a consequence of different locations of the heating surface relative to the distributor and the splash zone. The authors suggest that as long as the heater is well immersed in the dense bed, well above the region affected by the distributor, with fluidization well developed, the heat transfer coefficient should not be affected by bed depth. Experimental data from the lower half of the bed, $0.13 \leq z/H_0 < 0.5$, for $U < 0.8$ m/s and 250 μm quartz sand support this. It should be noted that they used group B particles and their study did not extend to the turbulent fluidization regime. Our experimental results obtained from the middle of the bed and extending into the freeboard, show that there is a significant effect of axial distance, but only for low gas velocities. An explanation is offered below.

The axial heat transfer coefficient profiles for the two static bed heights investigated for FCC particles are combined and plotted against the normalized axial distance, z/H_0, in Figure 4.8a for

$U<U_c$ and in Figure 4.8b for $U \geq U_c$. Heat transfer coefficients in the region $0.8<z/H_0<1$ overlap for similar gas velocities regardless of static bed height.
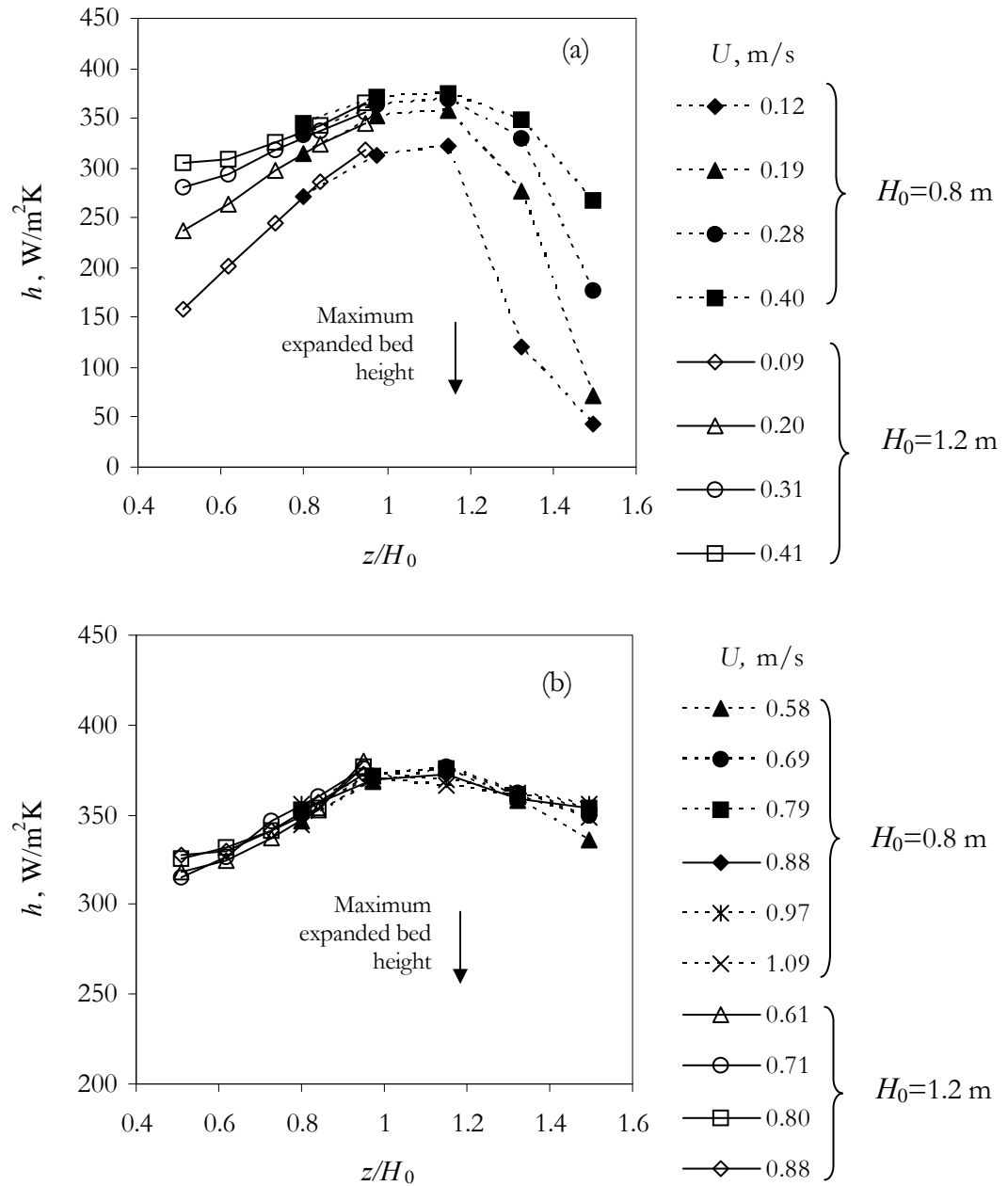
Figure 4.8. Evolution of axial profiles of heat transfer coefficient for FCC with increasing superficial gas velocity (FCC, *r/R*=0) (open symbols: *H*₀ = 0.8 m, filled symbols: *H*₀ = 1.2 m)

Figure 4.9 shows h as a function of superficial gas velocity for the same dimensionless vertical position, $z/H_0=0.8$, for both static bed heights. At the same relative height, it is seen that the variation in H_0 had a negligible effect. This confirms the effect of the proximity of the bed surface (splash zone) on the higher heat transfer coefficients measured in the shallower bed ($H_0 = 0.8$ m) (Figure 4.2), with the one-section heater tube kept at a fixed height above the distributor, its bottom 0.51 m above the distributor plate.

From Figure 4.8, the following trends are apparent: 1) the highest heat transfer coefficients were measured for $1 \le z/H_0 < 1.2$; 2) for low gas velocities ($U<U_c$), h increased with increasing height in the dense bed, then decreased above the expanded bed surface (Figure 4.8a); and 3) beyond the onset of turbulent fluidization ($U \ge U_c$), the axial distribution of heat transfer coefficients was more uniform (Figure 4.8b).
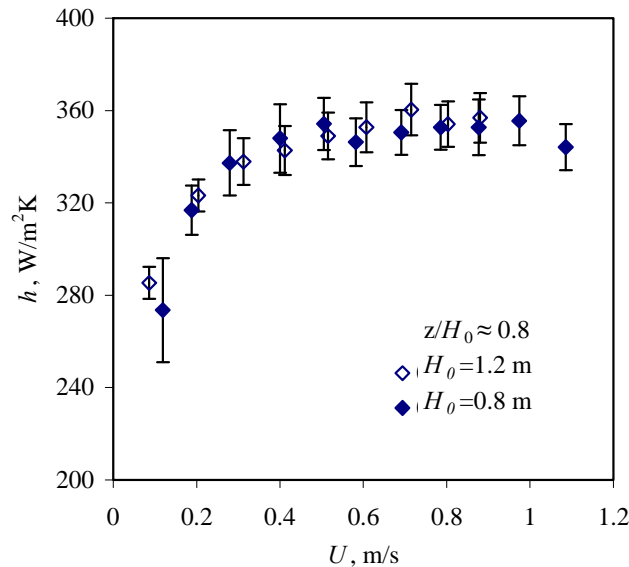
Figure 4.9. Effect of static bed height on h vs. U at $z/H_0 \approx 0.8$. Error bands show ± 2 standard deviations.

The highest heat transfer coefficients were measured for $1 \le z/H_0 < 1.2$ (Figure 4.8), where the transition from the dense bed to the freeboard takes place, as revealed by axial profiles of mean cross-sectional voidage plotted on Figure 4.10. The increase in voidage from the dense bed to the freeboard is sharp at very low velocities, but more gradual at higher U. The review by Leckner (2006) for group B particles in a fluidized bed boiler shows maximum heat transfer near the bed

surface. The vigorous particle movement in this region was confirmed from comparison of the heat transfer results with the erosion along the heat exchange tubes. High and flat *h* in the $1 \leq z/H_0 < 1.2$ region was also observed by Baskakov and Zvyagin (1976).
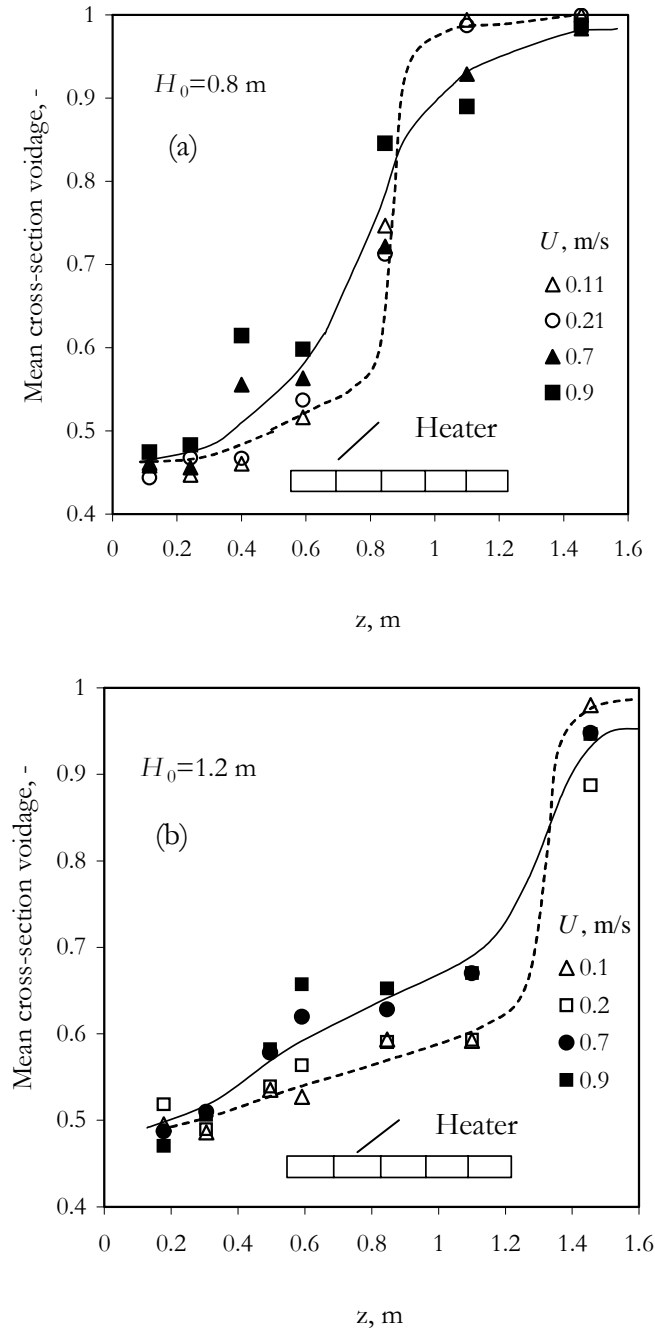
Figure 4.10. Axial profiles of cross-sectional mean voidage in the region of the heater location a) H_0=0.8m, b) H_0=1.2 m (dotted lines: $U<U_c$, solid lines: $U>U_c$)

For $U<U_c$, the increase in h with increasing z in the dense bed region, 0.4 $<z/H_0$ <1 (Figure 4.8a) might be caused by increased particle exchange at the heater surface at higher heights due to increased bubble coalescence and splitting. The decrease of the axial heat transfer coefficient with z at z/H_0>1.2 is due to the low particle concentration in the freeboard. As U increases, more fine particles are ejected into the freeboard and higher h is found at higher in the column. With the onset of turbulent fluidization ($U{\geq}U_c$), the heat transfer coefficient is more uniform and higher than at lower U (Figure 4.8b). When turbulent fluidization is reached, the two-phase flow structure gradually breaks down, causing a more homogenous flow. The boundary between the dense bed and the freeboard also becomes diffuse and particle entrainment becomes significant. The transition from dense bed to freeboard is more gradual as shown on Figure 4.10. Consequently, h varies less with height and is higher. The highest h is still in the region 1<z/H_0<1.2, but this maximum is very flat.

A study by Hamidipour et al. (2005b) in the bubbling and turbulent fluidization regimes reported axial distributions of contact time and contact length of particles at the wall surface. Axial distributions of particle contact time and contact distance were found to be more uniform in turbulent fluidization and extended to higher bed levels than for bubbling. It was assumed that the homogeneity of the bed causes the contact time distribution to become flatter, while bed expansion extended the higher coefficients to higher bed levels. These findings support the greater uniformity of h extending to higher bed levels in turbulent fluidization portrayed on Figure 4.8b.

The experimental results show that there is no sharp transition with the onset of turbulent fluidization. Instead, the change is gradual, reflecting the gradual nature of the transition to turbulent bed flow structure.

4.2.3.1. Effect of particle properties

Heat transfer coefficients for FCC and alumina particles in the 0.29 m diameter column with the bubble cap distributor and the heater located in the centre of the column are plotted in Figure 4.11. The measured heat transfer coefficients are similar, with h_{max} slightly higher for FCC particles (~4%). Similar heat transfer coefficients are expected as FCC and alumina particles have similar thermal properties and mean diameters. The small difference is most probably due to differences

in particle density and shape which affect the hydrodynamics. The most common correlation for estimating h_{max} is that of Zabrodsky (1966):

$$h_{max}=35.7 \; d_p^{\;-0.36} \; \varrho_p^{\;0.2} \; k_g^{\;0.6} \tag{4.1}$$

which predicts a slightly higher maximum heat transfer coefficients (5% difference) for the FCC particles.
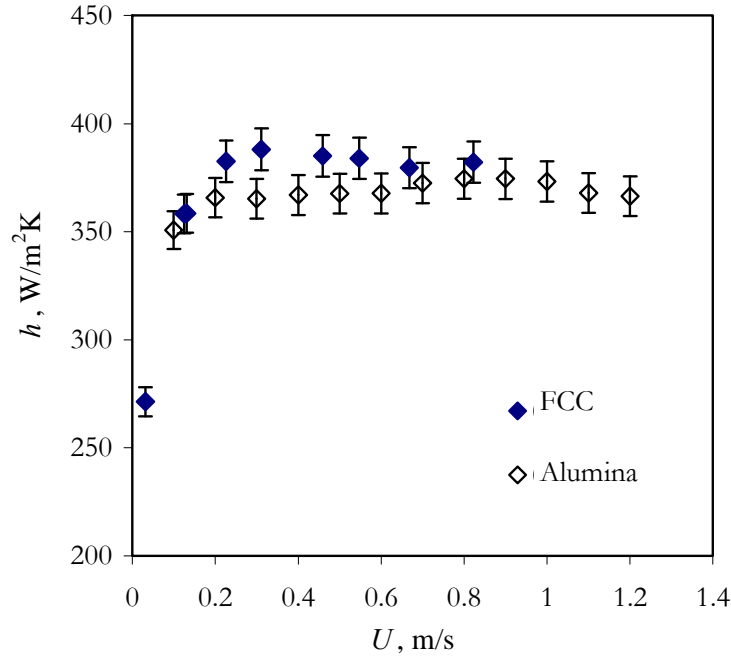
Figure 4.11. Comparison of *h* for FCC and alumina particles as a function of *U*. Error bars represent ±2 standard deviations. (*D$_t$*=0.29 m, bubble cap distributor, *H$_0$*=0.8 m, *z$_h$*=0.6 m)

4.2.4. Effect of distributor

The effect of the distributor on heat transfer was reviewed by Gelperin and Einstein (1971) who state that the distributor geometry can have a very important influence on heat transfer, not only near the distributor, but over the entire bed volume. The distributor has a considerable influence on the initial size and number of gas bubbles, affecting heat transfer. Experimental results of Shirai et al. (1961) for 160 µm catalyst particles in a column of diameter 0.28 m with perforated plates show that smaller open area ratios (from 0.05 to 3.5%) led to faster increases in heat transfer coefficient with increasing *U*. The influence of the distributor gradually diminished with increasing

U, becoming negligible beyond $U > U_{opt}$, which, for their experiments was ~0.8 m/s. Chapter 3 suggests that this velocity is close to the onset of turbulent fluidization.
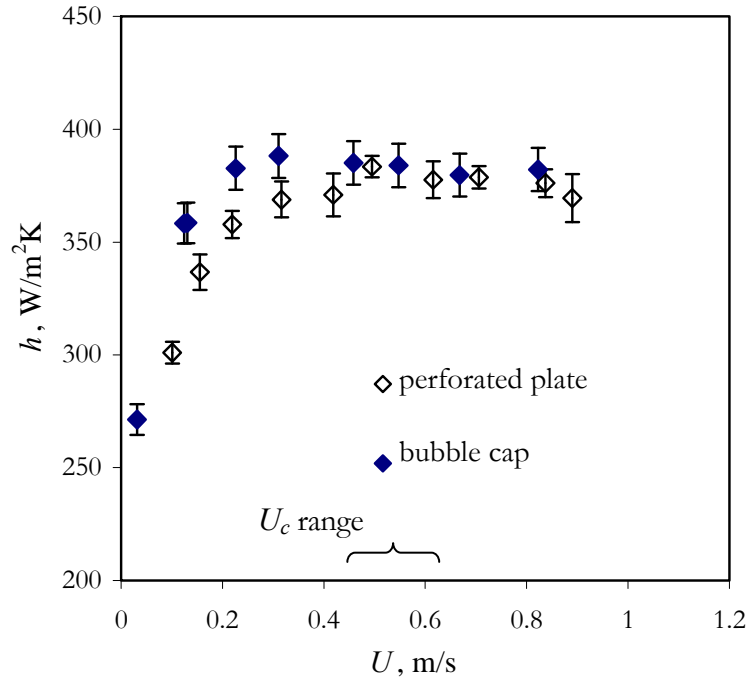
Figure 4.12. Effect of distributor design on heat transfer coefficients plotted against superficial gas velocity. Error bars represent ±2 standard deviation. (FCC, H_0=0.8 m, r/R=0)

In the present work, two distributor configurations were tested, a bubble cap (BC) with an open area ratio of 1% and a perforated plate (PP) with a ratio of 3.5%. Details are given in Chapter 2. The effect of the distributor on the heat transfer coefficients is shown on Figure 4.12. The bold symbols represent the bubble cap distributor data, whereas the open symbols are for the perforated plate. It is apparent that slightly higher h was measured for the bubble cap distributor for $U<U_c$. However, once the turbulent regime was reached, the heat transfer coefficients were not affected by the distributor. Note that the heater was located in the upper half of the bed, where the effect of the distributor is expected to be limited. The difference in the bubbling regime is likely due to different initial bubble size and frequency influenced by the distributor (Grewal et al., 1979). Slightly higher characteristic frequencies in the power spectrum of the differential pressure signal at low U were measured for the bubble cap distributor implying that bubbles appear at the heater surface more frequently for the lower open area ratio. These results also appear to be in

89

agreement with those of Shirai et al. (1961), i.e., smaller open area ratios lead to longer h for $U <$ U_c.

Although the open area ratio was different for the two distributors, their pressure drops were similar (Figure 4.13). This could have been caused by the mesh inserted between the perforated plates, adding to the pressure drop. Theoretical analysis of the pressure drop across the two investigated distributors by Sobrino et al. (2008) confirmed this. They also reported higher U_c for the bubble cap distributor based on the maximum standard deviation of pressure fluctuations as observed in our work (Chapter 3). However, our analysis of dense bed height H' and local voidage did not show any significant effect of the distributor on the transition velocity.
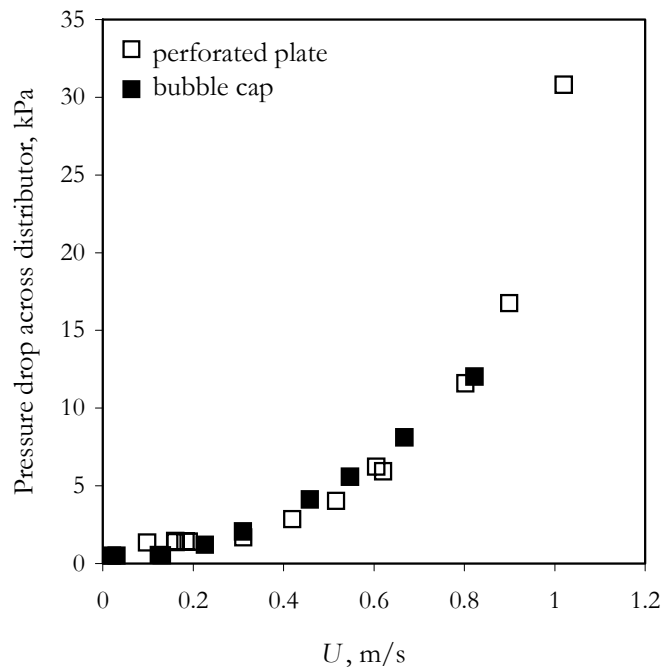
Figure 4.13. Pressure drop across two distributors vs. superficial gas velocity (FCC, D_t=0.29 m, H_0=0.8 m)

4.3. Experimental results for alumina particles in columns of different diameter

To be able to apply the laboratory data to large commercial units, knowledge of the effect of scale–up is required. Scaling of fluidized beds is not straightforward and is often based on experience (Grace, 2006). Scaling laws exist, derived from fundamental equations, but they can lead to a scaled

model operating in a different flow regime or particles belonging to a different Geldart group. The scaling laws serve better for modifying existing equipment than for new processes (Knowlton et al., 2005).

The set of independent parameters proposed by Glicksman (2003) is:

$$\frac{U^2}{gL}, \frac{\rho_p}{\rho_g}, \frac{\rho_g U d_p}{\mu}, \frac{\rho_g UL}{\mu}, \frac{G_s}{\rho_p U}, \frac{H}{D_t}, \text{bed geometry}, \varphi, \text{PSD (particle size distribution)} \quad (4.2)$$

The first dimensionless group, introduces the effect of scale, where L is a typical bed dimension, either bed diameter, D_t or bed height, H. In our study of the effect of column diameter, the bed height was kept constant so this dimensionless group takes the form $U^2/(gD_t)$.

According to Glicksman (2003), if the hydrodynamics in both large and small columns are scaled well, convection heat transfer could be scaled as well as it is closely related to the bed hydrodynamics. Data on the effect of column diameter on heat transfer are scarce. Wunder (1980) performed experiments with 55, 200 and 670 μm glass particles in columns of diameter 0.080, 0.2 and 0.690 m. In the largest column, h_{max} was slightly (~15%) higher and shifted to higher gas velocities.

The effect of the column diameter on heat transfer can be attributed to the different hydrodynamics in columns of different sizes. Larger units have been reported to give higher mixing rates and to exhibit different flow structures than scaled-down counterparts (Matsen 1996). This might be due to the existence of different circulation patterns, or even different fluidization regimes in columns of different diameter.

It is likely that when both large and small units operate in the turbulent fluidization regime, the effect of bed diameter on heat transfer is small. In bubbling beds, column diameter affects void size and circulation patterns, thus affecting particle renewal at the heat transfer surface. In turbulent beds, the flow structure is more homogenous, and voids are unstable and of smaller scale. Hence one expects that scale–up should be easier for turbulent beds than for bubbling ones (Knowlton et al., 2005).

In this project, the effect of column diameter was investigated by comparing data from the 1.56 m ID column located at CSIRO in Australia, to those from the UBC unit of diameter 0.29 m. Details are provided in Chapter 2. Static bed heights were kept constant near H_0=0.8 m. The particles were identical and obtained from the same batch of alumina. The same probes and data acquisition system were also utilized in both columns.

4.3.1. Circulation patterns and radial local voidage distribution

Due to the different H_0/D_t ratios in the two columns, it was expected that the circulation patterns in the bed would differ. The radial profile of the local voidage is given in Figure 4.14. The highest voidage in the bubbling bed was measured in the central region of the smaller column; the bed was deep enough for voids formed at the distributor to fully coalesce and rise in the centre
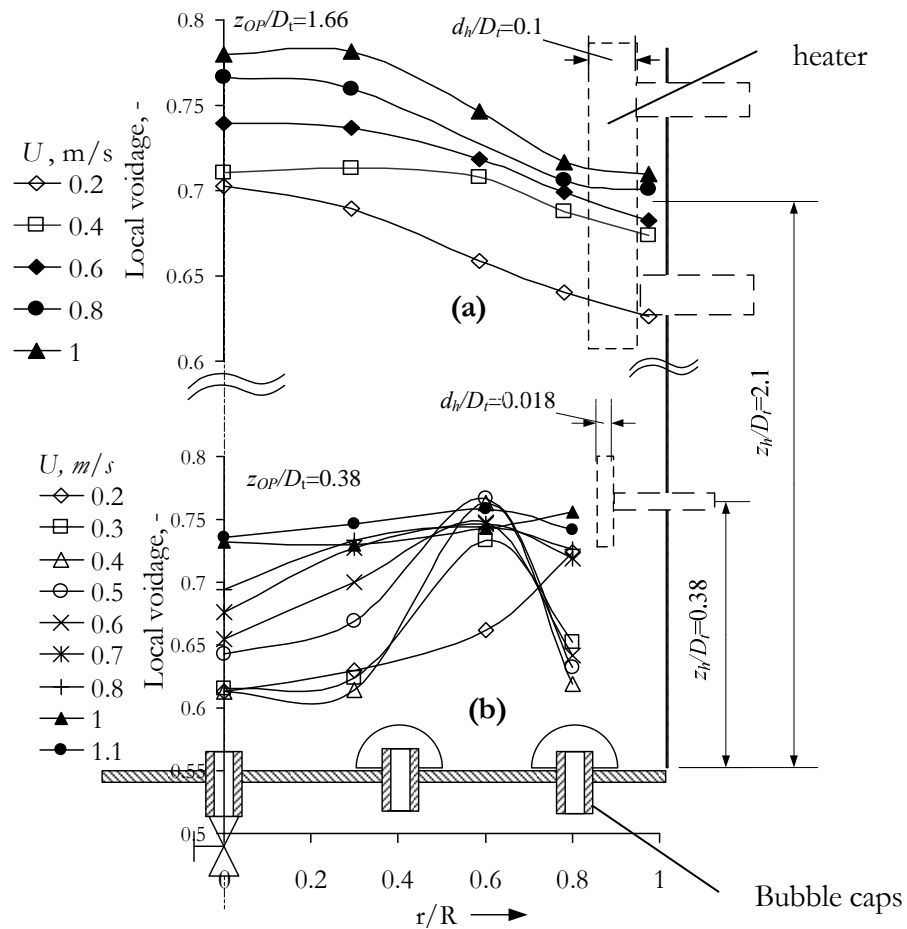
Figure 4.14. Radial profile of time-mean local voidage: (a) D_t=0.29 m, z_{OP}=0.47 m; (b) D_t=1.56 m, z_{OP}=0.6 m.

(Grace and Harrison, 1968). In the larger column, typical circulation patterns of shallow beds were observed, with voids rising primarily near $r/R=0.5$ and downwards bulk solids movement at the centre of the column and near the outer wall ("gulf steaming") (see Figure 4.15a). Note that the central bubble cap was blocked off in both columns. Details of the local hydrodynamics obtained from the optical probe are given in Chapter 3.
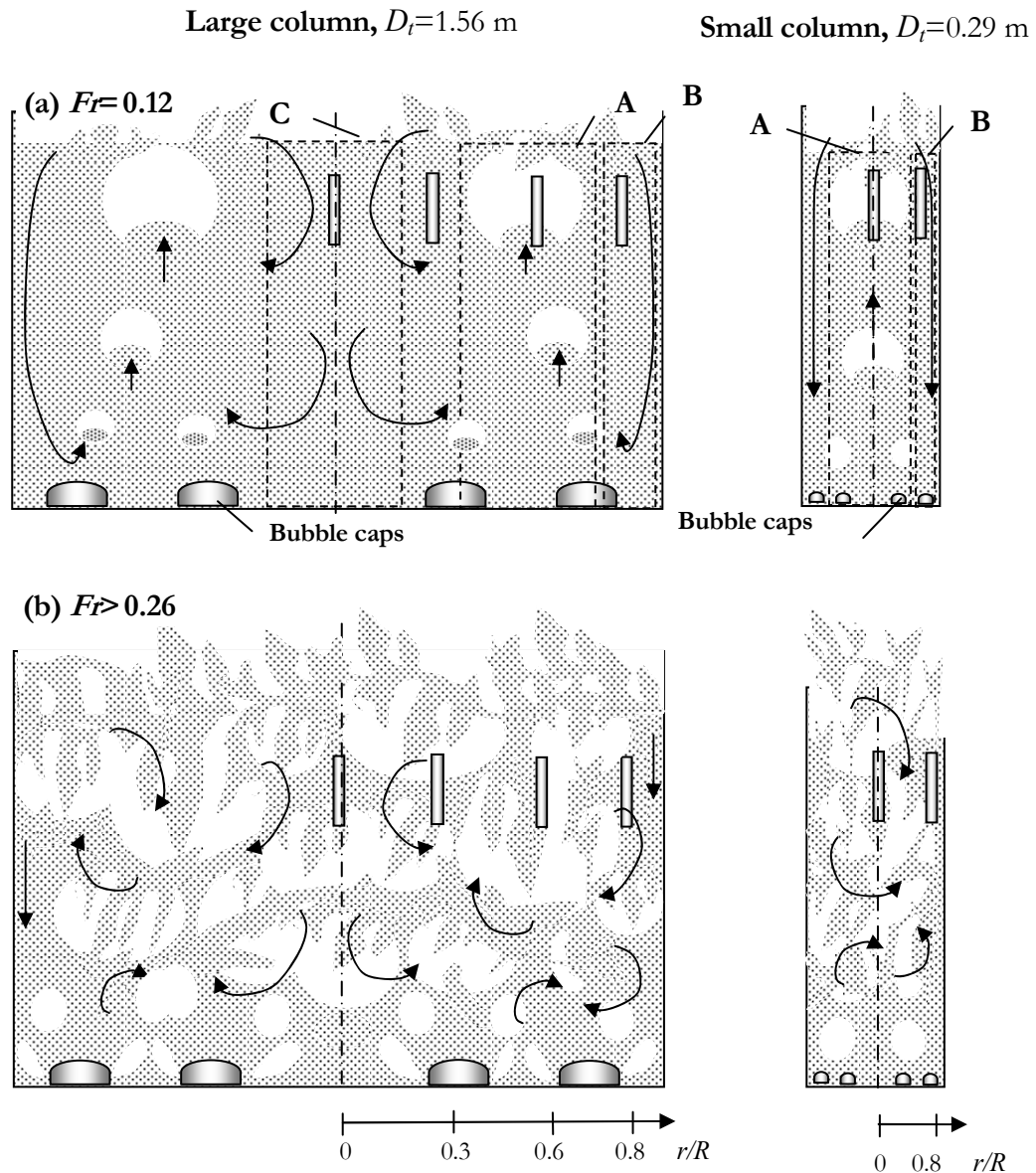
Figure 4.15. Schematic of the circulation patterns in the large column (D_t=1.56 m) and smaller column (D_t=0.29 m). Arrows represent typical particle circulation patterns. a) Bubbling bed (Fr<0.12), b) Turbulent bed (Fr>0.26).

The likely circulation patterns, based on the local voidage measurement, are illustrated in Figure 4.15a for a bubbling bed, and in Figure 4.15b for a turbulent bed. Three specific regions are marked in Figure 4.15a: A – a region of high void concentration, B – a region affected by the wall, and C – a region of intense bulk movement of particles (not present in the small column in the vicinity of the heater). As the superficial gas velocity changed, the boundaries and locations of these regions changed. For example, for U=0.2 m/s, region A was near r/R=0.8, but shifted towards r/R=0.6 with increasing gas velocity.

4.3.2. Effect of superficial gas velocity and radial position

4.3.2.1. 0.29 m ID column

Experimental results for heat transfer coefficients in a 0.8 m deep bed of alumina particles, measured at various radial positions with the heater 0.6 m above the distributor, are plotted against the superficial gas velocity in Figure 4.16. With the onset of bubbling the heat transfer coefficient became high in the central region of the bed and remained relatively unchanged over wide range of velocities. At radial locations in the wall region, h increased steeply with increasing superficial gas velocity and reached maximum near U_c. (Figure 4.16).

The optimum velocity for heat transfer, U_{opt}=0.17 m/s, calculated from Todes' correlation (Zabrodsky, 1966) is close to the velocity at which h at r/R=0 changes its trend and reaches a maximum. Near U=0.2 m/s, the mean bubble size is $D_b \approx 0.5 D_t$ estimated by the Mori and Wen (1975) correlation and the bubble size, velocity and frequency are all significantly influenced by wall effects (Hovmand and Davidson, 1971). This affects the frequency of particle exchange at the heater surface and hence the heat transfer coefficient.

It is likely that near U = 0.4-0.6 m/s (local voidage $\varepsilon \approx$ 0.7), the onset of turbulent fluidization took place. The flow structure in turbulent fluidization is characterized by a gradual breakdown of the bubble/emulsion phase, replaced by short-lived unstable voids of irregular shape, containing significant numbers of particles and particle clusters. With this evolution of flow structure, bubbles are no longer the "driving force" for particle circulation. As the bed became more homogenous with the breakdown of the two-phase flow structure, the mechanism of particle renewal at the

surface changed. The more homogenous flow structure was then reflected in the uniform radial distribution of heat transfer coefficients at higher *U*, as shown in Figure 4.17. The heat transfer continues to be dependent on particle contact with the surface in the turbulent flow regime, but particle renewal (establishing the contact time and frequency) is no longer dominated by the voids.
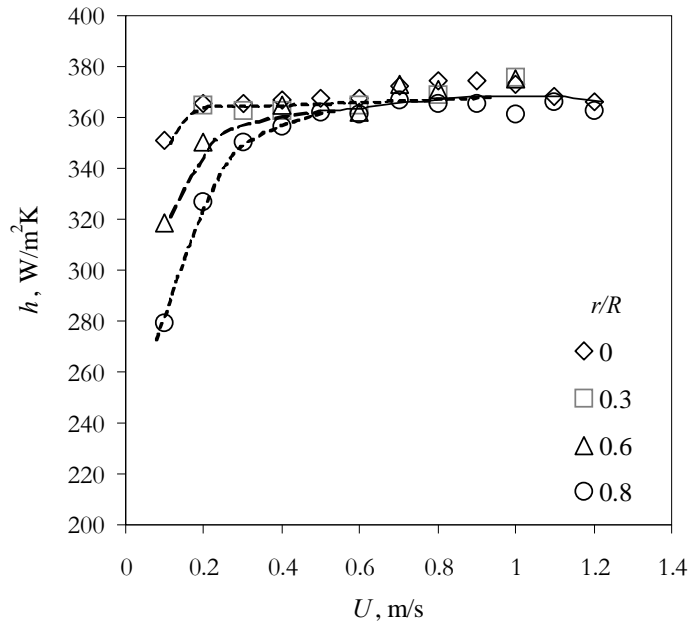
Figure 4.16. Effect of superficial gas velocity on heat transfer coefficients measured at different radial locations (Alumina, bubble cap distributor, D_t=0.29 m, H_0=0.8 m)

Hamidipour et al. (2005b) measured contact times and frequencies of particles at the wall and found a wider distribution in the turbulent regime than for bubbling. Hamidipour et al. (2005a) also reported that for sand (group B) particles, the particle contact time, as well as the contact frequency, decreased with increasing *U*, reaching a minimum at the onset of turbulent fluidization and then increasing with further increase in *U*. Generally, contact time models predict a monotonic decrease of contact time at low *U* approaching a fixed value at high *U*. Our alumina particles fell near the A/B boundary in Geldart's classification, and it was uncertain whether they would follow the trend as reported by Hamidipour et al. (2005a).
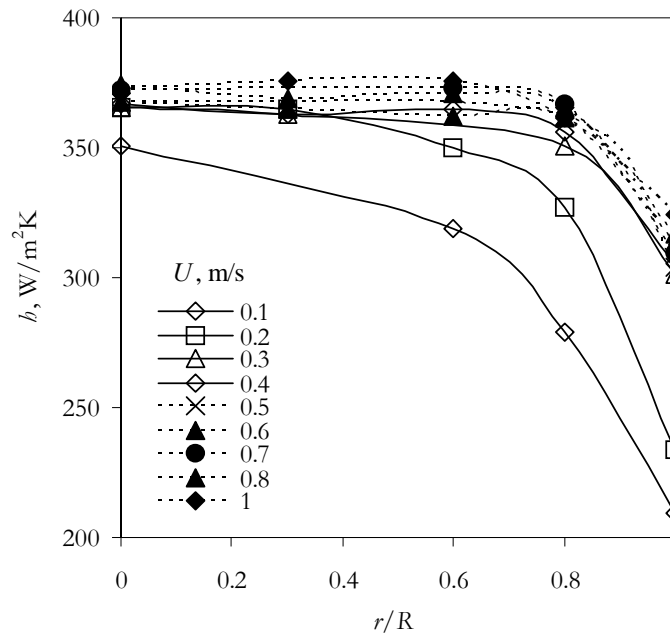
Figure 4.17. Radial profile of heat transfer coefficients (Alumina,
D_t = 0.29 m, bubble cap distributor, H_0=0.8 m)

 The frequency of particle contact with the heater surface at low gas velocities can be evaluated from the bubble frequency (Mckain et al., 1994). For U=0.2 m/s and r/R=0, the dominant frequency of the optical probe signal occurred at ~2.5 Hz at z=0.47 m and ~1.3 Hz at z=0.75 m, decreasing to ~0.6 Hz with increasing U (Figure 3.21). These values are comparable to the particle contact frequencies reported by Hamidipour et al. (2005b). In the turbulent fluidization regime, the dominant frequency from the optical probe signal could not be unambiguously identified. The signal was random with its power intensity widely distributed among frequencies. However, two mechanisms are possible beyond U_c: (a) the frequency of exchange of particles increases in the turbulent fluidization flow regime, reducing the particle contact time, but its effect is balanced by increased voidage in the central region of the column; and (b) near the wall, the frequency of exchange of particles is unaffected by U and the local voidage does not change significantly in the turbulent fluidization flow regime, so heat transfer remains unchanged. Once suspension density is significantly reduced near the heater, the heat transfer coefficient is expected to decrease with increasing U.

4.3.2.2. 1.56 m column

Measured heat transfer coefficients at various radial positions in the large column are plotted against superficial gas velocity in Figure 4.18. The heat transfer coefficients follow trends similar to those in the smaller column, except at r/R=0.8, i.e. near the wall where the heat transfer coefficients decreased and then increased again as U increased. This can be explained by the shifting trajectory of the rising voids, most probably due to bubble coalescence. At low gas velocities ($U \approx 0.2$ m/s), the presence of voids near the wall promotes the exchange of particles at the heater surface, leading to higher heat transfer coefficients. Individual voids were detected from the optical probe and differential pressure signals, with a dominant frequency of ~1.8 Hz (Figure 3.24). As the vertical trajectory of voids shifted to r/R=0.6 (region A in Figure 4.15), h started to decrease in the wall region (region B on Figure 4.15), reaching a minimum at $U \approx 0.4$ m/s. For U>0.4 m/s, the local flow structure changed, with the voids at r/R=0.6 becoming large and unstable, gradually creating a more homogenous flow structure across the bed; h started to increase again at r/R=0.8.
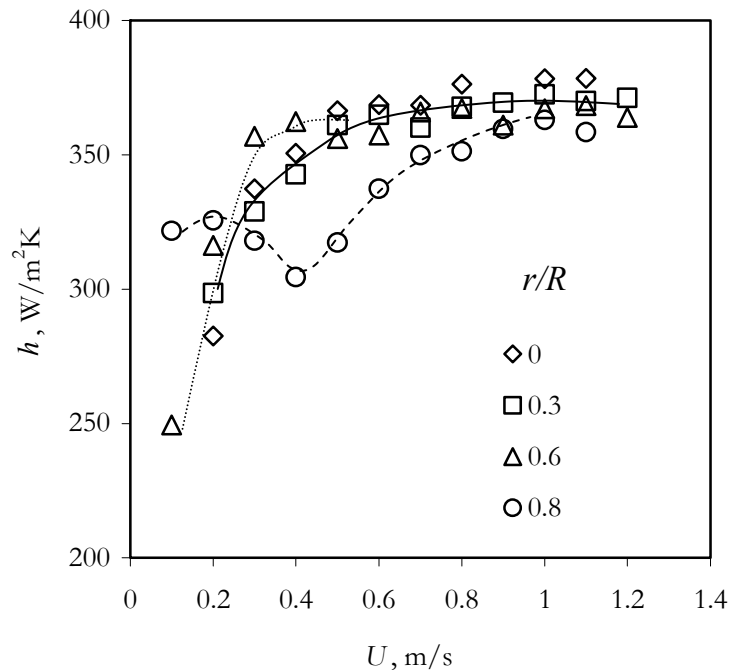
Figure 4.18. Heat transfer coefficient measured at different radial locations as a function of superficial gas velocity (Alumina, D_t=1.56 m, bubble cap distributor, H_0=0.8 m, z =0.6 m)

A significant change of the trend in the h vs. U curve at $r/R = 0.6$ is evident at $U \approx 0.4$ m/s in Figure 4.18. This change corresponds to the appearance of random local voidage fluctuations, indicating instability of the voids. At low gas velocities, heat transfer in this region (A in Figure 4.15) was promoted by frequent particle renewal due to bubbles passing the heat transfer surface, similar to the central region of the 0.29 m diameter column. With the change in local flow structure near the heater, the mechanism of particle renewal was altered, as reflected in the heat transfer. A maximum h was reached gradually and could not be unambiguously determined. However, the entire range of velocities corresponding to high heat transfer coefficients exceeded the optimum velocity calculated by the Todes correlation (Gelperin and Einstein, 1971) (U_{opt}=0.17 m/s), indicating that this correlation needs revision for larger columns.

In the central region of the column, i.e. $r/R = 0$ and 0.3 (region C in Figure 4.15a), h_{max} was reached more gradually (Figure 4.18). Although up to U=0.4 m/s the local voidage was close to that at minimum fluidization and the optical probe signal did not show bubble activity (Figure 3.25), the heat transfer coefficient was still relatively large and followed the same trend as at r/R=0.6 (Figure 4.18). It might be expected that h would be lower due to the absence of voids, but this was not the case. It appears that this region is well mixed and strongly influenced by the voids at r/R=0.6. Bulk particle motion or "gulf streaming" with velocities comparable to those of the voids might be responsible for bringing fresh particles to the heater surface in the central region. Alternatively, a higher particle concentration could lead to more particles contacting the surface, compensating for the reduced renewal frequency.

The reproducibility of the measured heat transfer coefficient shown in Figure 4.18 was checked for several radial locations. Tests were performed where U was randomly changed, or continuously increased and then brought back to original value. The reproducibility was within the experimental error of $\pm$ 5%.

The evolution of the radial heat transfer profiles with increasing U is presented in Figure 4.19. The radial profiles of h correspond to the local voidage profiles measured by the optical probe (Figure 4.5). At low gas velocity h was always highest where bubbles pass. With the breakdown of the two-phase flow structure at high gas velocities, h became uniform across the bed and did not vary significantly up to the highest U investigated.
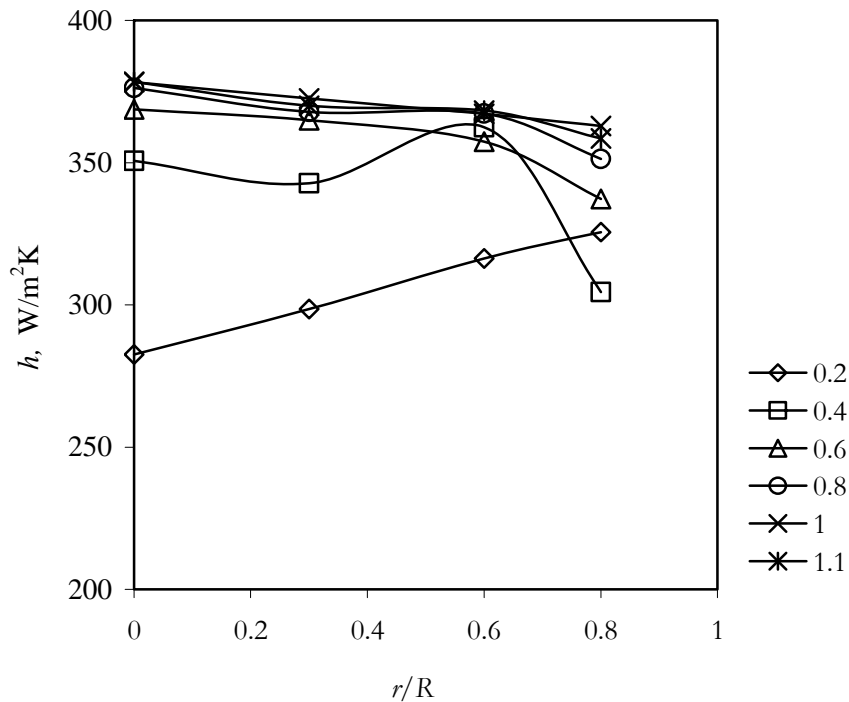
Figure 4.19. Evolution of radial profiles of *h* with increasing *U*
(Alumina, *D_t*=1.56 m, bubble cap distributor, *H_0*=0.8 m)

4.3.3. Effect of column diameter

At low gas velocities, *h* in both columns was heavily influenced by the voids, following the trend of the local voidage. However, this was not the case in the central region of the larger column. Figure 4.20 illustrates the dependence of *h* on local voidage for both large and small columns. For $\varepsilon < 0.7$ (low *U*), the heat transfer coefficient increased with increasing voidage, due to enhanced stirring by the voids. All data points follow the curve A and B (corresponding to regions A and B in Figure 4.15a), except those from the central region of the larger column (region C in Figure 4.15a). In this region the heat transfer coefficient increased, although the local voidage remained low. This might be due to different mechanism controlling the particle renewal at the heat transfer surface. For $\varepsilon \geq 0.7$ (high *U*) the flow structure changed (Figure 4.15b), and the heat transfer became independent of the local voidage at all radial positions. With further increases in local voidage, the heat transfer coefficients likely decrease (see data presented in Martin, 1980).
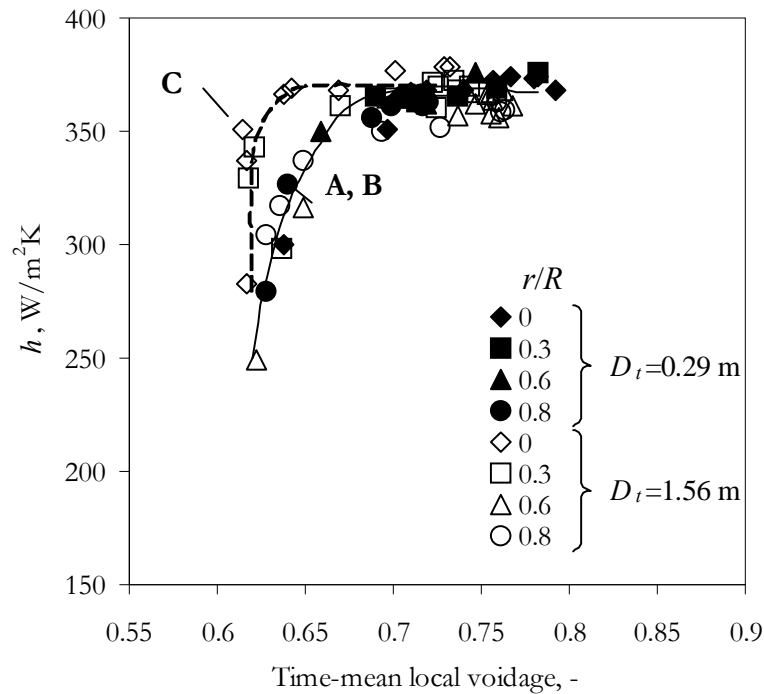
Figure 4.20. Heat transfer coefficient vs. time-mean local voidage at corresponding radial positions for 0.29 m column (filled symbols) and 1.56 m column (open symbols). A, B and C correspond to the regions marked on Figure 4.15a. (Alumina, bubble cap distributor, H_0=0.8 m, z_h=0.6 m)

The maximum values of h were similar in the two columns, in both cases occurring when the flow structure became turbulent. However, the superficial gas velocities at which the highest values of h were reached were higher in the larger column.

The measured heat transfer coefficients in the two columns are plotted against $Fr=U/(g\ D_t)^{0.5}$ in Figure 4.21 with solid symbols denoting the larger column and open symbols the smaller one. h follows curve A in the region of the preferred void flow (r/R=0 for D_t=0.29 m and r/R=0.6 for D_t=1.56 m) and curve B in the wall region (r/R=0.8) for both columns. The two curves enclose the range of measured heat transfer coefficients at other radial positions (not plotted in the figure). Different h vs. U trends were observed in the wall region (r/R=0.8), due to different circulation patterns in the two columns. The curve for r/R=0.8 in the large column exhibits a dip near Fr=0.12. The mechanism controlling the heat transfer changed with increasing Fr at this radial position. At very low Fr, voids were rising at this radial position, and data points are close to curve

A. When voids appeared closer to $r/R=0.6$ with increasing U, h decreased and started to follow curve B.
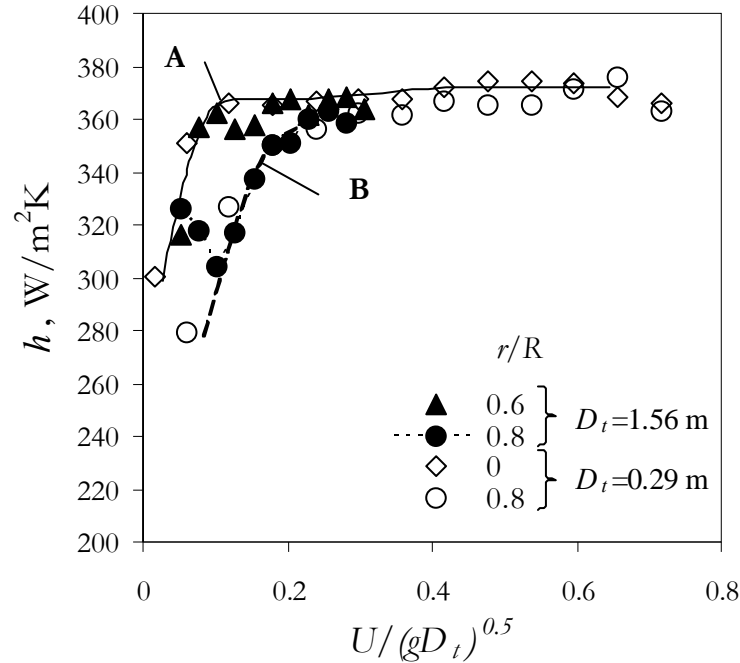
Figure 4.21.Heat transfer coefficients in the large (filled symbols) and small (open symbols) columns at different radial locations in the bed plotted against $Fr= U/(g D_t)^{0.5}$. Curve A: region of rising voids; Curve B: region of mainly dense phase. (Alumina, bubble-cap distributor, z_h=0.6 m)

It appears that for $Fr>0.26$, h becomes independent of r/R for both columns. This critical Fr probably marks the completion of the transition from bubbling to turbulent fluidization for both columns, described in Chapter 3.

Figure 4.21 shows that for the same Fr where the flow structures near the heater are similar, the heat transfer coefficients are similar. Fr appears to be a useful scaling parameter for the effects of superficial gas velocity and bed diameter on h.

4.4. Summary

- Maximum h occurred for U close to U_c. Although U_c was affected by bed depth, the occurrence of the maximum heat transfer coefficient shifted correspondingly. In turbulent

beds, the heat transfer coefficients were distributed more uniformly, both radially and axially, and did not change significantly with increasing U as long there was no significant increase in voidage near the heater.

- In bubbling beds, the heat transfer depended on many parameters which affected void size, frequency, and circulation pattern. For $U<U_c$, h follows the same trend as the standard deviation of pressure fluctuations for FCC particles.

- The highest heat transfer coefficients of the axial profiles were in the splash zone with $z/H_0 \approx$ 1-1.2 due to increased mixing of particles in this region.

- The effect of static bed height on h could be captured by utilizing the normalized axial distance z/H_0. For a heater location at fixed z in the upper half of the bed, the proximity of the bed surface affected the heat transfer coefficients, but only in the bubbling flow regime.

- The effect of changing the distributor was small and only observed in the bubbling regime. The bubble-cap distributor with its smaller open area ratio produced slightly higher heat transfer coefficients. Beyond U_c, h was virtually the same for the two distributors.

- The superficial gas velocity at which the bed-to-surface heat transfer coefficient reached a maximum was found to increase with increasing column diameter and was affected by the radial location of the heater. This change in trend was due to the changing hydrodynamics caused by instability of the voids and onset of turbulent fluidization.

- The highest h was measured in the turbulent fluidization regime, independent of column diameter, confirming the benefit of operating within the turbulent fluidization flow regime from a heat transfer point of view. Scale-up is also easier in the turbulent regime.

- The highest h in bubbling beds was observed where most voids rise: in a shallow bed the highest h occurred at half the column radius, whereas in a deep bed in the small column, h was highest in the centre. In turbulent beds, the radial position of the heat exchanger was less important as h was distributed quite uniformly.

- The effect of superficial gas velocity on heat transfer for columns of different diameter were well scaled by $Fr=U/(gD_t)^{0.5}$ as long as similar local flow structures were present near the heater.

5. TRANSIENT HEAT TRANSFER AT THE COLUMN WALL

5.1. Introduction

In bubbling beds, the correlation between bubbles and heat transfer is well established (Chen et al., 2005). Instantaneous probe experiments (Ozkaynak and Chen, 1980) have confirmed experimentally that a heat transfer surface is alternately contacted by bubbles and packets of particles (emulsion) and that the heat transfer occurs primarily when the packets contact the heat transfer surface. In addition, Mckain et al. (1994) reported that the frequency of bubbles matches the frequency of heat transfer fluctuations at low gas velocities in agreement with the packet model originally suggested by Mickley and Fairbanks (1955).

With the increased use of CFB boilers in the late 1980's, the focus of fluidized bed heat transfer research shifted to the wall and the upper dilute region of fast fluidized beds. In circulating fluidized beds, similar to bubbling beds, the packet renewal mechanism was confirmed by simultaneous measurements of transient concentration of particles and heat transfer (Wu et al., 1991). The alternating phases at the heat transfer surface were identified as dilute suspension and descending particle clusters. Studies have also proven the dominant role of particle clusters in the heat transfer process for circulating fluidized beds (Chen et al., 2005).

Turbulent beds are characterized by increased homogeneity of the flow structure. The reduced difference between the dense and dilute phases makes application of the packet renewal theory challenging. In the literature, fluctuations of the instantaneous heat transfer coefficient at the wall have not been correlated with particle concentrations or surface coverage in turbulent beds. The heat transfer experiments with an immersed vertical tube, presented in Chapter 4, suggest that the dominant mechanism of heat transfer changes as the bed undergoes transition to turbulent fluidization. The objective of this chapter is to observe the change in the dominant mechanisms of heat transfer as the hydrodynamic regime changes from bubbling to turbulent

with increasing superficial gas velocity, by correlating the variations of the local hydrodynamics with the fluctuations of the instantaneous heat transfer coefficient.

Several probes for simultaneous measurement of transient *h* and local particle concentration have been reported. Wu et al. (1991) and Griffith et al. (2000) mounted small heat transfer probes at the wall of a circulating fluidized bed combined with capacitance probes for instantaneous measurement of local particle concentrations. Ozkaynak and Chen (1980), Olsson and Almstedt (1995) and Li et al. (2004) used an instrumented tube with heat flux sensors of the thermocouple type and capacitance probes in bubbling fluidized beds at low gas velocities. Three methods can be used to obtain the heat transfer coefficient: constant heat flux, constant temperature and heat/cool sink with measurable heat flux (Louge, 1997). To ensure a fast response and reduce thermal inertia, constant temperature at the heat transfer surface was shown (Renganathan and Turton, 1989) to be the best method.

There are several important requirements for the design of instantaneous heat transfer probes: fast response (able to capture the fluctuations of local voidage), non-disruptiveness to the local flow, easy temperature control, and allowance for heat losses. The use of capacitance, optical or pressure probes in characterizing hydrodynamics involves measuring volumes that differ from that of the heat transfer probe. Furthermore, the heat transfer and capacitance probes are usually some distance apart. Other disadvantages are that, in the case of capacitance probes, the tip of the probe might interfere with the local flow, whereas differential pressure measurements might capture remote signals. In the current study, in addition to having probes of small measuring volume (e.g. optical probes), the heat transfer probe was designed to be transparent to allow observation and video recording of the actual conditions at the heat transfer surface.

5.2. Methodology

5.2.1. Equipment and instrumentation

The experiments were carried out in the 0.29 m ID Plexiglas fluidized bed column described in Chapter 2. The bubble cap distributor was used. The column was filled with alumina particles (d_p=82 μm, ϱ_p=2700 kg/m^3) to a static height of 0.8 m.

The heat transfer probe was designed to: a) not disrupt the local flow, b) have a fast response, c) be able to record and control temperature at the surface, and d) have a transparent heating surface. In the literature, to allow easy control of temperature, electrically heated wall probes (Wu et al., 1991; Griffith et al., 2000) have used the heating element as a temperature sensor based on the relationship between the resistance and temperature. Three means of providing the relationship between electrical properties and temperature while allowing a transparent heating surface were evaluated here: conductive polymers (Skotheim et al., 1997), indium thin oxide (ITO) heaters (Honeywell, 2003), and transparent thin wire heaters (Minco, 2008).

Conductive polymers and ITO coatings give visually clear surfaces, but they have disadvantages. Electrically conductive polymers are relatively new materials. The relationship between their temperature and resistance depends on the composition of the polymer and tends to be non-linear. The electrical properties of the conductive polymer are also less favourable as transparency increases. In order for the ITO film to be transparent, it needs to be very thin (a few nanometers). ITO can be coated on a glass or plastic film and there are commercially available heaters. However, both conductive polymers and ITO films can withstand only very low power (<1 W), and can be easily damaged, changing their electrical properties and thus the temperature calibration. There are many uncertainties for conductive polymers or ITO films, making their application as sensors unreliable.

Although thin wire transparent heaters do not give 100% visually clear surfaces, their stability and endurance provide great advantages. A Thermal-clear™ transparent heater produced by Minco was chosen for the probe. This heater consisted of a thin Ø30 μm Ni wire embedded in a polyester film with dimensions 14.6 x 55.9 mm. The overall thickness of the heater was 0.25 mm. The specific geometry of the embedded 30 μm wire is shown on Figure 5.1. The heating element acted as a temperature sensor, utilizing the linear relationship, plotted in Figure 5.2, between the temperature of the probe and the wire resistance:

$$T_{wire} = 4.4 \, R - 135.7 \tag{5.1}$$

where, R is in ohms and T_{wire} in ^{0}C.
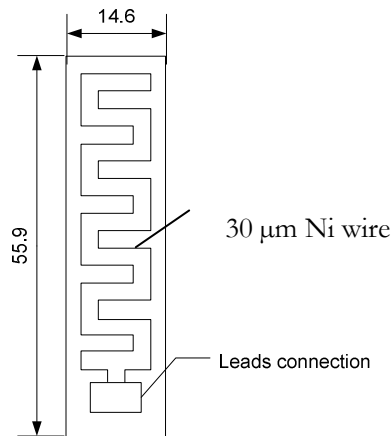
**Figure 5.1. Geometry of transparent heater probe heating element.
Dimensions are in mm.**

$$T = 4.4R - 135.7$$
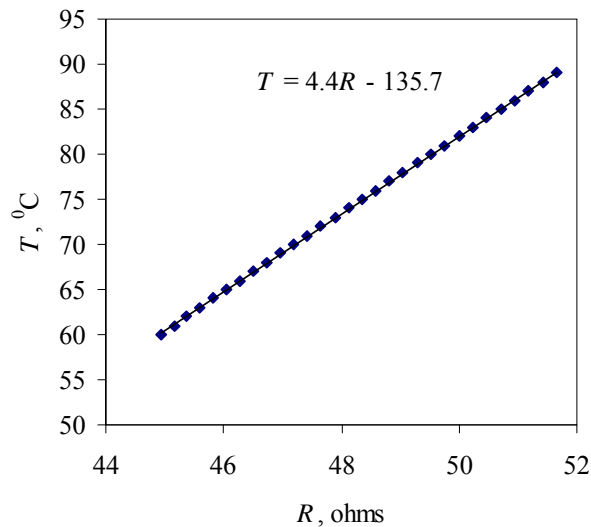
Figure 5.2. Temperature vs. resistance calibration for heater wire.

The transparent heater probe was attached to a support and then to the column wall. A drawing of the support appears in Figure 5.3. The transparent heater (1) was glued to the 6 mm thick inner Plexiglas plate (2) having the same curvature as the inside of the column. The area where the heater was placed was recessed, to ensure that the heater was flush with the plate and did not disturb the flow. The 6 mm outside Plexiglas plate (3) had a diameter larger than the inner plexiglas plate and was curved to fit the column outside diameter. The two Plexiglas plates were screwed (8) together with a rubber gasket (4) between them, creating a 3 mm thick air gap. This air gap provided insulation and reduced the heat losses from the back of the probe. The outer Plexiglas plate of the assembled probe support was secured to the column wall by screws (7). The probe support contained four openings (5) where pressure or optical probes could be

mounted. These openings were plugged when not in use. A photograph of the probe mounted on the column wall, with its centre 0.6 m above the distributor plate, appears in Figure 5.4.
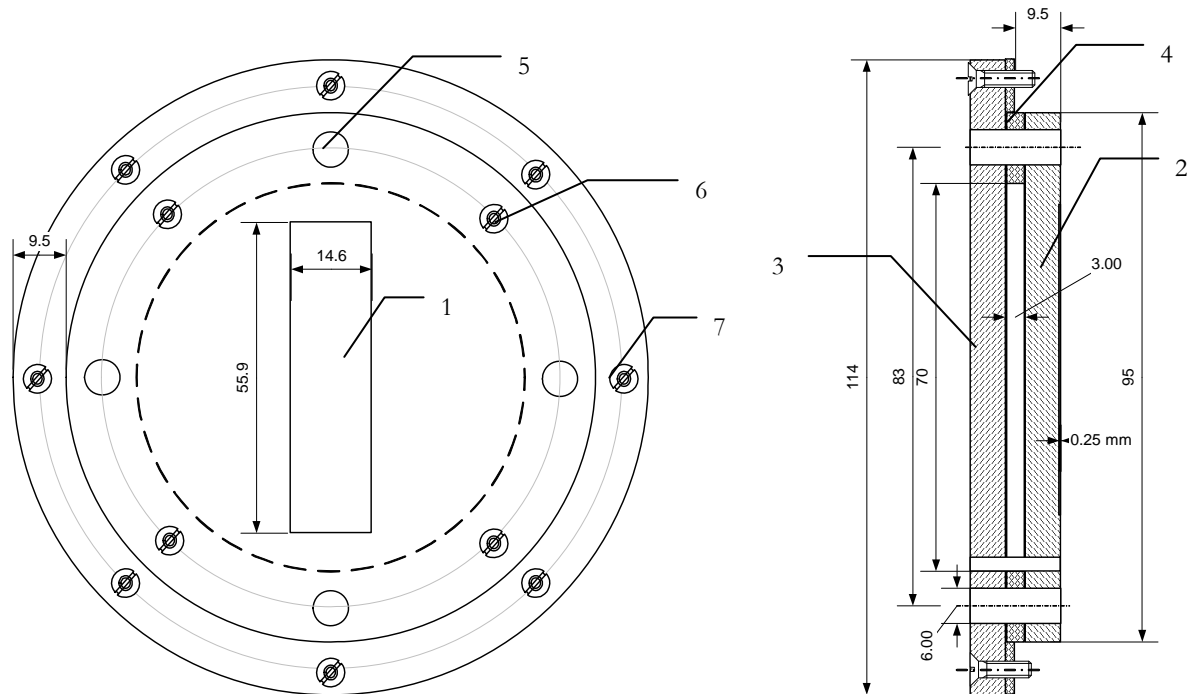
Figure 5.3. Drawing of probe support. All dimensions are in mm.

1- recess for transparent heater, 2- inner Plexiglas plate, 3- outer Plexiglas plate, 4- rubber gasket, 5- openings for optical and pressure probes, 6 –screws holding inner and outer Plexiglas plates together, 7 - screws for mounting probe support onto column wall.
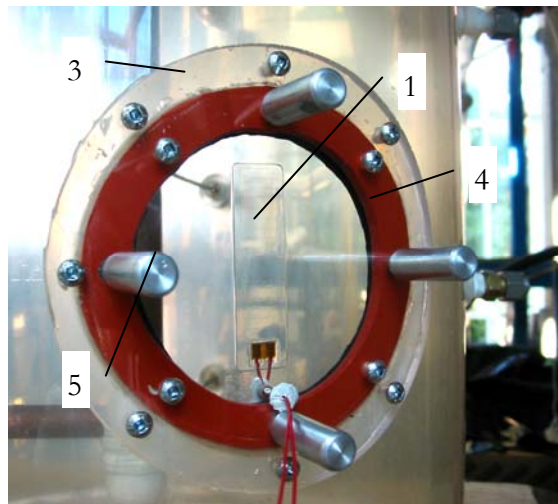
Figure 5.4. Photo of transparent transient heater probe mounted at wall.

1- recess for transparent heater, 3- outer Plexiglas plate, 4- rubber gasket, 5- plugs for optical and pressure probes.

Power in the range of 2.5-4 W was supplied to the heater by a programmable power supply, Xantrex XDL35-5P. The maximum allowable power density recommended by the manufacturer, for the transparent heater, is 0.4-1.6 W/cm^2 for heat sink temperatures of 15-90 ^0C. The heat generated in the heating element,

$$Q_g = P = I^2 R \tag{5.2}$$

was distributed through the thin polyester film into which the wire was embedded. Heat from the probe is dissipated to the fluidized bed from its face and from the back by conduction through the supporting Plexiglas plate. A portion of the heat conducted through the latter continues by conduction through the air gap and the outer Plexiglas plate from the probe support to the surroundings, while some heat conducted in the lateral direction is dissipated back into the bed. Although conduction through the back of the probe is three-dimensional, the problem was simplified by introducing a conduction shape factor for the conduction through the inner Plexiglas plate and assuming one-dimensional conduction through the air gap and outer plexiglas plate. A schematic of the heat losses from the probe is presented in Figure 5.5. The energy balance based on this schematic is:

$$Q_g = Q_{back} + Q_{wall} + Q_{bed} \tag{5.3}$$

where Q_{back} is the heat loss through back of probe by conduction, Q_{wall} the heat loss from surrounding wall to bed, and Q_{bed} = heat loss from probe surface to the bed.
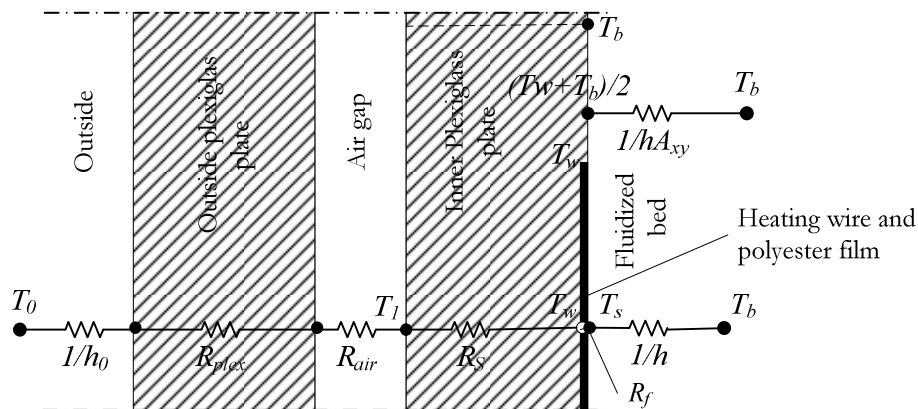
Figure 5.5. Schematic of heat losses from probe.

The conduction shape factor method was used to evaluate the thermal resistance through the inner Plexiglas plate, approximating the heater area with a disk. The thermal resistance is then (Incropera and DeWitt, 2001):

$$R_s = \frac{1}{2d_e k} = \frac{1}{2k\sqrt{\frac{4A_{eff}}{\pi}}}$$

(5.4)

where A_{eff} is an effective area, described below. The heat conducted through the back of the probe is then:

$$Q_{back} = \frac{1}{R_{back}}(T_w - T_0)$$

(5.5)

where:

$$R_{back} = R_s + R_{air} + R_{plex} + 1/h_o$$

(5.6)

where R_{air} is the conduction resistance through the air gap, R_{plex} the conduction resistance through the outer Plexiglas plate and h_0 the heat transfer coefficient to the outside air.

The heat loss from the inside wall surrounding the probe to the fluidized bed was estimated as:

$$Q_{wall} = hA_{xy}\left(\frac{T_w + T_b}{2} - T_b\right)$$

(5.7)

where A_{xy} is the surface area at the wall surrounding the probe with $T_w > T > T_b$. Although the temperature of the wall decreased from T_w to T_b away from the heating surface, the temperature of A_{xy} was assumed to be uniform at $(T_w + T_b)/2$. The boundaries of the area A_{xy} shrink as convection from the probe surface becomes more dominant, so the heat loss from A_{xy} is reduced (see Figure 5.6). For heat transfer coefficients in the range 100-400 W/m^2K (typical of fluidized beds) the resistance to the conduction through the back of the probe is higher than the resistance to convection to the bed ($Bi>10$). This means that heat losses through the probe's support are significantly reduced and most of the heat generated in the thin wire is transferred to the bed.
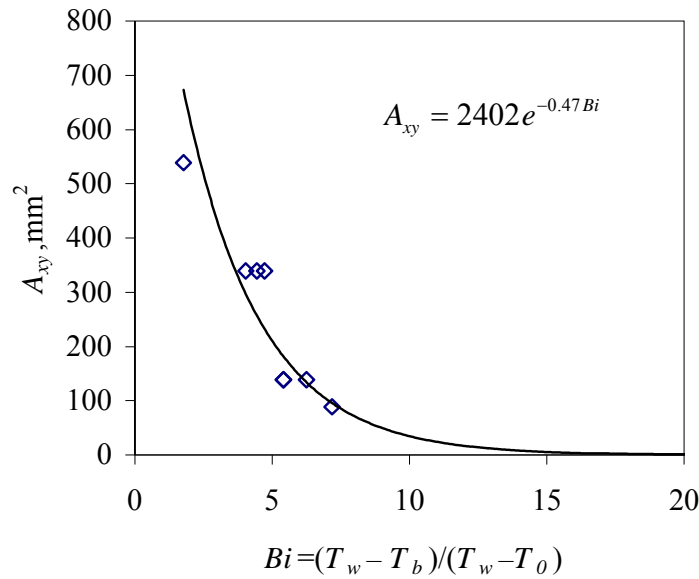
Figure 5.6. Variation of surface area surrounding the probe
(A_{xy}) with increasing Biot number (Bi) used for heat losses estimation.

The effective areas, A_{eff} and A_{xy}, were measured for natural air convection at variable ($T_w - T_b$)/($T_w - T_0$) (where T_0 is the temperature of the back of the probe support) with the probe mounted on the column wall. The temperature distribution at and around the probe surface was measured using liquid crystal sheets with resolution 1-2 ^{0}C. A photograph showing the temperature distribution at the probe surface is shown in Figure 5.7. Because of the geometry of the wire, the outer wire segments act as guard heaters keeping the area surrounded by them at uniform temperature. The effective heat transfer area of the probe having its temperature held within ± 0.5 ^{0}C was measured from the images of temperature distribution across the heating surface. The measurements were performed with the image analysis software (ImageJ) that detected the coloured surface area. The average effective surface area was 261 ± 15.4 mm^2 from repeated measurements.

If we combine equations (5.5) and (5.7), we obtain:

$$Q_g = I^2 R_e = \frac{A_{eff}}{R_{back}}(T_w - T_0) + hA_{xy}\left(\frac{T_w + T_b}{2} - T_b\right) + \left(\frac{1}{R_f + 1/h}\right)A_{eff}(T_w - T_b) \qquad (5.8)$$

The last term in equation (5.8) is the heat transferred from the face of the probe to the bed. R_f is the thermal resistance through the polyester film supporting the thin wire. This expression was

verified by comparing measured forced air convection heat transfer coefficients with those calculated by correlations from the literature (Incropera and DeWitt, 2001), as shown in Table 5.1. Natural and forced convection experiments were performed in an empty column with the heater probe mounted on the column wall. The set-up was the same as for the fluidized bed experiments.
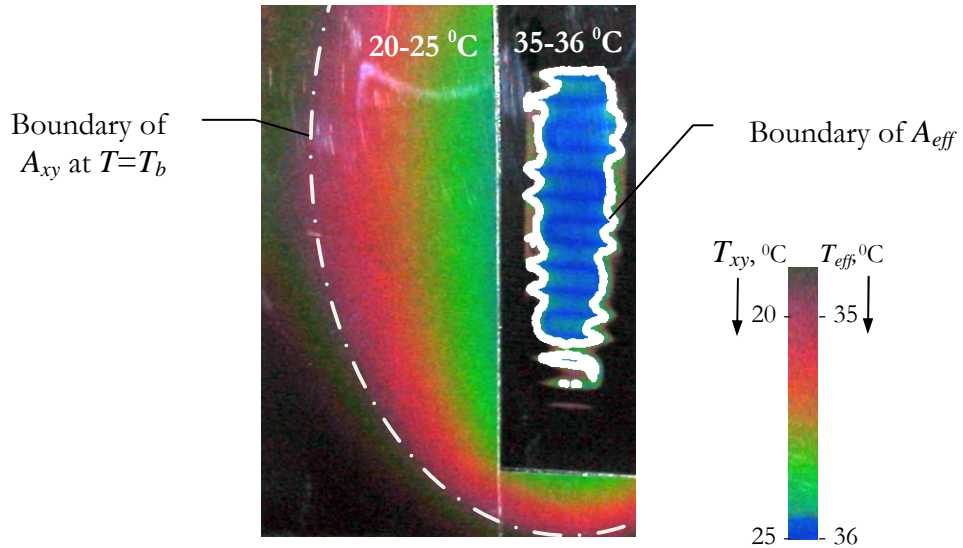
Figure 5.7. Temperature distribution at probe surface (T_{eff}) and surrounding wall (T_{xy}) measured by liquid crystal sheets (LCS) rated at 35-36 ^{0}C and 20-25 ^{0}C respectively. Coloured (gray area bounded by white line) is within the range of temperatures for which the LCS is calibrated.

Natural convection was calculated from the correlation of Churchill and Chu (1975):

$$Nu_N = \left\{0.825 + \frac{0.387 Ra_L^{1/6}}{\left[1 + (0.492/\Pr)^{9/16}\right]^{8/27}}\right\} \qquad (5.9)$$

Here Ra_L is the Rayleigh number and Pr is the Prandtl number.

The correlation used to calculate h for forced air convection was advocated by Kays (1955):

$$Nu_F = 3.66 + \frac{0.0668(D_t/l)Re_D \Pr}{1 + 0.04\left[(D_t/l)Re_D \Pr\right]^{2/3}} \qquad (5.10)$$

Here D_t is the diameter of the column, l the length of the probe and Re_D the Reynolds number based on the column diameter.

The combined heat transfer coefficient for natural and forced convection was recommended by Incropera and DeWitt (2001) as:

$$Nu = \left(Nu_N{}^n \pm Nu_F{}^n\right)^{1/n}$$

(5.11)

with $n=3$.

Table 5.1. Measured values of h compared with correlations for air convection

	Experimental	Calculated	Equation
Natural convection	7.4	6.3	(5.9)
$U=0.3$ m/s	12.1	13.0	(5.9) and (5.10)
$U=0.4$ m/s	13.8	13.5	(5.9) and (5.10)

When the probe is exposed to fluidized bed, where h is high, the heat losses by conduction in the probe support become insignificant and equation (5.8) becomes:

$$Q_g = \left(\frac{1}{R_f A_{eff} + 1/h}\right) A_{eff}\left(T_w - T_b\right)$$

(5.12)

The corresponding heat transfer coefficient is:

$$h = \frac{1}{\dfrac{A_{eff}\left(T_w - T_b\right)}{I^2 R_e} - A_{eff} R_f}$$

(5.13)

The uncertainty analysis of the errors arising from the accuracy of the instrumentation and the 5.9% error in A_{eff} (from repeated measurements) leads to overall estimated error of 6.3% for each h determined from equation 5.13.

The inertia of the probe system was overcome by maintaining the temperature of the heat transfer surface within a narrow range, $\pm 0.5\ ^0$C. Control was provided by a personal computer connected to the programmable power supply. The program used PI (proportional-integral) control for the temperature. Its algorithm is given in Figure 5.8. Communication between the personal computer and the programmable power supply was established by the RS232 protocol.

The response time of the system was tested with the probe mounted on the column wall, by injecting gas through a port below the heat transfer probe, while the bed was held at minimum

fluidization conditions. The 90% response time was estimated to be 0.098 s, as illustrated in Figure 5.9. Fluidized bed frequencies are generally less than 10 Hz, so this response time was deemed to be satisfactory.
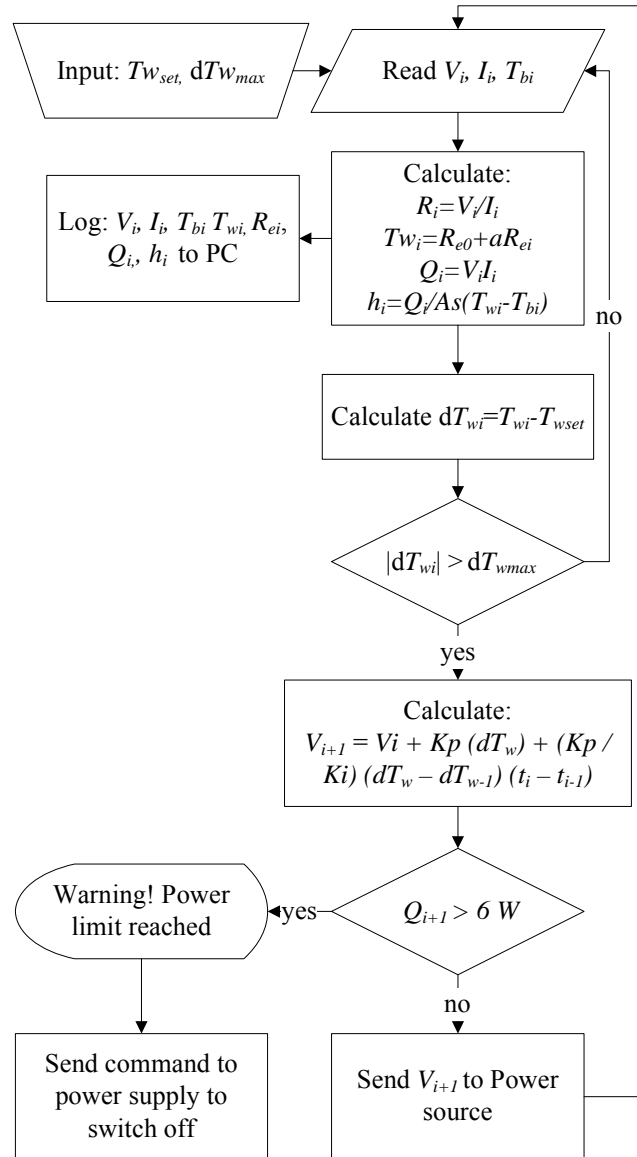
Figure 5.8. Software algorithm used to control heater temperature.

dTw_{max}= allowed variation of heater temperature from set point, *Tset* =heater temperature set point, *Kp* and *Ki* are coefficients

The novelty of the probe lies in its transparency, which allows acquiring images of the conditions at the heat transfer surface simultaneously with the heat transfer coefficient. Video images were taken with a Canon XL1 video-camera at 30 Hz. To synchronize the video images with the heat

transfer data, the "timecode" (time marker given to each video frame) in SMPTE (Society of Motion Picture and Television Engineers) format was "stamped" in the log file simultaneously with the instantaneous heat transfer measurement. To obtain the "timecode" from the video in real time, the Lanc protocol output of the camera was used. A "Rosetta stone", manufactured by Addenda Electronics, converts the Lanc protocol to a PC compatible RS232 protocol. The sampling frequency was the same as for the heat transfer coefficient (50 Hz), higher than the frequency of acquiring images. For each superficial gas velocity, 1000 to 1500 images were obtained. The operating conditions for the transient experiments are given in Table 5.2.
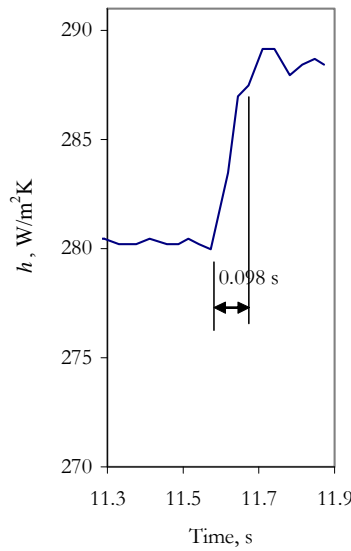
Figure 5.9. Response of heater probe to sudden impingement of jet on its surface.

Table 5.2. Operating conditions for transient heat transfer experiments.

D_t	0.29 m
H_0	0.8 m
Distributor	Bubble cap
Particles	Alumina
d_p (mean size)	82 μm
Distance above distributor	0.6 m
U	0.03 – 1.2 m/s

5.3. Results and discussion

5.3.1. Transient heat transfer coefficient

The time-mean heat transfer coefficient, measured by the transparent probe and averaged over 120 s intervals, is plotted in Figure 5.10. It rises steeply with increasing U after the onset of bubbling, reaches a maximum at ~0.4 m/s, and then decreases slightly.
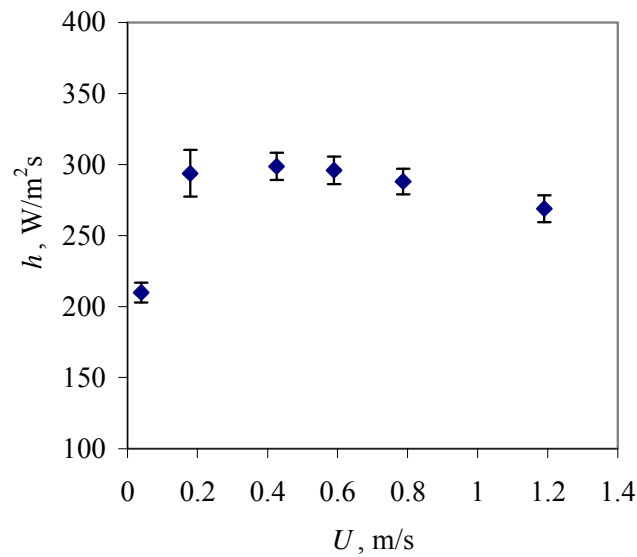
Figure 5.10. Time-mean heat transfer coefficient measured at wall vs. superficial gas velocity. Error bars represent ±2 standard deviations.

Histograms of the heat transfer signals are presented in Figure 5.11. It is apparent that the shape of the distribution changed as the superficial gas velocity increased, from slightly skewed to the left at U=0.03 m/s (Figure 5.11a) to a wide distribution for U=0.18 m/s (Figure 5.11b). In the range of turbulent fluidization, the distribution is close to Gaussian (Figure 5.11c). At high superficial gas velocities, the distribution became skewed to the left with a sharp peak at higher values of h and possibly a very small secondary peak emerging at lower h (Figure 5.11d).
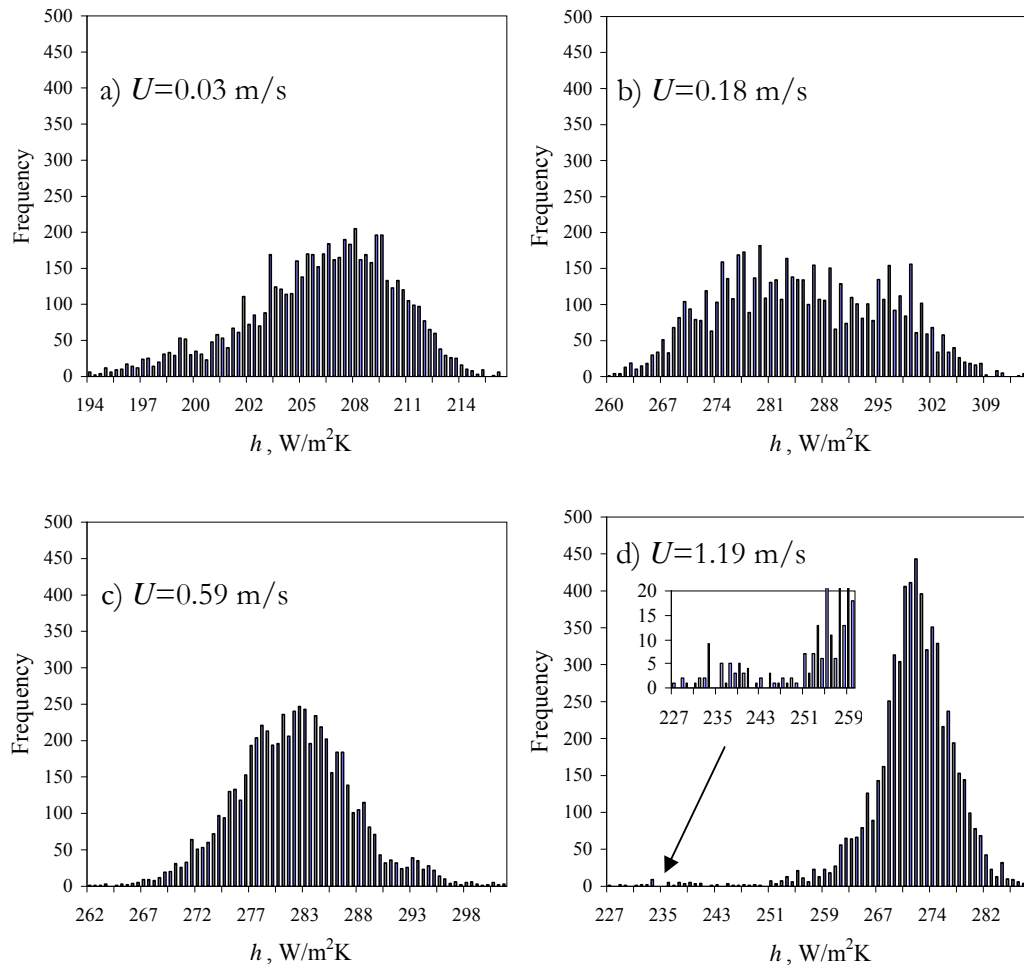
Figure 5.11. Distribution of transient *h* at different superficial gas velocities.

5.3.2. Relationship between transient heat transfer coefficient and differential pressure fluctuations

Figure 5.12 shows the cross-correlation of transient *h* and differential pressure across the heater probe. At low gas velocity (*U*=0.03 m/s), there was a dense descending layer of particles at the wall and no voids could be detected at the probe surface. Rising bubbles in the core of the column caused pressure fluctuations and affected the downwards motion of particles at the wall. Renewal of particles at the heat probe is related to voids rising in the core. This explains the strong cross-correlation between differential pressure (DP) and *h* at *U*=0.03 m/s on Figure 5.12. Transient *h* and DP signals are plotted in Figure 5.13.
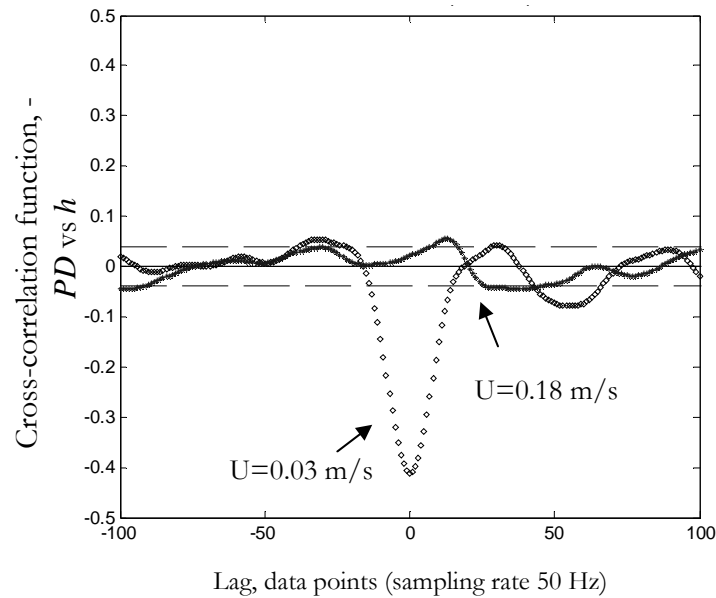
Figure 5.12. Cross-correlation function of *h* and differential pressure across probe. Δz_{DP}=0.063 m.
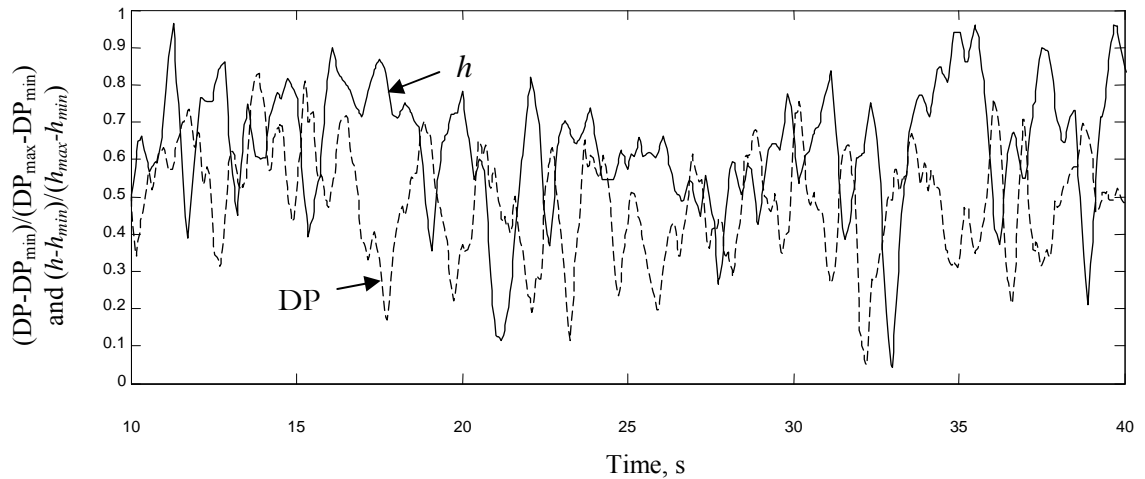
Figure 5.13. Normalized transient *h* and differential pressure (DP) across heat transfer probe for *U*=0.03 m/s. Δz_{DP}=0.063 m.

As the gas velocity increased, voids began to appear throughout the dense layer of particles at the wall, contributing to particle exchange and increasing *h*. In this case, the cross-correlation between PD and *h* weakened (Figure 5.12, *U*=0.18 m/s) because a second mechanism (fast voids appearing randomly at the wall) contributed to particle renewal.

5.3.3. Relationship between transient heat transfer coefficient and local voidage

The relationship between the heat transfer and local voidage near the heat transfer surface was examined by two optical probes, 13.5 mm above and 13.5 mm below the heater (83 mm apart). The cross-correlation between the signals of the two optical probes is shown in Figure 5.14. The degree of correlation gives an indication of the vertical dimension of flow entities passing the heat probe. For very low superficial gas velocity, U=0.03 m/s, no voids appeared at the probe. The voidage remained as at minimum fluidization, and visual observations showed layers of particles descending. For U=0.18 and 1.2 m/s, there were peaks in the correlation function close to zero time lag indicating that there were flow entities passing the lower probe that appeared at the upper probe. The correlation coefficients are not very high as there were many bubbles that appeared at one probe but not the other. In the transition region (U=0.43 m/s) the correlation is further decreased as the voids were less stable and more erratic.
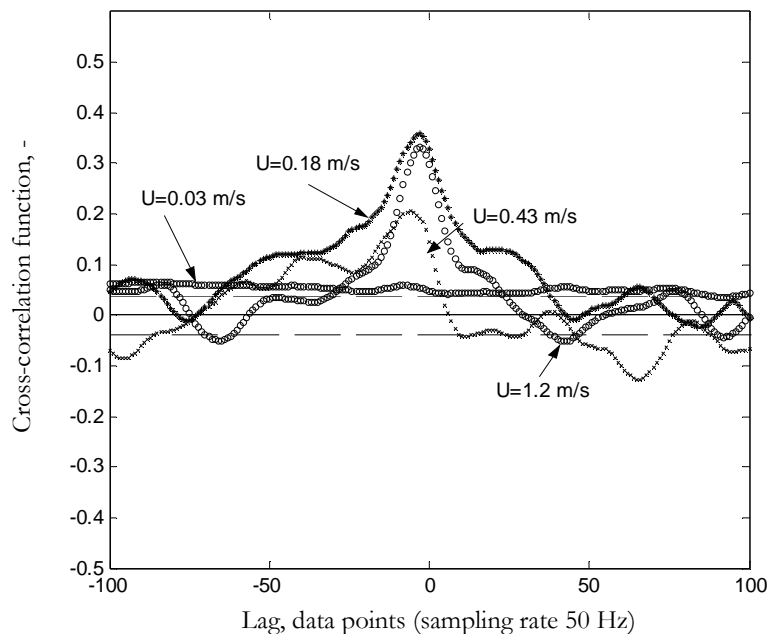
Figure 5.14. Cross-correlation function of optical signal from probes located above and below heat transfer probe (Δz_{OP}=0.083 m).
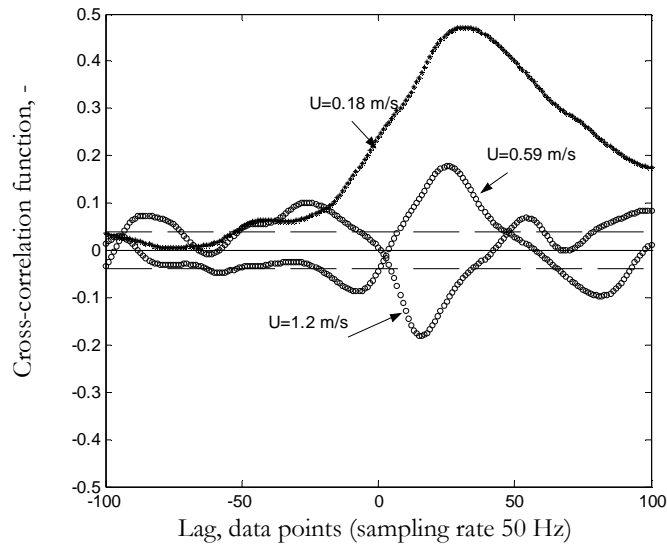
Figure 5.15. Cross-correlation function of transient heat transfer coefficient and voidage from lower optical probe.
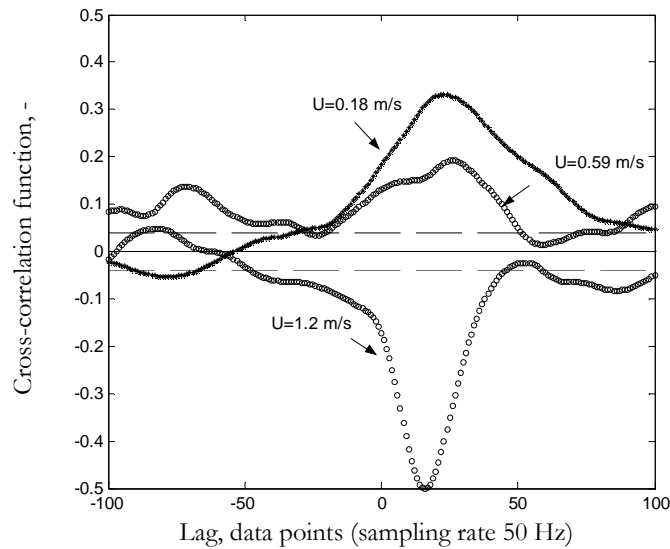
Figure 5.16. Cross correlation function of transient heat transfer coefficient and voidage from upper optical probe.

Cross-correlation functions of the optical probe signals and the transient heat transfer coefficient are given in Figures 5.15 and 5.16. At low gas velocities (e.g. *U*=0.18 m/s) the peak in the distribution of correlation coefficients is positive and wide. The maximum correlation coefficient between transient *h* and the lower optical probe is higher than that between *h* and the upper optical probe. Image analysis shows that most of the voids appearing at the bottom travel upwards, but not always vertically. This is likely why the cross–correlation coefficient is higher for the lower optical probe (Figure 5.15) than for the upper one (Figure 5.16). For greater

120

superficial gas velocities (U=1.2 m/s), the peak in the cross-correlation function is negative, suggesting that the increased voidage starts to play a role in reducing the heat transfer rate. The maximum cross-correlation coefficient is higher for the upper optical probe than for the lower one.

For a 30 s interval, transient h and local voidage measurement for U=0.18 m/s are shown in Figure 5.17a. Almost every peak in local voidage is followed by a peak in transient h. Thus, the cross-correlation between the local voidage and heat transfer is relatively strong and positive at U=0.18 m/s (Figure 5.16). The markings A and B in Figure 5.17a correspond to images of the heating surface shown in Table E.1. of Appendix E.

At high velocities (U>0.6 m/s), increased voidage plays a more significant role. The dense phase starts to break down and the heat transfer surface is exposed to gas for longer intervals. Voids residing longer at the surface caused dips in the transient h signal. Such a void is present at point C in Figure 5.17c, and its development is illustrated in Table E.3 of Appendix E. The shape of the void changes as it lingers at the heat transfer surface. The maximum cross-correlation between the heat transfer coefficient and upper optical probe occurs close to 0 lag (Figure 5.16). The maximum cross-correlation coefficient is stronger for the upper optical probe than the lower one. Some voids appeared at the top of the heat transfer probe and disappeared before reaching the bottom optical probe. Although it seems unlikely that the voids would descend, this was observed in the upper region of the bed, approximately 1/3 of the bed height below the bed surface when the bed was turbulent. Small voids comparable to the size of the heat transfer probe were observed to linger on the wall, changing direction in an oscillatory manner before disappearing. Similar phenomena were observed and simulated in liquid–gas systems (Shafer and Zare, 2000), where small bubbles were descending at the wall. This was explained by small voids being dragged down by liquid descending near the walls, balancing liquid being dragged up by the large bubbles at the axis. In the turbulent fluidized bed, as more gas passes through the core region, many particles are displaced towards the top of the bed and ejected into the freeboard as clusters. It is possible that when these clusters lose their momentum, they fall back near the wall, dragging small voids downwards. Consecutive images of a descending small void at the probe surface (C on Figure 5.17b) are shown in Table E.2 of Appendix E.
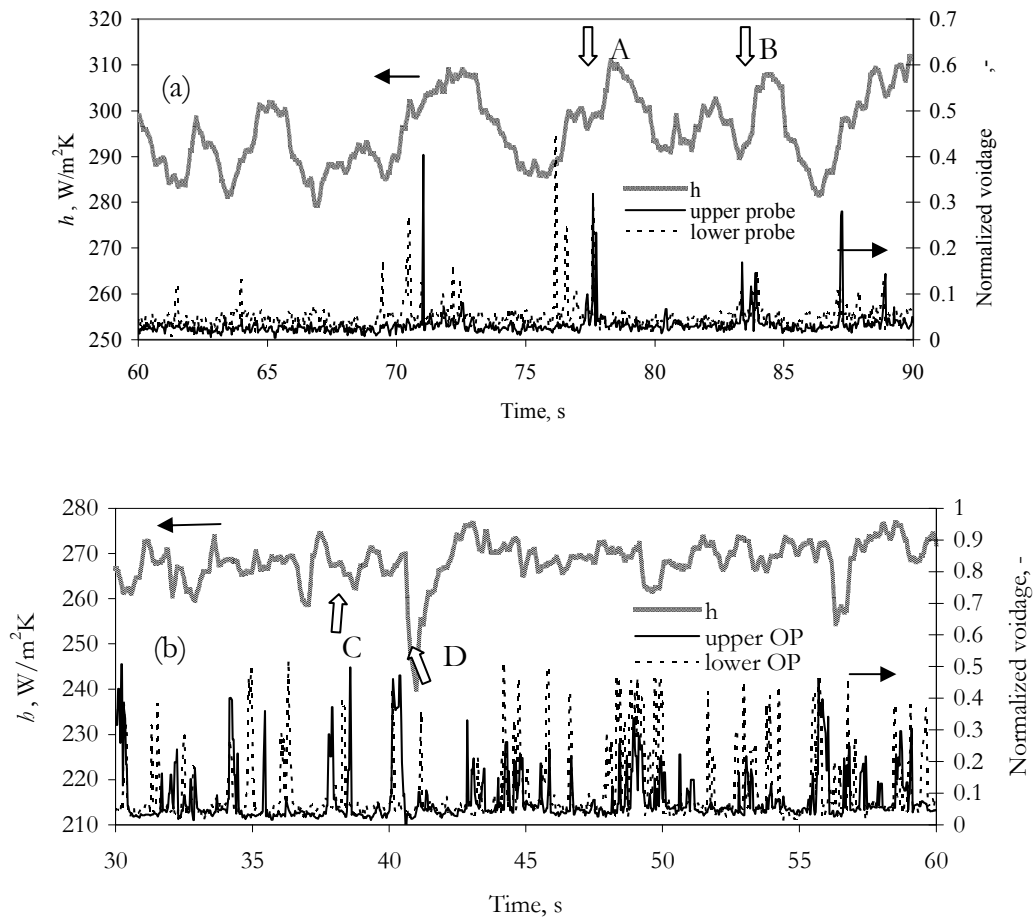
Figure 5.17. Instantaneous heat transfer coefficient and local voidage from optical probes (OP), a) *U*=0.18 m/s, b) *U*=1.2 m/s.

5.4. Image analysis

Video clips of the heat transfer surface (60-120 s long) at five superficial gas velocities (*U*=0.18, 0.4, 0.6, 0.8 and 1.2 m/s) were analyzed with DV (digital video) timecode overlaid on the original video clip to assure that information was not lost when images were captured from the video. 1000 images covering a period of 60 s were saved from each video sequence. The images were converted to 8 bit grayscale (2^8=256 shades of gray, where 0 is black and 255 is white). The image of the fully covered probe was subtracted from the rest of the images in the set to eliminate shadows and to mask the area occupied by the heating wire. Then, binary images were obtained by selecting a threshold within which the voids appearing at the surface were visible. Image analysis software, ImageJ, and custom-made scripts, were used for batch conversion of

the images, for statistical analysis (mean, standard deviation, kurtosis and skewness) of shades of gray at the probe surface, and to measure the area fraction (surface coverage, f_A) in binary images. The area analyzed was the area inside a circle of area 0.0016 m^2 surrounding the heater probe (dashed circle in Figure 5.18), excluding the bottom where the leads were connected. Binary and grayscale images showing voids appearing at the surface are shown in Appendix E.

(a)   (b)
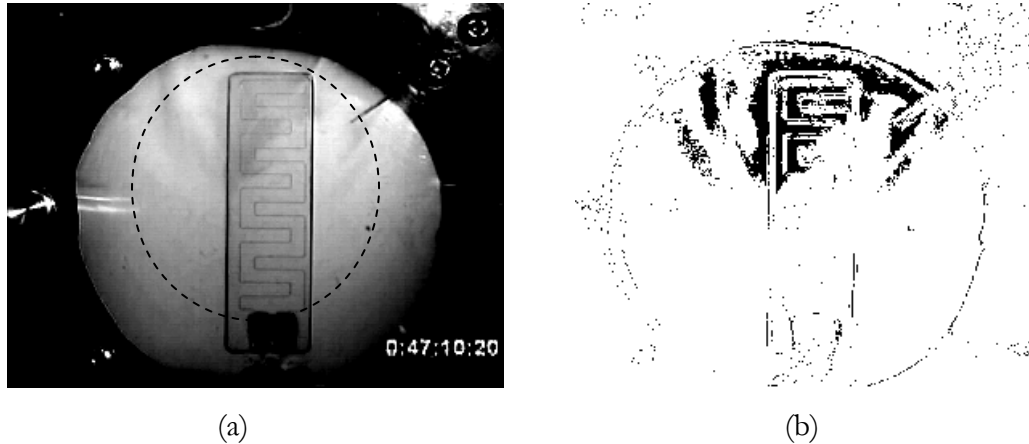
**Figure 5.18. Image of heater probe: a) 8 bit grayscale, b) binary.
Dashed circle represents area analyzed.**

The measured mean grayscale for the analyzed area, G_{mean}, was normalized, to obtain surface coverage, f_A, based on

$$f_A = \frac{G_{mean} - G_{min}}{G_{max} - G_{min}} \qquad (5.14)$$

Here G_{max} and G_{min} correspond to grayscale values of fully covered and fully exposed surfaces respectively.

This image processing method was verified by manually detecting surface coverage from 100 images. The two methods are compared in Figure 5.19, where both the grayscale and binary images results do not differ by more than $\pm$ 3 % from the manually determined surface coverage.

Normalized local voidages measured by the optical probes flush with the wall above and below the heater probe are shown in Figure 5.20, together with the surface coverage obtained from the

binary images. Most of the peaks in the optical probes signals were also detected by image analysis.
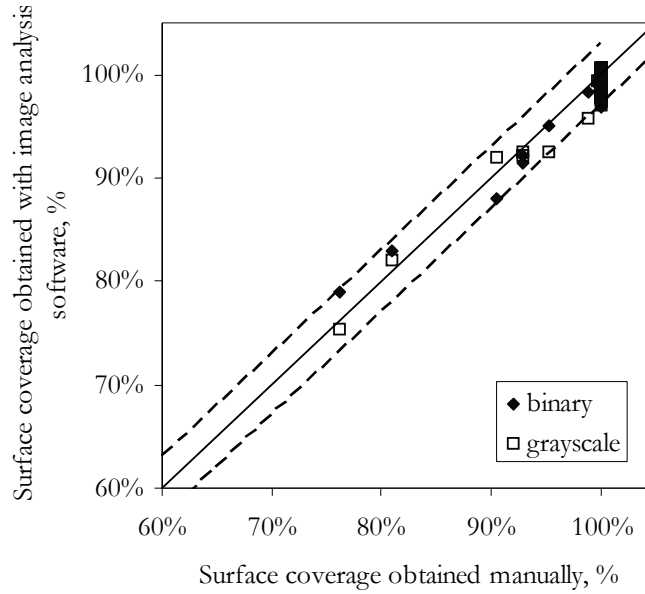
Figure 5.19. Surface coverage measured manually compared with surface coverage obtained by image analysis software from grayscale and binary images. *U*=0.18 m/s
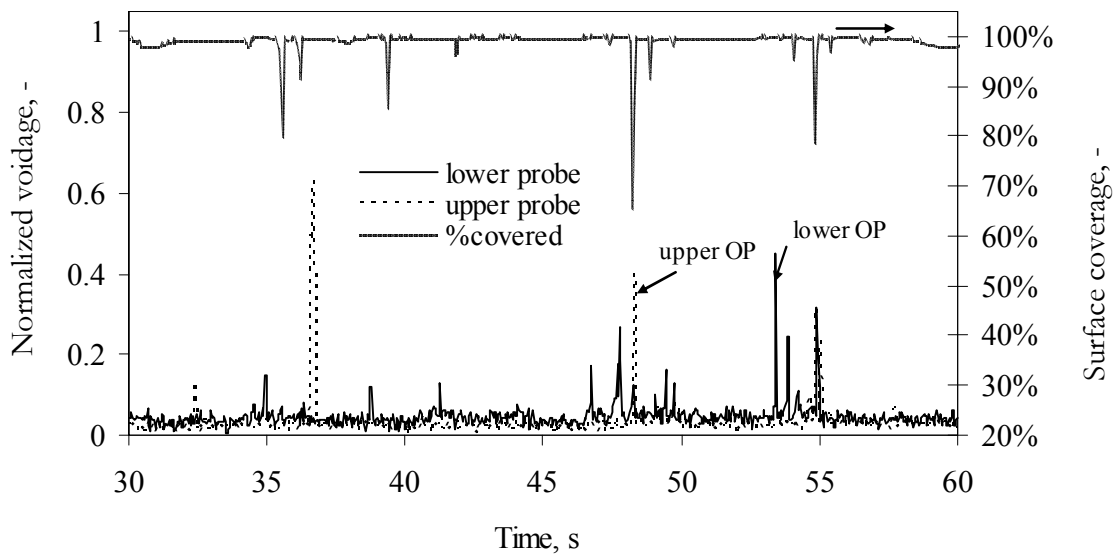
Figure 5.20. Variation of surface coverage (measured from grayscale and binary images) and local voidage from optical probes above and below heater probe for *U*=0.18 m/s.

5.4.1. Effect of surface coverage on instantaneous heat transfer coefficients

The surface coverage obtained from image analysis represents the fraction of the analyzed surface that is covered by the dense phase. Note that this differs from 1-ε which represents the fraction of solids per unit volume.

Because the sampling rate of the heat transfer data differed from the sampling rate of the video images, a moving average filter was applied in the following form:

$$h_{mav} = (h_{i-2} + h_{i-1} + h_i + h_{i+1} + h_{i+2})/5 \tag{5.15}$$

The variations of the surface coverage and heat transfer coefficient with time are shown in Figure 5.21. A to D denote instants corresponding to images of the probe surface in Tables D.1 to D.3. of Appendix E.
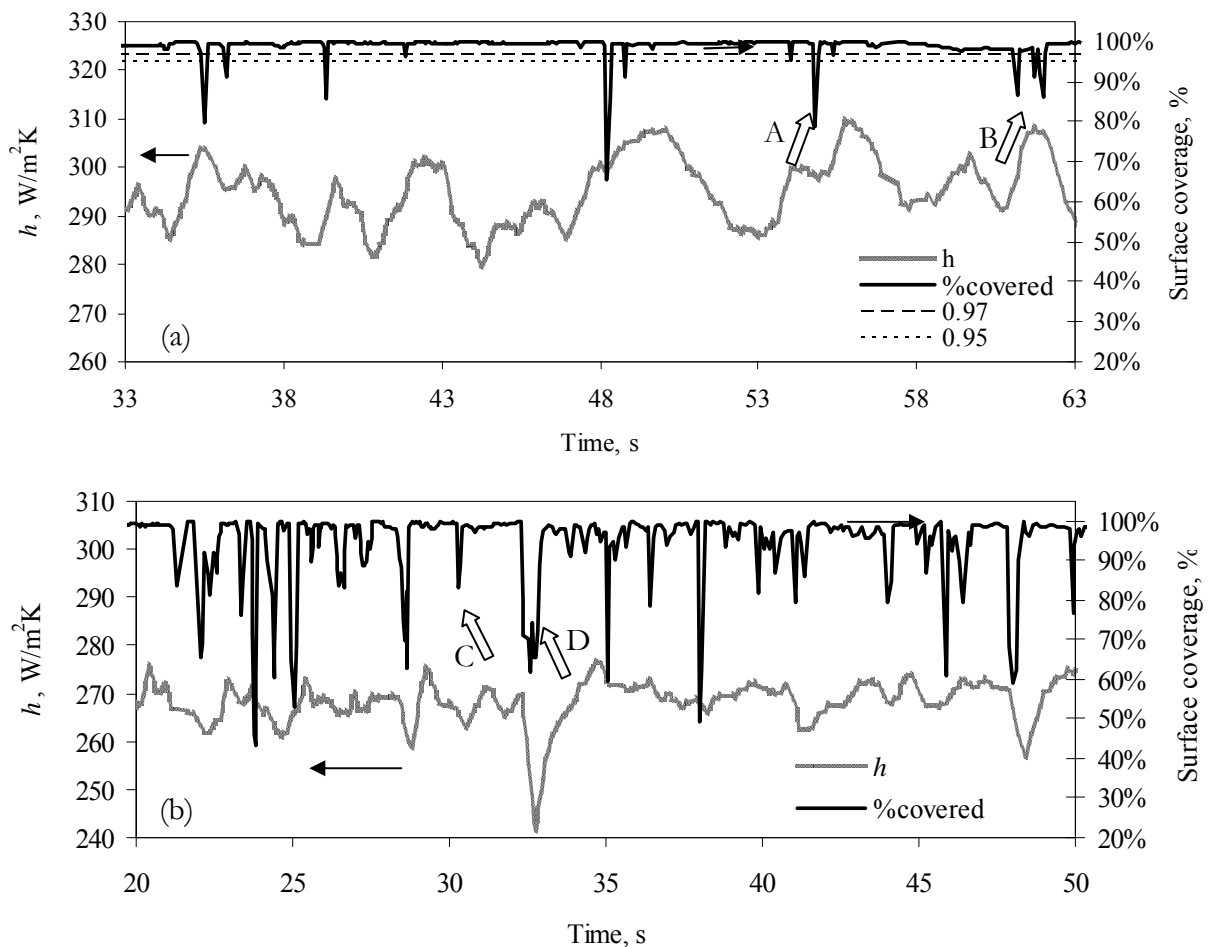
Figure 5.21. Variation of surface coverage and instantaneous heat transfer coefficient with time for: a) *U*=0.18 m/s, b) *U*=1.2 m/s. Moving average filter applied.

The time-mean surface coverage as a function of superficial gas velocity is plotted in Figure 5.22. Because the surface was completely covered by dense phase most of the time, the time-mean surface coverage is close to 100% and decreases slightly for $U>0.6$ m/s, when the voids start appearing more frequently. The distribution of the surface coverage is skewed with a peak close to 100%. The minimum surface coverage (vertical lines) is lower at high velocities, as larger voids were present at the probe surface.
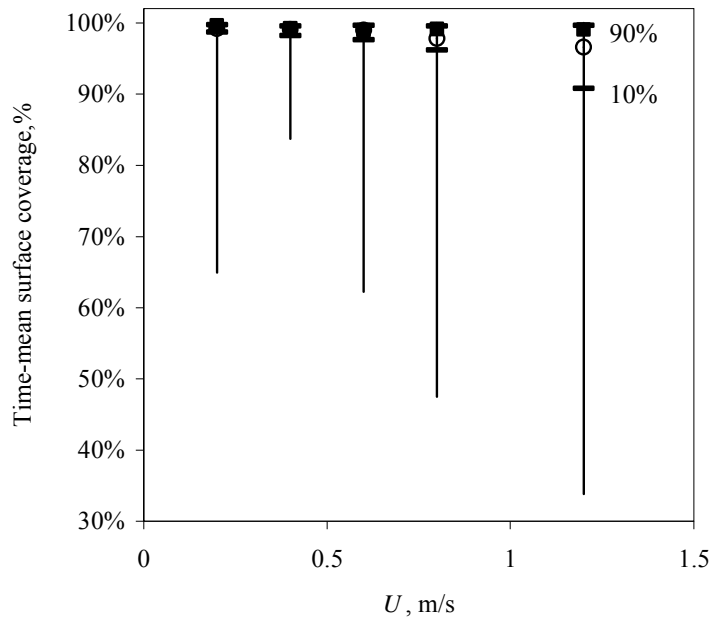
Figure 5.22. Time-mean surface coverage vs. superficial gas velocity. Vertical lines represent minimum and maximum surface coverage, horizontal lines mark 10th and 90th percentiles.

To evaluate how often voids appeared at the surface, the crossing frequency was estimated as half of the number of crossings of the signal around a selected threshold. As the error of the completely covered surface was estimated to be less than ±3% (from Figure 5.19), the threshold was set at 0.95 to avoid including noise introduced by the image analysis. For surface coverage below this mark, it was assumed that voids, even as small as 5% of the investigated surface area, are present at the surface. The error of using a different threshold, 97% surface coverage, is plotted with the error bars on the figure. A higher threshold than 0.97 might include variations of completely covered surface, and would produce errors, whereas a threshold below a 0.95 would exclude data points where voids were present but occupied only a small portion of the surface. The results are presented in Figure 5.23. Crossing frequency obtained from the

normalized optical probe signal at a threshold of 0.95 is also plotted. It appears that the two methods produced similar results. A threshold crossing frequency of 0.97 was also estimated and plotted as error bars in the figure. The crossing frequency increased rapidly for $U>0.6$ m/s indicating increased appearance of voids at the column wall.
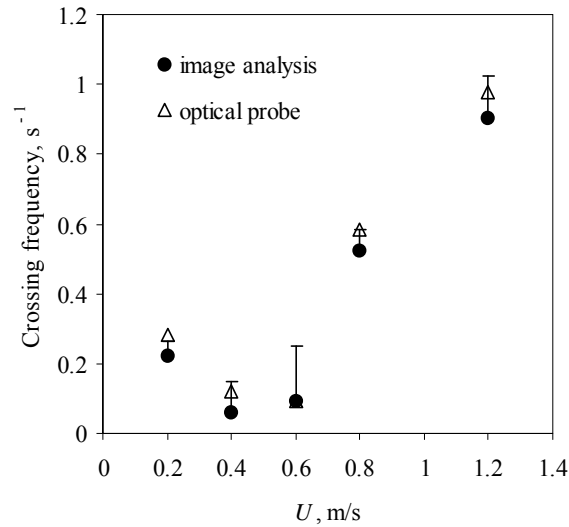
Figure 5.23. Crossing frequency vs. superficial gas velocity for threshold at 0.95. Error bars represent crossing frequency for surface coverage threshold at 0.97.
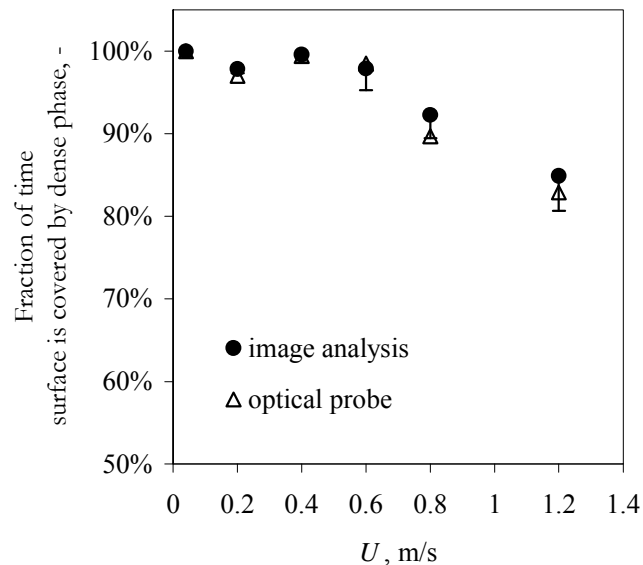
Figure 5.24. Fraction of time when surface is more than 95% occupied by dense phase vs. superficial gas velocity. Error bars represent surface coverage threshold at 0.97.

The fraction of time during which more than 95% of the probe was covered by the dense phase is presented in Figure 5.24. The error bars represent the effect of shifting the threshold to a

surface coverage of 97%. Results from the optical probe for the fraction of time the normalized voidage was >0.95 are also plotted, indicating that whether the fraction of time the dense phase is present was obtained two-dimensionally from image analysis, or three-dimensionally from the optical probe, did not have a significant effect. At low gas velocities, the probe remained covered by the dense phase, whereas for U>0.6 m/s it started to decrease with more frequent appearance of voids.

The cross-correlation function of the surface coverage and instantaneous h was also calculated. The relatively high cross-correlation coefficients for U=0.18 m/s were negative, mostly with negative time lag, indicating that void appearance at the surface generally preceded the increase in instantaneous the heat transfer coefficient (Patil et al., 2006). The cross-correlation coefficients are not very high, probably because voids are not the only mechanism contributing to particle renewal, as particles are also brought at the surface by streams (clusters) of particles. Mostoufi and Chaouki (2004) consider that particles move in the bed: (a) as single particles, (b) associated with voids (e.g. in wakes or clouds), and (c) as clusters in the dense (emulsion) phase. For dense beds and velocities in the range of bubbling and turbulent, they assumed the contribution from single particle movement to be negligible.

The cross-correlation function for U=1.2 m/s, presented in Figure 5.25, shows high positive correlation close to 0 lag, meaning that exposure to gas began to affect h directly.

The analysis of Zarghami et al. (2007) provides a model for the residence time of particles, related to heat transfer. This model follows the trend of the experimental particle residence time from earlier studies (Hamidipour et al., 2005a). The particle contact time decreased with increasing U in a bubbling bed, passed through a minimum at U_c and then increased in the turbulent bed. The residence time model contains two terms, particle residence time associated with bubbles (particles in the wakes) and residence time due to clusters in the emulsion phase. Due to a lack of information on bubble and emulsion fraction and frequency in the vicinity of the wall, they used a corrected fraction of bubbles and emulsion in the bed. Our study of the local voidage and surface coverage at the column wall provides experimental data on the void fraction and frequency that can be applied directly to the particle residence time model proposed by Zarghami et al. (2007).
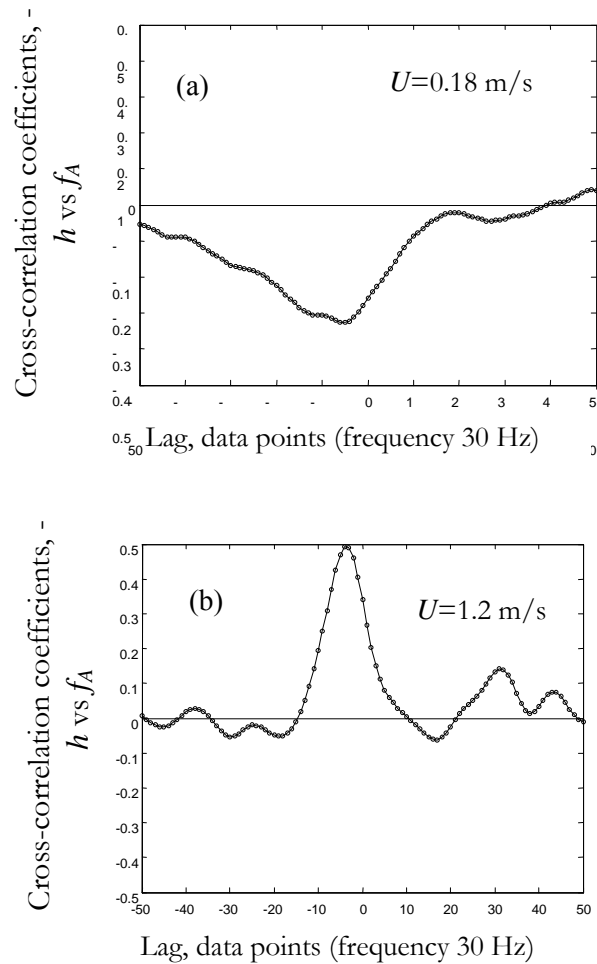
Figure 5.25. Cross-correlation function of instantaneous heat transfer coefficient and surface coverage for a) *U*=0.18 m/s and b) *U*=1.2 m/s. Moving average filter was applied.

5.5. Summary

- For a very low gas velocity (*U*=0.03 m/s), close to *U*$_{mf}$, the heat transfer surface remained covered by a layer of slowly descending particles, balancing the particles carried up by bubbles in the bed core. Variations of instantaneous *h* were strongly correlated with pressure fluctuations, indicating the relationship between bubbles rising in the bed core and erupting at the surface and heat exchange at wall.

- In the bubbling regime (e.g. *U*=0.18 m/s), voids appeared at the wall accidentally, stayed briefly at the heat transfer surface and promoted particle renewal by introducing fresh

particles from the core of the bed into the slowly descending dense layer of particles. This resulted in a high positive correlation coefficient between h and the local voidage fluctuations and a negative cross-correlation between h and surface coverage.

- In the transition region (0.4≤U≤0.6), h reached a maximum and particles were frequently exchanged at the surface, but there was no dominant particle renewal mechanism related to voids. Both enhancing and reducing effects of void presence on h were indicated and the cross-correlations between h and local voidage, and h and surface coverage were not significant. With increasing U, the increasing presence of voids began to reduce heat transfer.

- For gas velocities in the turbulent regime (e.g. U>0.6 m/s), h decreased due to prolonged exposure of the heat transfer surface to voids. The frequency of voids at the surface rapidly increased for U>0.6 m/s. The correlation between the instantaneous h and local voidage fluctuations was strong and negative.

Chapter 6

6. HEAT TRANSFER MODELING IN TURBULENT FLUIDIZED BEDS

6.1. Introduction

Heat transfer in fluidized beds has been investigated extensively resulting in a vast number of empirical and semi-empirical correlations. Since the heat transfer is affected by many factors, the applicability of the correlations tends to be limited to certain ranges of conditions. Although the mechanisms of heat transfer are established, models that give reliable predictions for a wide range of operating conditions and that cover the transition from one fluidization flow regime to another are not available.

In Chapter 1, a major gap in the heat transfer literature was identified, namely, turbulent fluidization has rarely been considered in heat transfer studies. Of the reviews on heat transfer, only those of Botterill (1986) and Kunii and Levenspiel (1991b) mentioned the turbulent flow regime. Aside from the work of Hashimoto et al. (1990) and Staub (1979), no correlations explicitly intended for turbulent beds were found in the literature. Because the turbulent flow regime is situated between bubbling and fast fluidization, there are correlations for bubbling beds that extend to high gas velocities, and correlations for the bottom zone of circulating fluidized beds, that may cover turbulent beds. Therefore, the first part of this chapter compares different models and correlations published in the literature for dense beds to our experimental data.

The most flexible model relating heat transfer to hydrodynamics is the packet renewal model proposed by Mickley and Fairbanks (1955). To be able to apply the packet renewal model, hydrodynamic parameters such as the fraction of time that the heat transfer surface is occupied by particle packets and the time spent at the heating surface are needed. In the second part of this chapter, the methodology for obtaining the needed parameters from the transient local voidage is presented, and a probability packet renewal model is proposed that is expected to

cover bubbling and turbulent fluidization by capturing the gradual changes and the coexistence of flow structures typical for the flow regimes considered.

6.2. Comparison of models and correlations from the literature with experimental data from this work

Some of the most significant models and correlations, reported to cover wide ranges of conditions, are compared to our experimental data to test their applicability to turbulent beds.

The correlations of Wender and Cooper (1958), Vreedenberg (1960), Martin (1980) and Molerus and Wirth (1997), presented in Appendix A, are compared to our experimental data for FCC particles (from Chapter 4) in Figure 6.1. The shaded area represents the range of experimental time-mean heat transfer coefficients, h, for FCC particles and r/R=0 to 1, H_0=0.8– 1.2 m, with both bubble cap and perforated plate distributors. The Wender and Cooper (1958) correlation over-predicts h when C_R=1. Martin's model, in which the local voidage measured by an optical probe was used, gives good agreement at low gas velocities, but over-predicts h in the turbulent regime. The best fit is the semi-empirical correlation by Molerus and Wirth (1997), which yelds results within 10% error (for a radial location at the bed axis) and predicts the right trend in the range of superficial gas velocities investigated. In the correlations of Martin (1980) and Molerus and Wirth (1997), some of the required coefficients were obtained from the experimental data of Wunder (1980), where the geometry of the heater and column size were similar to those in this work.

The predicted heat transfer coefficients for alumina particles, based on Martin's model, are plotted against local voidage in Figure 6.2. Experimental time-mean heat transfer coefficients for alumina particles for different radial positions in 0.29 and 1.56 m ID columns are also plotted. The model does not include column diameter or radial position, which in turbulent fluidization do not have significant effects, and it generally over-predicts h.
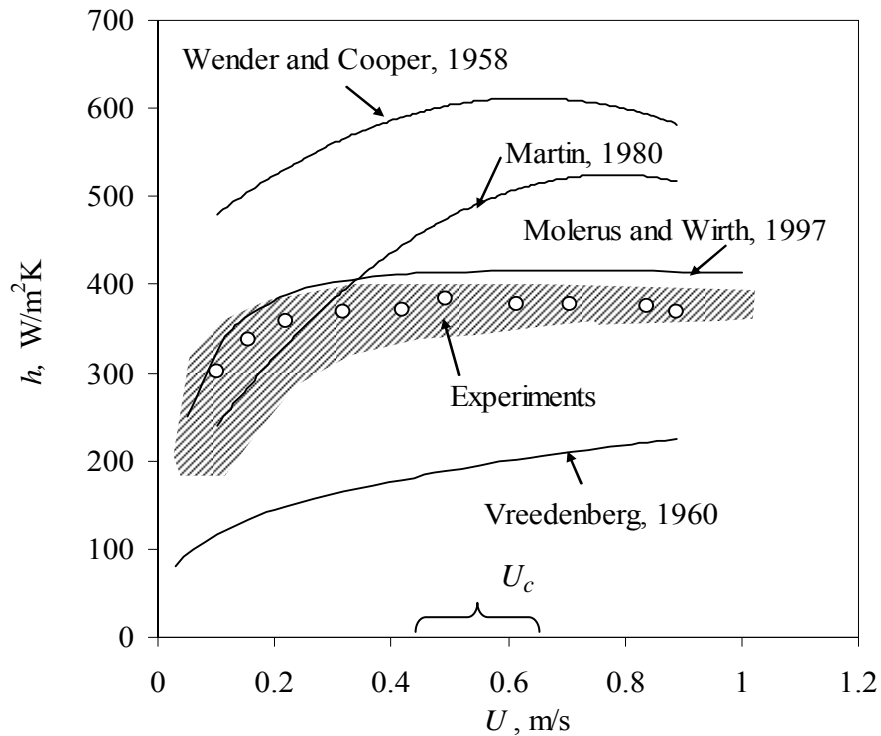
Figure 6.1. Comparison of published heat transfer correlations with experimental data. Circles represent experimental data points for FCC at *r/R*=0. Shaded area shows measured *h* at different radial positions, static bed heights, and distributors. (*D$_t$*=0.29 m, *H$_0$*=0.8-1.2 m, *r/R*=0-0.8, *z$_h$*=0.6 m).

Depending on how voidage was estimated, Martin's model might predict different trends in the *h* vs. *U* curve beyond *h$_{max}$* (Figure 6.3). When the cross-sectional average voidage is estimated from the measured differential pressure, the model follows the correct trend, but over-predicts *h* (line 1 on Figure 6.3). However, when the local voidage is based on that measured by the optical probe, the model predicts decreasing *h* with *U* increasing beyond 0.2 m/s (line 2 in Figure 6.3), due to the increase in local voidage at the bed axis. The decreasing trend is even more pronounced when the voidage is calculated from the two-phase theory (equation (A.9.) in Appendix A), as suggested by Martin, 1980 (Figure 6.3, line 3).

The semi-empirical correlation of Molerus and Wirth (1997) was compared to our alumina results for *r/R*=0 in Figure 6.3 (line 4). The comparison shows that the correlation prediction was not as good as for FCC particles and over predicted *h* by 43%.
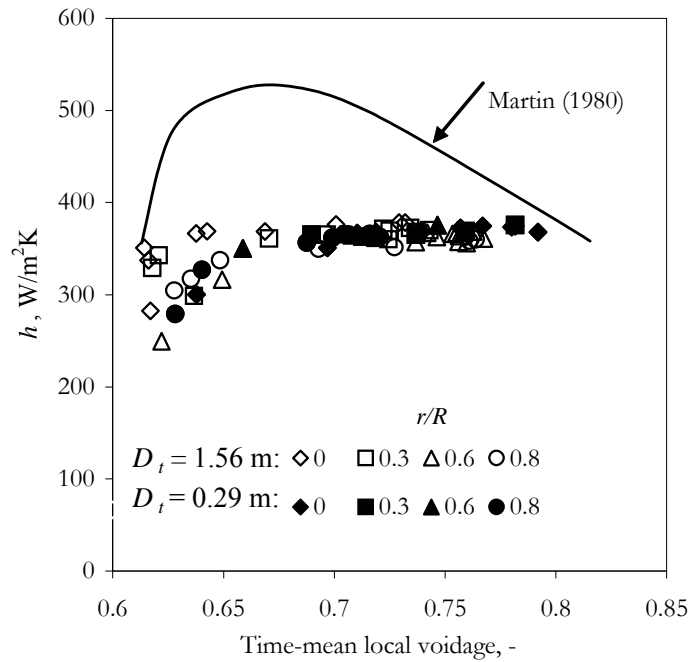
Figure 6.2. Comparison of *h* predicted by Martin's model and experimental results vs. time mean local voidage at different radial positions. (Alumina, D_t=0.29 and 1.56 m, bubble cap distributor, H_0=0.8 m, r/R=0~0.8, z_h=0.6 m)
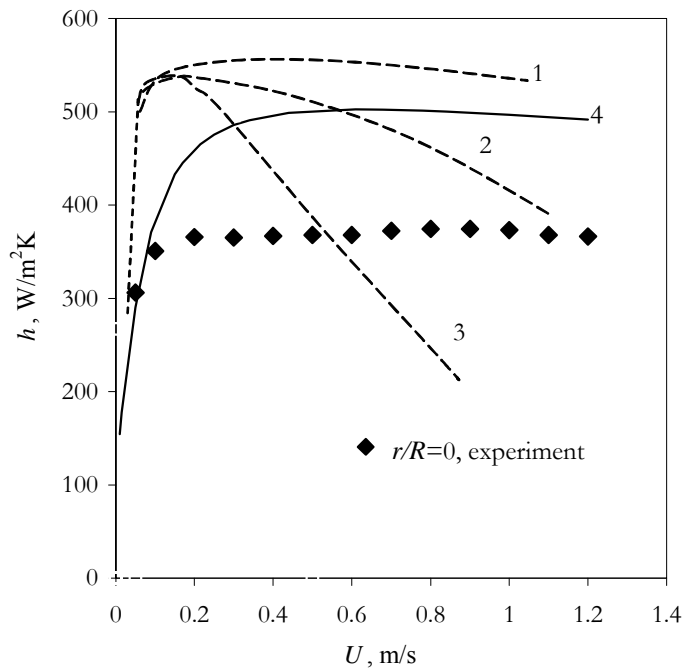
Figure 6.3. Martin (1980) model predictions based on: 1- cross-sectional mean voidage, 2- local voidage measured by optical probe, 3- voidage calculated from two-phase theory and Molerus and Wirth (1997) model predictions (line 4) vs. *U*. (Alumina, D_t=0.29 m, bubble cap distributor, H_0=0.8 m, r/R=0, z_h=0.6 m)

6.3. Hydrodynamic parameters for packet renewal model

The most flexible model regarding the adaptability to the specific hydrodynamics is the packet renewal model first proposed by Mickley and Fairbanks (1955) (presented in Chapter 1). In order to apply the packet renewal model, hydrodynamic parameters such as the time fraction that the heat transfer surface is occupied by particle packets, their frequency and the time they spend at the heating surface are needed.

The fraction of time during which the heat transfer surface is occupied by bubbles (voids), δ_v, has been measured by different methods in the literature (Baskakov et al., 1973; Ozkaynak and Chen, 1980, Chandran and Chen, 1982), but a general correlation applicable to a wide range of conditions is not available (Chen et al., 2005). Most reported data were obtained at low superficial gas velocities. The term void fraction or void phase fraction, δ_v, in this work is defined as the fraction of time during which the heating surface is occupied by bubbles/voids during the total sampling sequence. The bed is usually considered to be composed of only two phases (dense and void phases) so that $\delta_d + \delta_v = 1$. For the heat transfer process, the fraction of time the dense phase is present at the surface, δ_d, is important. The term dense phase fraction is also used here for δ_d.

Baskakov et al. 1973 studied void fraction and particle contact time based on temperature fluctuations measured by a thermofoil at the surface of small immersed vertical tubes (d_t=15 and 30 mm) at the bed axis in columns of diameter 92 and 98 mm. Their data were correlated in terms of a modified particle Froude number (quantity in square brackets):

$$\delta_v = 0.33 \left[\frac{U_{mf}^2 \left(U/U_{mf} - A\right)^2}{d_p g} \right]^{0.14} \tag{6.1}$$

$$t_{pc} = 0.44 \left[\frac{d_p g}{U_{mf}^2 \left(U/U_{mf} - A\right)^2} \right]^{0.14} \left(\frac{d_p}{d_t} \right)^{0.225} \tag{6.2}$$

where the empirical coefficient A was found to depend on tube size.

The coefficients in the correlation were modified for horizontal tubes by Kim et al. (2002), giving a lower void fraction and increased average particle contact times.

Cui et al. (2000) proposed correlations for the void fraction of FCC and sand particles for both bubbling and turbulent fluidization. Data were obtained from optical probes, using the probability distribution of the signal to distinguish between the void and dense phases, yielding:

$$\delta_v=0.466+0.534\exp[-(U-U_{mf})/0.413] \quad \text{(Sand)} \tag{6.3a}$$

$$\delta_v=1-\exp[-(U-U_{mf})/0.62 \quad \text{(FCC)} \tag{6.3b}$$

These two equations predict lower void fractions than equation (6.1). Note that the void fraction can be sensitive to the method applied (Bi and Su, 2001).

The frequency at which particle packets exchange at the heating surface is another important parameter in fluidized bed heat transfer. Because bubbles are the dominant sources of stirring in bubbling beds, it is assumed that the packet renewal frequency is similar to the bubble frequency. In bubbling beds, the latter can be determined from the dominant frequency in the pressure fluctuations (Sharma and Turton, 1998) or crossing frequency of the optical probe signal (Ellis, 2003). It is challenging to determine the dominant packet renewal frequency beyond bubbling as the fluctuations in the bed become more random.

Di Natale et al. (2008) correlated particle renewal frequency (assuming, as a first approximation, that it is the same as the void frequency) based on experimental data in the literature and obtained:

$$f_v=k\,Re_p^{0.287}\,d_p^{-1}, k=2.045\cdot10^{-4}\,\text{m/s} \tag{6.4}$$

This empirical correlation was based on data for $U \leq 0.5$ m/s, i.e. mainly in bubbling beds. Its applicability to turbulent beds was not tested.

Particle contact time has received considerable research and continues to be a subject of study (e.g. Wang and Rhodes, 2003; Hamidipour et al., 2005a and 2005b; Zarghami et al., 2007). Empirical correlations in the literature were suggested with monotonic dependence on the superficial gas velocity, U, often without paying attention to flow regime change.

Whereas, in the core region of the bed, the particle contact time can be estimated from the ratio of the fraction of time during which particle packets are present and the frequency at which the packets arrive at the surface, at the wall, coefficients were applied to compensate for the wall effect. Lu et al. (1993) proposed that the particle contact time at the wall be calculated from the

local bubble frequency (equation 6.5). The coefficient of 2/3 was introduced by fitting the experimental data, leading to:

$$t_{pc_{wall}} = \frac{2}{3} \frac{(1 - \delta_b)}{\dfrac{\delta_b V_b}{D_b}}$$

(6.5)

Zarghami et al. (2007) assumed that the particle contact time at the wall can be attributed to two modes of transport of particles: particles associated with voids and those associated with dense phase clusters leading to:.

$$t_{pc\,wall} = t_{cb} + t_{ce} = a \frac{\delta_e}{f_b} + b \frac{\delta_b}{f_{cl}} = a \frac{\delta_e}{\dfrac{\delta_b V_b}{D_b}} + b \frac{\delta_b}{\dfrac{\delta_{cl} V_{cl}}{D_{cl}}}$$

(6.6)

where t_{cb} is the contact time of particles associated with bubbles, calculated from the dense phase fraction in the bed and the frequency of bubbles, and t_{ce} is the contact time of clusters in the dense phase, calculated from the void fraction and frequency of dense phase clusters. The coefficients a and b represent the probabilities of bubbles or clusters being present near the wall relative to their probabilities in the core. These probability coefficients were determined experimentally from the radial profiles obtained by radioactive particle tracking, giving a=0.7 and b=6.52. The contact time of particles associated with bubbles was calculated in the same manner as by Lu et al. (1993), and the probability coefficient was close to the coefficient obtained the latter authors. Zarghami et al. (2007) suggested empirical correlations for the parameters needed in their model (bubble diameter, D_b, bubble velocity, V_b, cluster diameter, D_c, cluster velocity, V_c), based on U, U_{mf}, ε_{mf} and $H(z)$. Their model predicts an increase in particle contact time at the wall in the turbulent regime for sand particles.

6.3.1. Effect of threshold voidage on determination of hydrodynamic parameters in the packet renewal model

Many researchers (Ozkaynak and Chen, 1980; Chandran and Chen, 1982; Wu et al., 1989; McKain, 1994; Kim et al., 2002) have observed the fluctuations in instantaneous local particle concentrations (or voidage) near the heat transfer surface, confirming the packet renewal mechanism. Pressure, capacitance and optical probes have been used to determine the voidage

fluctuations. The challenge remains to identify the particle packets and their properties from local voidage fluctuations, especially in distinguishing between the dense and void phases.

In the packet renewal model for dense (bubbling) beds, the bed is divided into two phases: a dense phase with voidage close to ε_{mf} (emulsion) and a void phase (bubbles). The packets are assumed to have a density close to that of the bed under minimum fluidization conditions. To establish the presence of these dense packets at the heat transfer surface, a threshold local voidage close to ε_{mf} would be appropriate. Care should be taken not to include variations within the dense phase itself. Because the distribution of the local voidage around the peak near ε_{mf} (Figure 6.4) can be assumed to be Gaussian (Lin et al., 2001), a safe threshold would be the 95% confidence interval:

$$\varepsilon_{(1)} = \varepsilon_{mf} + \mathrm{SE}_{\varepsilon_{mf}} = \varepsilon_{mf} + 1.96\,\mathrm{SD}_{\varepsilon_{mf}} \tag{6.7}$$

where, $\mathrm{SE}_{\varepsilon_{mf}}$ = standard error and $\mathrm{SD}_{\varepsilon_{mf}}$ = standard deviation.

The voidage, $\varepsilon_{(1)}$ can be selected as a threshold to establish the presence and frequency of dense packets. The fraction of time during which the local voidage is less than $\varepsilon_{(1)}$, gives the time fraction of dense packets, δ_d (Figure 6.5a). The void (bubble) fraction would then be $\delta_v = 1 - \delta_d$.

In circulating fluidized beds (CFBs), the particle packets contributing to higher heat transfer rates are usually called clusters or streamers, representing congregated particles suspended in the gas descending along the wall of the riser. Clusters in the upper region of the CFB are assumed to travel upward in the core and downward near the wall. The time-mean voidage of the clusters/streamers depends on the mean suspension density (Lints and Glicksman, 1993). Kim et al. (2000) studied clusters in the freeboard using FCC particles and set the threshold at $(\varepsilon_{\min} + \varepsilon_{\max})/2$ to establish the frequency and time fraction during which a probe surface was exposed to clusters. Sharma et al. (2000) used a threshold of $\varepsilon_{CS} + 2\mathrm{SD}_{\varepsilon_{CS}}$, where ε_{CS} is the time-mean cross-sectional voidage, determined from the pressure drop across the column cross-section. Schweitzer et al. (2001) assumed the peak in the dense phase is symmetrical and set the threshold at $2\varepsilon_{peak} - \varepsilon_{mf}$.

In turbulent fluidized beds, the distinction between the dense and dilute phases is ambiguous. Gradual disappearance of the dense phase and increased concentration of particles in the void

phase has been reported in the turbulent fluidization regime (Bi and Su, 2001; Cui et al., 2000). The distribution of local voidage (Figure 6.4) shows a decrease in the intensity of peak close to ε_{mf} in the turbulent bed, gradually becoming closer to the intensity of the second peak at higher voidages, particularly with FCC particles. Although the peak at ε_{mf} is lower in intensity than in the bubbling regime, a peak exists, even at the highest velocity investigated, well into the turbulent regime. Lin et al. (2001) observed the peak to be close to ε_{mf} until the transport velocity was reached. The transient local voidage in the turbulent fluidized bed indicates that for times when the probe is not exposed to the dense phase (Figure 6.5), there are intense variations in the intermediate range of local voidage, with peaks appearing from the void phase, similar to clusters in fast fluidized beds. Because the flow structure changes gradually with increasing superficial gas velocity and both bubbling and turbulent flow structures can be present, different voidage thresholds may be needed to capture the hydrodynamics of different hydrodynamic regimes. Bi and Su (2001) used the midpoint in the local voidage distribution, $0.5(\varepsilon_{min}+\varepsilon_{max})$. The effect of alternative threshold voidages was reviewed by Bi and Su (2001) and Ellis (2003).
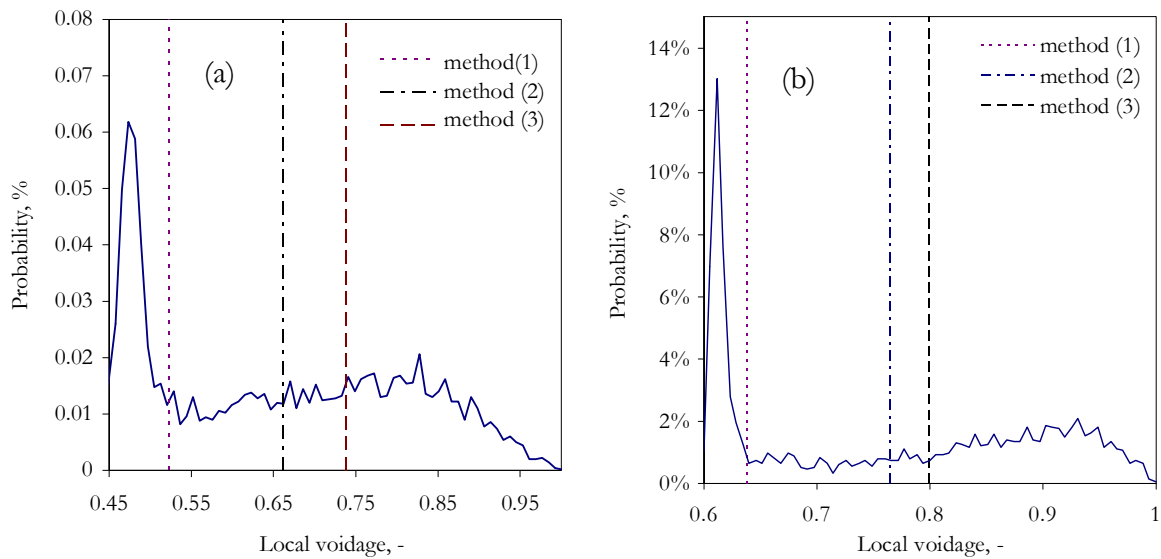
Figure 6.4. Distribution of local voidage for $U/U_c = 1.6$ at $r/R=0$ for: a) FCC b) alumina. Threshold voidages from different methods are indicated.

Here, three thresholds are compared:

(1) a local voidage just above that for minimum fluidization conditions: $\varepsilon_{mf} + 2SD_{\varepsilon mf}$;

(2) the time mean voidage, ε_{mean}; and

(3) the midpoint between the maximum and minimum measured voidages, $0.5(\varepsilon_{min} + \varepsilon_{max})$.

The corresponding threshold voidages for $U/U_c = 1.6$ with the probe at the bed axis for FCC and alumina particles are marked on the probability distribution plot of local voidage (Figure 6.4) and on time traces of local voidage for FCC particles in Figure 6.5.
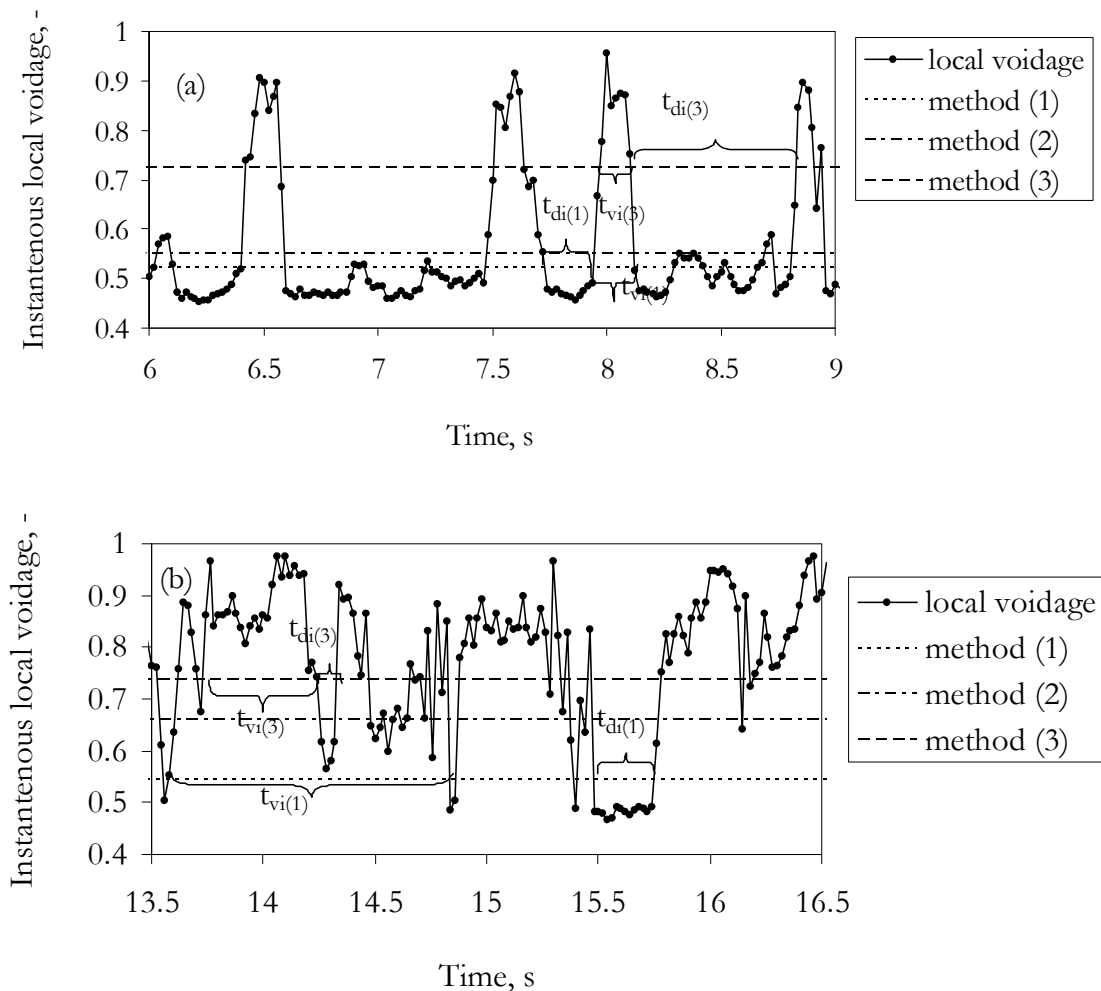
Figure 6.5. Instantaneous local voidage and effect of different thresholds on instantaneous dense phase, t_{di} and void phase t_{vi} contact times. a) $U=0.1$ m/s, b) $U=0.72$ m/s (FCC, $r/R=0$, perforated plate, $H_0=0.8$ m).

Based on these three thresholds, the time fraction of dense phase, crossing frequency and contact time were obtained. The time fraction that the surface is occupied by the dense phase was calculated as follows.

The frequency of the particle packets (caused by the passing bubbles in a bubbling bed) was assumed to be close to the crossing frequency of the local voidage at the selected threshold, obtained as:

$$f_c = \frac{\text{number of crossings}/2}{t_{tot}} \tag{6.8}$$

The average contact time of the dense packet is then estimated to be:

$$t_d = \frac{1-\delta_v}{f_c} = \frac{\delta_d}{f_c} \tag{6.9}$$

Dense/void phase fractions, crossing frequency and contact time were estimated by all three methods, with indices (1), (2) and (3) being used to distinguish between the methods. The results for the void fraction of FCC and alumina particles at $r/R=0$ obtained by the three methods are presented in Figure 6.6. Correlations by Cui et al. (2000) (equation (6.3b)) and Baskakov et al. (1973) (6.1) are also plotted.
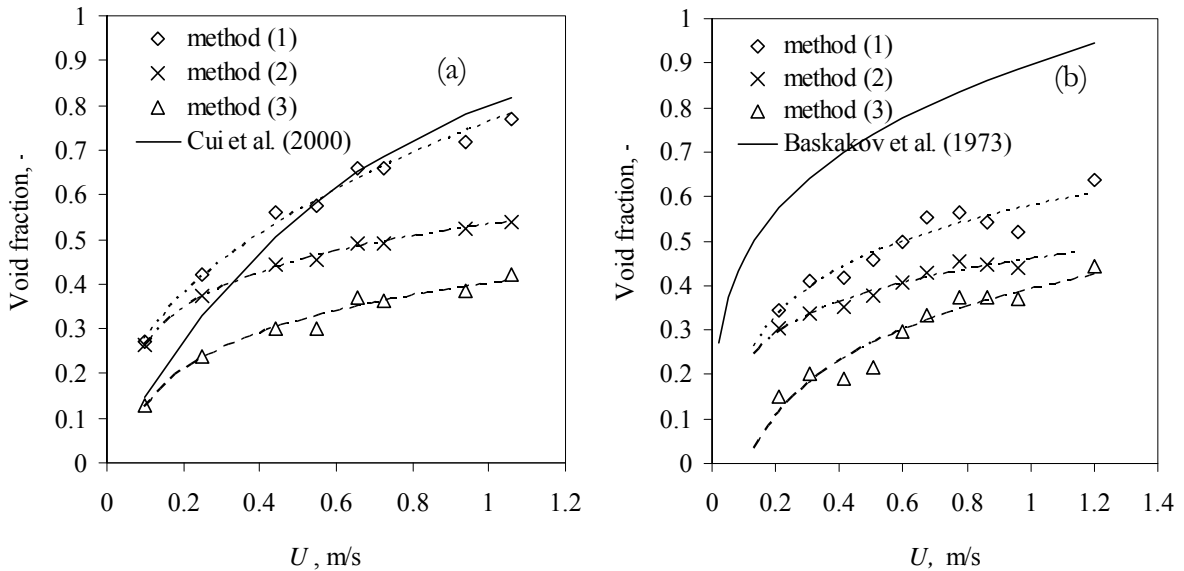
Figure 6.6. Effect of threshold on void fraction: a) FCC, b) alumina. (H_0=0.8m, r/R=0, z_{OP}=0.47 m)

As expected, the threshold close to the voidage at minimum fluidization (method 1) gave the highest void fraction and method (3) the lowest. Baskakov's correlation over-predicted the void fraction. This was also reported by Kim et al. (2002), who compared their own data with data from other authors. The correlation by Cui et al. (2000) gave good predictions of the void fraction for FCC particles obtained by method (1). It should be noted that the superficial gas velocity at which the dense phase and void fractions at the bed axis obtained by method (1) are balanced (i.e. each phase covers the probe half of the time $(1-\delta_d)=0.5$), corresponds to the onset of turbulent fluidization for both FCC and alumina particles. Beyond this condition, the dense phase loses dominance and the turbulent flow structure becomes increasingly prominent. Lin et al. (2001) suggested that the void fraction be used to determine the probability of the void phase. In a turbulent bed, the dense phase gradually gives way to the void phase with increasing U. However, the void phase contains a significant volumetric fraction of particles in turbulent beds which should not be neglected.
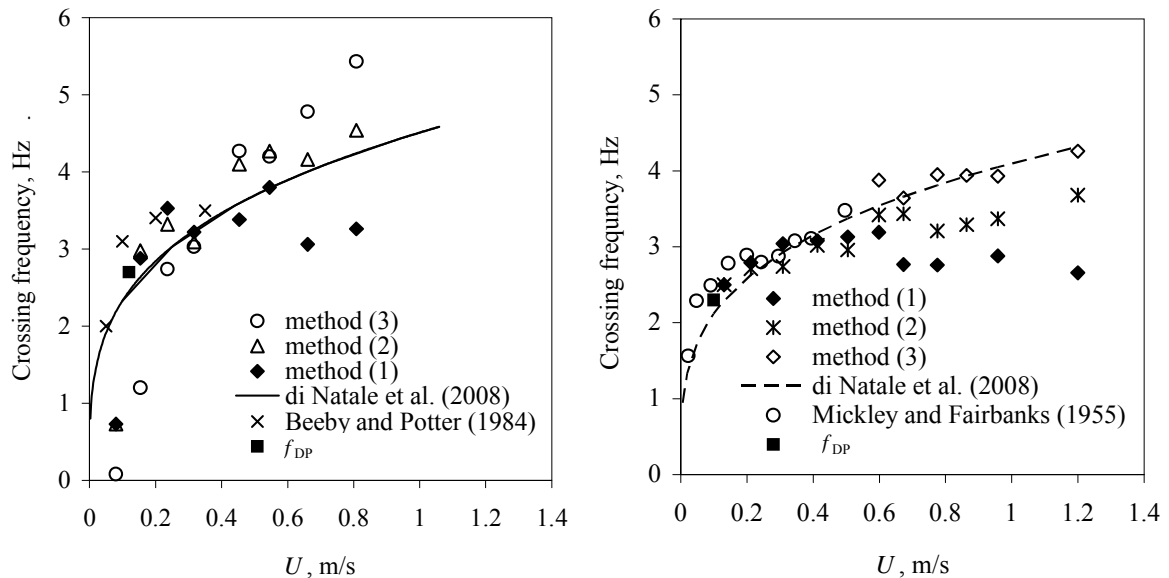
Figure 6.7. Effect of threshold voidage on crossing frequency for:
a) FCC, b) alumina. (r/R=0, z_{OP}=0.47 m, bubble cap distributor).

When the three tested threshold methods were applied to the crossing frequency, the discrepancy was more evident in the turbulent regime than in the bubbling regime (Figure 6.7). As the dense phase becomes less present in the turbulent region $(1-\delta_d>0.5)$, the threshold method starts to play a significant role. The crossing frequency obtained from method (1)

increases with U in the bubbling regime but levels off (or slightly decreases) in the turbulent bed, as the time interval between packets with voidage close to ε_{mf} becomes longer (t_{di} on Figure 6.5b). However, in the turbulent regime, variations in the intermediate range of voidages appear, which method (1) fails to capture. The thresholds at higher voidages, (methods (2) and (3)), show a continuous increase of crossing frequency with U in the turbulent regime, steeper for method (3). This might be due to streams of particles at high gas velocities causing the signal to cross more frequently at intermediate voidages. Ellis (2003) also noted that the crossing frequency of the local voidage signal in turbulent beds depends on the threshold selected.

The Di Natale et al. (2008) correlation for void frequency shows good agreement with our experimental data in the bubbling regime. In addition, the crossing frequency obtained from the local voidage signal at low gas velocities is similar to the dominant frequency in the power spectrum of the differential pressure signal, f_{DP} (square symbols on Figure 6.7). For the turbulent bed, the Di Natale et al. (2008) correlation is close to the crossing frequency from method (2) for FCC particles and method (3) for alumina particles. The experimental data of Beeby and Potter (1984) for 57 μm FCC particles and Mickley and Fairbanks (1955) for 70 μm glass beads in bubbling beds are also plotted in Figure 6.7. Their measurements are close to our data.

For the average contact time, method (3) gave higher values in a bubbling bed, whereas in a turbulent bed the method selected had little effect. At low gas velocities the crossing frequency is similar for all three methods, but the dense phase fraction is lower for method (1), resulting in a shorter contact time. In the turbulent regime, the dense phase fraction from method (1) is lower than from method (3). However, the crossing frequency is also lower from method (1) than from method (3), and therefore the particle contact time is similar.

The mean voidage of each phase (dilute/dense) and its standard deviation, from the three methods, were also estimated. The results for bubbling (U=0.1 m/s) and turbulent (U=1.1 m/s) beds are summarized in Table 6.1.

Table 6.1. Effect of threshold on average dense/dilute phase voidage for FCC particles at bed axis.

	Threshold	Voidage of dense phase	Voidage of dilute phase
method (1)			
U=0.1 m/s	0.54	0.48±0.02	0.72±0.12
U=1.1 m/s	0.55	0.50±0.03	0.76±0.10
method(2)			
U=0.1 m/s	0.55	0.49±0.02	0.73±0.12
U=1.1 m/s	0.69	0.56±0.08	0.80±0.07
method (3)			
U=0.1 m/s	0.73	0.48±0.06	0.83±0.07
U=1.1 m/s	0.74	0.59±0.09	0.83±0.06

The average voidage remains close to ε_{mf} with threshold method (1), and its variation is small. Method (1) is appropriate for bubbling beds where the dense phase is dominant, capturing the bubble frequency and the fraction of time the probe is exposed to the dense phase. When methods (2) and (3) were applied, the average voidage and the standard deviation of the dense phase increased with *U* as the dense phase was less present. Thus, dense phase "expansion" was predicted. However, ε_{mf} still occurs, but less often and for shorter intervals than in bubbling.

Method (3) seems to be more appropriate for local voidage fluctuations in turbulent beds, as it captures the low-voidage peaks from the void phase (marked on Figure 6.5b). The intermediate voidage peaks might be due to clusters suspended in the void phase. Here it will be called the "intermediate phase". The average voidage and standard deviation, calculated from data between the thresholds ($\varepsilon_{(1)} < \varepsilon_{int} \leq \varepsilon_{(3)}$), changed only slightly with increasing *U* ($\varepsilon_{int} \approx 0.62 \pm 0.06$ for FCC). This threshold division, i.e. heat transfer by dense packets with ε_{mf}, packet of intermediate voidages, (ε_{int}), and dilute suspension/gas ($\varepsilon_v = \varepsilon_{(3)}$) in turbulent beds is considered here. Method (1) provides the properties of dense phase packets, dominant in bubbling, whereas method (3) establishes the probability and frequency of clusters of intermediate voidage in the turbulent bed.

6.4. Probability packet renewal model for bubbling and turbulent beds

The heat transfer coefficient changes gradually with increasing *U,* as the bed goes through a transition from one flow regime to another, with no abrupt change in the hydrodynamics. This gradual transition in hydrodynamics was also reported by others (e.g. Hamidipour et al., 2005b; Ellis, 2003; Abba et al., 2003). To allow for the gradual transition and co-existence of flow structures typical for bubbling and turbulent beds, a probability model based on the packet renewal heat transfer theory is proposed.

It is assumed that there are two types of particle packets: (1) dense phase clusters with voidage close to ε_{mf}, and (2) clusters of intermediate voidage $\varepsilon_{int} = 0.5(\varepsilon_{min} + \varepsilon_{max})$, in the void phase. In bubbling beds, the dense phase dominates and the particles are stirred by rising bubbles. The renewal rate of particles at the heat transfer surface depends on the bubble frequency. As the dense phase presence gradually lessens and turbulent structures become increasingly present, there is an additional contribution to the conductive heat transfer from clusters of intermediate voidage. The probability of the latter clusters is estimated based on the time fraction of each phase at the surface.

The probability of a dense packet of voidage ε_{mf} at the surface was assumed to be equal to the dense phase fraction estimated by method (1):

$$\delta_d = 1 - \delta_{v(1)} \qquad (6.10)$$

The dilute phase is further divided into an intermediate phase and a void phase based on method (3) to obtain the intermediate phase fraction:

$$\delta_{int} = 1 - \delta_{v(3)} \qquad (6.11)$$

The probability of the packet of intermediate phase, with voidage $\varepsilon_{int} = 0.5(\varepsilon_{min} + \varepsilon_{max})$, at the probe surface in the total sampling sequence is then $(1 - \delta_d)\delta_{int}$.

The sum of the probabilities of the three "phases" is equal to 1. Hence:

$$\delta_d + (1 - \delta_d)\delta_{int} + (1 - \delta_d)\delta_v = 1 \qquad (6.12)$$

where $\delta_v = 1 - \delta_{int}$ is the void phase fraction.

The heat transfer coefficient is then:

$$h = \delta_d h_d + (1 - \delta_d)\delta_{int}h_{int} + (1 - \delta_d)\delta_v h_v,$$ (6.13)

where δ_d, δ_{int} and δ_v are the time fractions of the dense, intermediate and void phases and h_d, h_{int} and h_v are the average heat transfer coefficients for each phase, respectively. If we neglect the void phase contribution, as gas convection is relatively small compared to the other two components, then:

$$h = 1.13\left[\delta_d\sqrt{\frac{k_{effd}\rho_p(1-\varepsilon_{mf})c_{pp}}{t_d}} + (1-\delta_d)\delta_{int}\sqrt{\frac{k_{eff\,int}\rho_p(1-\varepsilon_{int})c_{pp}}{t_{int}}}\right]$$ (6.14)

For the time fraction the surface is exposed to dense phase packets δ_d, the average contact time of the dense phase is given by:

$$t_d = \frac{\text{dense phase fraction}}{\text{dense phase frequency}} = \frac{\delta_d}{f_d} = \frac{1 - \delta_{(1)}}{f_{(1)}}$$ (6.15)

where $f_{(1)}$ is the frequency obtained by method (1).

For the average contact time of the packets from the intermediate phase, threshold voidages were obtained from method (1) and (3). The crossing frequencies, $f_{(1)}$ and $f_{(3)}$, are similar for low gas velocities, and both indicate renewal by bubbles. As turbulent flow structures increase in importance with increasing U, the frequencies from the two methods diverge (Figure 6.7). While $f_{(1)}$ continues to detect packets from the dense phase (less frequent with increasing U), $f_{(3)}$ detects both dense phase packets and packets of intermediate voidage suspended in the large voids, and continues to increase. As we are interested in estimating the contribution of particle packets with voidages higher than ε_{mf}, suspended in the void phase, frequency $f_{(1)}$, the frequency of dense packets, is subtracted from $f_{(3)}$, the frequency of both dense and intermediate packets. The average time the packets of intermediate voidage are present at the probe can then be estimated by:

$$t_{int} = \frac{\text{intermediate phase fraction}}{\text{frequency of intermediate phase}} = \frac{(1-\delta_d)\delta_{int}}{f_{(3)} - f_{(1)}}$$ (6.16)

6.4.1. Experimental results and correlations for the hydrodynamic parameters in the probability packet renewal model

6.4.1.1. Effect of radial position, particle properties and distributor on dense phase fraction

The dense phase fractions for alumina particles and method (1) (described in section 6.3.1), at three radial positions, $r/R=0$, 0.8 and 1, in the column of 0.29 m diameter, and one radial position, $r/R=0.6$, in the 1.56 m diameter column are plotted on Figure 6.8. The fraction of time the probe was occupied by the dense phase was, as expected, higher in the wall region and lower in the core. The column diameter did not significantly affect the dense phase fraction at radial locations with similar flow structure ($r/R=0$ for $D_t=0.29$ m, and $r/R=0.6$ for $D_t=1.56$ m) (see Chapter 3).
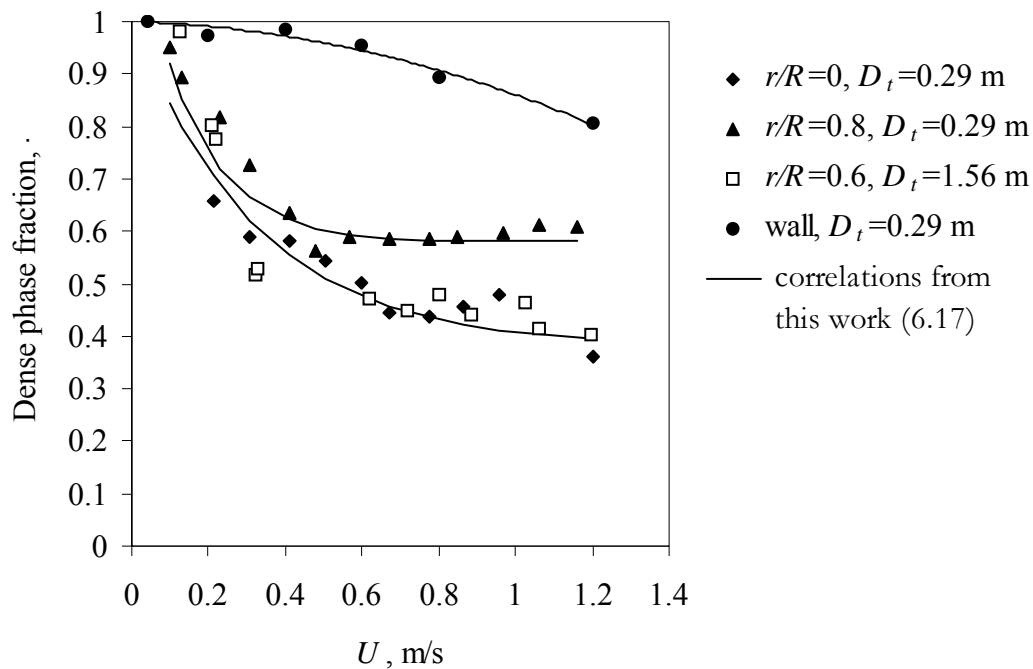
Figure 6.8. Fraction of time during which the surface is covered by dense phase at different radial locations and column diameters. (Alumina, $D_t=0.29$ m, $H_0=0.8$ m, bubble cap distributor, $z_{OP}=0.47$ m)

Exponential curves were fitted for each operating condition using the relationship proposed by Cui et al. (2000);

$$\delta_d = 1 - a + b \exp\left(-\frac{U - U_{mf}}{c}\right) \tag{6.17}$$

with coefficients a, b and c given in Table 6.2. These correlations were used for the calculation of *h*.

Table 6.2. Constants in equation (6.17).

D_t, m	Particles	r/R	a	b	c, m/s
0.29	Alumina	0	0.62	0.62	0.32
0.29	Alumina	0.8	0.42	0.62	0.15
1.56	Alumina	0.6	0.62	0.62	0.32
0.29	FCC*	0	1	1	0.62

*Coefficients for FCC particles from Cui et al. (2000).

Figure 6.9 presents the effect of particle properties and gas distributor at *r/R*=0 in the 0.29 m column. The effect of the distributor on the dense phase fraction in the core region of the bed of FCC particles was insignificant. However, the dense phase fraction decreases less rapidly for the alumina particles than for the FCC particles indicating more gradual disappearance of the dense phase. Results from Chandran and Chen (1980) for 256 μm sand are also plotted on Figure 6.9. Values of the dense phase fraction at low gas velocities are similar to our results.
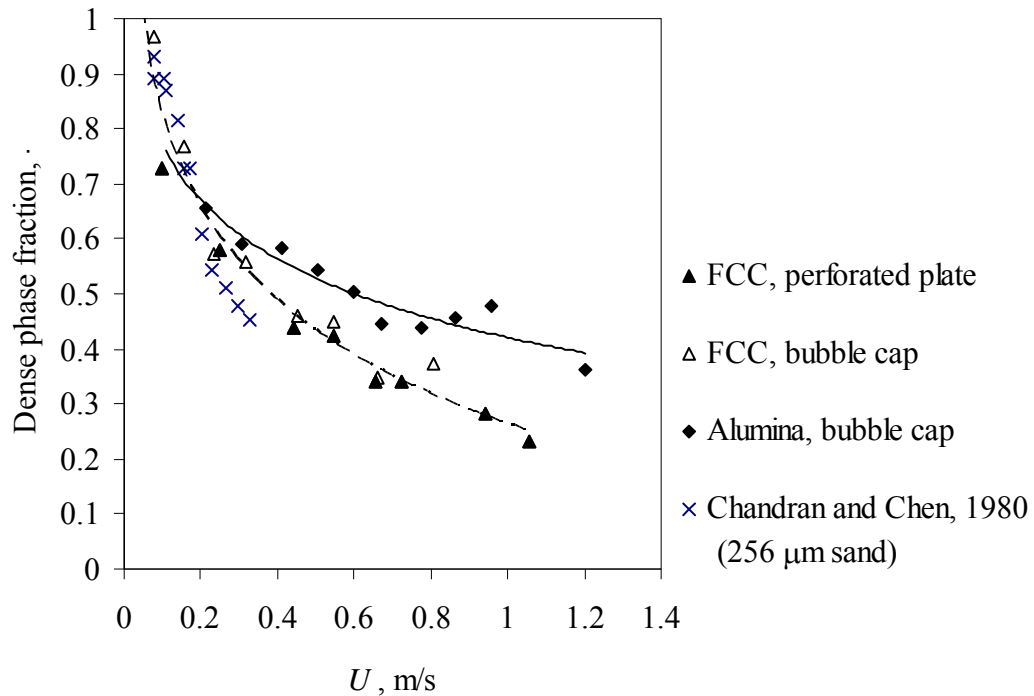
**Figure 6.9. Effect of particle properties and distributor type on
dense phase fraction z_{OP}=0.47 m, r/R=0.**

The probability of all three phases (dense, intermediate and void), based on the time fraction spent by each phase at the surface, is shown in Figure 6.10 for four experimental conditions. The curves for the intermediate phase were obtained by least squares polynomial curve fitting of the experimental data. The more gradual decrease of the dense phase fraction for alumina (Figure 6.10a) than for FCC (Figure 6.10c) at the axis supports the observations of a more gradual transition to turbulent fluidization for group B particles., which are most likely to exhibit slugging in laboratory-scale units (Brereton and Grace, 1992). Moreover, the intermediate phase increases in importance more rapidly for FCC than for alumina particles, indicating an increased turbulent flow structure in the FCC. Near the wall (Figure 6.10d), the dense phase fraction remains the same over a wide range of velocities in the turbulent regime.
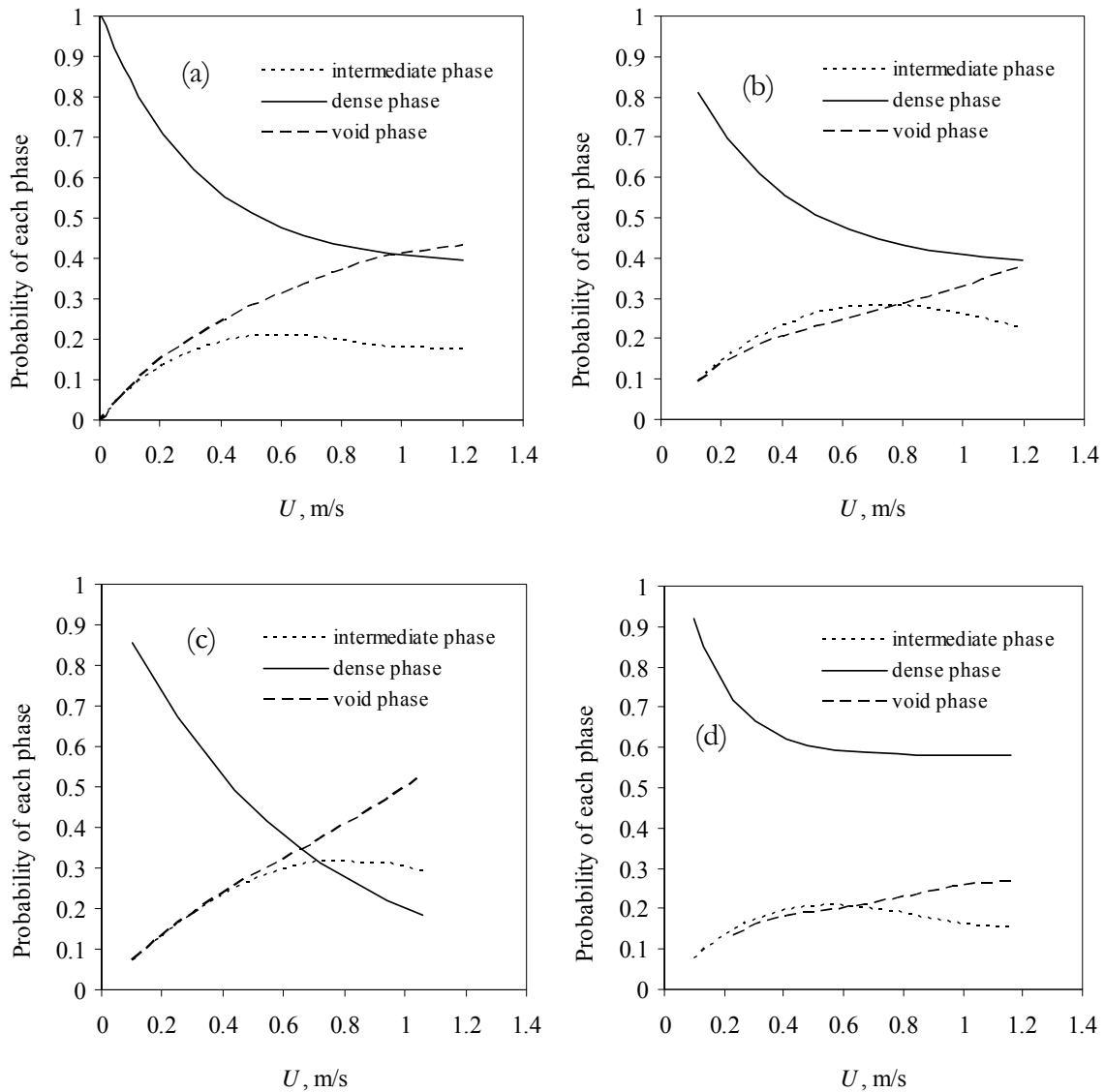
Figure 6.10. Probability of dense, intermediate and void phases at the probe surface for: a) alumina, *r/R*=0; *D$_t$*=0.29 m; b) alumina, *r/R*=0.6, *D$_t$*=1.56 m; c) FCC, *r/R*=0, *D$_t$*=0.29 m; d) alumina, *r/R*=0.8, *D$_t$*=0.29 m.

6.4.1.2. Packet contact time

The average time particles in the dense phase spend at the surface was estimated from the fraction of time the surface is occupied by the particle packet and the crossing frequency given by equation (6.15). The results for alumina particles at *r/R*=0 in the 0.29 m column and *r/R*=0.6 in the 1.56 m column are shown in Figure 6.11. The average contact time of particles from the dense phase decreases steeply at low gas velocities and then levels off. This steep decrease results

from the decrease in dense phase fraction and increase in crossing frequency as more bubbles rise. As the turbulent fluidization regime was approached, the dense phase fraction decreased, the dense packets became less frequent and the average particle contact time remained almost constant. Data from Ozkaynak and Chen (1980) for 256 μm sand particles are also plotted on Figure 6.11.
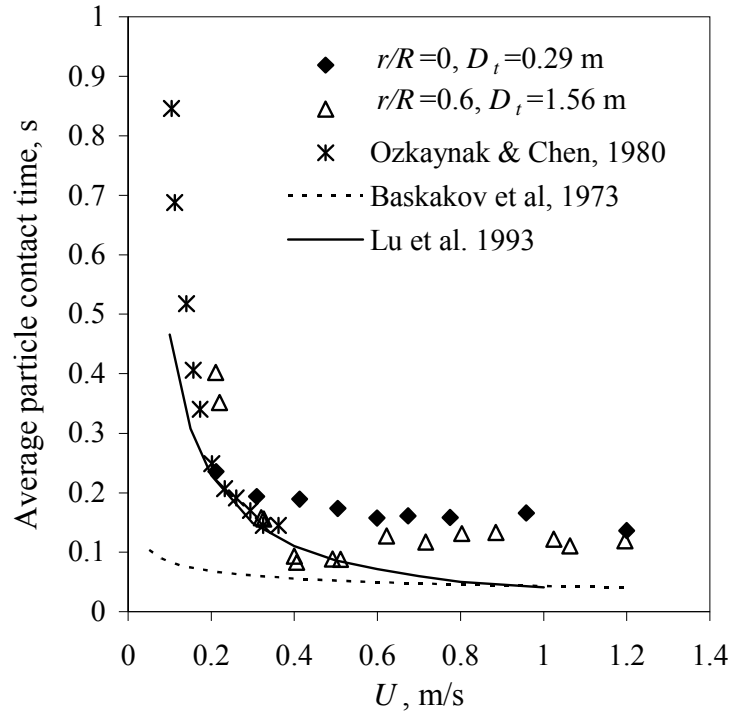
Figure 6.11. Average packet contact time vs. superficial gas velocity, *U*, for alumina particles in columns of different diameter in the region of high voidage.

The crossing frequency of the local voidage signal obtained by method (1) for alumina particles at four radial positions (r/R=0, 0.8, 0.9 and 1), is plotted against superficial gas velocity in Figure 6.12. The trend is similar for all four radial positions, increasing with increasing U in the bubbling bed and slightly decreasing in the turbulent bed. The latter trend was observed by Ellis (2003) who attributed the decrease in the crossing frequency to large voids passing up the core region of the bed at higher U. At the wall, the onset of turbulent fluidization and intense mixing caused more frequent voids and thus increased the crossing frequency. The difference between the frequencies from methods (1) and (3) is also plotted (dotted line). Note that the resulting difference is close to the crossing frequency at the wall.
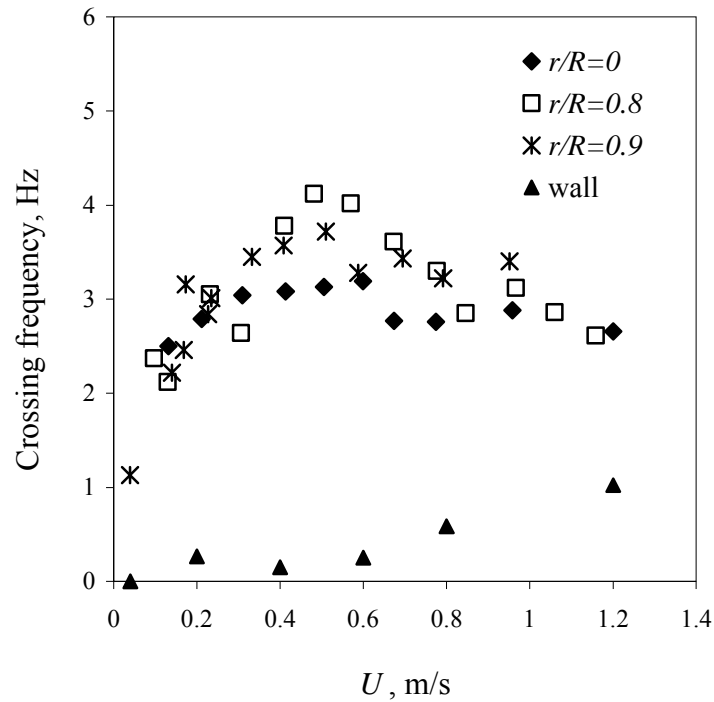
Figure 6.12. Effect of radial position and superficial gas velocity on crossing frequency. (Alumina, D_t=0.29m, H_0=0.8 m, bubble cap distributor)

Figure 6.13 shows that for FCC particles at r/R=0, the average contact time of particles from the dense phase decreased gradually in the range of velocities investigated. In the turbulent bed, the particle contact time was close to the contact time at the wall measured by Hamidipour et al. (2005a) using radioactive 420 and 500 μm tracer particles in a bed of FCC particles. The agreement with our data is favourable.
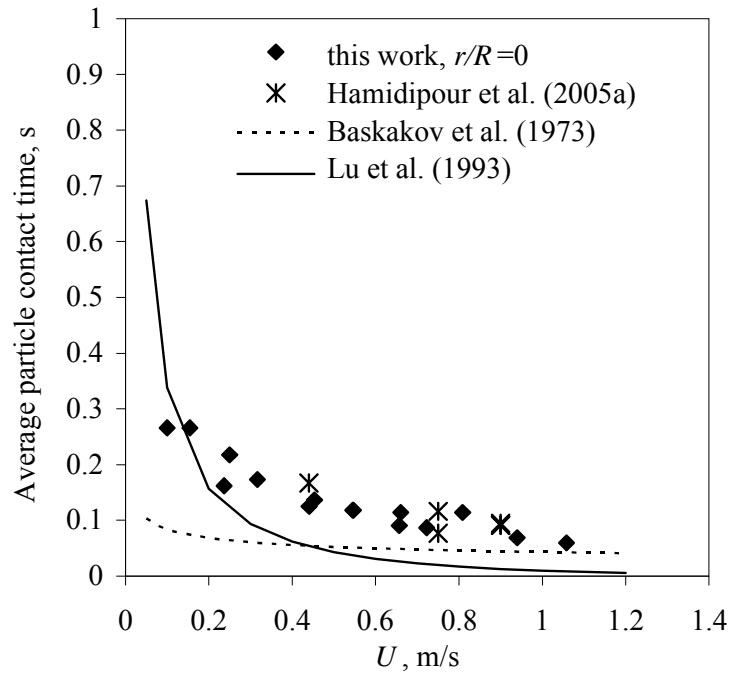
Figure 6.13. Average particle contact time vs. *U* for FCC at *r/R*=0.

For alumina particles near the wall region (*r/R*=0.8) of the 0.29 m column, the average contact time began to increase in the turbulent bed (Figure 6.14) as a result of the slightly decreasing frequency of dense packets while the fraction of dense packets remained unchanged with increasing *U*. An increase in particle contact time was measured at the wall in the turbulent regime for sand particles by Hamidipour et al. (2005a) and modeled by Zarghami et al. (2007). They observed a minimum particle contact time at the onset of turbulent fluidization and explained it in terms of a change in the flow structure, whereby, in bubbling beds, increasing *U* increases the bubble velocity, causing particles to move faster at the wall, in turn reducing the particle contact time. In turbulent beds, void velocity no longer increases with increasing *U*, and in addition, the extra gas passes mostly through the core while particles spend more time near the wall. Increasing particle contact time, after a very shallow minimum extending over a range of *U*, was also found by Goossens (1986) who estimated the particle contact time from a boundary layer penetration model.
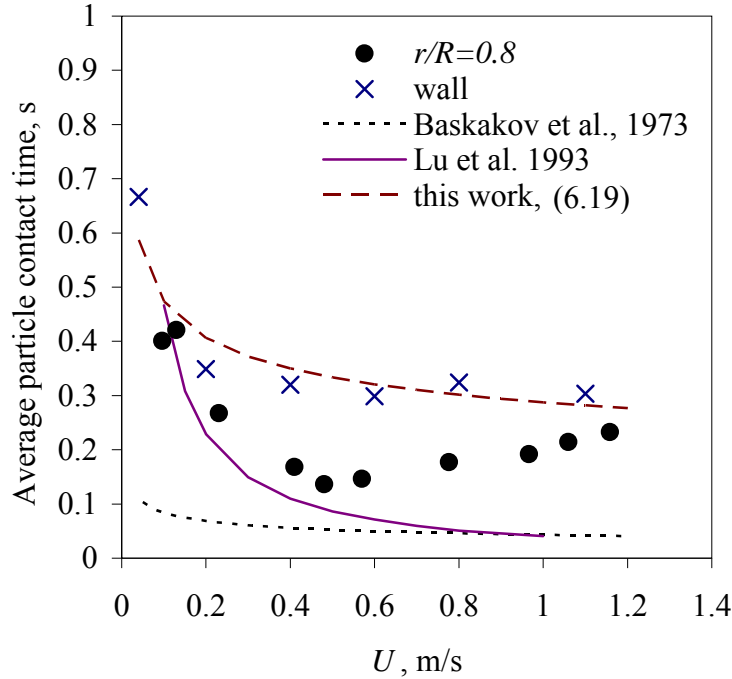
**Figure 6.14. Average packet contact time near and at the wall for
alumina particles.**

At the wall itself, the probe was covered by the dense phase at low gas velocities, gradually becoming exposed to voids (Figure 6.8) as the bed became turbulent. It was assumed that packet renewal at the wall surface is governed by the rising voids in the core (*r/R=0*), as identified from our transient *h* study (Chapter 5). Therefore the particle contact time at the wall can be estimated by:

$$t_{wall} = \frac{\text{dense phase fraction at the wall}}{\text{void frequency in the core}} = \frac{\delta_{d\,wall}}{f_{v_{core}}} \tag{6.18}$$

The frequency of rising voids in the core region was assumed to correspond to the crossing frequency of the optical probe signal at *r/R=0*, obtained by method (1), which also corresponds to the dominant frequency in the power spectrum of the differential pressure signal. The fraction of time the dense phase is present at the wall (Figure 6.8) was measured by an optical probe flush with the wall. The optical probe results for the dense phase fraction also correspond to results from the image analysis presented in Chapter 5.

The average contact time at the wall from equation (6.18), plotted in Figure 6.14 (**x** symbols), follows the trend predicted by Lu et al. (1993) at low superficial gas velocities and then remains relatively unchanged at ~0.3 s for $U \geq 0.4$ m/s.

The data for the average wall contact time from equation (6.18) were correlated using the modified particle Froude number suggested by Baskakov et al. (1973) giving:

$$t_{wall} = 0.61 \left[\frac{d_p g}{U_{mf}^2 \left(U / U_{mf} - 1 \right)^2} \right]^{0.1} \tag{6.19}$$

Above correlation is plotted in Figure 6.14.

6.4.2. Comparison of calculated and measured heat transfer coefficients

The estimated time-average heat transfer coefficient from equation (6.14) is compared to the measured h in Figure 6.15. Dense and intermediate phase fractions and contact times were determined experimentally. Least square curves are fitted through the experimental hydrodynamics data to avoid scatter. The solid line represents the total h calculated by equation (6.14), whereas the dashed and dotted lines represent the contributions from the dense and the intermediate phases, respectively. The effective thermal conductivities of the dense and intermediate packets were calculated from Kunii and Levenspiel (1991b) (Table A.1 in Appendix A), using the corresponding average local voidages of the packets, with these voidages assumed to be equal to ε_{mf} for the dense clusters and ε_{int}=0.5 ($\varepsilon_{min}+\varepsilon_{max}$) for the packets of the intermediate clusters. Particle properties are given in Table 2.2.

For the experimental data taken at the bed axis in the smaller column, the model predictions are within ± 7% and ±12% for FCC and alumina particles, respectively (Figures 6.15a and d). It is apparent that the heat transfer coefficients calculated considering only the dense phase contribution underestimated h at high gas velocities where turbulent flow structure is expected to be dominant and a significant fraction of particles are present in the void phase. The error from excluding the intermediate phase contribution is seen in Figure 6.15d to be greater for the FCC particles, which exhibit more typical turbulent flow structure over the range of velocities investigated than the alumina. The transition to turbulent fluidization for alumina particles is of a different nature. The local flow structure varies intermittently between bubbling and turbulent-like flow structure in the range of velocities studied. The dense phase fraction decreases very

gradually, on the one hand, and the increase in intermediate phase is slow, on the other hand. The trend of *h* vs. *U* for alumina particles is consistent with the gradual change in the flow structure. For alumina, the contribution of the intermediate phase appears to be slightly underestimated. This might be related to the threshold adopted to estimate the properties of the intermediate phase.
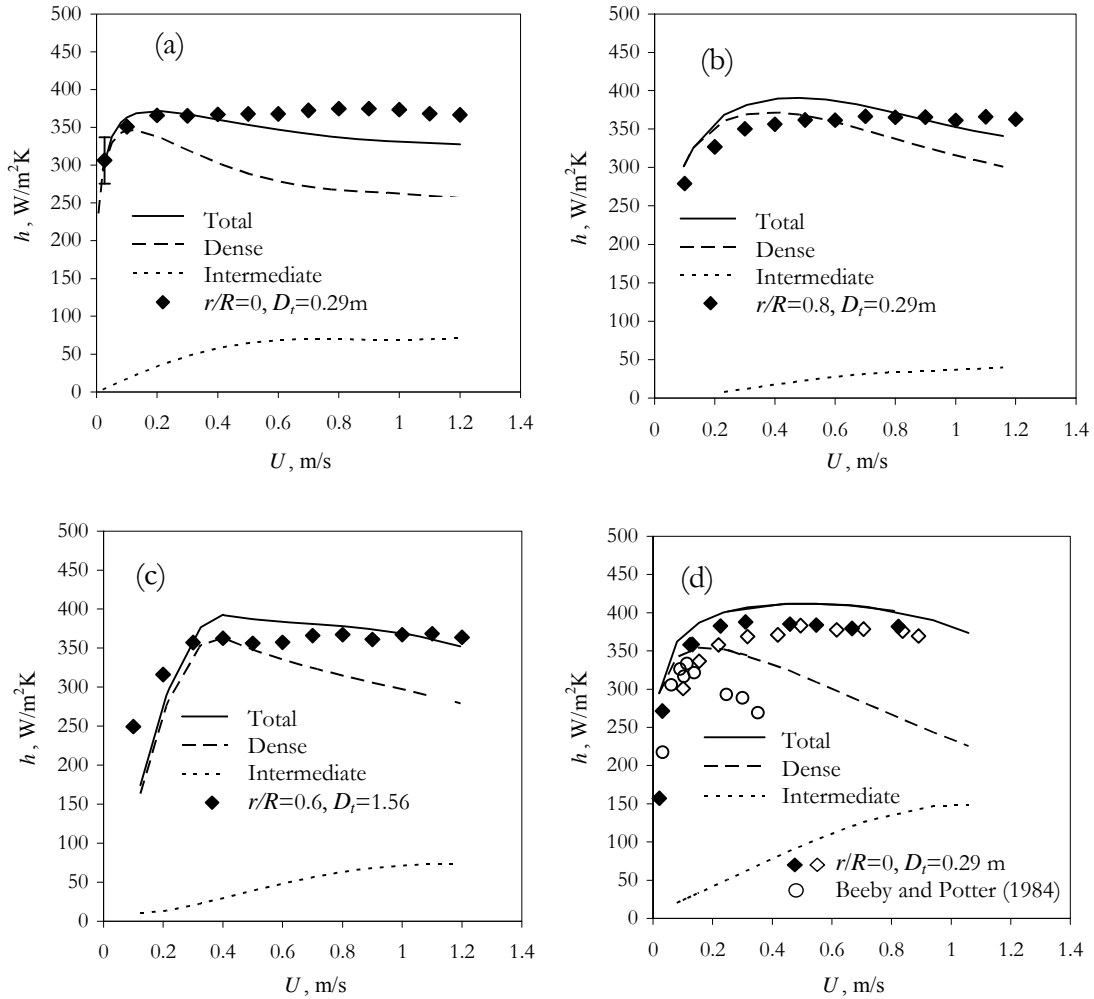
Figure 6.15. Comparison between heat transfer model predictions and experimental results for: a) – c) alumina; d) FCC (open diamonds=perforated plate; filled diamonds=bubble cap; circles=data from Beeby and Potter (1984)).

At the wall, it can be assumed that the dense phase packets are the dominant heat carriers. The heat transfer coefficient at the wall was calculated only from the contribution of the dense phase packets in equation (6.14). The packet contact time was calculated from equation (6.18). The thermal conductivity of the packet, $k_{effwall}$, was calculated from the Kunii and Levenspiel (1991b)

(equation A.2 in Table A.1 of Appendix A). The thermal resistance suggested by Molerus and Wirth, 1997 (Table A.2 in Appendix A) is included in the model. The model prediction and the experimental h are plotted against U in Figure 6.16. The model shows very good agreement with the experimental data, within ±10 %.
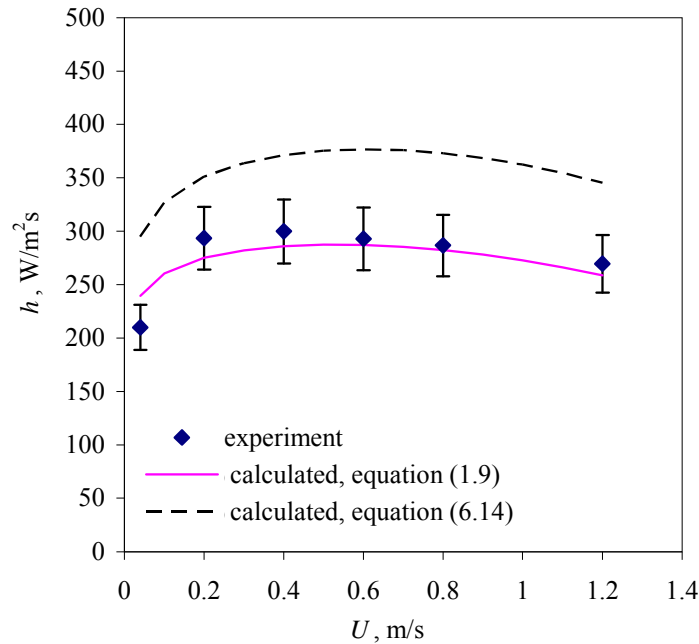
Figure 6.16. Heat transfer coefficient at the wall vs. U compared with model predictions. (Alumina, bubble cap distributor, H_0=0.8 m, D_t=0.29 m)

The proposed probability model needs to be tested against other experimental data. Note that it requires knowledge of local hydrodynamics. More research should be conducted to derive more general correlations for the time fraction and contact times for each phase.

6.5. Summary

- Comparison of our experimental heat transfer data to correlations from the literature indicates that most of the models and correlations work well at very low superficial gas velocities when the flow structure is bubbling. The most successful previous equation in describing the trend and values of h vs. U, even at high superficial gas velocities, was the semi-empirical correlation of Molerus and Wirth (1997).

- The packet renewal models published in the literature work well at low superficial gas velocities when measured local hydrodynamics are used. In bubbling beds, the heat transfer undoubtedly depends on bubble properties, and any parameter affecting the bubble properties influences the heat transfer. In turbulent beds, when dense particle packets become less present and more particles are suspended in the void phase, the method used to determine the hydrodynamic parameters in the packet renewal model plays an important role.

- The transition to the turbulent regime is gradual, with bubbling and turbulent flow structures coexisting in the range of superficial gas velocities investigated. A probability model, incorporating the fractions of particle packets typical for the specific hydrodynamic regimes, provides a rational approach to include the coexistence of different flow structures. This study revealed the need of turbulent bed hydrodynamics (indicated by fluctuations in the intermediate range of local voidages) to be included in the heat transfer models. Specific to this model is the contribution of an intermediate cluster phase to the total heat transfer coefficient, representing the particle streamers or packets suspended in the void phase at higher U. Assuming only two phases (dense phase at ε_{mf} and void phase at $\varepsilon_v=1$) in turbulent beds causes h to be underestimated.

- At the wall, the particle contact time was calculated from the dense phase fraction at the wall and frequency of voids in the core region, which was found to be higher than predicted in the turbulent flow regime. A new correlation for the particle contact time at the wall, when applied to the packet renewal model, worked well in predicting h.

Chapter 7

7. CONCLUSIONS AND RECOMMENDATIONS

7.1   Conclusions

This work is distinguished from other heat transfer studies in fluidized beds by the flow regime investigated. The effect of the changes in trends and features of the bed hydrodynamics at the onset of turbulent fluidization on the heat transfer process, suspected from the few studies reviewed in Chapter 1, was confirmed by extensive experimental work that included columns of two different diameters, two types of particles, two types of distributors, different static bed heights, and measurement at various radial and axial locations. Here, some of the most important findings are summarized.

- The onset of turbulent fluidization was defined at the superficial gas velocity where the two-phase flow structure starts to break down. From optical probes, this breakdown occurred locally, depending on the distance from the bed surface, circulation patterns and radial location. The transition was found to be more gradual for group AB particles (alumina) than for group A particles (FCC). For FCC particles, the method chosen to determine U_c did not play a significant role and this is expected to apply to group A particles in general.

- The heat transfer coefficient reach a maximum close U_c, the superficial gas velocity corresponding to onset of turbulent fluidization. Although U_c was affected by bed depth and radial location, the occurrence of the maximum heat transfer coefficient shifted correspondingly. In turbulent beds, the heat transfer coefficients were more uniformly distributed, both radially and axially, and did not change significantly with increasing superficial gas velocity, U, as long there was no significant increase in voidage near the heater. The effect of radial and axial position, static bed height, column diameter and distributor on the immersed tube-to-bed heat transfer coefficient became insignificant in the turbulent fluidization regime due to the well-mixed, homogenous local flow structure. By using appropriate correlations for the transition velocity, U_c, these findings can be applied to

selected ranges of operating conditions for processes benefitting from high and uniformly distributed heat transfer coefficients, as well as design decisions on where to locate heat transfer surfaces in the bed.

- Comparison of our experimental heat transfer data to correlations from the literature indicates that the semi-empirical correlation of Molerus and Wirth (1997) was the most successful in describing the trend and values of h vs. U, even at high superficial gas velocities, where other correlations failed.

- Different circulation patterns were found in the 0.29 m and 1.56 m diameter columns at lower gas velocities. The flow in the larger, relatively shallow bed was greatly influenced by the distributor configuration, which also influenced the nature of the transition to turbulent fluidization. U_c could not be established from the standard deviation of pressure fluctuations in the large column as no maximum could be identified. More accurate results on the transition from two-phase to turbulent fluidization were obtained from the optical probe. The transition is gradual, progressing radially from regions of higher voidage, where the highest h was measured in bubbling beds, to regions of low voidage. When the bed became fully turbulent, the local flow structure was similar in the two columns.

- The heat transfer coefficient reached a maximum and was independent of column diameter in the turbulent fluidization flow regime, confirming the benefit of operating within this flow regime from heat transfer and scale–up points of view. The superficial gas velocity at which the bed-to-surface heat transfer coefficient reaches a maximum was higher for the larger column. The effect of superficial gas velocity on heat transfer for columns of different diameter was scaled well by $Fr=U/(gD_t)^{0.5}$ at radial positions where similar local flow structures were present near the heater.

- A novel transparent heat transfer probe was developed which provided valuable insight on the heat transfer mechanism at the wall at the transition to turbulent fluidization, by allowing simultaneous measurement of the transient heat transfer, surface coverage, pressure and local voidage fluctuations. It was found that when the heat transfer surface remained covered by a layer of descending particles, instantaneous local coefficients, h, were strongly correlated with differential pressure fluctuations, confirming the relationship between bubbles rising in

the bed core and heat exchange at wall. This observation was used to estimate the particle contact time from the measured dense phase fraction at the wall and the frequency of voids in the core. The particle contact time was higher than predicted by correlations in the turbulent regime. The correlation for the particle contact time at the wall obtained in this work, worked well in predicting h when applied to the well-known packet renewal model.

- The gradual transition to the turbulent fluidization regime, with bubbling and turbulent flow structures coexisting, as observed in the hydrodynamics study, was reflected in the evolution of h with U. A probabilistic approach to heat transfer modeling was developed. The proposed model is based on the packet renewal theory and the probability of particle packets for the specific hydrodynamic regime to be present at the heat transfer surface. This approach allows for a gradual transition between flow regimes. It was shown that assuming distinctive two-phase flow, dense packets at ε_{mf} and bubbles with $\varepsilon \approx 1$, causes h to be underestimated in the turbulent flow regime. Therefore, the proposed model includes additional contribution of packets of intermediate voidages that reflect the typical turbulent flow structures. The model covers a wide range of operating conditions, changing smoothly from one flow regime to another in columns of different diameters and from the core of the bed to the wall, as long as the required hydrodynamic parameters are known. The model was tested using the experimental hydrodynamic data for the effect of radial position, column diameter, and for group A and AB particles. The applicability of this model for improvement or design of new processes is limited by the lack of general correlations for the required hydrodynamic parameters for the intermediate phase. This contrasts with the dense phase, where equations are available in the literature for bubbling beds.

7.2 Recommendations for future research

- It was shown in Chapter 3 that different criteria produce different results for the onset of turbulent fluidization. Because of the complexity of the pressure signal, the method of maximum standard deviation of pressure fluctuations is not always dependable. Further research on the onset of turbulent fluidization with group AB or B particles is needed to establish reliable methodology. The effect of immersed objects on the transition to turbulent fluidization also needs more attention.

- This work utilized the novel transparent heat transfer probe to determine the relationship between surface coverage and instantaneous heat transfer coefficient. The advantage of having visual access to the heat transfer surface should be exploited more, with further studies to obtain information on particle movement at the surface, to indentify clusters and measure their properties (size, velocity, and direction of flow) aided by imaging techniques.

- Future work needs to be conducted on the effect of scale. While in this work H_0 was kept constant and the column diameter was varied, studies that include the geometrical scaling d_t/D_t=const. and H_0/D_t=const. for shallow and deep beds would be of interest.

- The packet renewal model is difficult to apply in practice, as it needs knowledge of specific hydrodynamic parameters. Further research on the hydrodynamics recognizing the coexistence of bubbling and turbulent flow structures is needed. The flow structure typical for turbulent fluidization, characterized by increased fluctuations in the intermediate range of local voidages, needs to be investigated. Furthermore, the probability approach of heat transfer modeling should be extended to cover the transition between turbulent and fast fluidization flow regimes.

REFERENCES

Abba, I. A., Grace, J. R., Bi, H. T. and Thompson, M. L. (2003) "Spanning the flow regimes: Generic fluidized-bed reactor model", AIChE Journal, vol. 49, pp. 1838-1848.

Andreux, R., Gauthier, T., Chaouki, J. & Simonin, O. (2005) "New description of fluidization regimes", AIChE Journal, vol. 51, pp. 1125-1130.

Baeyens, J. and Geldart, D. (1974) "Investigation into slugging fluidized beds", Chemical Engineering Science, vol. 29, pp. 255-265.

Baskakov, A.P. (1964) "The mechanism of heat transfer between a fluidized bed and a surface" Int. Chem. Eng. vol. 4, pp. 320–324.

Baskakov, A.P., Berg, B.V., Vitt,O.K., Fillippovsky N.F., Kirakosyan V.A., Goldohin J.M. and Figiola R.S. (1973) "Heat transfer to objects immersed in fluidized bed", Powder Technology, vol. 8, pp. 273–282.

Baskakov, A.P. and Zvyagin, S.V. (1976) "Investigation of heat transfer in the space above an inhomogeneous fluidized bed", vol. 30, pp. 8-11.

Basu, P., Halder, P.K. and Nag, P.K. (1986) "Heat transfer in turbulent fluidized beds", Heat Transfer 1986, Proceedings of the 8th International Heat Transfer Conference., Hemisphere Publ. Corp., Washington, DC, USA, San Francisco, CA, USA, pp. 2599-2603.

Basu, P. and Nag, P. K. (1996) "Heat transfer to walls of a circulating fluidized-bed furnace" Chemical Engineering Science, vol. 51, pp. 1-26.

Beeby, C. and Potter, O.E. (1984) "Heat transfer between a horizontal tube bundle and fine particles with air or steam", AIChE Journal, vol. 30, pp. 977-980.

Bi, H. T., Grace, J. R. and Lim, K. S. (1995) "Transition from bubbling to turbulent fluidization", Industrial and Engineering Chemistry Research, vol.34, pp. 4003-4008.

Bi, H. T. (1999) "Pressure and voidage fluctuations in slugging fluidized beds", Canadian Journal of Chemical Engineering, vol. 77, pp. 568-572.

Bi, H.T. and Su, P. (2001) "Local phase holdups in gas-solids fluidization and transport", AIChE Journal, vol. 47, pp. 2025-2031.

Bi, H.T. and Grace, J.R. (1995) "Effect of measurement method on the velocities used to demarcate the onset of turbulent fluidization", Chemical Engineering Journal, vol. 57, pp. 261-271.

Bi, H.T., Ellis, N., Abba, I.A. and Grace, J.R. (2000) "State-of-the-art review of gas-solid turbulent fluidization", Chemical Engineering Science, vol. 55, pp. 4789-4825.

Botterill, J. S. M. (1986) "Fluid bed heat transfer" in Gas fluidization technology, Ed. D. Geldart, Wiley, Chichester, New York.

Brereton, C. and Grace, J. R. (1992) "Transition to turbulent fluidization", Chemical Engineering Research and Design, vol. 70, pp. 246-251.

Chandran, R. and Chen, J.C. (1982) "Bed-surface contact dynamics for horizontal tubes in fluidized beds", vol. 28, pp. 907-914.

Chatfield, C. (2001) Time-series forecasting, Chapman & Hall/CRC.

Chen, A. and Bi, H. T. (2003) "Pressure fluctuations and transition from bubbling to turbulent fluidization", Powder Technology 133 237-246.

Chen, J.C. (2003), "Heat transfer in fluidized beds" in Handbook of Fluidization and Fluid-Particle Systems, ed. W. Yang, Marcel Dekker, New York, pp. 257-286.

Chen, J.C., Grace, J.R. and Golriz, M.R. (2005) "Heat transfer in fluidized beds: Design methods", Powder Technology, vol. 150, pp. 123-132.

Churchill, S.W. and Chu, H.H.S. (1975) "Correlating equations for laminar and turbulent free convection from a vertical plate", International Journal of Heat and Mass Transfer, vol. 18, p.p. 1323-1329.

Coleman, H., W. and Steele, W.G. (1998) Experimentation and Uncertainty Analysis for Engineers, 2nd edn, John Wiley & Sons, New York.

Constantineau, J.P., Grace, J.R., Lim, C.J. and Richards, G.G. (2006) "Generalized bubbling-slugging fluidized bed reactor model.", Chemical Engineering Science, vol. 62, pp. 70-81.

Cui, H., Mostoufi, N. and Chaouki, J. (2000) "Characterization of dynamic gas-solid distribution in fluidized beds", Chemical Engineering Journal, vol. 79, pp. 133-143.

Darton, R.C., LaNauze, R.D., Davidson, J.F. and Harrison, D. (1977) "Bubble growth due to coalescence in fluidised beds", Transactions of the Institution of Chemical Engineers, vol. 55, pp. 274-280.

Davidson, J.F. & Harrison, D. 1963, Fluidized Particles. Cambridge University Press, New York.

Denloye, A.O.O. and Botterill, J.S.M. (1978) "Bed-to-surface heat transfer in a fluidized bed of large particles" Powder Technology, vol. 19, pp. 197–203.

Di Natale, F., Lancia, A. and Nigro, R. (2007) "Surface-to-bed heat transfer in fluidized beds: Effect of surface shape.", Powder Technology, vol. 174, pp. 75-81.

Di Natale, F., Lancia, A. and Nigro, R. (2008) "A single particle model for surface-to-bed heat transfer in fluidized beds", Powder Technology, vol. 187, pp. 68-78.

Dunham, G.E., Mann, M.D. and Grewal, N.S. (1993) "Dependence of transition to turbulent fuidization on static bed depth in a fluidized bed", Preprints of the fourth international conference on circulating fluidized beds, ed. A.A. Avidan, Somerset, PA.

Ellis, N. (2003) Hydrodynamics of gas-solid turbulent fluidized beds., Ph.D. dissertation, University of British Columbia, Vancouver.

Ellis, N., Bi, H.T., Lim, C.J. and Grace, J.R. (2004), "Hydrodynamics of turbulent fluidized beds of different diameters", Powder Technology, vol. 141, pp. 124-136.

Flamant, G., Gauthier, D. and Zerguerras, S. (1998) "Effect of particle diameter and particle size distribution on the wall-to-fluidized bed heat transfer", Trends in Heat, Mass and Momentum Transfer, vol. 4, pp. 61-75.

Gabor, J.D. (1970) "Wall-to-bed heat transfer in fluidized and packed beds", Chemical Engineering Progress, Symposium Series 66 no. 105, pp. 76-86.

Geldart, D. (1973) "Types of Gas Fluidization", Powder Technology, vol. 7, pp. 285-292.

Gelperin, N.I. and Einstein, V.G. (1971) "Heat Transfer in Fluidized Beds" in Fluidization, eds. J.F. Davidson and D. Harrison, Academic Press, London, New York, pp. 471-536.

Gidaspow, D. (1994) Multiphase flow and fluidization: continuum and kinetic theory descriptions, Academic Press, Boston.

Glicksman, L.R. (2003), "Fluidized Bed Scale-up" in Handbook of fluidization and fluid-particle systems, ed. W. Yang, Marcel Dekker, New York, pp. 1-38.

Goosens, W.R. A. (1986) " A boundary layer penetration model to the heat transfer to a vertical wall in glass-fluidized bed" in Heat and Mass Transfer in Fixed and Fluidized Beds, Ed. van Swaaij, W.P.M. and Afgan, N., Hemisphere Pub. Corp., Washington.

Grace, J. R., Chaouki, J., Pugsley, T. (2005) "Fludized bed reactor" in Encyclopedia of Chemical Processing, ed. S. Lee., vol. 1, pp. 1009-1021.

Grace, J.R. and Harrison, D. (1968), "The distribution of bubbles within a gas-fluidized bed", Institution of Chemical Engineers, Symposium Series, 30, pp. 105-113.

Grace, J.R. (1982) "Fluidized bed hydrodynamics" in Handbook of Multiphase Systems, ed. G. Hetsroni, Hemisphere, Washington, D.C., pp. 1024.

Grace, J.R. (2000) "Reflections on turbulent fluidization and dense suspension upflow", Powder Technology, vol. 113, pp. 242-248.

Grace, J.R. (2006) "Hydrodinamics of Fluidization" in Multiphase Flow Handbook, ed. C.T. Crowe, CRC Press, pp. 5.1-5.29.

Grewal, N.S., Saxena, S.C., Dolidovich, A.F. and Zabrodsky, S.S. (1979) "Effect of distributor design on heat transfer from an immersed horizontal tube in a fluidized bed", Chemical Engineering Journal and the Biochemical Engineering Journal, vol. 18, pp. 197-201.

Griffith, A.E., Louge, M. and Mohd-Yusof, J. (2000) "Simultaneous, noninvasive measurements of convective heat transfer and solid volume fraction at the wall of an entrained gas-solid suspension", Review of Scientific Instruments, vol. 71, pp. 2922-2927.

Hamidipour, M., Mostoufi, N., Sotudeh-Gharebagh, R. and Chaouki, J. (2005a), "Experimental investigation of particle contact time at the wall of gas fluidized beds", Chemical Engineering Science, vol. 60, pp. 4349-4357.

Hamidipour, M., Mostoufi, N., Sotudeh-Gharebagh, R. and Chaouki, J. (2005b), "Monitoring the particle-wall contact in a gas fluidized bed by RPT", Powder Technology, vol. 153, pp. 119-126.

Harrison, D. and Grace, J.R. (1971) "Fluidized bed with internal baffles" in Fluidization, eds. J.F. Davidson and D. Harrison, Academic Press, London, New York, pp. 599-626.

Hashimoto, O., S. Mori, S. Hiraoka, I.Yamada, T. Kojima and K. Tsuji. (1990) "Heat transfer to the surface of vertical tubes in the freeboard of a turbulent fluidized bed", International Chemical Engineering, vol.30, pp. 254-258.

Honeywell, (2008)Transparent Heaters 78000 Series [Homepage of Honeywell International Inc.], [Online]. Available: http://content.honeywell.com/sensing/prodinfo/heaters/transparentHeaters.pdf.

Hovmand, S. and Davidson, J.F. (1971) "Pilot plant and laboratory scale fluidized reactors at high gas velocities; the relevance of slug flow" in Fluidization, eds. J.F. Davidson and D. Harrison, Academic Press, London, New York..

Incropera, F. P. and DeWitt, D. P. (2001) Fundamentals of Heat and Mass Transfer (5th Ed.) New York, Wiley.

Issangya, A.S. (1998) Flow dynamics in high density circulating fluidized beds, Ph. D. Thesis, University of British Columbia.

Kays, W. M. (1955) "Numerical Solutions for Laminar Flow Heat Transfer in Circular Tubes" Trans. ASME, vol. 77, pp. 1265–1274.

Khan, A.R., Richardson J. F. and Shakiri, K. J. (1978) "Heat Transfer Between a Fluidized Bed and a Small Immersed Surface" in Fluidization, Eds. J. F. Davidson and D. L. Keairns, Cambridge University Press, New York.

Kim, S. W., Namkung, W. and Kim, S. D. (2000) "Solids Behaviour in Freeboard of FCC Regenerator", Journal of Chemical Engineering of Japan, vol. 33, pp. 78-85.

Kim, S.W., Ahn, J.Y., Kim, S.D. and Lee, D.H. (2002) "Heat transfer and bubble characteristics in a fluidized bed with immersed horizontal tube bundle", International Journal of Heat and Mass Transfer, vol. 46, pp. 399-409.

Knowlton, T.M., Karri, S.B.R. and Issangya, A. (2005) "Scale-up of fluidized-bed hydrodynamics", Powder Technology, vol. 150, pp. 72-77.

Ku, A. C., M. Kuwata, and Staub, F. W. (1981) "Heat transfer to horizontal tube banks in a turbulent fluidized bed of large particles", AIChE Symposium Series, 77 (208), pp.359-367.

Kunii, D. and Levenspiel, O. (1991a) "General equation for the heat-transfer coefficient at wall surfaces of gas/solid contactors", Industrial & Engineering Chemistry Research, vol. 30, pp. 136-141.

Kunii, D. and Levenspiel, O. (1991b) Fluidization engineering, 2nd ed., Butterworth-Heinemann, Boston.

Lancia, A., Nigro, R., Volpicelli, G. and Santoro, L. (1989) "Transition from slugging to turbulent flow regimes in fluidized beds detected by means of capacitance probes", Powder Technology, vol. 56, pp. 49-56.

Leckner, B. (2006) "Heat and Mass Transfer" in Multiphase Flow Handbook, ed. C.T. Crowe, CRC Press, pp. 5.30-5.54.

Leu, L., Hsia, Y. K. and Chen, C. C.. (1997) "Wall-to-bed heat transfer in a turbulent fluidized bed", AIChE Symposium Series, 317, pp. 83-86.

Li, H., Wang, Y. and Yang, J. (2004) "Local instantaneous temperature and time-averaged heat transfer coefficient in the bottom zone of a circulating fluidized bed", International Journal of Energy Research, vol. 28, pp. 433-448.

Lin, Q., Wei, F. and Jin, Y. (2001) "Transient density signal analysis and two-phase micro-structure flow in gas–solids fluidization", Chemical Engineering Science, vol. 56, pp. 2179-2189.

Lints, M. C., and Glicksman, L. R. (1993) "Parameters governing particle-to-wall heat transfer in a circulating fluidized bed" In A. Avidan, Proceedings of the 4th International Conference on Circulating Fluidized Bed, Somerset, PA. pp. 297–304.

Liu J., Grace J. R. and Bi H. T. (2001) "Novel multifunctional optical-fiber probe: I. Development and validation" AIChE Journal, vol. 49, pp. 1405 – 1420.

Louge, M. (1997), "Experimental techniques" in Circulating Fluidized Beds, eds. J.R. Grace, A.A. Avidan and T.M. Knowlton, Blackie, Glasgow, pp. 312-368.

Lu, J.D., Flamant, G. and Snabre, P. (1993) "Towards a generalized model for vertical walls to gas-solid fluidized beds heat transfer-1. particle convection and gas convection", Chemical Engineering Science, vol. 48, pp. 2479-2492.

Makkawi, Y.T. and Wright, P.C. (2002) "Fluidization regimes in a conventional fluidized bed characterized by means of electrical capacitance tomography", Chemical Engineering Science, vol. 57, pp. 2411-2437.

Martin, H. (1980) "Waerme- und stoffuebertragung in der wirbelschicht", Chem.-Ing.-Tech., vol. 52, pp. 199-209.

Martin, H. (1984) "Heat transfer between gas fluidized beds of solid particles and the surfaces of immersed heat exchanger elements", part I, Chemical Engineering and Processing, vol.18 pp.157-169.

Mathur, A., Saxena, S. C. and Chao, A. (1986) "Heat transfer from an immersed vertical tube in a gas-fluidized bed", Industrial and Engineering Chemistry, Process Design and Development vol.25, p.p. 156-163.

Matsen, J.M. (1996) "Scale-up of fluidized bed processes: Principle and practice", Powder Technology, vol. 88, pp. 237-244.

Mckain, D., Clark, N., Atkinson, C. and Turton, R. (1994) "Correlating local tube surface heat transfer with bubble presence in a fluidized bed", Powder technology, vol. 79, pp. 69-79.

Mickley, H.S. and Fairbanks, D.F. (1955) "Mechanism of heat transfer to fluidized beds", AIChE Journal, vol. 1, pp. 374-384.

Minco (2008) Thermal-Clear™ transparent heaters, [Homepage of Minco], [Online]. Available: http://www.minco.com/uploadedFiles/Products/Thermofoil_Heaters/Thermal-Clear/hs202g-thermal_clear.pdf.

Molerus O. and Wirth K. -E. (1997) <u>Heat Transfer in Fluidized Beds</u>, Chapman and Hall, New York.

Molerus, O., Burschka, A. and Dietz, S. (1995a), "Particle migration at solid surfaces and heat transfer in bubbling fluidized beds - I. Particle migration measurement systems", Chemical Engineering Science, vol. 50, pp. 871-877.

Molerus, O., Burschka, A. and Dietz, S. (1995b), "Particle migration at solid surfaces and heat transfer in bubbling fluidized beds - II. Prediction of heat transfer in bubbling fluidized beds", Chemical Engineering Science, vol. 50, pp. 879-885.

Mori, S. and Wen, C.Y. (1975) "Estimation of bubble diameter in gaseous fluidized beds", AIChE Journal, vol. 21, pp. 109-115.

Mostoufi, N. and Chaouki, J. (2004) "Flow structure of the solids in gas-solid fluidized beds", Chemical Engineering Science, vol. 59, pp. 4217-4227.

Nakajima, M., M. Harada, M. Asai, R. Yamazaki and G. Jimbo, "Bubble fraction and voidage in an emulsion phase in the transition to a turbulent fluidized bed". In: P. Basu, M. Horio and M. Hasatani, Editors, Circulating Fluidized Bed vol. III, Pergamon, Oxford (1991), pp. 79–84.

Oka, S.N. and Anthony, E. J. (2003), <u>Fluidized Bed Combustion</u>, Marcel Decker Inc.

Olsson, S.E. and Almstedt, A.E. (1995) "Local instantaneous and time-averaged heat transfer in a pressurized fluidized bed with horizontal tubes: influence of pressure, fluidization velocity and tube-bank geometry", Chemical Engineering Science, vol. 50, pp. 3231-3245.

Ozkaynak, T.F. and Chen, J.C. (1980) "Emulsion phase residence time and its use in heat transfer models in fluidized beds", AIChE Journal, vol. 26, pp. 544-550.

Patil, D.J., Smit J., van Sint Annaland, M., and Kuipers, J.A.M. (2006) "Wall-to-Bed Heat Transfer in Gas–Solid Bubbling Fluidized Beds", AIChE Journal, vol. 52, pp. 58–74.

Pohlhausen, K. (1921) "Zur näherungsweisen Integration der Differentialgleichung der laminaren Grenzschicht", J. Appl. Math. Mech. vol. 1, pp. 252–268.

Renganathan, K. and Turton, R. (1989) "Thermal inertia effects in fluidized bed to surface heat transfer", 1989 International Conference on Fluidized Bed Combustion: FBC - Technology for Today, Apr 30-May 3 1989, ASME, New York, USA, San Francisco, CA, USA, pp. 1095.

Rhodes, M. (1996) "What is turbulent fluidization?", Powder Technology, vol. 88, pp. 3-14.

Rhodes, M.J. and Geldart D. (1986) "Transition to turbulence" in Fluidization V, Eds. K. Østergaard and A. Sorensen, Engineering Foundation, New York pp. 281–288.

Sanderson, J., Rhodes, M. (2003) "Hydrodynamic similarity of solids motion and mixing in bubbling fluidized beds", AIChE Journal, vol. 49, pp. 2317-2327.

Saxena, S. C. (1989) "Heat transfer between immersed surfaces and gas-fluidized bed" in Advances in Heat Transfer, Ed. Hartnett J. P. and Irvine T.F. , Academic Press.

Schlünder, E. U. (1971) "Wärmeübergang an bewegte Kugelschüttungen bei kurzfristigem Kontakt". Chemie-Ingenieur-Technik 43, pp. 651–654.

Schweitzer, J., Bayle, J. and Gauthier, T. (2001), "Local gas hold-up measurements in fluidized bed and slurry bubble column", Chemical Engineering Science, vol. 56, pp. 1103-1110.

Sharma, A.K., Tuzla, K., Matsen J. and Chen J.C. (2000) "Parametric effects of particle size and gas velocity on cluster characteristics in fast fluidized beds", Powder Technology, vol. 111, pp. 114–122.

Sharma, K.R. and Turton, R. (1998) "Mesoscopic approach to correlate surface heat transfer coefficients with pressure fluctuations in dense gas-solid fluidized beds", Powder Technology, vol. 99, pp. 109-118.

Sjosten, J., Golriz, M.R., Nordin, A. & Grace, J.R. (2004) "Effect of particle coating on fluidized-bed heat transfer", Industrial and Engineering Chemistry Research, vol. 43, pp. 5763-5769.

Skotheim, T.A., Elsenbaumer, R.L. and Reynolds, J.R. (eds) (1997) <u>Handbook of Conducting Polymers</u>, 2nd edn, Dekker, New York.

Sobrino, C., Ellis N. and de Vegaa M. (2008) "Distributor effects near the bottom region of turbulent fluidized beds", Powder Technology, in press.

Staub, F. W. (1979) "Solids circulation in turbulent fluidized beds and heat transfer to immersed tube banks", Journal of Heat Transfer vol. 101, pp. 391-396.

Staub F. W. (1982) "Flow and heat transfer in large particle turbulent fluidized beds", Proceedings of CIESC/AIChE joint meeting of Chemical Engineering, 1 pp. 392-400.

Stein M., Y. L. Ding, J. P. K. Seville and D. J. Parker. (2000) "Solids motion in bubbling gas fluidized beds", Chemical Engineering Science vol.55, pp. 5291-5300.

Stewart P.S.B. and Davidson J.F., (1967) "Slug flow in fluidised beds", Powder Technology 1 (1967), pp. 61–80.

Sun, G. and Chen, G. (1989) "Transition to turbulent fluidization and its prediction", Fluidization VI : Proceedings of the International Conference on Fluidization, eds. J.R. Grace, L.W. Shemilt and M.A. Bergougnou, Engineering Foundation, New York, N.Y., pp. 33.

Sunderesan, S. R. and Clark, N. N. (1995) "Local Heat-Transfer Coefficients on the Circumference of a Tube in a Gas-Fluidized Bed", International Journal Multiphase Flow, vol. 21, pp. 1003-1024

Svensson, A., Johnsson, F. and Leckner, B. (1996a) "Bottom bed regimes in a circulating fluidized bed boiler", International Journal of Multiphase Flow, vol. 22, pp. 1187-1204.

Svensson, A., Johnsson, F. and Leckner, B. (1996b), "Fluidization regimes in non-slugging fluidized beds: the influence of pressure drop across the air distributor", Powder Technology, vol. 86, pp. 299-312.

Todes, O. M. (1965) " Applications of fluidized beds in the chemical industry", Part 2. Leningrad: Znanie. pp. 4–27.

Tunkey, J. W. (1977), <u>Exploratory Data analysis</u>, Reading, MA: Addison-Wesley.

van der Schaaf, J., Schouten, J.C., Johnsson, F. and van den Bleek, C.M. (2002) "Non-intrusive determination of bubble and slug length scales in fluidized beds by decomposition of the power spectral density of pressure time series", International Journal of Multiphase Flow, vol. 28, pp. 865-880.

Verloop, J. and Heertjes, P.M. (1974) "Periodic pressure fluctuations in fluidized beds", Chemical Engineering Science, vol. 29, pp. 1035-1042.

Vreedenberg, H.A. (1960) "Heat transfer between fluidized bed and vertical tube", Chemical Engineering Science , vol. 11, pp. 274-285.

Wang, X.S. and Rhodes, M.J. (2003) "Determination of particle residence time at the walls of gas fluidized beds by discrete element method simulation", Chemical Engineering Science, vol. 58, pp. 387-395.

Shafer, N.E. and Zare, R. N., (1991) "Through a beer glass darkly", Physiscs Today, vol. 44, pp. 48-52.

Wender, L., and G.T. Cooper. (1958) "Heat transfer between fluidized solids beds and boundary surfaces -- Correlation of data", Chemical Engineering Progress, vol.4, pp. 15-23.

Wu, R.L., Lim, C.J., Grace, J.R. and Brereton, C.M.H. (1991) "Instantaneous local heat transfer and hydrodynamics in a circulating fluidized bed", International Journal of Heat and Mass Transfer, vol. 34, pp. 2019-2027.

Wunder, R. (1980), Warmeubergang an vertikalen warmetauscherflachen in gaswirbelschichten, Dr-Ing. Dissertation, Technical University of Munich, Munich.

Yang, J.-S, Liu, Y. A. and Squires, A. M. (1986) "Shallow Fluid Beds of 'Master Beads'" in Fluidization V, Eds. K. Østergaard, A. Sorensen, pp. 409-416.

Zabrodsky, S.S. (1966) Hydrodynamics and Heat Transfer in Fluidized Beds, MIT Press, Cambridge, MA.

Zarghami, R., Mostoufi, N., Sotudeh-Gharebagh, R. and Chaouki, J. (2007) "Analysis and modeling of particle–wall contact time in gas fluidized beds", Chemical Engineering Science, vol. 62, pp. 4573-4578.

APPENDIX A

A. Previous studies on heat transfer in fluidized beds

A.1 Effect of different parameters on heat transfer coefficient

Below is a summary of the effect of different parameters on convective heat transfer coefficients. Note that most of the parametric studies were conducted in bubbling or slugging beds with group B particles.

Particle properties (d_p , ρ_p, c_{pp} , k_p , shape, coating, PSD)

Smaller and lighter particles give higher heat transfer coefficients. The decrease of heat transfer coefficient for larger particles occurs because the effective thickness of the gas film between the particles and heat transfer surface increases as the particle size, d_p, increases and the surface-to-volume ratio decreases. For small particles, the particle convective component is dominant and heat transfer is controlled by the volumetric heat capacity of the particles ρ_p, c_{pp}, and the gas thermal conductivity, k_g (Grace, 1982; Saxena, 1989). The thermal conductivity of the particles, k_p, was found to be insignificant (Gelperin and Einstein, 1971; Grace, 1982; Molerus and Wirth, 1997). Particle coating (Sjosten et al., 2004) and particles size distribution (PSD) (Flamant et al., 1998) were also found to affect heat transfer.

Gas properties (ρ_g , k_g, c_{pg}, μ_g)

Increasing k_g increases the heat transfer coefficient due to increased conduction through the gas layer between the particles and the heat transfer surface. Gas heat capacity, c_{pg}, and density, ρ_g, are significant for large particles when the convective component of heat transfer is dominant (Molerus and Wirth, 1997). The effect of the gas viscosity, μ_g is incorporated in the effect that it causes on the bed hydrodynamics.

Heat transfer surface configuration: size (l_t, d_t), geometry, location (r/R, z/H) and orientation

Short heat transfer surfaces give higher heat transfer coefficients due to more frequent renewal of the particles on the surface. For shorter surfaces, the lateral exchange of particles is more significant than for longer surfaces where the flow of particles is parallel to the surface (Molerus et

al., 1995b) However, with the increased lateral exchange of particles and short contact times in turbulent beds, it is uncertain if the probe length would have the same effect. For immersed surfaces the effect of tube diameter, d_t, on the heat transfer coefficient is rather complex as it is connected with column geometry, operating conditions and gas-solid system properties. Nevertheless, the effect of tube diameter is secondary. More on the effect of tube diameter on heat transfer coefficient is given in the review by Saxena (1989). The overall heat transfer coefficient in bubbling fluidized beds does not differ greatly for vertical and horizontal tubes, and the same is expected for turbulent beds. Many investigations of the distribution of local heat transfer coefficients around a horizontal tube in bubbling fluidized beds (e.g. Sunderesan and Clark, 1995) report the maximum heat transfer coefficient near the 9 and 3 o'clock positions. Heat transfer coefficients there are higher because of the short lateral surface and they compensate for the very low heat transfer coefficients below and above the tube in the overall heat transfer coefficient. The effect of inclined surfaces has not been reported in the literature for turbulent beds, but as for bubbling regimes, it is likely that inclination other that vertical or horizontal should be avoided. The geometry of the end of vertical tube tip was studied by Di Natale et al. (2007) who showed that geometry has an effect on heat transfer.

Static bed height (H_0)

Gelperin and Einstein (1971) note that H_0 does not influence the heat transfer coefficient and suggested it will have an influence only when the heat transfer surface is not fully immersed in the bed, i.e for surfaces completely or partly in the freeboard region. For shallow fluidized beds, h, increases with increasing H_0 (Yang et al., 1986).

Superficial gas velocity (U)

Starting from the minimum fluidization velocity, the heat transfer coefficient increases and reaches a maximum. Some researchers suggest that the maximum corresponds to the onset of turbulent fluidization. From the reviewed data (Table B.2), increasing U beyond that for maximum heat transfer coefficient yields two different trends: (1) the heat transfer coefficient reaches an asymptotic maximum and does not change much with further increase in velocity; and (2) the heat transfer coefficient decreases with increasing velocity and asymptotically approaches an almost constant value. The first trend was usually reported for smaller and lighter type A particles, while

the second trend was found for type B particles and laboratory scale columns. Research is needed to clarify the maximum heat transfer coefficient with increasing U.

Pressure (*p*)

Higher system pressure gives higher heat transfer coefficients (Hashimoto et al., 1990; Wunder, 1980). This could be due to smoother fluidization and to the increase in gas density affecting gas convection.

Temperature (*T*)

Increasing temperature gives higher heat transfer coefficients as reported by many authors for bubbling and fast fluidized beds (Botterill et al., 1986; Wu et al., 1989). This is likely due to increased k_g, but may also reflect changes in hydrodynamics and appreciable radiation effects for T >600 ^{0}C.

Unit size and configuration (distributor, D_t, H)

Many studies reported the effect of bed hydrodynamics on convective heat transfer. As the bed hydrodynamics is influenced by the size and geometry of the column, it is expected that convective heat transfer will also be affected. It was found that for larger CFB units, convective heat transfer is increased, probably due to increased mixing induced by the formation of large eddies (Basu and Nag, 1996). However, for bubbling beds, Gelperin and Einstein (1971) state that the data in the literature show different trends and the effect of D_t cannot be assessed a priori. The effect of design features when scaling-up should be also taken in consideration. Wunder (1980) performed experiments with 200 and 670 μm glass particles in three columns of diameter 0.080, 0.2 and 0.690 m. In the largest column, h_{max} was slightly higher (~15%) and shifted to higher gas velocities.

From this analysis, it can be concluded that the effect of different parameters is complex. It is sometimes impossible to isolate and study the effect of a single parameter and studies are needed to reveal or confirm the effect of different parameters on heat transfer in the turbulent fluidization regime. Many parameters influence the heat transfer rate by affecting the hydrodynamics of the bed. Considering that there are hydrodynamic features and trends specific for the fluidization regimes, it will be of interest to study the effect of the transition from one fluidization flow regime to another on the heat transfer trends.

A.2 Effective thermal conductivity and gas layer thermal resistance in the packet renewal model

Table A.1. Correlations for effective thermal conductivity of particle packets

Author	Correlations for k_{eff}	Notes
Gabor (1970)	$k_{eff}=0.9065/((0.13/k_g)+(0.667/k_p))$	(A.1)
Kunii & Levenspiel (1991b)	$k_{e\,ff} = \varepsilon_{mf}k_g + (1-\varepsilon_{mf})k_p\left[\dfrac{1}{(\delta_f/d_p)(k_p/k_g)+2/3}\right]$ $k_{e\,ffwall} = \varepsilon_{mf}k_g + (1-\varepsilon_{mf})k_p\left[\dfrac{1}{(\delta_{fwall}/d_p)(k_p/k_g)+1/3}\right]$	(A.2)

Table A.2. Thermal resistances employed in packet renewal model

Author	Correlation	Notes
Baskakov (1964)	$R_w=d_p/2k_w$	
Botteril (1986)	$R_w=d_p/10k_w$	
Molerus and Wirth (1997)	$R_w = \dfrac{l_l/0.09}{k_g}$	$l_l=\left[\dfrac{\mu}{\sqrt{g}(\rho_p-\rho_g)}\right]^{2/3}$ -length scale
Lints and Glicksman, (1993)	$\delta_f=0.0282d_p(1-\varepsilon_{susp})^{-0.59}$	Upper, dilute zone of CFB

A.3   Other models and correlations on bed-to-surface heat transfer

A.3.1   Kinetic theory analogy

The Nusselt number for conduction from particles in Martin's model is:

$$Nu_{cond} = \frac{h_{cond}d_p}{k_g} = (1-\varepsilon)Z\left[1-e^{-N}\right]$$

(A.3)

where, the dimensionless contact time, N, is:

$$N = Nu_{sp}/\kappa Z$$

(A.4)

To obtain the non-dimensional contact time, the group $\kappa = 4\ d_p/V_p\ t_c$ was assumed constant, where t_c is the time necessary to displace one particle over a distance proportional to its diameter and V_p is the particle velocity. Values of $\kappa = 2$ to 4 were obtained from the experimental data of Wunder (1980). The term Z may be interpreted as a dimensionless quantity for particle convective transfer, with

$$Z = \frac{\rho_p c_{pp}}{6k_g}\sqrt{\frac{gd_p^{\ 3}(\varepsilon-\varepsilon_{mf})}{5(1-\varepsilon_{mf})(1-\varepsilon)}}$$

(A.5)

Nu_{sp} in equation (A.4) is given by:

$$Nu_{sp} = 4\left[\left(1+\frac{2\Lambda}{d_p}\right)\ln(1+\frac{d_p}{2\Lambda})-1\right]$$

(A.6)

Nu_{sp} represents the theoretical maximum heat transfer coefficient between a surface and a spherical particle during point contact (Schlünder, 1971). Λ is the modified free path of gas molecules:

$$\Lambda = \left(\frac{2}{\gamma}-1\right)\frac{k_g}{p}\frac{\sqrt{2\pi RT/M}}{\left(c_{pg}-\dfrac{R}{2M}\right)}$$

(A.7)

where

$$\gamma = \left[1+10^{\{(0.6B-1-1000/T)B\}}\right]^{-1}$$

(A.8)

is an accommodation coefficient. $B=2.8$ for air at 298 K and $\gamma=0.9$.

To estimate the bed voidage, Martin suggested:

$$\frac{\varepsilon - \varepsilon_{mf}}{1 - \varepsilon_{mf}} = \frac{U - U_{mf}}{U_b + (U - U_{mf})}, \; U_b \approx 0.71\sqrt{gD_b} \tag{A.9}$$

where U_b is the bubble velocity.

A.3.2 Empirical correlations

Because heat transfer in fluidized beds is dependent on many parameters, empirical correlations are usually applicable over very narrow ranges of conditions and should be used only with caution.

One of the popular correlations for immersed vertical tubes is that by Vreedenberg (1960), who correlated a large number of experimental data from different authors by

$$\frac{h(D_t - d_t)}{k_g}\left(\frac{d_t}{D_t}\right)^{1/3}\left(\frac{k_g}{c_{pp}\mu_g}\right)^{1/2} = C\left(\frac{U(D_t - d_t)\rho_p}{\mu_g}\right)^n \tag{A.10}$$

For $\left(\dfrac{Ud_p\rho_p}{\mu_g}\right) < 2050$, C=2.7 10^{-16} and n=3.4.

This correlation does not include voidage and it predicts a continuous increase of the heat transfer coefficient with increasing superficial gas velocity, contrary to evidence that h passes through a maximum. However, it does include the column and immersed tube diameters.

Another empirical correlation for immersed vertical tubes that covers a wide range of experimental conditions is that of Wender and Cooper (1958):

$$\frac{hd_p}{k_g(1-\varepsilon)}\left(\frac{k_g}{c_{pg}\rho_g}\right)^{0.43} = 3.5 \cdot 10^{-4} C_R\left(\frac{\rho_g d_p U}{\mu_g}\right)^{0.23}\left(\frac{c_{pp}}{c_{pg}}\right)^{0.8}\left(\frac{\rho_p}{\rho_g}\right)^{0.66} \tag{A.11}$$

where the constant C_R depends on the radial position in the bed with C_R=1 at the axis.

Staub (1979) suggested that in the turbulent fluidized bed regime, solids flow and heat transfer correlations based on bubbling bed flow are not expected to predict measured performance. He proposed a turbulent fluidized bed solids flow model and heat transfer model, equation (A.12), that shows satisfactory agreement with their immersed tube bank heat transfer data for large particles. The particle and gas velocities were modeled assuming multiple upflow and downflow channels. The correlations for the average particle velocity include the average voidage and spacing between tubes, i. e.,

$$Nu = Nu_{gas}\left[1+\left(\frac{150}{d_p 10^6}\right)^{0.73}\left(\frac{0.42\rho_p(1-\bar{\varepsilon})\Delta Z_m^{0.4}}{\rho_g}\right)\right] \tag{A.12}$$

where ΔZ_m is the spacing between the tubes.

Hashimoto et al. (1990) derived a correlation for heat transfer to tubes in the freeboard. Equation (A.13) represents data obtained with a large-scale cold model apparatus at ambient temperature and atmospheric pressure and data from high temperature and pressure experiments, at 500 K and 4 to 9.4 MPa in a bench scale apparatus using the same particles as in the cold model. The proposed correlation, which includes the diameter of the column, is

$$Nu = 0.0326\,\text{Re}^{1.9}\left(\frac{c_{pp}}{c_{pg}}\right)^{1.9}\left(\frac{\rho_p}{\rho_g}\right)^{0.8}\left(\frac{D_t}{d_p}\right)^{-0.6} \tag{A.13}$$

APPENDIX B

B. Maximum heat transfer coefficient and optimum superficial gas velocity

Many correlations in the literature were derived for the maximum heat transfer coefficient, usually presented in the dimensionless form:

$Nu = a\, Ar^{\,b}$

Comparison between h_{max} in our experiments and the maximum calculated from these correlations is given in Table B.1. The best predictions were obtained by the Molerus and Wirth (1997) and Denloye and Botterill (1977) correlations.

Table B.1. Comparison between h_{max} from correlations and experiments

Author	Alumina	Error	FCC	Error
Molerus and Wirth (1997)	498	43%	415	8%
Martin (1980)	542	44%	528	38%
Zabrodski (1966)	554	47%	526	37%
Khan et al. (1978)	295	-22%	220	-42%
Denloye and Botterill (1977)	429	14%	459	20%

The Zabrodsky group (1966) conducted studies on the optimal superficial gas velocity, U_{opt}, at which h reaches a maximum. The most commonly used correlation for U_{opt} is by Todes (1965):

$$\mathrm{Re}_{opt} = \frac{Ar}{18 + 5.22\sqrt{Ar}} \tag{B.1}$$

This correlation predicts that h_{max} occurs at lower gas velocities than observed for most conditions in our work and in the work of Sun and Chen (1989), Basu et al. (1986) and Staub et al. (1979) who reported near coincidence of the onset of turbulent fluidization and h_{max}. Note that the maximum in the h vs. U curve is often difficult to establish because the curve is flat in the range of U where h is highest.

The review of heat transfer studies in Table B.2 leads to the observation that the development of the h vs. U curve changes when bubble growth becomes limited; either due to instability of bubbles (e.g. turbulent fluidization) or restrictions by geometry and configuration of the bed and the immersed surface(s) (slugging beds). The superficial gas velocity at which the maximum heat

transfer coefficient occurs (U_{opt}) for fluidized beds where slugging conditions were likely (bed deep enough and bubble growth limited by column diameter or tube spacing) were compared to the superficial gas velocity at the onset of slugging (U_{ms}), calculated from Stewart and Davidson (1967). Experimental data for U_{opt} for studies that extend to superficial gas velocities beyond U_c (calculated by the correlation of Dunham et al. (1993) for studies where U_c was not reported), were included in the analysis of the relationship between U_c and U_{opt}.

The ratios U_{opt} / U_{ms} and U_{opt} /U_c from the studies in Table B.2 appear in Figure B.1. It appears that, for lower Archimedes numbers, the maximum heat transfer coefficient was closer to U_c, while for higher Archimedes numbers (Ar>100), it was close to U_{ms} if slugging conditions were satisfied. The few cases where U_{opt} is near U_c at high Ar, were performed in beds with H_0/D_t 1 (Wunder, 1980; Basu et al. 1986). Thus, slugging did not occur, and the onset of turbulent fluidization was reported by Basu et al. (1986).
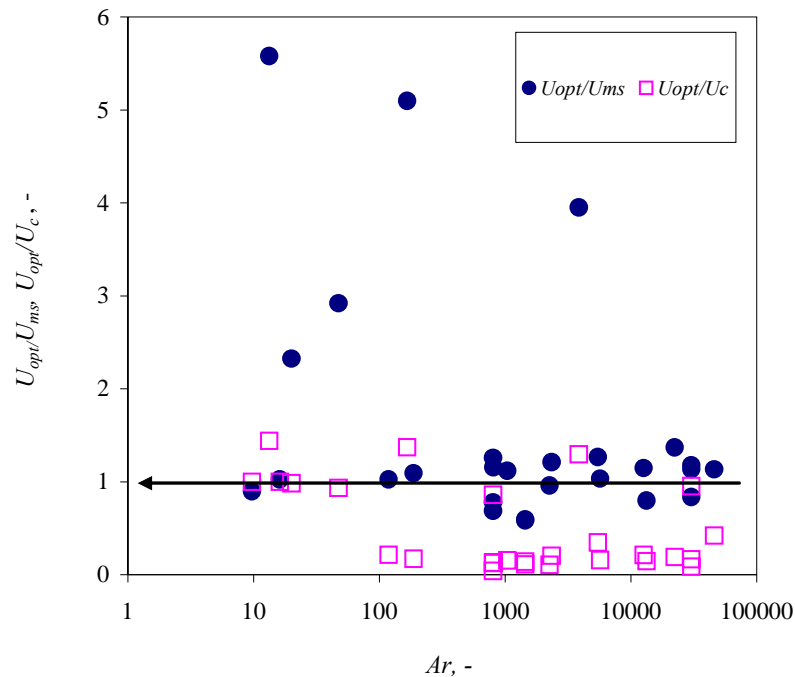
Figure B.1. Comparison of U_{opt} /U_{ms} and U_{opt}/U_c plotted as a function of Archimedes number. U_{opt} from experiments. U_{ms} and U_c, if not reported, were calulated by correlations of Stewart and Davidson (1967) and Durgham et al. (1993), respectively.

For fluidized systems that retain a relatively stable two-phase flow structure with increasing gas velocity (e.g. slugging), the effect of increased void fraction on h is significant and the heat transfer coefficient reaches a peak and starts to decrease at lower superficial gas velocities. However, if the turbulent flow structure takes over, the contribution from clusters suspended in the void phase shifts the maximum h to higher gas velocities. This might explain the discrepancies in the reported U_{opt} values in the literature.

.

Table B.2. Data used in Figure B.1.

Reference	Ar	D_t	U_{mf}	d_p	ρ_p	U_{opt}	U_{ms}	U_c	heat exchanger	notes
Sun et al. (1989)	10	0.8	0.002	54	1800	0.35	0.39	0.35	immersed tube	reported onset of turbulent
Wunder (1980)	13	0.2	0.002	55	2335	0.70	0.13	0.49	immersed tube	
Sun et al. (1989)	16	0.8	0.002	64	1800	0.40	0.39	0.40	immersed tube	reported onset of turbulent
this work	20	0.29	0.003	70	1700	0.55	0.24	0.56	immersed tube	
this work	48	0.29	0.006	80	2700	0.70	0.24	0.75	immersed tube	
Al-Busoul and Abu-Ziad (2000)	119	0.142	0.012	132	1500	0.18	0.18	0.84	immersed sphere	
Basu et al. (1986)	166	0.102	0.018	122	2665	0.8	0.16	0.58	wall probe	reported onset of turbulent
Al-Busoul and Abu-Ziad (2000)	187	0.142	0.019	128	2600	0.20	0.18	1.19	immersed sphere	
Wunder (1980)	805	0.2	0.037	200	2925	0.18	0.23	1.44	immersed tube	
Wunder (1980)	805	0.08	0.037	200	2925	0.11	0.16	2.82	immersed tube	
Wunder (1980)	805	0.69	0.037	200	2925	0.50	0.40	0.58	immersed tube	
diNatale et al. (2004)	809	0.1	0.036	210	2540	0.20	0.17	1.54	immersed tube	
Al-Busoul and Abu-Ziad (2000)	1046	0.142	0.060	227	2600	0.25	0.22	1.64	immersed sphere	
Hilal and Gunn (2002)	1449	0.09	0.058	325	1228	0.11	0.19	1.01	wall	
Hilal and Gunn (2002)	1449	0.29	0.058	325	1228	0.17	0.29	1.25	wall	
diNatale et al. (2004)	2264	0.1	0.071	290	2700	0.20	0.21	1.93	immersed tube	
Al-Busoul and Abu-Ziad (2000)	2346	0.142	0.084	357	1500	0.30	0.25	1.48	immersed sphere	
Basu et al. (1986)	3861	0.102	0.140	348	2665	1.1	0.28	0.85	wall probe	reported onset of turbulent
Wunder (1980)	5479	0.2	0.122	400	2490	0.40	0.32	1.16	immersed tube	
Al-Busoul and Abu-Ziad (2000)	5721	0.142	0.176	400	2600	0.35	0.34	2.26	immersed sphere	
Hilal and Gunn (2002)	12678	0.29	0.289	500	2950	0.60	0.52	2.86	wall	
Barreto et al., (1985)	13350	0.2	0.283	534	2550	0.38	0.48	2.62	immersed tube	reported slugging
diNatale et al. (2004)	22314	0.1	0.301	590	3160	0.60	0.44	3.19	immersed tube	
Wunder (1980)	30247	0.2	0.345	670	2925	0.45	0.54	2.74	immersed tube	
Wunder (1980)	30247	0.08	0.345	670	2925	0.55	0.47	6.55	immersed tube	
Wunder (1980)	30247	0.69	0.345	670	2925	0.80	0.71	0.84	immersed tube	
Wunder (1980)	45912	0.2	0.424	770	2925	0.70	0.62	1.67	immersed tube	

APPENDIX C

C. Heat losses from electrically heated vertical tube

To estimate heat losses, a two-dimensional model was constructed using FEHT (Finite Element Heat Transfer) software, where the heater tube was approximated as a vertical wall. The following volumes (illustrated on Figure C.1b) were defined:

1) Copper shell
2) Thermally conductive cement
3) Heating element
4) Teflon

Heat transfer by convection from the copper heat transfer surface was assumed to be given by $Q_b=hA_s(T_s -T_b)$. Because of symmetry, no heat flux was assumed in the horizontal direction, behind the heater axis. The temperatures of the bed, T_b (or surrounding air flow), the copper surface, T_s, and the Teflon near the ends of the heater tube, T_{tt} and T_{bt}, were measured with the heater mounted in the column, surrounded by flowing air (empty column) or in the fluidized bed. The heat loss, Q_l, by conduction through the Teflon was estimated from the program simulation iteratively.

As a first approximation, it was assumed that all the heat generated in the heating element was transferred by convection from the heater surface, without heat losses, and the convection heat transfer coefficient could be estimated as:

$$h_0 = \frac{Q_g}{A_s(T_s - T_b)} \qquad (C.1)$$

The estimated h_0, measured T_b, Q_g and temperatures near the end of the heater tube were used as inputs for the two-dimensional model. Iterations for h were repeated until the difference between the copper surface temperature obtained by the simulation (T_{si}) and the measured value (T_s) was small, $|T_s–T_{si}| \leq 0.1 \ ^0C$. The heat flux through boundary 1-1 in Figure C.1a was then noted. The heat losses were expressed as a percentage of the heat generated in the heating element vs. initial heat transfer coefficient (Figure 2.20) and correlated by:

$$Q_l/Q_g = 0.49 \ h_0^{-0.56} \qquad (C.2)$$

When equation (C.1) and equation (C.2) are substituted into equation (2.1), the actual h with the heat losses included is estimated from:
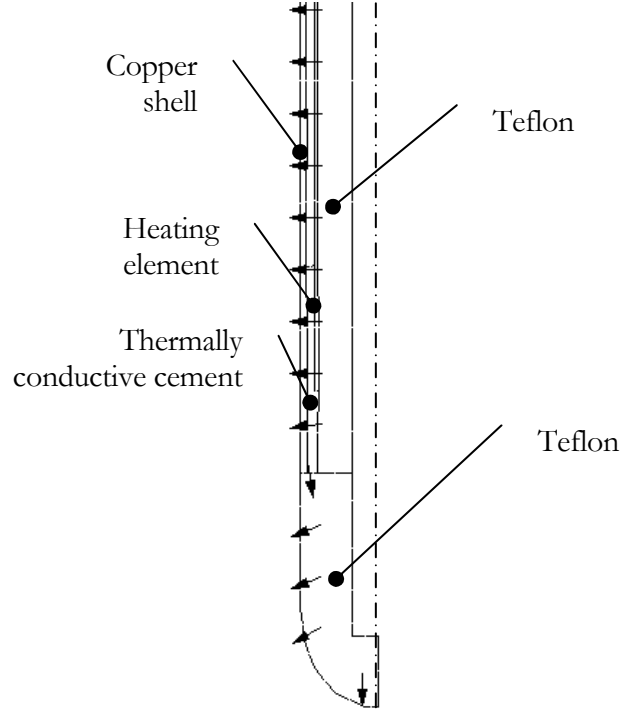
$$h = h_0 \left(1 - 0.49 h_0^{-0.56}\right) \qquad\qquad (C.3)$$

a) Temperature distribution   **b) Temperature gradients**
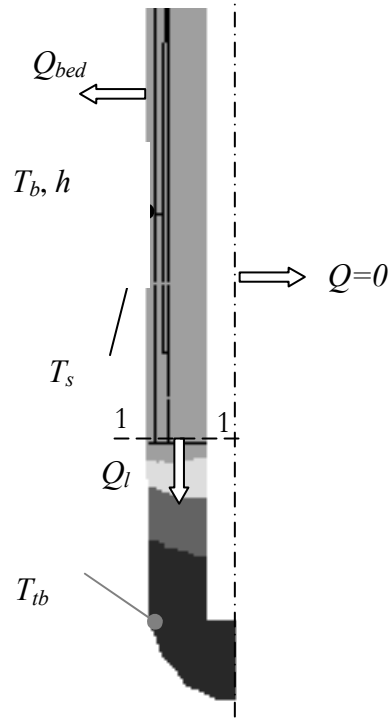
25.00 ■ 30.03 ■ 35.06 ■ 40.09 □ 45.12 ■ 50.15 °C

Figure C.1. Snapshot of software simulation of a) temperature distribution, b) temperature gradient. Conditions given in the table below. (Only lower half of heater is shown.)

h_0, W/m^{2}K	T_b, ^{0}C	T_s, ^{0}C	T_{tb}, ^{0}C	T_{tt}, ^{0}C	P, W	Q_l%
300	25	47.5	25.5	25	66	2%

To verify the method for heat loss evaluation, experiments without particles present in the column were conducted and the results compared to correlations from the literature (Incropera and DeWitt, 2001).

This set of experiments and simulations were conducted by keeping the power to the heater constant. The results obtained by the simulation are shown in Figure C.2. The heat losses decreased as the temperature difference increased, remaining close to 10% for T_s-T_b>20°C. For the fluidized bed experiments the temperature difference between the bed and the heat transfer surface was kept at ~20°C.
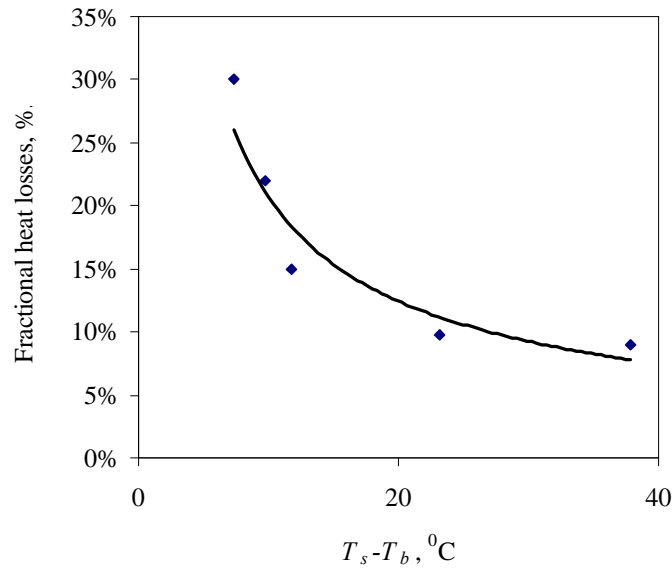
Figure C.2. Fractional heat losses as a function of temperature difference between the heat surface and the surrounding air flow.

The experimental results for heat transfer by air convection estimated with and without heat losses are compared in Figure C.3 with the heat transfer coefficients calculated from correlations. Correlations for free convection from a vertical surface by Churchill and Chu (1975) and forced convection from a vertical surface derived by Pohlhausen (1921) for laminar flow were used for calculations, as recommended by Incropera and DeWitt (2001). The figure shows that the heat transfer coefficients were overestimated if allowance for the heat losses was not included.
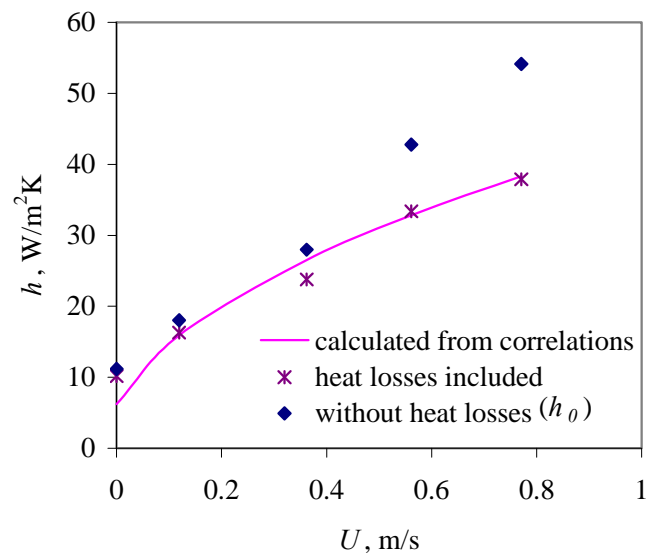
Figure C.3. Comparison of measured heat transfer coefficient with and without heat losses included and calculated from correlations for forced (Pohlhausen, 1921) and free (Churchill and Chu, 1975) air convection.

APPENDIX D

D. Drawings of traversing arm used in 1.56 m column.

Parts #: 1, 2, 4, 5, 9, 12, 13, 16, 17 supplied by UBC

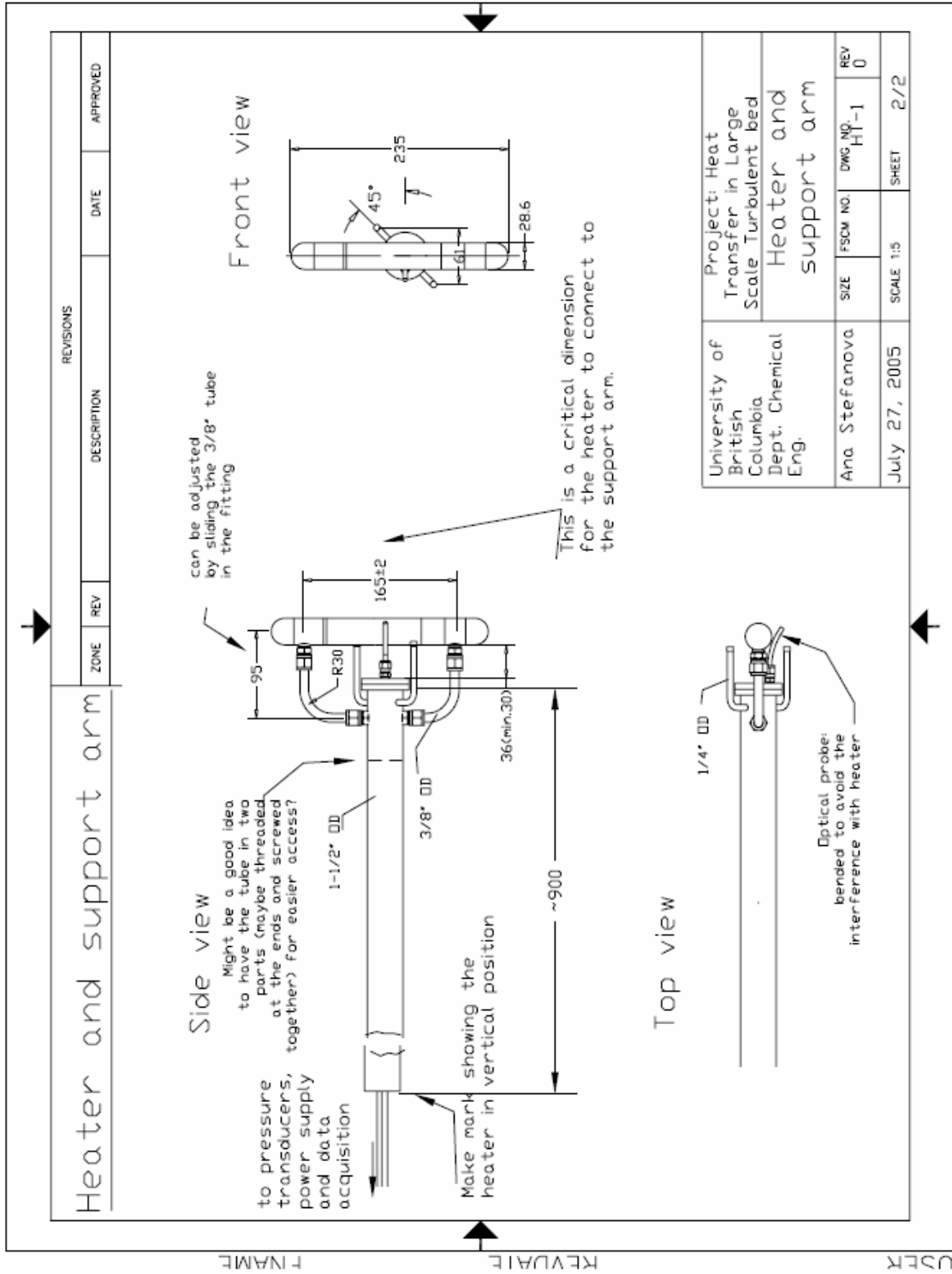| #	Description	Qty.
1	Heater	1
2	Teflon connecting and insulating pieces	5
3	Pressure taps (filter on tip)	2
4	Connection 3/8" ODtube – 1/4NPT male (BT)	2
5	Copper tube 3/8" OD	2
6	Connection 3/8" OD tube bored trough	2
7	Steel tube 1-1/2" OD with 2"OD flange (DWG HT-2)	1
8	Flange 2"OD (DWG HT-3)	1
9	Optical probe 4mmOD, tip 5mmOD, 400mm long	1
10	Connection 1/4OD Tube, bored trough	1
	not shown on drawing	
11	Gasket between 2" flanges	1
12	Electric wires from heater to power supply	1pair
13	Thermocouple wires 22AWG from heater to DAS	6pairs
14	Tubes 1/4"OD connecting to pressure sensors	2
15	Connecting rubber pieces for 1/4" tubes	2
16	Optical cable (extension for optical probe)	1pair
17	Swagelok 1-1/2" BT	1

University of British Columbia
Dept. Chemical Eng.
2216 Main Mall
Vancouver BC

Project: Heat Transfer in Large Scale Turbulent bed

Heater and Support Arm

Ana Stefanova

July 27, 2005

SIZE	FSCM NO.	DWG NO.		REV
		HT-1		0
SCALE		SHEET	1/2	

ZONE	REV	DESCRIPTION	DATE	APPROVED

REVISIONS

APPENDIX E

E. Images of heat transfer surface of the transparent probe at the wall.

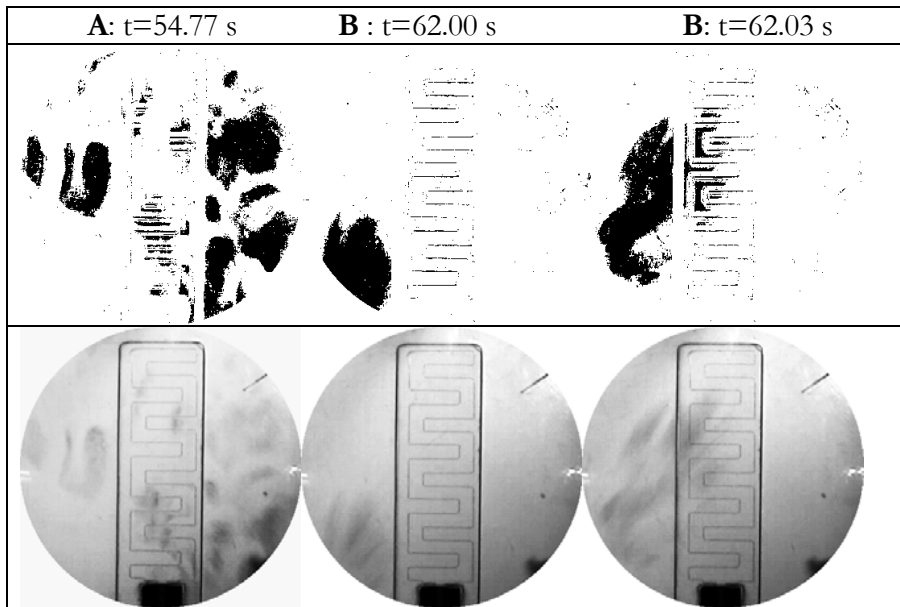**Table E.1. Typical binary and grayscale images of the probe surface with void present for *U*=0.18 m/s.**

| **A**: t=54.77 s | **B** : t=62.00 s | **B**: t=62.03 s |

Table E.2. Consecutive binary and greyscale images of descending void at the probe surface for *U*=1.2 m/s
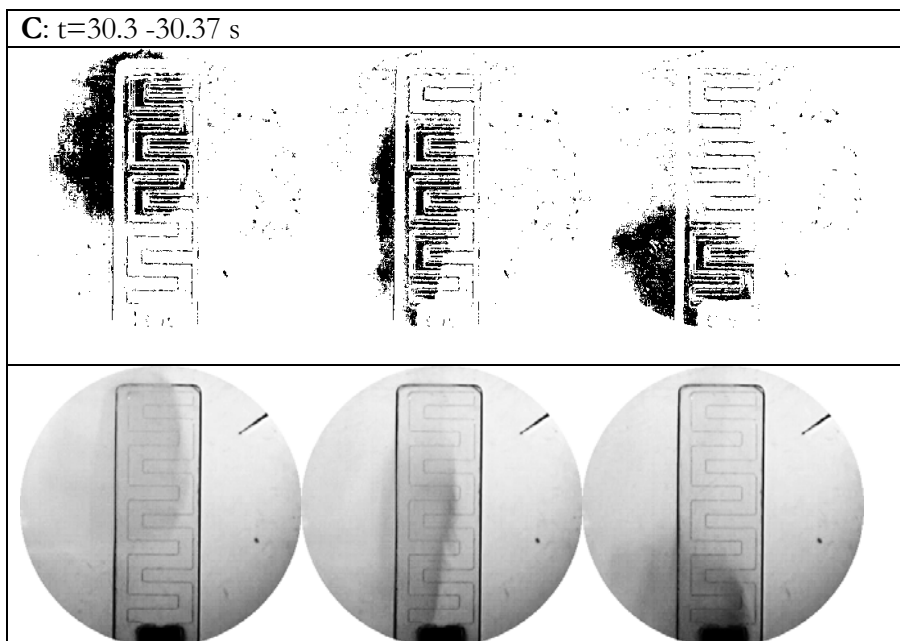

C: t=30.3 -30.37 s

Table E.3. Consecutive binary and greyscale images of the probe surface showing prolonged void presence for *U*=1.2 m/s

D: t=32.33 (first image) – 32.93 s (last image)

-